



Provided by the author(s) and University of Galway in accordance with publisher policies. Please cite the published version when available.

Title	The Mechanical Performance of Permanent and Bioabsorbable Metal Stents
Author(s)	Grogan, James A.
Publication Date	2012-09-13
Item record	<a href="http://hdl.handle.net/10379/3744">http://hdl.handle.net/10379/3744</a>

Downloaded 2024-04-16T23:20:26Z

Some rights reserved. For more information, please see the item record link above.



# The Mechanical Performance of Permanent and Bioabsorbable Metal Stents

**James A. Grogan**

**Supervisors:** Prof. Peter McHugh and Prof. Sean Leen



A thesis submitted to the National University of Ireland as fulfilment of the requirements for the Degree of Doctor of Philosophy.

Mechanical and Biomedical Engineering,

National University of Ireland, Galway.

2013

# Contents

<b>Abstract</b>	<b>vi</b>
<b>Acknowledgements</b>	<b>viii</b>
<b>List of Publications</b>	<b>x</b>
<b>1. Introduction</b>	<b>1</b>
1.1. Chapter Summary . . . . .	1
1.2. Heart Disease and its Treatment . . . . .	2
1.2.1. Ischaemic Heart Disease . . . . .	2
1.2.2. Percutaneous Coronary Intervention . . . . .	4
1.3. Past and Present Coronary Stents . . . . .	6
1.3.1. Stent Mechanics . . . . .	6
1.3.2. Bare Metal Stents . . . . .	8
1.3.3. Drug Eluting Stents . . . . .	9
1.3.4. Stent Manufacture . . . . .	10
1.4. Numerical Methods in Stent Analysis and Design . . . . .	10
1.4.1. Finite Element Analysis . . . . .	10
1.4.2. Modelling of Stent Materials . . . . .	12
1.5. Future Developments in Coronary Stents . . . . .	13
1.5.1. Thinner Struts in Permanent Stents . . . . .	13
1.5.2. Bioabsorbable Metal Stents . . . . .	16

## Contents

1.6. Stent Fracture . . . . .	18
1.7. Thesis Motivations and Aims . . . . .	19
1.8. Thesis Overview . . . . .	20
<b>2. Background</b>	<b>22</b>
2.1. Chapter Summary . . . . .	22
2.2. The Mechanics of Microscale Devices . . . . .	23
2.2.1. Structure and Deformation of Metallic Crystals . . . . .	23
2.2.2. Size Effects in Metallic Components . . . . .	28
2.2.3. Numerical Modelling of Size Effects . . . . .	29
2.3. The Mechanics and Corrosion of Absorbable Metal Stents . . . . .	32
2.3.1. Magnesium Corrosion Studies . . . . .	32
2.3.2. Iron Corrosion Studies . . . . .	38
2.3.3. Numerical Modelling of Corrosion . . . . .	38
2.3.4. Absorbable Metal Stent Mechanics . . . . .	40
<b>3. Theory</b>	<b>42</b>
3.1. Chapter Summary . . . . .	42
3.2. Continuum Mechanics . . . . .	43
3.2.1. Deformation and Stress . . . . .	43
3.2.2. Equilibrium Equations and Principle of Virtual Work . . . . .	48
3.3. Material Constitutive Behaviours . . . . .	49
3.3.1. Isotropic Linear Elasticity Theory . . . . .	49
3.3.2. Large Strain Elasticity Theory . . . . .	50
3.3.3. $J_2$ Plasticity Theory . . . . .	54
3.3.4. Crystal Plasticity Theory . . . . .	56
3.4. The Finite Element Method . . . . .	60
3.4.1. The Finite Element Method in Structural Problems . . . . .	61
3.4.2. Implicit and Explicit Solution Schemes . . . . .	64
3.4.3. Strain Measures in Abaqus . . . . .	66

*Contents*

3.5. ALE Adaptive Meshing . . . . .	67
3.6. Optimization Methods . . . . .	68
<b>4. The Mechanical Performance of Permanent and Absorbable Metal Stents</b>	<b>75</b>
4.1. Chapter Summary . . . . .	75
4.2. Introduction . . . . .	76
4.3. Methods . . . . .	78
4.4. Results . . . . .	85
4.5. Discussion . . . . .	88
4.6. Conclusions . . . . .	92
<b>5. Microscale Mechanics of Permanent and Absorbable Metal Stents</b>	<b>95</b>
5.1. Chapter Summary . . . . .	95
5.2. Introduction . . . . .	96
5.3. Statistical Size Effects in FCC Materials . . . . .	96
5.3.1. Methods . . . . .	96
5.3.2. Results . . . . .	105
5.3.3. Discussion . . . . .	115
5.4. Statistical Size Effects in Magnesium . . . . .	121
5.4.1. Methods . . . . .	121
5.4.2. Results . . . . .	127
5.4.3. Discussion . . . . .	132
5.5. Accounting for Statistical Size Effects in Stent Design . . . . .	134
5.6. Study Limitations . . . . .	137
5.7. Conclusions . . . . .	140
<b>6. A Phenomenological Corrosion Model for Magnesium Stents</b>	<b>143</b>
6.1. Chapter Summary . . . . .	143
6.2. Introduction . . . . .	144

## Contents

6.3. Methods . . . . .	145
6.3.1. Alloy Characterisation . . . . .	145
6.3.2. Corrosion Model Development . . . . .	150
6.3.3. Corrosion Model Calibration and Validation . . . . .	152
6.3.4. Stent Application . . . . .	155
6.4. Results . . . . .	158
6.4.1. Alloy Characterisation . . . . .	158
6.4.2. Corrosion Model Calibration . . . . .	160
6.4.3. Stent Application . . . . .	163
6.5. Discussion . . . . .	165
6.6. Limitations . . . . .	167
6.7. Conclusions . . . . .	169
<b>7. Designing an Optimum Bioabsorbable Metal Stent</b>	<b>171</b>
7.1. Chapter Summary . . . . .	171
7.2. Introduction . . . . .	172
7.3. Methods . . . . .	173
7.3.1. ALE Corrosion Model . . . . .	174
7.3.2. Effects of corrosion on AMS performance . . . . .	176
7.3.3. Corrosion Damage Model . . . . .	187
7.4. Results . . . . .	189
7.4.1. Parameter and Optimization Studies . . . . .	189
7.4.2. In-Vivo Deployment Simulations . . . . .	191
7.5. Discussion . . . . .	197
7.5.1. ALE Corrosion Model . . . . .	197
7.5.2. Parameter and Optimization Studies . . . . .	199
7.5.3. In-Vivo Deployment Simulations . . . . .	200
7.6. Limitations . . . . .	201
7.7. Conclusions . . . . .	202

<b>8. Physical Modelling of AMS Corrosion</b>	<b>204</b>
8.1. Chapter Summary . . . . .	204
8.2. Introduction . . . . .	204
8.3. Methods . . . . .	205
8.4. Results . . . . .	210
8.5. Discussion . . . . .	214
8.6. Limitations . . . . .	217
8.7. Conclusions . . . . .	217
<b>9. Discussion and Conclusions</b>	<b>219</b>
9.1. Chapter Summary . . . . .	219
9.2. Thesis Summary . . . . .	219
9.3. New Stent Design Recommendations and Insights . . . . .	223
9.4. Future Work . . . . .	226
9.5. Conclusions . . . . .	227
<b>A. Appendices</b>	<b>229</b>
A.1. Soft Tissue Material Models . . . . .	229
A.2. Corrosion Model Verification . . . . .	230
A.3. Corrosion Damage Model Implementation . . . . .	236
A.4. Time Scaling in the Corrosion Subroutines . . . . .	239

# Abstract

Developments in metallic coronary stents are toward permanent devices with thinner struts and bioabsorbable devices. To facilitate the development of these promising technologies an improved understanding of thin-strut and bioabsorbable stent mechanical performance is important. The work presented in this thesis uses computational mechanics to investigate the mechanical performance of corroding bioabsorbable metal stents and computational micromechanics to investigate the performance of thin metallic struts undergoing large plastic deformation.

The short-term mechanical performance of stents consisting of a range of bioabsorbable and permanent metals is first investigated using typical stent modelling approaches. It is found that devices consisting of bioabsorbable metals can match the short-term scaffolding performance of permanent stents, however the former has a greater risk of fracture. The mechanical performance of permanent and bioabsorbable stent struts undergoing large deformations is then investigated in more detail, using micromechanical analyses based on crystal plasticity theory. Lower limits on suitable strut thicknesses for bioabsorbable and permanent stents are identified, based on predictions of microstructure-dependent ductility size effects.

A corrosion model is developed for bioabsorbable metal stents and is calibrated

## *Abstract*

and validated based on immersion experiments on thin bioabsorbable alloy foils. The model is used to predict the scaffolding performance of stents undergoing corrosion in the body. It is found that the form of corrosion undergone by the device in the body has a strong influence on scaffolding performance. In particular, it is predicted that experimentally observed localized corrosion leads to a significant decrease in scaffolding duration relative to an ideal uniform corrosion behaviour, pointing to recommendations for future alloy development for such applications.

# Acknowledgements

First I would like thank my supervisors Prof. Peter McHugh and Prof. Sean Leen for their support, expertise and contagious enthusiasm for this research.

Next I would like to thank my funding body, the Irish Research Council (IRC) for their financial support and the SFI/HEA funded Irish Centre for High End Computing (ICHEC) for the provision of indispensable computational facilities and support. Thanks to the NUI Galway technical staff: Mr. Pat Kelly, Mr. William Kelly, Mr. Liam Brennan, Mr. Cormac O'Brien and Dr. Eadaoinn Timmons, for their help with equipment and manufacturing. Dr. Barry O'Brien provided many useful insights into magnesium corrosion and gave me the chance to have a useful meeting with those in the medical device industry, which was much appreciated. Thanks to my colleagues in Politecnico di Milano: Dario, Francesco and Gabriele, who made me very welcome on my visits and for insightful discussions on magnesium corrosion and modelling.

I would like to thank my many friends and colleagues at NUI Galway, in particular the former Skylab gang: Ciaran, Claire, Evelyn, Neil, Oliver and Teng for sharing the PhD experience. Thanks also to everyone in the 'New Engineering Building' for the good times at lunch. Thanks to my friends Cian, Emer, Greg, Jason, Karl, Mike, Ryan (*et al.*) and the old engineering crew (and Darren) for the

## *Acknowledgements*

many adventures during the last few years.

Finally, thanks to my loving parents and brothers, David and Niall, without whose support this work would not have been possible.

# List of Publications

The work presented in this thesis has appeared in the following publications:

**Chapter 4:** JA Grogan, SB Leen, and PE McHugh. Comparing coronary stent material performance on a common geometric platform through simulated bench-testing. *Journal of the Mechanical Behavior of Biomedical Materials*, 12:129-138, 2012.

**Chapter 5:** JA Grogan, SB Leen, and PE McHugh. Influence of statistical size effects on the plastic deformation of coronary stents. *Journal of the Mechanical Behavior of Biomedical Materials*, 20:61-76, 2013.

**Chapter 6:** JA Grogan, BJ O'Brien, SB Leen, and PE McHugh. A corrosion model for bioabsorbable metallic stents. *Acta Biomaterialia*, 7(9):3523-33, 2011.

**Chapter 7:** JA Grogan, SB Leen, and PE McHugh. Optimizing the design of a bioabsorbable metal stent using computer simulation methods. *Biomaterials*, 34:8049-60, 2013.

The following publications, arising from work in this thesis, are in submission:

*List of Publications*

**Chapter 5:** JA Grogan, SB Leen, and PE McHugh. Computational micromechanics of bioabsorbable magnesium stents. In submission, 2013.

**Chapter 8:** JA Grogan, SB Leen, and PE McHugh. A physical corrosion model for bioabsorbable metallic stents. In submission, 2013.

# 1. Introduction

## 1.1. Chapter Summary

Coronary stents are widely used in the treatment of heart disease. The long-term presence of the stent in the body is associated with in-stent restenosis and late-stent thrombosis, two major causes of failure of the stenting procedure. Two promising future developments for reducing the prevalence of these stent-related diseases are permanent stents with thinner struts and bioabsorbable metal stents.

In order to facilitate the development of next generation stents, it is important that the mechanics of the device are well understood. Two areas where current knowledge is lacking are the role of size effects in governing the performance of thin stent struts and the mechanics of bioabsorbable stents during corrosion. Improving the current understanding of these two aspects of stent mechanics will aid in the design of next generation devices and in improving the success rates of the stenting procedure.

Heart disease and coronary stenting are introduced in **Sections 1.2** and **1.3**. The use of numerical modelling in stent design is discussed in **Section 1.4**. Future

directions in stent design are discussed in **Section 1.5** and stent fracture, an important consideration in stent analysis and design, is discussed in **Section 1.6**. Thesis motivations and an overview of the contents of subsequent chapters are given in **Sections 1.7** and **1.8** respectively.

## 1.2. Heart Disease and its Treatment

### 1.2.1. Ischaemic Heart Disease

Ischaemic heart disease (IHD) is a condition characterized by restricted blood supply to the heart muscle. IHD can lead to severe chest pain, known as angina. In more severe cases it can also lead to death of the tissue, or myocardial infarction. IHD is the most common cause of death in Europe, accounting for one in five mortalities [1].

The heart is a muscle that pumps oxygenated blood throughout the body. The muscle tissue in the heart, or myocardium, also requires a supply of oxygenated blood. This is delivered through narrow tubular vessels known as the coronary arteries, shown in Fig. 1.1. The walls of healthy coronary arteries are comprised of three distinct layers; the intima, the media and the adventitia, shown in Fig. 1.2. Each layer consists of a network of helically wound elastic fibres, embedded in an elastic matrix of connective tissue. The intima forms the artery's inner wall and includes a single layer of endothelial cells on its inside surface. These cells form a semi-permeable barrier between the inside of the artery wall and the bloodstream. The media is the middle layer of tissue and contains layers of vascular smooth muscle cells. These cells control the calibre of the artery through their contraction and relaxation. The adventitia is the outer-most layer and consists

## 1. Introduction

primarily of collagenous connective tissue.

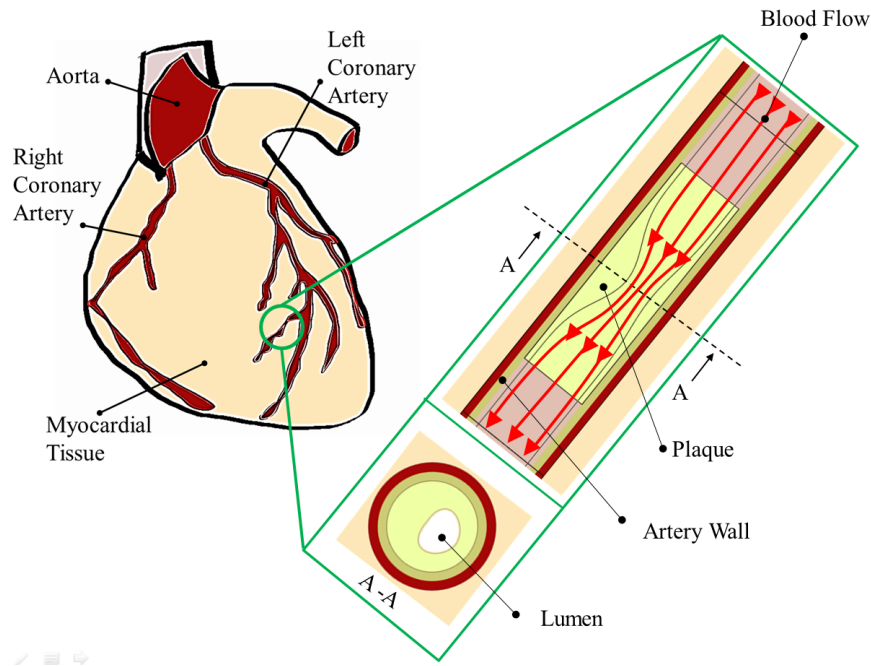


**Figure 1.1.:** The coronary arteries and their branches. A cross-section of a diseased arterial region is shown in the outset.

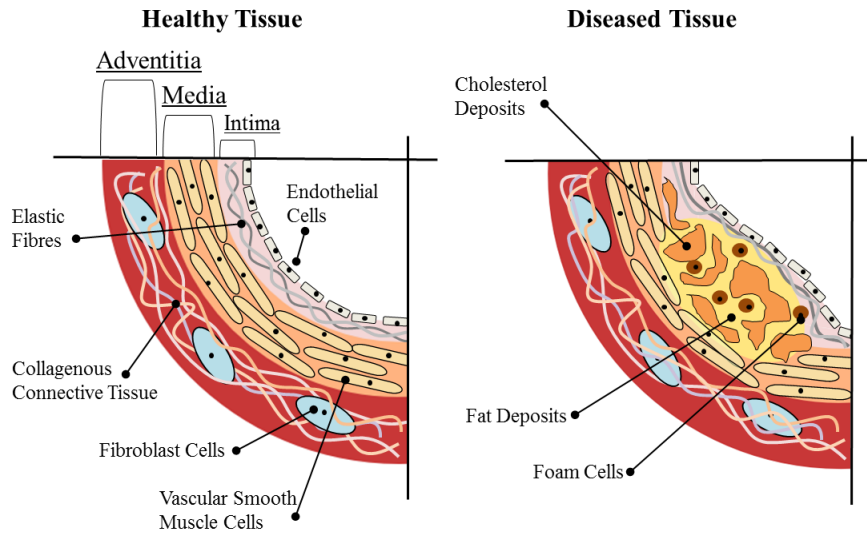


**Figure 1.2.:** The composition of healthy and diseased regions of the artery wall.

Over time, the inner diameter, or lumen, of the coronary arteries can be reduced due to the build-up of deposits in the artery wall and associated blood clotting. This build up, shown in Fig. 1.2 and known as plaque, can contain foam cells, fatty deposits such as cholesterol, and fibrous tissue. The gradual accumulation of deposits in the plaque can result in rupture of the intimal layer, exposing the deposits in the plaque to the blood-stream. The artery can become blocked

due to the gradual build-up of plaque or, more commonly, due to the formation of blood clots, or thrombus, from the release of deposits into the blood-stream. This blockage of the artery cuts off the supply of oxygen and glucose to the heart tissue, which is a manifestation of IHD.

### 1.2.2. Percutaneous Coronary Intervention

Percutaneous coronary intervention (PCI) is a widespread and successful treatment for IHD, which involves manually or surgically removing blockages in the coronary arteries. Over one million PCI's are carried out each year across Europe [1], with coronary angioplasty and stenting being the most common form of the treatment [2]. A detailed description of coronary angioplasty is given in Baim [3].

Coronary angioplasty, shown in Fig. 1.3, involves making a small incision in the femoral artery. A guide-catheter, which is a flexible plastic tube, is inserted into artery and pushed through the vasculature to the opening of the coronary artery to be treated. A thin metallic guide-wire is passed through the catheter and is tracked along the artery until its tip passes through the blockage, or stenosis. A balloon catheter is then passed over the guide-wire to the site of the stenosis.

The balloon catheter is a flexible plastic tube onto which a polymeric balloon has been wrapped and bonded. A tubular metallic mesh, known as coronary stent, is crimped onto the outside of the balloon, shown in Fig. 1.4. Once the balloon catheter has been positioned, the balloon is inflated. As shown in Fig. 1.5, the inflation of the balloon crushes the plaque and re-opens the vessel. As the balloon is inflated, the stent is expanded in the vessel. When the balloon is deflated, the stent largely maintains its shape and is left behind to ensure scaffolding of the

## 1. Introduction

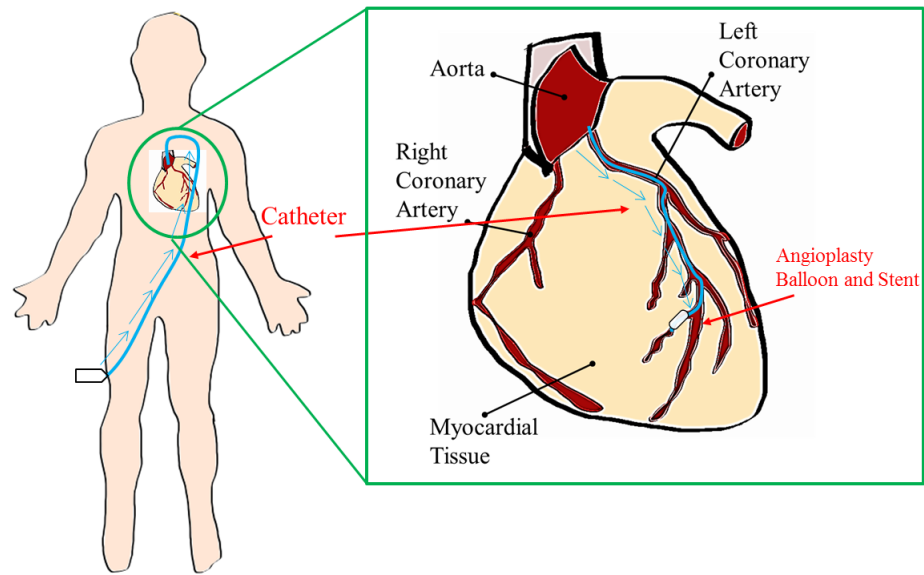


**Figure 1.3.:** The coronary angioplasty procedure. A catheter is inserted in the femoral artery and passed through the vasculature to the site of a blockage in the coronary arteries.

vessel.

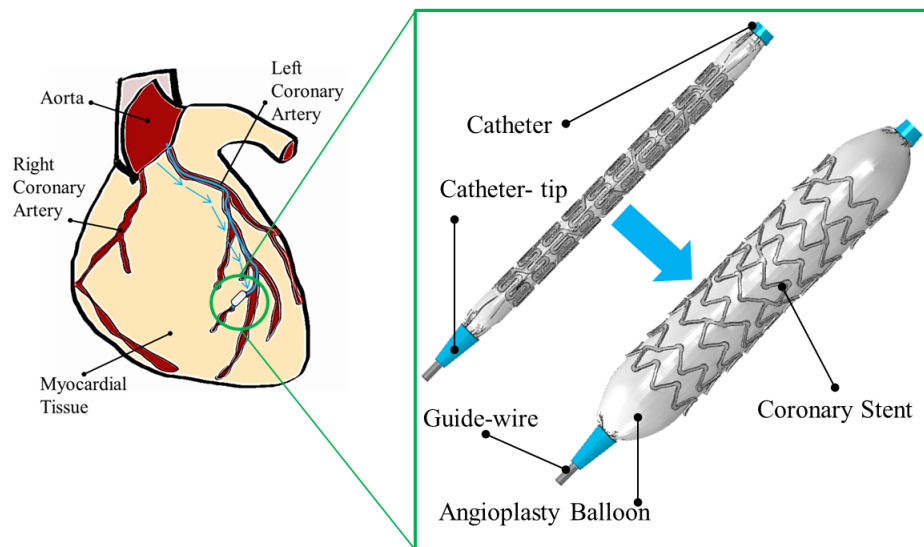


**Figure 1.4.:** The coronary angioplasty delivery system, consisting of a balloon catheter, guide-wire, stent and angioplasty balloon.

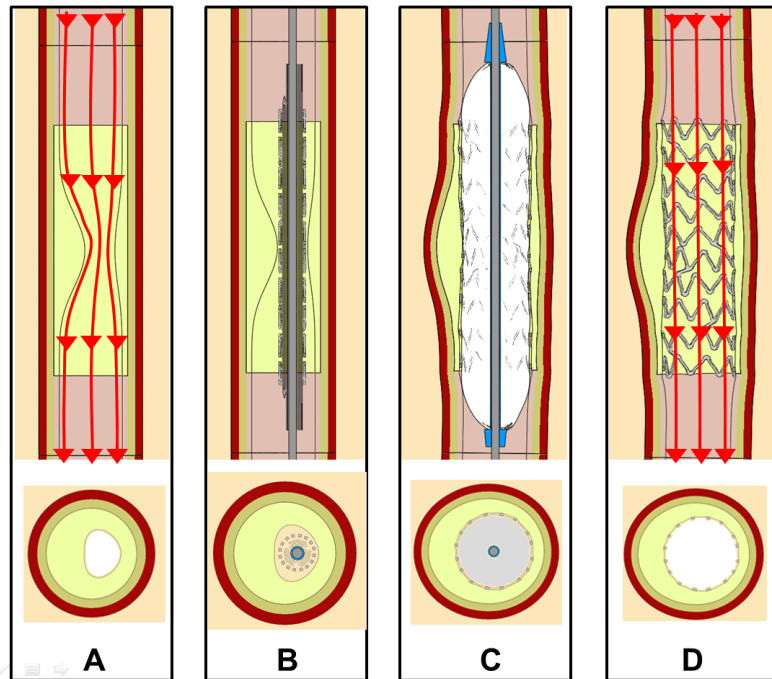


**Figure 1.5.:** Panel A depicts a stenosed coronary artery. The presence of a stenosis leads to a constriction of blood flow. During angioplasty a balloon catheter is inserted, shown in panel B, and the balloon is inflated, expanding a stent, shown in panel C. After the balloon is deflated the stent remains behind and keeps the vessel open, shown in panel D.

### 1.3. Past and Present Coronary Stents

Coronary stents play an important role in PCI and are now used in the vast majority of these procedures [2]. Gradual improvements in the design of coronary stents, since their first clinical application in the late 1980's, have led to marked improvements in the outcomes of PCI, as reviewed in detail in Garg and Serruys [4].

#### 1.3.1. Stent Mechanics

The first generation of balloon expandable stents consisted of hoops of wire in sinusoidal patterns that were welded at certain junctions along their length, such as the Medtronic DRIVER stent, or profiles that were laser cut from thin wall

## 1. Introduction

tubing, such as the Boston Scientific NIR stent. Both types of stent consisted of stainless steel (316L).

316L is an austenitic chromium-nickel stainless steel with a low carbon content and added molybdenum for enhanced corrosion resistance and mechanical properties. The alloy is quite suitable for stent applications due to its relatively high Young's Modulus, Ultimate Tensile Strength (UTS) and elongation at fracture, shown in Table 1.1. The alloy also exhibits suitable biocompatibility and reasonable visibility under x-ray imaging, known as radiopacity. Radiopacity is closely related to the density of metallic alloys, which is listed in Table 1.1 for 316L.

**Table 1.1.:** A comparison of the mechanical properties of typical stent materials.

Material	Young's Modulus (GPa)	Yield Strength (MPa)	UTS (MPa)	Elongation (%)	Density ( $\text{g cm}^{-3}$ )	Source
316L (Fe-18Cr-14Ni-2.5Mo)	193	340	670	48	7.95	[5]
L605 (Co-20Cr-15W-10Ni)	243	500	1000	46	9.1	[5]
PtCr (Fe-33Pt-18Cr-9Ni-2.6Mo)	203	480	834	45	9.9	[6]
WE43 (Mg-4Y-3REs-04Zr)	45	216	298	18	1.74	[7]
Iron (Armco)	211	170	270	36	7.87	[8]

Early balloon expandable stents, and their modern derivatives, are based on the principle of the plastic hinge, shown in Fig. 1.6. When the stent is being passed through the vasculature to the site of a blockage it needs to have a small outer diameter. During balloon inflation however, the outer diameter of the stent is increased by a factor of approximately three. This change in diameter is facilitated by the opening of hinge-like geometries in the stent's profile. The opening of the hinges leads to irreversible, or plastic, deformation of the underlying metal in the hinge region. When the angioplasty balloon is deflated, this plastic deformation is retained in the material at the hinges and the stent largely retains its shape,

as shown in Fig. 1.5.

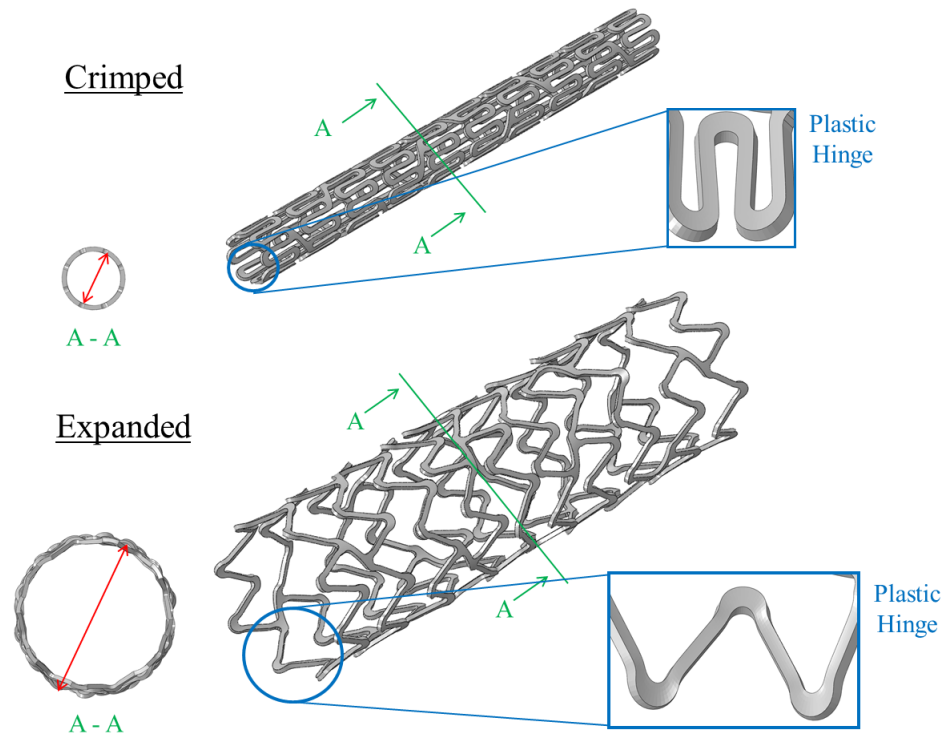


**Figure 1.6.:** The expansion of the stent is facilitated by the opening of hinge-like regions in the geometry, shown in the insets.

### 1.3.2. Bare Metal Stents

Early forms of PCI involved the inflation of the angioplasty balloon without a stent, which is now often referred to as ‘plain old balloon angioplasty’ (POBA). Coronary stents were introduced to overcome some of the limitations of the POBA procedure, in particular high incidence of vessel re-blockage, or restenosis [9]. This re-blockage was due to the tendency of the largely elastic vessel to return to its original configuration after balloon deflation, known as recoil, outright vessel collapse due to vasospasm, or blockage due to the healing response of the body to tissue damage induced by balloon inflation. The introduction of stents significantly reduced the occurrence of vessel recoil and collapse, leading to a 30% reduction in the overall incidence of restenosis when compared to balloon angioplasty alone [10, 11].

## 1. Introduction

Despite the success of this generation of bare metal stents (BMS's) in overcoming some of the limitations of balloon angioplasty, two clinical concerns related to the use of these devices emerged. The first was stent thrombosis, which is the activation of platelets in the vicinity of the exposed metal surfaces of the device and the eventual formation of a blood clot [12]. The second concern was in-stent restenosis (ISR), which is caused by the induced proliferation and migration of vascular smooth muscle cells at the treatment site, leading to the formation of new tissue, called neointima, around the struts of the stent. This process, which is known as neointimal hyperplasia, is shown in Fig. 1.7 and leads to re-blockage of the vessel. The occurrence of ISR contributed significantly to overall restenosis rates of 20-30% in BMS's [13]. Typically the treatment of restenosis requires repeat surgery to re-open the vessel and restore blood-flow, known as target lesion revascularization (TLR).

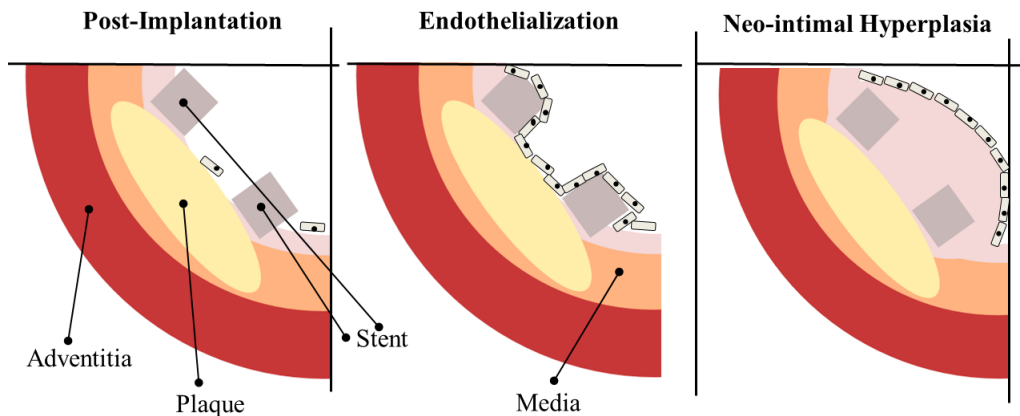


**Figure 1.7.:** Endothelialization and neo-intimal hyperplasia after stenting.

### 1.3.3. Drug Eluting Stents

A new generation of stents coated in a layer of anti-proliferative drugs was subsequently developed. These drugs inhibit the healing response of the body in the stented region and are contained in thin polymer coatings on the outer surface of the stent. The introduction of drug eluting stents (DES's) resulted in a significant reduction in the incidence of ISR, in turn leading to reductions in the

incidence of TLR of between 58% and 70% in DES's relative to BMS's [14]. This success has led to the widespread adoption of DES's, which are now used in approximately 75% of all revascularizations (surgeries including PCI and coronary artery bypass grafting) in the US [2].

### 1.3.4. Stent Manufacture

There are a number of different manufacturing routes for stents. Often stents are laser-machined from extruded thin-walled tubing (e.g. the Boston Scientific NIR stent). Other approaches include welding segments consisting of thin wires that have been bent into sinusoidal patterns (e.g. the Medtronic DRIVER Stent) and braiding and knitting thin wires (e.g. the Boston Scientific WALLSTENT). As part of the manufacturing process stents are usually cleaned in acid baths, heat treated to removed residual stresses and subject to electro-polishing, which results in a smooth surface finish and can impart improved corrosion resistance to alloys such as 316L. A final stage in the production process is usually the crimping of the stent onto the delivery system.

## 1.4. Numerical Methods in Stent Analysis and Design

### 1.4.1. Finite Element Analysis

In the context of stent design, numerical modelling amounts to the use of mathematical descriptions of the physical behaviour of the stent, delivery system and ar-

## 1. Introduction

terial tissue to attempt to describe and, in turn, predict their real-life behaviours. Due to the focus on the structural performance of the stent and the complexity of the physical behaviours involved in coronary angioplasty and stenting, finite element analysis (FEA) is typically employed as the numerical modelling method.

FEA, which is described in Ch. 3, plays an important role in the analysis and design of coronary stents. This is reflected by it being a mandatory part of the design process for stents seeking regulatory approval for clinical use in the US [15]. The advantages of using FEA in stent design are that:

- there is reduced reliance on experimental testing, which can prove costly over the many iterations required during stent development
- it facilitates the use of numerical optimization methods, which can be used to identify device designs with favourable characteristics in an efficient and systematic manner
- it allows stent performance to be assessed in conditions that may not be practical to replicate experimentally
- it allows the prediction of performance metrics that would not be feasible to determine experimentally, such as stress states in hinges
- it can give an improved fundamental understanding of the mechanisms that govern the overall physical behaviour of the stent, which can be exploited to improve device design.

Overall, numerical modelling of stent performance through FEA facilitates the development of coronary stents with improved performance and thus, improved

clinical outcomes. Detailed reviews of the use of FEA in the numerical modelling of coronary angioplasty and stenting are given in Martin and Boyle [16] and Morlacchi and Migliavacca [17].

### 1.4.2. Modelling of Stent Materials

An important part of the application of FEA in modelling the performance of stents is the approach taken in modelling the mechanical behaviour of the underlying stent material.

By far the most common approach in modelling the elasto-plastic deformation of alloys in balloon expandable stents is to assume isotropic linear elasticity and use isotropic  $J_2$  plasticity theory, both of which are described in Ch. 3. Some examples of studies using this approach are Dumoulin and Cochelin [18], Migliavacca *et al.* [19], Mortier *et al.* [20], Gastaldi *et al.* [21], Pant *et al.* [22] and Conway *et al.* [23]. The use of  $J_2$  plasticity theory implicitly assumes that the underlying stent material is homogenous. As will be discussed further in Ch. 2, in reality, metallic alloys used in stents are not homogenous, as they are made up of many metallic crystals or grains, each with a different crystallographic orientation, and as such, a different deformation behaviour for a given applied stress. The assumption of homogeneity is often valid in relatively large components with many metallic grains through their dimensions. However, this is not necessarily the case for microscale components such as coronary stents, which have regions with dimensions on the same order as the grain sizes of their underlying alloy.

## 1.5. Future Developments in Coronary Stents

Despite the success and widespread adoption of DES's, ISR and stent thrombosis remain as undesirable outcomes of coronary stenting. Stent thrombosis is a serious condition, which has 10 to 30% mortality rates [4] and occurs in 0.36% to 0.6% of treated patients each year up to, and possibly beyond, five years after stenting [24, 25, 14, 26]. ISR is usually less serious, but requires repeat surgery to correct. It is reported in over 200 000 cases annually in the US alone [27], even when DES's are employed.

The occurrence of stent thrombosis has been associated with stent fracture, poor apposition of the stent to the surrounding tissue, stent under-expansion, early cessation of dual-anti-platelet therapy and hypersensitivity to polymer coatings on DES's [4]. Suggested underlying mechanisms for ISR in DES's include hypersensitivity to polymer coatings, coating delamination, stent fracture, non-uniform stent expansion and incomplete stent expansion [4].

Recent developments in stent technology to reduce the risks of ISR and stent thrombosis are reviewed in detail in Garg and Serruys [28]. Regarding the stent structure itself, two of the most important developments are: i) the development of stents with thinner struts and ii) the development of bioabsorbable stents.

### 1.5.1. Thinner Struts in Permanent Stents

The driver for stents with thinner struts stems from the desire for devices with increased flexibility and lower crossing-profile, or outside diameter. This facilitates device delivery and placement. There is also a possibility for reduced

## 1. Introduction

haemodynamic impact [29] and a potential for increased device conformability with thinner struts. The substantiation for the trend toward devices with thinner struts stems from the findings of the ISAR-STEREO clinical trials [30, 31], which suggest that thinner struts are associated with reduced rates of ISR.

For clarity, the term strut thickness, when used throughout this thesis, refers to the radial dimension of the stent strut in the final manufactured configuration, accounting for electro-polishing.

The first commercial DES, the Cordis CYPHER stent, was manufactured from 316L and had a strut thickness of 140  $\mu\text{m}$  [4]. Subsequent 316L DES's had lower strut thicknesses, such as the Boston Scientific TAXUS EXPRESS and TAXUS LIBERTÉ stents, which had thicknesses of 132 and 97  $\mu\text{m}$  respectively [4]. The introduction of two new types of alloy in stent manufacture, cobalt chromium and platinum chromium, has allowed for further reductions in strut thickness.

Cobalt chromium (CoCr) is a family of alloys containing varying degrees of cobalt, chromium and nickel. Two specific compositions have been used in stents, L605 alloy and MP35N alloy. L605 alloy has the greater density and strength of the two alloys. Also, as shown in Table 1.1, it has greater density than 316L, higher Young's Modulus and UTS and has comparable elongation at fracture. L605 has a face-centred-cubic (FCC) crystallographic structure, with its microstructure consisting of equiaxed metallic grains interspersed with carbide precipitates in the annealed condition [32]. The higher strength of L605 relative to 316L allows for the use of thinner struts while maintaining similar device radial strength, or ability to resist collapse under an applied external pressure. In addition, the higher density of the alloy also facilitates the use of thinner struts, as it leads to increased radiopacity for the material. Modern cobalt chromium stents, such as the Medtronic ENDEAVOR stent and Abbot Vascular XIENCE V stent

## 1. Introduction

have strut thicknesses of 91 and 81  $\mu\text{m}$  respectively [4]. A further generation of developmental L605 stents have significantly lower thicknesses, including the Meril BIOMIME and MITSU stent platforms, with strut thicknesses of 65 and 40  $\mu\text{m}$  respectively [33].

Platinum chromium (PtCr) is a speciality alloy designed for use in coronary stents [6]. The alloy primarily consists of a 316L base, with some of the iron and nickel content of 316L replaced with platinum. As shown in Table 1.1, PtCr alloy has a comparable Young's Modulus, UTS and elongation at fracture to L605, but has higher density. This means that PtCr can potentially be used in stents with thinner struts than L605 without compromising visibility. At present it has been employed in the Boston Scientific ELEMENT stent platform, which has a strut thickness of 81  $\mu\text{m}$  [28]. PtCr consists of equiaxed austenitic grains with an average grain size of 24  $\mu\text{m}$  [6].

In the design of coronary stents it is often stated that a minimum number of grains, for example eight to ten [34], should be maintained through the dimensions of the strut to prevent marked reductions in ductility and compromised fatigue performance [34, 32, 35, 36, 6]. Maintaining this number of grains places an obvious lower bound on feasible strut dimensions, for a given grain size. Naturally, the grain size can be reduced, however this often leads to changes in the material's mechanical behaviour, for example increased Yield Strength due to the Hall-Petch effect [37], which is undesirable.

While there has been a reasonable amount of experimental characterisation of the effects of having few grains through strut dimensions for 316L [34, 35, 36], no such data has been presented for newer stent materials such as L605, PtCr or magnesium alloys. Given that L605 and PtCr are now being actively used in stents with struts that are significantly thinner than those of 316L stents, it

is important in the future development of these devices that lower limits on the number of grains through the strut thickness are identified for these materials.

### 1.5.2. Bioabsorbable Metal Stents

Bioabsorbable metal stents, also referred to as biodegradable stents, have attracted much recent interest due to their potential for addressing a number of the limitations of permanent stents. The idea of the bioabsorbable stent is that it provides the scaffolding and drug delivery platform of existing stents while the artery heals, and then dissolves in the vessel wall when it is no longer required. Since the stent is no longer present in the vessel after a certain period of time, these devices have the potential to eliminate the risk of late and very-late stent thrombosis and late ISR [38]. Further potential advantages are the possibility of repeat PCI in the treatment site, reduced long-term haemodynamic impact, the restoration of vasomotion and the facilitation of positive arterial remodelling [38].

Bioabsorbable stents have not yet been adopted in widespread clinical use, however they have shown promise in initial clinical trials. A detailed overview of recent developments and clinical trials associated with bioabsorbable stents is given in Bourantas *et al.* [39]. Bioabsorbable, or simply absorbable, metal stents (AMS's) developed to date have consisted of magnesium alloys or pure iron, with only the former being implanted in humans. Two in-human clinical trials have been conducted on magnesium stents, namely the PROGRESS-AMS trial [40] and the DREAMS trial [41]. The PROGRESS-AMS trial used the Biotronik MAGIC stent, which was a BMS based on the magnesium alloy WE43. The results of the trial, which was conducted on 63 patients, showed that the technology in general had promise, but the observed TLR rates of 26.7% were unsatisfac-

## 1. Introduction

tory. This poor performance was attributed to neo-intimal hyperplasia (45% of the lumen loss) and premature loss of device scaffolding. The DREAMS trial used the Biotronik DREAMS stent, which is an updated version of the MAGIC stent with a drug-coating, a modified version of the WE43 alloy and a modified device geometry. 12 month results showed a significant improvement in terms of late lumen loss and the incidence of TLR (4.7% vs. 26.7%) relative to the MAGIC stent [41].

A number of magnesium alloys have been proposed for AMS applications, with a range of different mechanical and corrosion properties [42]. Common to magnesium and its alloys, however, are a lower density, Young's Modulus, UTS and elongation at fracture than 316L, as shown in Table 1.1 for magnesium alloy WE43. This brings challenges in terms of designing AMS's with comparable scaffolding performance to permanent stents, which consist of materials with superior mechanical properties [43]. In contrast to the FCC structure of 316L, magnesium and its alloys have a hexagonal-close-packed (HCP) crystallographic structure.

It is clear from the performance improvements between the MAGIC and DREAMS stents that improved AMS design can lead to significantly improved clinical outcomes for these devices. Due to the novelty of AMS's very few numerical methods have been developed to aid in the design of the device structure and there is little understanding of how these devices behave as they corrode in the body. The development of new numerical methods for modelling AMS's and their corrosion will facilitate the development of this promising technology.

## 1.6. Stent Fracture

Due to its strong link with ISR and stent thrombosis, accounting for stent fracture is an important analysis and design consideration in coronary stent development. The occurrence of stent fracture has not been well characterized in coronary stents, with rates of 1 to 2%, 1 to 7.7% and as high as 29% reported [44, 45, 46, 47]. However, once fracture has been identified it leads to ISR or stent thrombosis in 70 to 80% of cases [4]. The lack of knowledge and conflicting evidence regarding stent fracture rates has been attributed to the difficulty in observing fractures in the body [4].

Stent fracture can be due to excessive deformation during the device deployment phase (balloon expansion and removal) or due to fatigue loading that arises due to the pulsatile nature of the blood-stream. Investigations of stent fracture in calcified lesions have reported high cycle fatigue (HCF) as the primary mode of device fracture [48]. In testing for stent fractures the FDA recommends accelerated fatigue testing of devices for the equivalent of 10 years of service, or approximately 400 million cycles [15]. The typical industrial practice for analysing stent fracture risk is to perform FEA of the device undergoing loading that is representative of that experienced in the body. Alternating and mean stresses at critical locations in the device are then predicted and used as part of a Goodman analysis, combined with S-N data for the stent material, to predict device factors of safety. While there is no direct recommendation for suitable material constitutive models in the FDA guidance documents for analysing fatigue [15], as discussed in Section 1.4 the vast majority of stent analyses are based on the use of continuum plasticity theories.

HCF is usually the focus when analysing stent fracture risks in the current generation of stents. However, with the development of stents with thinner struts,

and in light of experimental evidence that suggests that the number of grains through the strut thickness significantly affects device ductility [34, 35, 36], it is clear that it is also important to evaluate fracture risks during the deployment phase to ensure that a suitable strut thickness is maintained for a given grain size. In addition, with the development of bioabsorbable stents, consisting of metals with inferior ductility to 316L and L605, see Table 1.1, there is an increased risk of device fracture during the deployment phase, which should be accounted for in device analysis and design.

## 1.7. Thesis Motivations and Aims

With over one million PCI's carried out each year in Europe alone, of which a sizeable number involve coronary angioplasty and stenting, any improvement in device performance and clinical outcome can be beneficial for a large number of patients. The development of permanent stents with thinner struts and bioabsorbable stents has the potential to significantly improve the outcomes of coronary stenting. The goal of this thesis is to aid the design of this next generation of coronary stents through improving the current understanding of device mechanics, using numerical modelling.

The first aim of this thesis is to characterise the short-term (deployment phase) mechanical performance of a range of permanent and bioabsorbable metal stents using typical finite element (FE) modelling approaches. The second aim is to use micromechanical approaches to perform a more detailed assessment of the performance of individual struts consisting of a broad range of permanent and bioabsorbable metals undergoing large deformations, typical of those undergone during stent expansion. This allows for predictions of suitable strut thicknesses

## 1. Introduction

for permanent and bioabsorbable stents, and in particular addresses the important question of minimum possible strut thicknesses in coronary stents.

The third aim is to characterise the mechanical performance of AMS's following the deployment phase, as they corrode in the body. This is accomplished through the experimental characterisation of the corrosion behaviour of a bioabsorbable metal in a simulated physiological solution and the development and application of a number of numerical corrosion models for AMS's.

Through achieving these aims, the work in this thesis provides new insights into the mechanical performance of next generation coronary stents, including detailed predictions of device fracture risks in the deployment phase, and a number of specific design recommendations for permanent and bioabsorbable metal stents.

### 1.8. Thesis Overview

The thesis begins by reviewing the literature associated with the mechanics of microscale devices and absorbable metal stents in **Chapter 2**. The theoretical framework used in this thesis and its numerical implementation are presented in **Chapter 3**. In **Chapter 4** numerical modelling is used to compare the mechanical performance of a range of permanent and bioabsorbable metal stents during the deployment phase, based on the simulation of *in-vitro* bench-testing. This comparison addresses a gap in the current understanding of the mechanics of bioabsorbable metal stents and serves as a baseline for assessing both permanent and bioabsorbable stent performance in subsequent chapters. In **Chapter 5** numerical modelling and crystal plasticity theory are used to assess the mechanics of thin struts consisting of permanent and bioabsorbable metals undergoing large

## 1. Introduction

deformations. Microstructure-dependent ductility size effects in these metals are predicted and their implications in dictating suitable strut thicknesses for permanent and bioabsorbable stents are identified. In **Chapter 6** the effects of corrosion on the mechanical performance of thin bioabsorbable metal foils is assessed. A phenomenological corrosion model is developed to capture the experimental observations and is then applied in modelling the corrosion of a stent in the body. In **Chapter 7** the corrosion model developed in Ch. 6 is used to directly compare the mechanical performance of corroding AMS's and permanent stents in the body. This comparison builds on the comparison in Ch. 4, as it now includes the effects of corrosion and uses *in-vivo* deployment simulations. Through the use of optimization methods, AMS designs with favourable performance compared to existing commercial designs are also identified. In **Chapter 8** a physical corrosion model is developed. The predictions of AMS performance in Ch. 7 are built upon by assessing the differences in predicted mechanical performance obtained when physical and phenomenological descriptions of the corrosion process are employed. In **Chapter 9** the main outcomes of the previous chapters are summarized and integrated, leading to an overall set of design recommendations for the next generation of coronary stents.

## 2. Background

### 2.1. Chapter Summary

Grain sizes in metals that constitute coronary stents are often similar to the dimensions of the stent struts. This means that the mechanics of individual grains can strongly affect the overall performance of the strut. The change in mechanical performance from ‘bulk’ behaviour, due to the similarity between the grain size and the strut dimension, is manifested as a statistical size effect (SSE). SSE’s are known to lead to reductions in the ductility of thin struts of many metals. Given that new alloys such as L605 are being used in thin-strut stents and magnesium alloys with relatively low ‘bulk’ ductility are being used in bioabsorbable stents, it is important to assess how SSE’s affect the performance of devices consisting of these materials. The structure and deformation of FCC and HCP metallic crystals are discussed in **Section 2.2.1**. Size effects, in particular SSE’s, and their role in dictating the mechanics of thin struts are discussed in **Section 2.2.2**. Numerical methods for capturing size effects in thin struts, which cannot be achieved using continuum plasticity theories alone, are discussed in **Section 2.2.3**.

When considering the mechanics of corroding AMS’s it is important that rele-

## 2. Background

vant corrosion mechanisms are considered. The corrosion of magnesium alloys in simulated physiological fluids and *in-vivo* is currently an active field of research. An overview of recent developments in this field is given in **Section 2.3.1**. There have been fewer studies on the corrosion of iron for AMS applications, with recent developments discussed in **Section 2.3.2**. Few methods for specifically modelling the corrosion of AMS's have been developed to date. A number of general corrosion modelling approaches that may be useful for modelling AMS corrosion are introduced in **Section 2.3.3**. The mechanical performance of AMS's before, or during, corrosion has not been widely reported, with most experimental data made available from reports on clinical trials. The current knowledge of AMS mechanical performance, based on experimental reports and numerical modelling, is overviewed in **Section 2.3.4**.

## 2.2. The Mechanics of Microscale Devices

### 2.2.1. Structure and Deformation of Metallic Crystals

Coronary stent struts consist of arrangements of metallic grains or crystals. Due to the small size of stent struts, their mechanical performance can be dictated by the behaviour of individual grains. In order to introduce the concept of statistical size effects, which arise due to the small number of grains through the stent strut dimensions, the structure and deformation of individual metallic crystals are first discussed.

Within a metallic crystal atoms are arranged in regular lattices. Two common lattice configurations consist of FCC and HCP repeating units, shown in Figs. 2.1a and 2.1b respectively. 316L and L605 alloys have a FCC lattice structure while

## 2. Background

magnesium and its alloys have a HCP lattice structure.

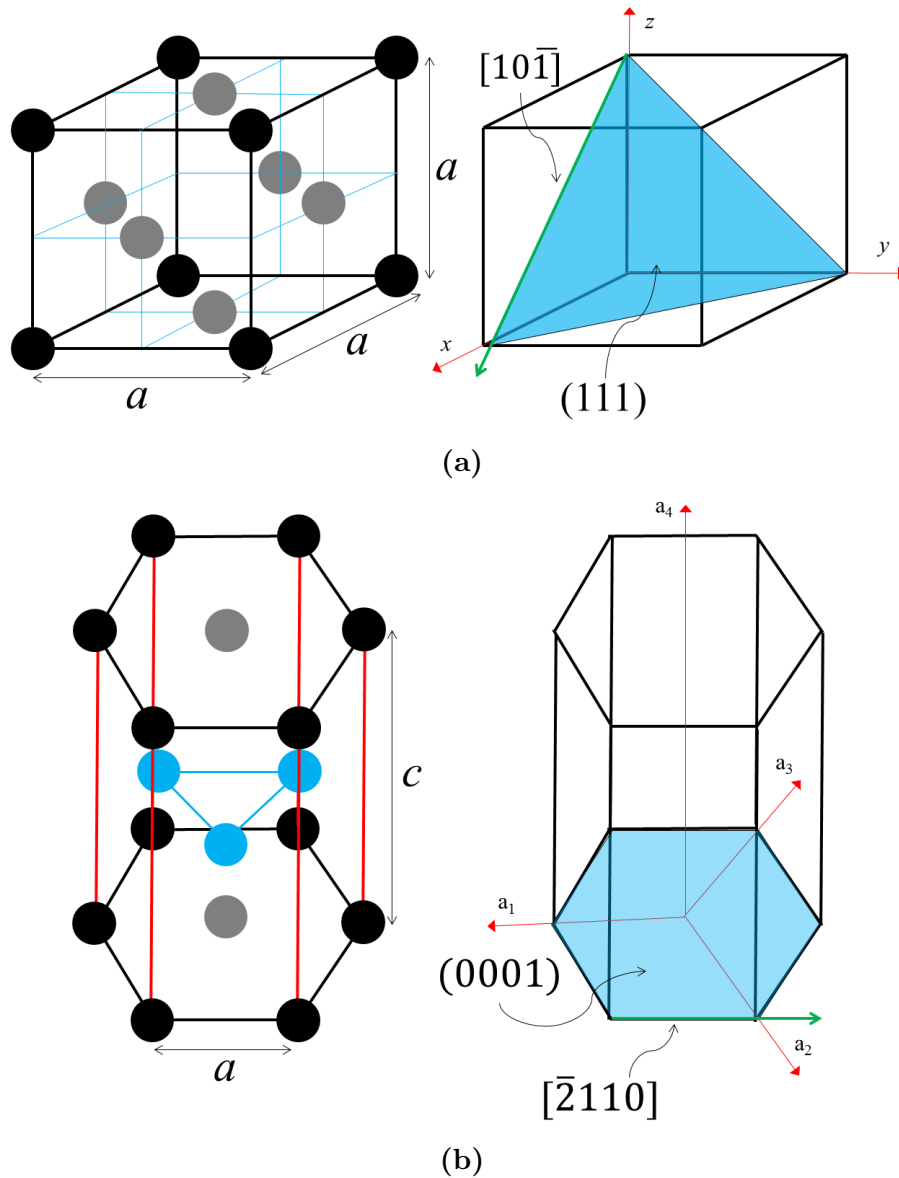


**Figure 2.1.:** (a) A schematic of a FCC crystallographic lattice on the left. On the right is a depiction of the plane  $(111)$  and direction  $[10\bar{1}]$  expressed in terms of Miller indices. (b) A schematic of a HCP crystallographic lattice on the left. On the right is a depiction of the plane  $(0001)$  and direction  $[\bar{2}110]$  expressed in terms of Miller-Bravais indices.

When a loading is applied to a crystal it can result in the stretching of the bonds between atoms in the lattice, which amounts to elastic deformation, shown in Fig. 2.2a. Alternatively, it can result in the breaking and reforming of bonds, which amounts to the movement of dislocations through the lattice structure, and plastic deformation, shown in Fig. 2.2b. The movement of dislocations under

## 2. Background

the action of applied loading typically leads to the deformation of the crystal along certain slip directions and on certain slip planes, which usually coincide with close-packed directions and planes within the lattice. A slip system is a combination of a slip plane and slip direction.

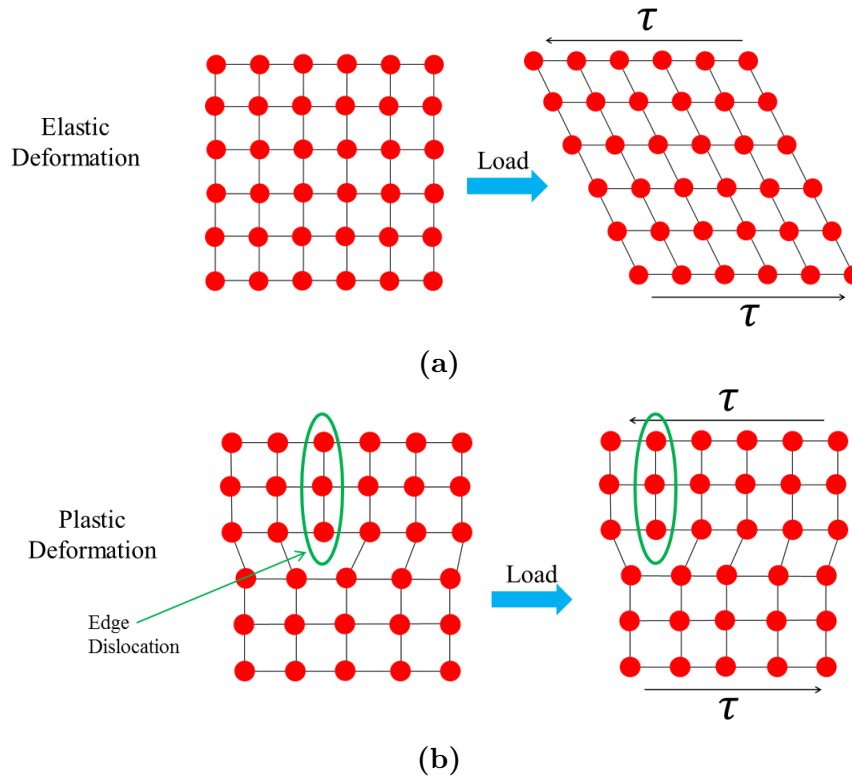


**Figure 2.2.:** (a) Elastic deformation occurs through the stretching of atomic bonds. (b) The breaking of bonds and formation of new bonds leads to dislocation motion and plastic deformation.

FCC metals (such as 316L, L605 and PtCtr) are subject to plastic slip, on the  $\{111\}$  planes and in the  $\langle 110 \rangle$  directions, with directions in the crystallographic lattice described using Miller indices (see Askeland [49]). As discussed in detail in Graff *et al.* [50], plastic deformation in HCP metals (such as magnesium alloys) is more complex, with the available slip planes and directions depending on the crystal aspect ratio,  $\frac{c}{a}$  in Fig. 2.1b. Despite it being possible to identify many potential slip planes within the HCP lattice, in reality, due to the low symmetry of the lattice, few of these are active during slip. This makes the accommodation of arbitrary deformations in the lattice through slip only difficult and can result in a significant degree of tensile twinning during deformation. Twinning is a

## 2. Background

process in which deformation is accommodated through re-orientation of some regions of crystallographic lattice about certain planes of symmetry, known as twin planes.

There is still debate surrounding which slip systems and twin planes are active during the deformation of magnesium, however a typical approach is to assume slip on the basal and prismatic planes,  $\{0001\}$  and  $\{1\bar{1}00\}$  respectively, in the  $\langle 11\bar{2}0 \rangle$  directions, and on the pyramidal planes  $\{11\bar{2}2\}$  in the  $\langle 11\bar{2}3 \rangle$  directions [50]. In addition, while twinning is not a form of crystallographic slip, its contribution to crystal deformation has been modelled as a slip on the  $\{10\bar{1}2\}$  planes in the  $\langle 10\bar{1}1 \rangle$  directions [50].

Considering the mechanics of single crystals, plastic slip  $\gamma$  occurs in a slip system in response to a resolved shear stress  $\tau$  acting on the system and can be considered to only occur once a critical resolved shear stress  $\tau_c$  on the slip system has been reached. The resolved shear stress on a slip system for an arbitrary overall stress state in the crystal can be found through Schmid's law. As a simple example of Schmid's law, consider the single crystal in Fig. 2.3 under tensile stress  $\sigma$ . The shear stress  $\tau$  acting on a certain slip plane, in a certain slip direction is:

$$\tau = \sigma \cos(\lambda) \cos(\varphi) \quad (2.1)$$

where  $\lambda$  and  $\varphi$  are the respective angles between the slip plane normal and slip direction and the line of application of the stress. The critical resolved shear stress in a slip system can increase with plastic slip in the crystal. This increase is associated with the greater number of dislocations in the lattice and the extra stress required to move dislocations that are in close proximity to each other, interstitial atoms and grain boundaries. The increase in  $\tau_c$  with slip is known as strain hardening. The amount of strain hardening that takes place on a given slip system can be a function of plastic slip on that system, known as

## 2. Background

self-hardening, or also a function of plastic slip on other slip systems, known as latent-hardening.

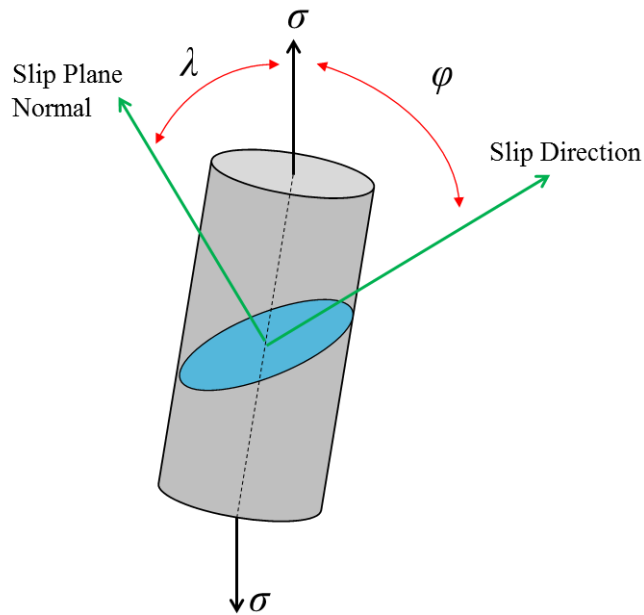


**Figure 2.3.:** A single crystal is loaded axially in tension with a stress,  $\sigma$ . Through the application of Schmid's law the resolved shear stress on the slip system in blue can be determined based on a knowledge of the slip direction and slip plane normal.

The crystal lattice is clearly not continuous in nature, however, for practical purposes, at certain scales, it is useful to attempt to describe the mechanics of single crystals in terms of that of a continuum. Crystal plasticity theory, which is described in detail in Ch. 3, attempts to describe plastic slip resulting from the motion of many dislocations as a continuum quantity, namely plastic shear strain. In doing so, it allows the mechanics of the crystal as it undergoes plastic slip, and spin, in response to resolved shear stresses acting along its slips systems to be expressed in the framework of continuum mechanics.

From this continuum perspective, if a single crystal is deformed, the orientation of the crystallographic lattice dictates its mechanical response. This means that, for a given loading condition, a crystal can have more or less resistance to plastic deformation depending on its lattice orientation. When there is a large number of crystals in a component, the overall behaviour of the component can be consid-

## 2. Background

ered to be an averaged response of its underlying, randomly orientated, crystals. This leads to a homogenous and often isotropic material behaviour, which can be well described using classical plasticity theories, such as  $J_2$  plasticity theory. However, when component dimensions are of a similar size to the metallic crystals, significant inhomogeneity can arise due to the different mechanical behaviours of individual crystals. The dependence of the mechanical performance of a component on the number of grains through its dimensions leads to a type of size effect known as a statistical size effect (SSE).

### 2.2.2. Size Effects in Metallic Components

SSE's can play an important role in dictating the mechanical behaviour of microscale components, including stent struts. They are discussed here in the general context of size effects in miniaturized components. As detailed in Geers [51], there are a number of size effect types that arise in the miniaturization of metallic components, and these can be classified as: i) statistical size effects, ii) intrinsic size effects, iii) strain gradient effects and iv) surface constraint effects.

SSE's arise when the geometric dimensions of components approach those of their metallic grains. These effects can result in the overall mechanical behaviour of the components being heavily influenced by the behaviour of relatively few grains, as observed in the studies of Murphy *et al.* [35], Janssen *et al.* [52], Weiss *et al.* [36] and Keller *et al.* [53]. Intrinsic size effects are related to intrinsic length scales within the metallic microstructure, such as the Burgers vector length, grain size and grain boundary width. An example is the Hall-Petch relationship, which predicts an increase in component strength with decreasing grain size [54, 55, 56], particularly that yield strength increases with the reciprocal of the square root of the grain diameter. Strain gradient effects are related to the absolute

## 2. Background

size of a component and arise from the development of geometrically necessary dislocations (GND) in the crystallographic lattice. These effects typically lead to strengthening of components with smaller dimensions [57, 58, 59, 51, 60]. Surface constraint effects are related to ability of dislocations to glide out of the surfaces of miniaturized components [61, 62] and can lead to either strengthening or weakening with miniaturization, depending on the surface condition.

SSE's are of particular interest in the development of coronary stents, due to the similarity in strut and grain dimensions and the current trend toward thinner struts. Due to SSE's, decreasing dimensions for a fixed grain size typically leads to reduced strength and ductility in metallic components, as their overall mechanical behaviour tends toward that of a single metallic grain. SSE's have been observed in a range of metals, including aluminium [63, 64, 65, 66], brass [67, 65], copper and copper alloys [63, 68], iron and steel [35, 36, 56] and silver [69]. Due to the important role of SSE's in determining the mechanical performance of thin components and, in the case of coronary stents, their relevance in the determination of suitable strut thicknesses, it is important to assess how SSE's affect the plastic deformation of coronary stents.

### 2.2.3. Numerical Modelling of Size Effects

Typical continuum plasticity theories used in stent analysis and design are incapable of accounting for SSE's, as they do not contain an inherent length scale. Numerical approaches that have been considered for accounting for SSE's, and other size effects, when modelling thin struts are discussed here.

The first approach focuses on homogenized modelling of the polycrystal aggregate, facilitated through the development of material constitutive laws with de-

## 2. Background

pendence of flow stress on ratios of grain size to specimen size. The second focuses on explicitly modelling the mechanical behaviour of individual crystals in the aggregate through continuum plasticity models, single crystal plasticity models or gradient enhanced single crystal plasticity models.

Using the first approach, Kim [70], Lai [71] and Yun *et al.* [72] updated a modified Hall-Petch relationship [54] to describe flow stress in sheets in tension as a function of applied strain and the volume ratio of surface grains to internal grains. Their approach assumed surface grains to be ‘weaker’ than internal grains following the work of Engel and Eckstein [73]. Model predictions in these studies showed good agreement with a range of experiments in terms of true stress-strain behaviour, although the chosen modelling approach is somewhat empirical in nature. Molotnikov *et al.* [74] used a similar approach in developing a constitutive model, with flow stress again depending on the ratio of surface to internal grains. In this case a more physical stress evolution law was employed, based on the models of Estrin *et al.* [75] and Tóth *et al.* [76].

Using the second approach, Chan *et al.* [77] studied the deformation of pure copper polycrystals in compression through explicit modelling of individual grains with different stress-strain behaviours using an isotropic continuum plasticity theory. Predictions showed agreement with corresponding compression experiments in terms of true stress-strain behaviour, although the method used did not account for anisotropy (or orientation dependence) in the plastic deformation of individual grains. Savage *et al.* [78], Murphy *et al.* [79] and Harewood and McHugh [80] modelled the deformation of polycrystals through explicitly modelling each grain using single crystal plasticity theory [81, 82] and FE simulations. These studies focused on the influence of SSE’s on the ductility of 316L struts of fixed aspect ratio, with good agreement achieved between predictions of strut ductility and the experiments of Murphy *et al.* [35]. Cao *et al.* [83] and

## 2. Background

Wang *et al.* [84] used a similar approach to study necking in thin 316L films and showed the ability of such modelling to capture decreases in flow stress due to reductions in the number of grains through specimen dimensions. Fülöp *et al.* [85] and Liang-Ying *et al.* [86] used similar models in predicting the influences of SSE's in Al foils, predicting reductions in flow stress in tension in foils with decreasing numbers of grains through their thickness. The latter study also predicted reduced normalized force in bending for foils with fewer grains through the thickness.

Bayley *et al.* [87], Geers [51] and Hoefnagels *et al.* [88] have studied the interaction of SSE's and other size effects in aluminium and nickel foils using gradient enhanced crystal plasticity FE modelling, based on modified versions of a model proposed by Evers *et al.* [89]. This approach has given important insights into competitive interactions between SSE's, which induce weakening behaviour and strain gradient effects, which promote strengthening. Geers [51] has predicted that a synergistic relationship exists between SSE's and other size effects in certain loading cases, while the modelling approach of Keller *et al.* [90] predicted strengthening in cases where average grain sizes were increased to be greater than the specimen thickness and also a dependence of the magnitude of SSE's on absolute grain size.

In summary, the mechanical performance of thin stent struts can depend markedly on the strut size and number of grains through the strut dimensions. These size effects cannot be captured using conventional continuum plasticity modelling techniques. Previous microscale modelling approaches have focused on SSE's in 316L, with good agreement achieved between model predictions and experimental results. Given that materials such as L605 and PtCr are now being used in stents with thinner struts and materials such as magnesium alloys with relatively low ductility are being used in bioabsorbable stents, it is important to investigate

the role of SSE's in the deformation of stents consisting of these new materials using numerical approaches.

### 2.3. The Mechanics and Corrosion of Absorbable Metal Stents

#### 2.3.1. Magnesium Corrosion Studies

In order to model the corrosion of AMS's an appreciation of the corrosion behaviour of magnesium alloys and iron in simulated physiological environments and in the body is required. Due to their relative success in orthopaedic and cardiovascular applications, to date there have been more studies on the corrosion of magnesium alloys for these applications than iron. The current understanding of the *in-vitro* and *in-vivo* corrosion of magnesium alloys is discussed here.

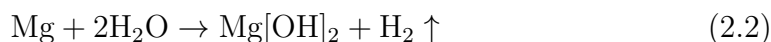
The corrosion behaviour of magnesium and magnesium alloys in aqueous and physiological environments is reviewed in Song *et al.* [91], Witte *et al.* [92] and Atrens *et al.* [93]. Many of the details on the mechanisms of magnesium corrosion in physiological environments, *in-vitro* or *in-vivo*, remain unknown and are the subject of on-going investigation. However, a number of basic behaviours have recently been elucidated.

A thin oxide layer naturally forms on the surface of magnesium in air. When the magnesium is placed in an aqueous solution the oxide layer acts as a semi-permeable barrier, resisting corrosion. Corrosion can begin in certain regions where the oxide layer has fractured or where it is obstructed by the presence

## 2. Background

of impurities, as depicted in Fig. 2.4a. Localized corrosion in regions where the protective coating has broken down can lead to the formation of local anodes and cathodes on the magnesium surface, with hydrogen evolved from the latter, as depicted in Fig. 2.4b. The onset of localized corrosion can be a result of an extended period of immersion in solution or the application of a potential difference greater than the pitting potential (the potential difference at which surface passivity breaks down, see Shreir *et al.* [94]) for magnesium in the solution. As shown in Figs. 2.4c and 2.4d, eventually the localized corrosion, which takes the form of mass loss at the local anode, leads to the development of large corrosion pits. Particle undermining as a result of these pits leads to further mass loss.

According to Atrens *et al.* [93], the corrosion process can be described in terms of a number of anodic and cathodic partial reactions where uni-positive  $\text{Mg}^+$  ions are released into solution and hydrogen gas is evolved. An accompanying chemical reaction involves the formation of magnesium hydroxide ( $\text{Mg}[\text{OH}]_2$ ) and further hydrogen gas evolution. The overall reaction can be expressed as follows:



Depending on the corrosive environment, the magnesium hydroxide, or other similar corrosion products, can be deposited back onto the corrosion surface, forming a semi-permeable protective barrier.

Magnesium alloys can be further subject to micro-galvanic corrosion. As shown in Fig. 2.5a, certain regions in the microstructure, such as grain boundaries and impurities, act as local cathodes, as they usually contain a greater volume of more cathodic metals, such as aluminium and iron. This means that the remaining magnesium rich matrix acts as an anode, where magnesium ions are preferentially dissolved in the solution. As depicted in Fig. 2.5b, the anodic magnesium matrix thus dissolves preferentially to the grain boundary regions, which is in contrast

## 2. Background

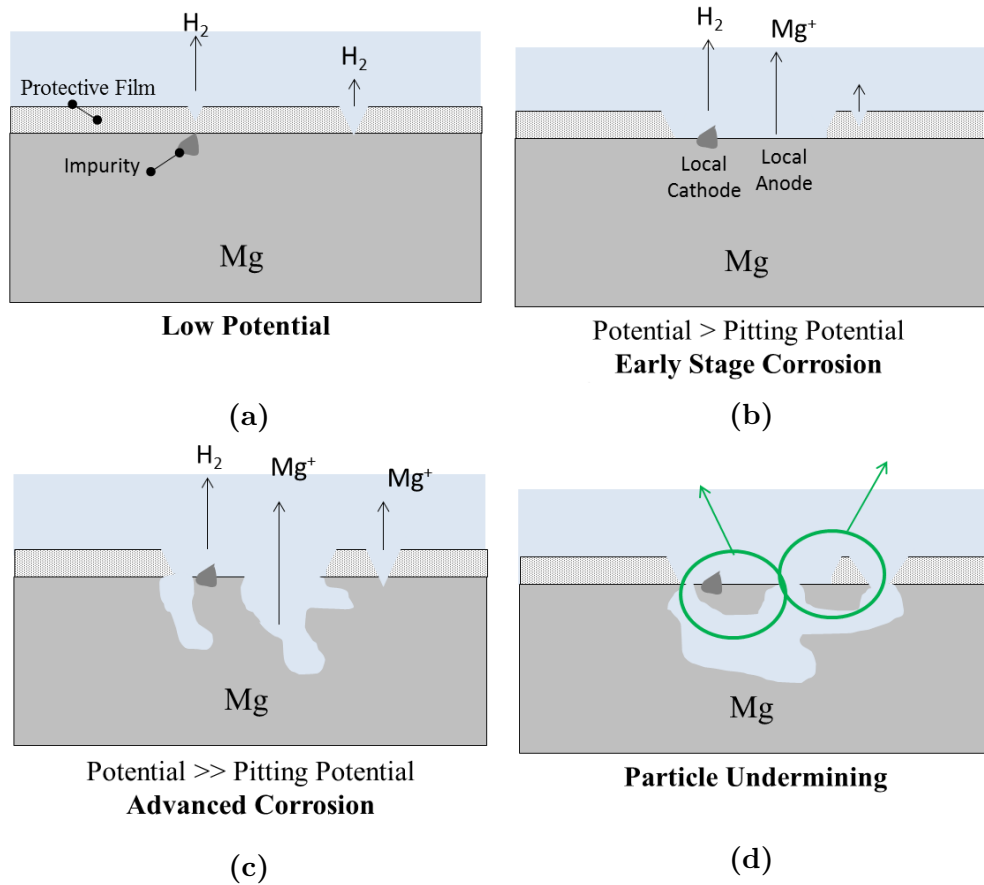


**Figure 2.4.:** A schematic of the corrosion mechanisms for magnesium in aqueous environments. (a) For short periods of immersion or for low applied potentials a protective oxide film covers the magnesium surface. There is a possibility of corrosion where there film is ruptured or in the vicinity of impurities. (b) Over time, or for higher applied potentials, the film is removed in a localized region and local cathodes and anodes can form on the surface. (c) After an extended period of time, or for applied potentials that are significantly greater than the pitting potential of magnesium in a solution, a large degree of localized corrosion occurs, with additional mass loss due to particle undermining possible, as depicted in (d).

## 2. Background

to preferential grain boundary corrosion typical of other alloys, such as steels and iron alloys [95].

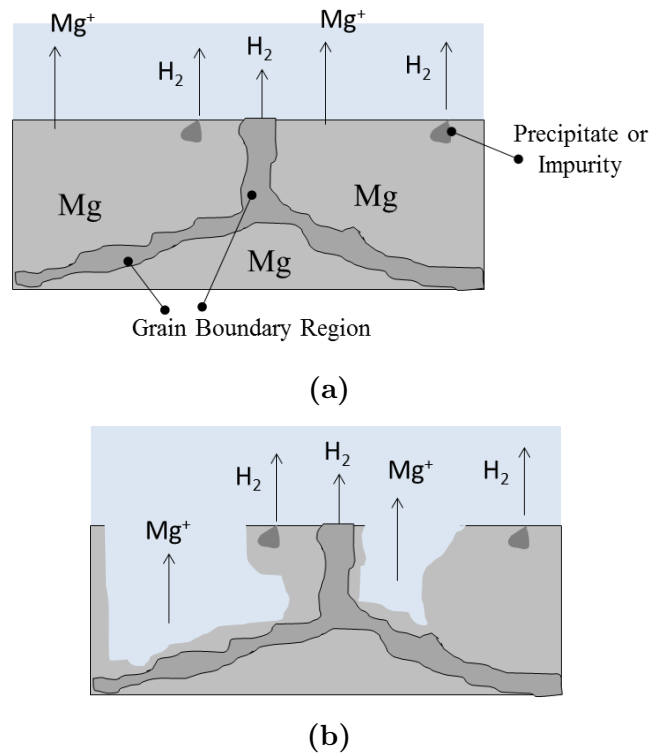


**Figure 2.5.:** A schematic of micro-galvanic corrosion in magnesium alloys in aqueous environments. (a) Grain boundary regions and impurities can act as local cathodes on the corrosion surface, where hydrogen is evolved. This leads to preferential corrosion of the surrounding anodic regions, where magnesium ions are dissolved, as depicted in (b).

The *in-vitro* and *in-vivo* corrosion behaviours of magnesium alloys can depend on many factors, including:

- alloy composition and processing conditions
- surface condition and the presence of surface coatings
- composition of the corrosive environment
- transport conditions in the corrosive environment

## 2. Background

- static and dynamic loading of the alloy.

As reviewed in Kirkland *et al.* [42], by varying the composition of magnesium alloys, the corrosion rate can be changed by over three orders of magnitude in modified Eagle's medium (MEM). Impurities such as iron, nickel and copper are highly detrimental to the corrosion performance of magnesium alloys [92], as they act as cathodic sites in the microstructure. The characteristics of the microstructure, such as the grain size and the distribution of secondary phases, also affect corrosion performance, with it shown for magnesium alloy AZ31 that smaller grains give improved corrosion resistance in NaCl and phosphate buffered saline (PBS) solutions [96, 97].

It has been reported that smoother surface finishes [98] and anodizing treatments [99], which increase the thickness of the protective oxide film, can improve the corrosion resistance of some magnesium alloys in NaCl and Hank's solutions. Hydroxyapatite coatings have been found to significantly reduce localized corrosion of AZ91 implants in simulated body fluid (SBF) [100]. The effect of polymer coatings on corrosion behaviour is not clear. The study of Wong *et al.* [101] reported improved corrosion resistance in AZ91 alloys coated in polycaprolactone (PCL) *in-vivo*, however the study of Chen *et al.* [69] reported that PCL and poly-L-lactic acid (PLLA) coatings increased corrosion rates *in-vitro*, possibly due to an un-anticipated chemical reaction between the coatings and the underlying alloy.

As discussed in Xin *et al.* [102], the *in-vitro* corrosion behaviour of magnesium alloys depends very much on the test media used. Typical media used for *in-vitro* corrosion testing include 0.9% wt NaCl, SBF, PBS, Hank's solution and Dulbecco's modified Eagle's medium (D-MEM). Differences in corrosion behaviours in different test media are attributed largely to differences in chlorine content and

## 2. Background

$\text{HCO}_3^-$  and  $\text{HPO}_4^{2-}$  ion content [102]. Chlorine is known to increase corrosion rates by breaking down the protective  $\text{Mg}[\text{OH}]_2$  barrier on the corrosion surface.  $\text{HCO}_3^-$  and  $\text{HPO}_4^{2-}$  ions are known to increase corrosion resistance due to the formation of carbonates and phosphates on the corrosion surface, which form a barrier that is not broken down by chlorine ions. The presence of proteins, for example serum albumin, has also been found to significantly reduce corrosion rates through their adsorption at the corrosion surface [103, 104].

Lévesque *et al.* [105] reported increased corrosion rates for magnesium AM60 alloy with increasing flow rates in Hank's solution. The transport of corrosion products and reactants *in-vivo*, to and from the corrosion surface, is also likely to play an important role in dictating corrosion rates, as discussed in Witte *et al.* [92]. It is suggested in Witte *et al.* [92] that differences in hydrogen solubility and diffusivity in different regions of the body may explain differences in reported corrosion rates in implants placed in different anatomical regions [106, 107].

Certain magnesium alloys when subject to static or cyclic loads have been found to be subject to stress corrosion cracking (SCC) and corrosion fatigue in aqueous environments [108, 109]. SCC occurs in magnesium alloys via inter-granular SCC and trans-granular SCC. Inter-granular SCC has been attributed to the formation of cracks due to preferential corrosion along grain boundaries that are rich in secondary phases [93]. Trans-granular SCC is not as well understood, but it is likely to be a result of local rupture of the protective oxide film, the formation of an initial pit and gradual crack opening from the pit driven by hydrogen embrittlement at the crack tip [93]. There have been few studies on SCC of magnesium alloys in physiological environments to date. Bobby Kannan *et al.* [110] have reported SCC in AZ91 alloy samples under constant extension rate tensile tests in SBF, however Bobby Kannan and Raman [111] reported little evidence of SCC in AZ91Ca alloys subject to slow strain rate testing in SBF.

## 2. Background

Gu *et al.* [7] have reported marked reductions in fatigue limits of AZ91D and WE43 alloys subject to cyclic loading in SBF, suggesting a susceptibility of these alloys to corrosion fatigue.

### 2.3.2. Iron Corrosion Studies

There have been fewer studies on the corrosion of iron for AMS applications than magnesium. It has typically been reported that iron and iron alloys undergo localized corrosion in both *in-vitro* tests in simulated physiological fluids [95, 112, 113] and in *in-vivo* tests [114, 115]. Preferential corrosion in the vicinity of grain boundaries has also been reported for iron alloys [95, 112]. The corrosion rate of pure iron is typically somewhat lower than magnesium alloys [113], with iron stents still being clearly visible in *in-vivo* tests up to 18 months after implantation [114]. The possibilities of increasing corrosion rates and reducing pitting susceptibility of pure iron through alloying and the use micro-forming processes have been investigated in a number of studies [95, 112, 116]. These studies have shown some potential in overcoming the limitations of pure iron for use in AMS applications.

### 2.3.3. Numerical Modelling of Corrosion

To date there have been few approaches developed specifically for modelling the corrosion of AMS's. However, the use of numerical modelling in studying corrosion in general is a highly active field. Numerical corrosion modelling approaches that may be useful for modelling AMS corrosion are discussed here.

The boundary element method has been applied to the study of corrosion of many

## 2. Background

metals, including magnesium [117, 118, 119, 120]. The focus of these models is on predicting corrosion current densities, which can be related to mass loss rates, for given potential fields. A limitation of these studies is that they assume no movement of the corrosion surface. A number of recent studies on magnesium and aluminium have employed the finite element method (FEM) and adaptive meshing to predict the evolution of the corrosion surface, driven by corrosion currents arising from potential fields [121, 122, 123]. The most advanced of these studies to date also accounts for the presence and re-deposition of corrosion products on the evolving corrosion surface and the diffusion of reactants and products through this layer [123].

While these physical corrosion models are important in terms of understanding the mechanisms of magnesium corrosion, to date they have only been applied to model specific 2-D problems, such as the evolution of a single pit or a crevice at a bimetallic interface. The extension of such models to the analysis of a complex 3-D structure, while also accounting for the mechanical behaviour of the structure (which is necessary for AMS analysis), is challenging due to the added computational expense and the difficulty in solving moving boundary problems in 3-D structures with complex evolving topologies.

The use of continuum damage mechanics to represent the effects of corrosion on the structural integrity of AMS's in a phenomenological manner is a promising way to avoid the practical difficulties associated with implementing physical corrosion models for a full 3-D AMS geometry. The possibility of using continuum damage mechanics in such a manner was included in early texts on the subject, e.g. Kachanov [124]. A number of studies have since applied these concepts to analytically model the effects of phenomena such as SCC and corrosion fatigue on the structural integrity of industrial components [125, 126]. Wenman *et al.* [127] applied continuum damage mechanics in 2-D FE models of SCC in stainless steel

## 2. Background

tubing, including the idea of removing elements once a critical degree of corrosion induced damage was reached. Gastaldi *et al.* [128] subsequently applied the methodologies of Wenman *et al.* [127] and da Costa Mattos *et al.* [126] to study the uniform and stress mediated corrosion of AMS geometries using FEA, based on assumed corrosion behaviours.

### 2.3.4. Absorbable Metal Stent Mechanics

As shown in Table 1.1, the mechanical properties of magnesium alloys and iron are inferior to those of conventional stent materials. As reported in Deng *et al.* [43], this makes the design of magnesium stents with acceptable mechanical performance challenging. Very little experimental data has been reported regarding the mechanical performance of AMS's. Data from the PROGRESS-AMS trial reported a 'collapse pressure' of 0.8 bar and elastic recoil of less than 8% for the MAGIC AMS, but did not report the test methodology used to obtain these measures [40]. For iron stents Peuster *et al.* [114] reported a recoil of 2.2%.

There have also been very few numerical studies on AMS mechanics. Aside from the work of this thesis (published in Grogan *et al.* [129] and Grogan *et al.* [130]), Wu *et al.* [131] simulated the deployment of 2-D magnesium hinges, reporting maximum strains and recoils. Gastaldi *et al.* [21] simulated the deployment and corrosion of a magnesium stent, again reporting maximum strains. Wu *et al.* [132] simulated the deployment and corrosion of magnesium stents with two different designs in stenosed vessels and reported predicted vessel recoils of between 6.2 and 11.8% and maximum device strains of between 0.103 and 0.153. Iqbal Sabir *et al.* [133] have also investigated deployment stresses, strains and recoil in magnesium stents, without considering corrosion.

## 2. Background

In summary, given the lack of published knowledge on the mechanics of magnesium stents and the absence of published FEA studies on the performance of iron stents, it is important that an in depth study on AMS mechanics is performed. Also, given that device corrosion will play an important role in dictating AMS mechanics, it is important that current corrosion modelling approaches are improved upon and tailored for the investigation of corroding AMS mechanics. Given that it is necessary for AMS's to at least match the scaffolding performance of modern permanent stents before they can be considered for clinical applications, a study of particular importance, which has not been carried out in the literature to date, is the direct comparison of the mechanical performance of magnesium, iron and modern permanent stents. This comparison is performed using FEA in Ch. 4 of this work.

# 3. Theory

## 3.1. Chapter Summary

Simulations performed in this thesis involve solving continuum mechanics problems. The theoretical framework, finite deformation kinematics, and governing equations for these problems are introduced in Section 3.2. Relevant material constitutive theories are overviewed in Section 3.3. The FEM, as implemented in the Abaqus commercial solvers (DS SIMULIA, USA), is the numerical tool used to solve these continuum mechanics problems and is introduced in Section 3.4.

Arbitrary Lagrangian Eulerian (ALE) adaptive meshing, which is used in Chs. 7 and 8, is discussed in Section 3.5. Optimization methods are used in Ch. 7 and are introduced in Section 3.6. Optimizations are performed using the open-source DAKOTA optimization toolkit (Sandia Laboratories, USA) and use the efficient global optimization (EGO) algorithm [134].

Throughout this chapter regular italic typeface ( $\pi$ ,  $\rho$ , etc.) denotes scalars and bold italic typeface ( $\mathbf{x}$ ,  $\boldsymbol{\sigma}$ , etc.) denotes vectors, tensors and matrices. The discussion of continuum mechanics is based on the use of a Cartesian co-ordinate system, resulting in the following set of basis vectors:  $\mathbf{e}_1 = (1, 0, 0)$ ,  $\mathbf{e}_2 = (0, 1, 0)$ ,

### 3. Theory

$\mathbf{e}_3 = (0, 0, 1)$ . Vectors can be represented in component form as:  $\mathbf{v} = v_i \mathbf{e}_i$ , where summation is assumed over repeated subscript Roman indices. Tensors (2nd order) can be represented in component form as:  $\mathbf{A} = A_{ij} \mathbf{e}_i \mathbf{e}_j$ , where  $\mathbf{ab}$  indicates the tensor product, with  $(\mathbf{ab})_{kl} = a_k b_l$ . Indices in parenthesis, e.g.  $\mathbf{A}^{(a)}$ , are not associated with the indicial notation used for vectors and tensors.

## 3.2. Continuum Mechanics

Computer simulations performed in this thesis are based in a finite deformation kinematic framework. A brief overview of this framework is given here. For more detailed descriptions the reader is referred to Belytschko *et al.* [135], Holzapfel [136], Dunne and Petrinic [137] and the Abaqus Theory Manual (DS SIMULIA, USA).

### 3.2.1. Deformation and Stress

Considering Fig. 3.1, a body initially encompassing the region  $\Omega_0$  in the reference configuration undergoes a motion  $\chi$  such that it subsequently encompasses the region  $\Omega$  in the current configuration. The position of a material point  $P$  relative to the fixed origin  $O$  is given by the vector  $\mathbf{X}$  in the reference configuration and the vector  $\mathbf{x} = \chi(\mathbf{X}, t)$  in the current configuration. The components of  $\mathbf{X}$ ,  $X_i$ , define the material coordinates of point  $P$  and the components of  $\mathbf{x}$ ,  $x_i$ , define the spatial coordinates. The displacement of  $P$  between the reference and current configuration is  $\mathbf{u} = \mathbf{x} - \mathbf{X}$ .

The vector  $d\mathbf{X}$ , which describes the infinitesimal line element in the reference

### 3. Theory

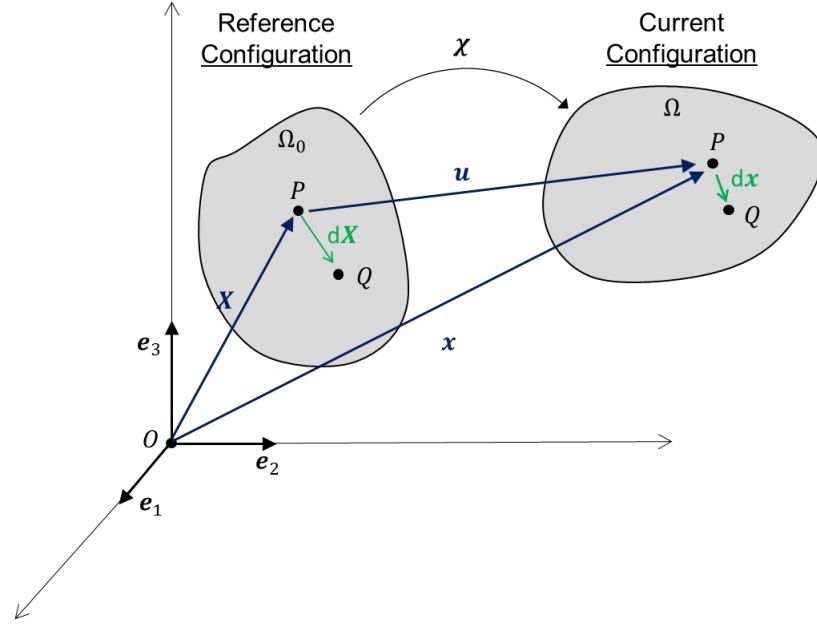


**Figure 3.1.:** A schematic of a body undergoing motion from the reference to current configuration.

configuration between the material points  $P$  and  $Q$  is transformed to  $d\mathbf{x}$  in the current configuration through the deformation gradient  $\mathbf{F}$ , where:

$$\mathbf{F} = \frac{\partial \mathbf{x}}{\partial \mathbf{X}} \text{ or } F_{ij} = \frac{\partial x_i}{\partial X_j} \quad (3.1)$$

The Green-Lagrange strain  $\mathbf{E}$  is given by:

$$\mathbf{E} = \frac{1}{2}(\mathbf{F}^T \cdot \mathbf{F} - \mathbf{I}) \text{ or } E_{ij} = \frac{1}{2} \left( \frac{\partial u_i}{\partial X_j} + \frac{\partial u_j}{\partial X_i} + \frac{\partial u_k}{\partial X_i} \frac{\partial u_k}{\partial X_j} \right) \quad (3.2)$$

where  $\mathbf{F}^T$  is the transpose of  $\mathbf{F}$ ,  $(\mathbf{A} \cdot \mathbf{F})_{ij} = A_{ik}F_{kj}$  for any tensor  $\mathbf{A}$  and  $\mathbf{I}$  is the identity tensor, with the property  $\mathbf{F} \cdot \mathbf{I} = \mathbf{F}$ . The infinitesimal strain  $\boldsymbol{\epsilon}$  can be found from the Green-Lagrange strain by assuming that the product of infinitesimals is negligible, giving:

$$\epsilon_{ij} = \frac{1}{2} \left( \frac{\partial u_i}{\partial X_j} + \frac{\partial u_j}{\partial X_i} \right) \quad (3.3)$$

The left and right Cauchy-Green tensors,  $\mathbf{B}$  and  $\mathbf{C}$  respectively, are useful mea-

### 3. Theory

asures of stretch, given by:

$$\mathbf{B} = \mathbf{F} \cdot \mathbf{F}^T \text{ and } \mathbf{C} = \mathbf{F}^T \cdot \mathbf{F} \quad (3.4)$$

According to the polar decomposition theorem the deformation gradient can be uniquely decomposed into an orthogonal rotation tensor  $\mathbf{R}$  and symmetric spatial and material stretch tensors,  $\mathbf{V}$  and  $\mathbf{U}$  respectively, according to:

$$\mathbf{F} = \mathbf{R} \cdot \mathbf{U} = \mathbf{V} \cdot \mathbf{R} \quad (3.5)$$

The eigenvectors and eigenvalues of  $\mathbf{U}$  are known as the respective principal referential axes and principal stretches,  $\hat{\lambda}_{a=1,2,3}$ . The logarithmic (true) strain  $\boldsymbol{\varepsilon}$  is:

$$\boldsymbol{\varepsilon} = \ln \mathbf{V} \quad (3.6)$$

The eigenvalues of  $\boldsymbol{\varepsilon}$  are the principal logarithmic strains. Results of simulations in this thesis are typically presented in terms of the maximum principal logarithmic strain,  $\varepsilon_{mp}$ .

The velocity  $\mathbf{v}$  of material point  $P$  is:

$$\mathbf{v} = \frac{\partial \mathbf{x}}{\partial t} \quad (3.7)$$

where the partial derivative with respect to time means the rate of change of  $\mathbf{x}$  for fixed  $\mathbf{X}$ . The spacial velocity gradient  $\mathbf{L}$  is:

$$\mathbf{L} = \frac{\partial \mathbf{v}}{\partial \mathbf{x}} = \frac{\partial \mathbf{v}}{\partial \mathbf{X}} \cdot \frac{\partial \mathbf{X}}{\partial \mathbf{x}} = \frac{\partial \mathbf{F}}{\partial t} \cdot \mathbf{F}^{-1} = \dot{\mathbf{F}} \cdot \mathbf{F}^{-1} \quad (3.8)$$

where  $\mathbf{F}^{-1}$  is the inverse of  $\mathbf{F}$ . The spatial velocity gradient can be decomposed into the symmetric rate of deformation tensor  $\mathbf{D}$  and the antisymmetric spin

### 3. Theory

tensor  $\mathbf{W}$ :

$$\begin{aligned}\mathbf{D} &= \frac{1}{2}(\mathbf{L} + \mathbf{L}^T) \\ \mathbf{W} &= \frac{1}{2}(\mathbf{L} - \mathbf{L}^T)\end{aligned}\tag{3.9}$$

Based on the definition of  $\mathbf{D}$  a rate of true strain (or natural strain in Malvern [138])  $\dot{\boldsymbol{\varepsilon}}$  can be identified as:

$$\dot{\boldsymbol{\varepsilon}} = \mathbf{D}\tag{3.10}$$

Under conditions where the principal referential axes remain fixed with respect to the material coordinates,  $\dot{\boldsymbol{\varepsilon}}$  can be integrated to yield a strain measure  $\boldsymbol{\varepsilon}$ :

$$\boldsymbol{\varepsilon} = \int_0^t \mathbf{D} dt\tag{3.11}$$

which for this case is equivalent to the logarithmic strain (Abaqus Theory Manual, DS SIMULIA, USA).

With reference to Fig. 3.2, the traction  $\mathbf{t}$  is the force per unit area that acts on an infinitesimal surface element  $dS$  in the vicinity of  $P$  in the current configuration. The surface element  $dS$  is described by its unit normal  $\mathbf{n}$ . The Cauchy (true) stress  $\boldsymbol{\sigma}$  is given by:

$$\mathbf{t} = \boldsymbol{\sigma} \cdot \mathbf{n}\tag{3.12}$$

The Cauchy stress is a symmetric tensor which can be expressed in terms of a deviatoric stress  $\mathbf{S}$  and a hydrostatic pressure stress  $p$  according to:

$$\boldsymbol{\sigma} = \mathbf{S} - p\mathbf{I}\tag{3.13}$$

with

$$p = \frac{-\text{Tr}(\boldsymbol{\sigma})}{3}\tag{3.14}$$

### 3. Theory

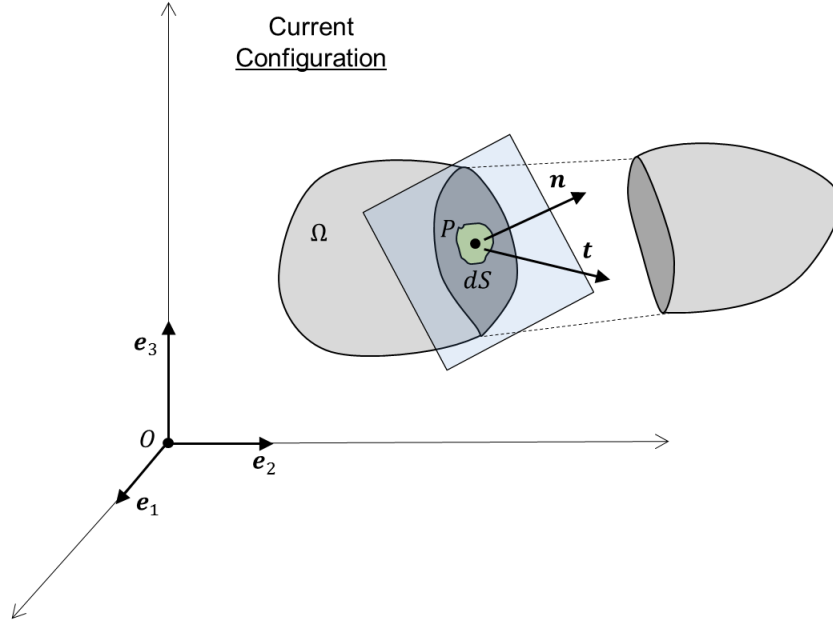


**Figure 3.2.:** A depiction of the traction vector  $\mathbf{t}$  on an internal surface of a body cut by a plane with normal  $\mathbf{n}$  in the current configuration.

where  $\text{Tr}(\boldsymbol{\sigma}) = \sigma_{ii}$ . The von Mises equivalent stress is:

$$\sigma_e = \sqrt{\frac{3}{2} S_{ij} S_{ij}} \quad (3.15)$$

The Kirchhoff stress  $\boldsymbol{\tau}$  is a symmetric tensor given by:

$$\boldsymbol{\tau} = J\boldsymbol{\sigma} \quad (3.16)$$

where  $J = \frac{d\Omega}{d\Omega_0}$  is the ratio of infinitesimal volumes in the vicinity of  $P$  in the current ( $d\Omega$ ) and reference ( $d\Omega_0$ ) configurations. The Piola stress is a non-symmetric tensor given by:

$$\mathbf{P} = J\boldsymbol{\sigma}\mathbf{F}^{-T} \quad (3.17)$$

while the nominal stress is:

$$\tilde{\boldsymbol{\sigma}} = J\mathbf{F}^{-1}\boldsymbol{\sigma} = \mathbf{P}^T \quad (3.18)$$

For material constitutive behaviours expressed in rate form a useful objective

### 3. Theory

stress rate is the Jaumann stress rate:

$$\overset{\nabla}{\boldsymbol{\sigma}} = \dot{\boldsymbol{\sigma}} - \mathbf{W} \cdot \boldsymbol{\sigma} + \boldsymbol{\sigma} \cdot \mathbf{W} \quad (3.19)$$

where  $\dot{\boldsymbol{\sigma}}$  is the time derivative of the Cauchy stress for a fixed  $\mathbf{X}$ .

Results of simulations in this thesis are presented in terms of Cauchy stress  $\boldsymbol{\sigma}$  and von Mises stress  $\sigma_e$ .

#### 3.2.2. Equilibrium Equations and Principle of Virtual Work

For bodies that are not subject to body forces the balance of linear momentum can be expressed in indicial notation as:

$$\frac{\partial \sigma_{ij}}{\partial x_j} = \rho \frac{\partial v_i}{\partial t} = \rho \dot{v}_i = \rho \ddot{u}_i \quad (3.20)$$

where  $\rho_0$  is the density in the reference configuration and  $\rho = J^{-1}\rho_0$ . When  $\boldsymbol{\sigma}$  is symmetric this can be written in tensor notation as:

$$\nabla \cdot \boldsymbol{\sigma} = \rho \frac{\partial \mathbf{v}}{\partial t} = \rho \dot{\mathbf{v}} = \rho \ddot{\mathbf{u}} \quad (3.21)$$

Eqs. 3.20 or 3.21 can be solved through the application of suitable boundary conditions and, if required, initial conditions. When using the FEM these equations are solved by expressing them through the principle of virtual work, which in rate form states that:

$$\delta \bar{W} = \int_{\Omega} (\nabla \cdot \boldsymbol{\sigma} - \rho \ddot{\mathbf{u}}) \cdot \delta \mathbf{v} d\Omega = 0 \quad (3.22)$$

### 3. Theory

where  $\delta\bar{W}$  is the increment in virtual work rate per unit volume and  $\delta\mathbf{v}$  is an arbitrary virtual velocity field that satisfies the kinematic boundary conditions of the problem. Through some manipulations, see Dunne and Petrinic [137], Eqn. 3.22 can be expressed as:

$$\int_{\Omega} \boldsymbol{\sigma} : \delta\mathbf{D}d\Omega = \int_{\partial\Omega} \mathbf{t} \cdot \delta\mathbf{v}d\partial\Omega - \int_{\Omega} \rho\ddot{\mathbf{u}} \cdot \delta\mathbf{v}d\Omega \quad (3.23)$$

where  $\boldsymbol{\sigma} : \delta\mathbf{D} = \sigma_{ij}\delta D_{ij}$  and  $\partial\Omega$  is the bounding surface of  $\Omega$ . This equation is approximated and solved using the FEM, as discussed in Section 3.4.

## 3.3. Material Constitutive Behaviours

### 3.3.1. Isotropic Linear Elasticity Theory

In this study isotropic linear elasticity is assumed for a number of polymeric materials that undergo small ( $< 5\%$ ) strains and also for the elastic portion of the elastic-plastic behaviour of metals. In isotropic linear elasticity the nominal stress  $\tilde{\boldsymbol{\sigma}}$  is related to the infinitesimal strain  $\boldsymbol{\epsilon}$  through:

$$\tilde{\sigma}_{ij} = \lambda\epsilon_{kk}\delta_{ij} + 2\mu\epsilon_{ij} \quad (3.24)$$

where  $\lambda$  and  $\mu$  are the Lamé constants and  $\delta_{ij}$  is the Kronecker delta, with the property:

$$\delta_{ij} = \begin{cases} 1 & i = j \\ 0 & i \neq j \end{cases} \quad (3.25)$$

Under the assumptions of infinitesimal deformation kinematics, stress measures become equal,  $\boldsymbol{\sigma} = \tilde{\boldsymbol{\sigma}} = \mathbf{P}$ . The Lamé constants can be derived from Young's

### 3. Theory

Modulus  $E$  and Poisson's Ratio  $\nu$  through:

$$\mu = \frac{E}{2(1 + \nu)} \text{ and } \lambda = \frac{\nu E}{(1 + \nu)(1 - 2\nu)} \quad (3.26)$$

For this theory it is also possible to define a fourth order tensor of elastic moduli  $\mathbf{K}$  such that:

$$\tilde{\boldsymbol{\sigma}} = \mathbf{K} : \boldsymbol{\epsilon} \text{ or } \tilde{\sigma}_{ij} = K_{ijkl}\epsilon_{kl} \quad (3.27)$$

In this thesis this isotropic elasticity theory is implemented in a finite deformation kinematic framework by using the Cauchy stress and the logarithmic strain in place of the infinitesimal measures used in Eqn. 3.24 (see the Abaqus Theory Manual, DS SIMULIA, USA).

#### 3.3.2. Large Strain Elasticity Theory

More general hyperelastic constitutive theories are employed in modelling the behaviour of soft, nearly incompressible, biological tissues undergoing large elastic strains. Hyperelastic materials are described in terms of a strain energy function  $U$  which defines the strain energy stored in a material per unit volume (in the reference configuration) as a function of deformation. In general, for a hyperelastic material:

$$\mathbf{P} = \frac{\partial U(\mathbf{F})}{\partial \mathbf{F}} \quad (3.28)$$

Based on Eqn. 3.17 the Cauchy stress is then:

$$\boldsymbol{\sigma} = \frac{1}{J} \mathbf{F} \cdot \frac{\partial U(\mathbf{F})}{\partial \mathbf{F}} \quad (3.29)$$

The hyperelastic material theories used in this thesis are discussed in detail in Holzapfel [136] and Holzapfel *et al.* [139]. The notation used in describing the theories in this section is based on that of the Abaqus Theory Manual (DS SIMU-

### 3. Theory

LIA, USA).

The volume preserving part of the deformation gradient  $\bar{\mathbf{F}}$  is:

$$\bar{\mathbf{F}} = J^{-\frac{1}{3}} \mathbf{F} \quad (3.30)$$

Isotropic hyperelastic materials can be described in terms of the distortional part of the left Cauchy-Green tensor (also known as the deviatoric stretch tensor)  $\bar{\mathbf{B}}$ :

$$\bar{\mathbf{B}} = J^{-\frac{2}{3}} \mathbf{B} \quad (3.31)$$

and the first and second invariants:

$$\bar{I}_1 = \mathbf{I} : \bar{\mathbf{B}} \quad (3.32)$$

and

$$\bar{I}_2 = \frac{1}{2}(\bar{I}_1^2 - \mathbf{I} : \bar{\mathbf{B}} \cdot \bar{\mathbf{B}}) \quad (3.33)$$

Based on this description,  $U = U(\bar{I}_1, \bar{I}_2, J)$  and from Eqn. 3.29 the Cauchy stress is given by:

$$\boldsymbol{\sigma} = \frac{2}{J} \text{dev} \left( \left( \frac{\partial U}{\partial \bar{I}_1} + \bar{I}_1 \frac{\partial U}{\partial \bar{I}_2} \right) \bar{\mathbf{B}} - \frac{\partial U}{\partial \bar{I}_2} \bar{\mathbf{B}} \cdot \bar{\mathbf{B}} \right) + \frac{\partial U}{\partial J} \mathbf{I} \quad (3.34)$$

where  $\text{dev}(\mathbf{A}) = \mathbf{A} - \frac{1}{3} \text{Tr}(\mathbf{A}) \mathbf{I}$  for any tensor  $\mathbf{A}$ .

The following form of  $U$ , known as a reduced order polynomial hyperelastic model (see the Abaqus Theory Manual, DS SIMULIA, USA), is used in this study for modelling the isotropic deformation of arterial layers and the elastic portion of the deformation of plaque tissue:

$$U = \sum_{\alpha=1,6} C^{(\alpha)} (\bar{I}_1 - 3)^\alpha + \frac{1}{D^{(\alpha)}} (J - 1)^{2\alpha} \quad (3.35)$$

### 3. Theory

where  $C^{(\alpha 0)}$  and  $D^{(\alpha)}$  are material constants. This model has previously been used for this purpose in Gastaldi *et al.* [21] and Conway *et al.* [23].

Anisotropic hyperelastic materials can be described in terms of the previous quantities and also the distortional part of the right Cauchy-Green strain tensor:

$$\bar{\mathbf{C}} = J^{-\frac{2}{3}} \mathbf{C} \quad (3.36)$$

and pseudo-invariants  $\bar{I}_4$  and  $\bar{I}_5$ . The pseudo-invariants are given by:

$$\begin{aligned} \bar{I}_4^{(\alpha\beta)} &= \mathbf{A}^{(\alpha)} \cdot \bar{\mathbf{C}} \cdot \mathbf{A}^{(\beta)} \text{ where } \alpha = 1, \dots, N; \beta = 1, \dots, \alpha \\ \bar{I}_5^{(\alpha\beta)} &= \mathbf{A}^{(\alpha)} \cdot \bar{\mathbf{C}}^2 \cdot \mathbf{A}^{(\beta)} \text{ where } \alpha = 1, \dots, N; \beta = 1, \dots, \alpha \end{aligned} \quad (3.37)$$

where  $\mathbf{A}^{(\alpha)}$  and  $\mathbf{A}^{(\beta)}$  are sets of unit vectors that describe  $N$  families of fibre directions in the material in the reference configuration and  $\bar{\mathbf{C}}^2 = \bar{\mathbf{C}} \cdot \bar{\mathbf{C}}$ . In this case  $U = U(\bar{I}_1, \bar{I}_2, J, \bar{I}_4, \bar{I}_5)$  and the Cauchy stress is given by:

$$\begin{aligned} \boldsymbol{\sigma} &= \frac{2}{J} \text{dev} \left( \left( \frac{\partial U}{\partial \bar{I}_1} + \bar{I}_1 \frac{\partial U}{\partial \bar{I}_2} \right) \bar{\mathbf{B}} - \frac{\partial U}{\partial \bar{I}_2} \bar{\mathbf{B}} \cdot \bar{\mathbf{B}} \right) + \frac{\partial U}{\partial J} \mathbf{I} \\ &+ \sum_{\alpha=1}^N \sum_{\beta=1}^{\alpha} \frac{\partial U}{\partial \bar{I}_4^{(\alpha\beta)}} \text{dev}(\bar{\mathbf{a}}^{(\alpha)} \bar{\mathbf{a}}^{(\beta)} + \bar{\mathbf{a}}^{(\beta)} \bar{\mathbf{a}}^{(\alpha)}) \\ &+ \sum_{\alpha=1}^N \sum_{\beta=1}^{\alpha} \frac{\partial U}{\partial \bar{I}_5^{(\alpha\beta)}} \text{dev}(\bar{\mathbf{a}}^{(\alpha)} \bar{\mathbf{a}}^{(\beta)'} + \bar{\mathbf{a}}^{(\alpha)'} \bar{\mathbf{a}}^{(\beta)} + \bar{\mathbf{a}}^{(\beta)} \bar{\mathbf{a}}^{(\alpha)'} + \bar{\mathbf{a}}^{(\beta)'} \bar{\mathbf{a}}^{(\alpha)}) \\ &+ \frac{\partial U}{\partial J} \mathbf{I} \end{aligned} \quad (3.38)$$

where:

$$\begin{aligned} \bar{\mathbf{a}}^{(\alpha)} &= \bar{\mathbf{F}} \cdot \mathbf{A}^{(\alpha)} \\ \bar{\mathbf{a}}^{(\alpha)'} &= \bar{\mathbf{B}} \cdot \mathbf{A}^{(\alpha)} \end{aligned} \quad (3.39)$$

The following form of  $U$  is used in this study to model the anisotropic behaviour

### 3. Theory

of fibre re-enforced layers of arterial tissue [139]:

$$\begin{aligned}
 U = & \mu(\bar{I}_1 - 3) \\
 & + \frac{k_1}{2k_2} \sum_{\alpha=4,5} \left( \exp \left[ k_2 \left\{ (1 - \rho_f) (\bar{I}_1 - 3)^2 + \rho_f (\bar{I}_{(\alpha)} - 1)^2 \right\} \right] - 1 \right) \\
 & + \kappa \frac{(J - 1)^2}{2}
 \end{aligned} \tag{3.40}$$

where  $\mu$ ,  $k_1$ ,  $k_2$  and  $\rho_f$  are material constants. The constant  $\kappa$ , which is related to the Bulk Modulus, controls compressibility in the tissue and is determined through numerical experiments. The parameter  $\rho_f$  controls the degree of fibre dispersion in the tissue, with isotropic behaviour when  $\rho_f = 0$  and perfect alignment of all fibres when  $\rho_f = 1$ . For the tissue model used in this study, there are two families of fibres which are assumed to be symmetrically arranged in the tubular tissue construct with no radial components. This means the vectors  $\mathbf{A}^{(\alpha)}$  and  $\mathbf{A}^{(\beta)}$  are simply described by the angle  $\alpha_f$  with the circumferential vessel direction, as depicted in Fig. 3.3.

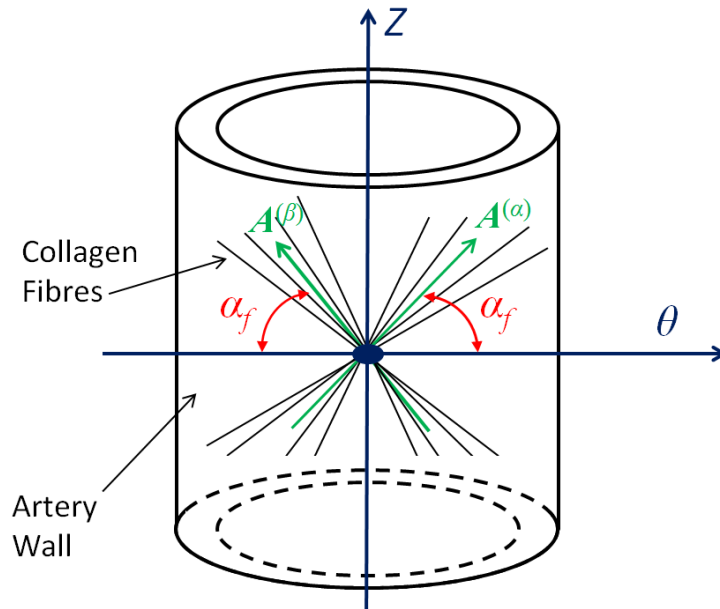


**Figure 3.3.:** A schematic of an artery showing dispersed fibres with mean fibre directions described by the vectors  $\mathbf{A}^{(\alpha)}$  and  $\mathbf{A}^{(\beta)}$ . Due to the assumed symmetry of the two fibre families the vectors are simply described by the angle  $\alpha_f$  with the circumferential vessel direction  $\theta$ .

### 3.3.3. $J_2$ Plasticity Theory

Metal and soft-tissue plasticity at the macroscale are modelled in this thesis using  $J_2$  plasticity theory with isotropic hardening. In applying  $J_2$  plasticity theory in the simulation of metals, elastic strains are assumed to be small and the total strain rate  $\dot{\boldsymbol{\varepsilon}}$  is decomposed into elastic  $\dot{\boldsymbol{\varepsilon}}^e$  and plastic  $\dot{\boldsymbol{\varepsilon}}^{pl}$  parts according to the classical additive decomposition of strain rate:

$$\dot{\boldsymbol{\varepsilon}} = \dot{\boldsymbol{\varepsilon}}^e + \dot{\boldsymbol{\varepsilon}}^{pl} \quad (3.41)$$

In rate independent plasticity a yield function  $f$  can be defined such that there is plastic flow when:

$$f(\boldsymbol{\sigma}) = 0 \quad (3.42)$$

For the von Mises yield criterion, the yield function is:

$$f = \frac{3}{2} S_{ij} S_{ij} - \sigma_Y^2 \quad (3.43)$$

where  $\sigma_Y$  is the yield stress, which is a function of plastic strain. For materials subject to associated plastic flow the determination of the plastic strain increment  $d\boldsymbol{\varepsilon}^{pl}$  follows from:

$$d\varepsilon_{ij}^{pl} = \frac{\partial g}{\partial \sigma_{ij}} d\lambda \quad (3.44)$$

where  $d\lambda$  is the plastic multiplier, which depends on the stress increment, and  $g$  is the flow potential. For  $J_2$  flow theory Eqn. 3.44 has the following form:

$$d\varepsilon_{ij}^{pl} = S_{ij} d\lambda \quad (3.45)$$

The increment in plastic work can take the following equivalent forms:

$$dW^{pl} = \sigma_{ij} d\varepsilon_{ij}^{pl} = \frac{2}{3} \sigma_e^2 d\lambda = \sigma_e d\varepsilon^{pl} \quad (3.46)$$

### 3. Theory

where  $d\bar{\varepsilon}^{pl} = \sqrt{\frac{3}{2}(d\varepsilon_{ij}^{pl}d\varepsilon_{ij}^{pl})}$  is the equivalent plastic strain increment. The plastic multiplier is then:

$$d\lambda = \frac{3}{2} \frac{d\bar{\varepsilon}^{pl}}{\sigma_e} \quad (3.47)$$

which can be substituted into Eqn. 3.45 to give:

$$d\varepsilon^{pl} = \mathbf{S} \frac{3}{2} \frac{d\bar{\varepsilon}^{pl}}{\sigma_e} \quad (3.48)$$

In Abaqus Eqn. 3.48 is used in incremental form along with Eqn. 3.43 to identify the increment in plastic strain for a known increment in total strain, based on a backward Euler integration method. Once the plastic strain increment is found the increment in stress  $d\boldsymbol{\sigma}$  can be identified by first finding the elastic strain increment from Eqn. 3.41:

$$d\varepsilon^e = d\varepsilon - d\varepsilon^{pl} \quad (3.49)$$

and substituting it into Eqn. 3.27

$$d\boldsymbol{\sigma} = \mathbf{K} : d\varepsilon^e \quad (3.50)$$

In applying  $J_2$  plasticity theory in the simulation of soft tissues, elastic strains cannot be assumed to be small. In this case the ‘Permanent Set’ model available in the Abaqus code (DS SIMULIA, USA) is used. This model uses a multiplicative split of the deformation gradient  $\mathbf{F}$  into elastic  $\mathbf{F}^e$  and plastic  $\mathbf{F}^p$  parts:

$$\mathbf{F} = \mathbf{F}^e \cdot \mathbf{F}^p \quad (3.51)$$

The elastic part of the deformation gradient is given by one of the hyperelastic constitutive behaviours described in the previous section and includes all material rotations. The plastic part of the rate of deformation tensor is given by an

### 3. Theory

associated flow rule based on the von Mises yield criterion:

$$\mathbf{D}^p = \boldsymbol{\tau}' \frac{3 \dot{\bar{\epsilon}}^{pl}}{2 \bar{\tau}} \quad (3.52)$$

where  $\boldsymbol{\tau}' = \text{dev}(\boldsymbol{\tau})$  and  $\bar{\tau} = \sqrt{\frac{3}{2}(\tau'_{ij}\tau'_{ij})}$ . A verification of the suitability of this model for simulating hyperelastic-plastic soft tissue behaviour is performed in Appendix A.1.

#### 3.3.4. Crystal Plasticity Theory

Crystal plasticity theory is a physically motivated plasticity theory that represents massive dislocation flow in a metallic crystal, along crystallographic slip systems, in terms of a continuum measure of plastic shear strain, or slip. The rate-dependent single crystal plasticity theory used in this work is based on that presented in Huang [140] and used in the studies of McGarry *et al.* [141], Savage *et al.* [78] and Harewood and McHugh [80].

In a crystallographic lattice, plastic slip  $\gamma$  occurs in slip systems due to an applied resolved shear stress  $\tau$  acting on that system. Similarly to Eqn. 3.51, the deformation gradient can be decomposed into elastic and plastic parts:

$$\mathbf{F} = \mathbf{F}^* \cdot \mathbf{F}^p \quad (3.53)$$

In this case however, the elastic part  $\mathbf{F}^*$  includes elastic lattice strains and rotations and the plastic part  $\mathbf{F}^p$  includes plastic strains and spin. The rate of deformation tensor  $\mathbf{D}$  and spin tensor  $\mathbf{W}$  can similarly be decomposed into elas-

### 3. Theory

tic (lattice) and plastic parts (see McGarry *et al.* [141]):

$$\begin{aligned} \mathbf{D} &= \mathbf{D}^* + \mathbf{D}^p \\ \mathbf{W} &= \mathbf{W}^* + \mathbf{W}^p \end{aligned} \quad (3.54)$$

$\mathbf{F}^p$  is related to the plastic slip rate by:

$$\dot{\mathbf{F}}^p \cdot \mathbf{F}^{p-1} = \sum_{\alpha=1, N} \dot{\gamma}^{(\alpha)} \mathbf{s}^{(\alpha)} \mathbf{m}^{(\alpha)} \quad (3.55)$$

where  $\dot{\gamma}^{(\alpha)}$  is the plastic slip rate on slip system  $\alpha$  and  $\mathbf{s}^{(\alpha)}$  and  $\mathbf{m}^{(\alpha)}$  are unit vectors defining respective slip directions and normals on each of the  $N$  active slip systems in the reference configuration. Plastic slip is governed by the resolved shear stress on each slip system  $\tau^{(\alpha)}$ , which is found through Schmid's law:

$$\tau^{(\alpha)} = \mathbf{m}^{*(\alpha)} \cdot \boldsymbol{\tau} \cdot \mathbf{s}^{*(\alpha)} \quad (3.56)$$

where  $\mathbf{s}^{*(\alpha)} = \mathbf{F}^* \cdot \mathbf{s}^{(\alpha)}$  and  $\mathbf{m}^{*(\alpha)} = \mathbf{m}^{(\alpha)} \cdot \mathbf{F}^{*-1}$ . The plastic slip rate is related to the resolved shear stress through the following power-law rate-dependent relationship:

$$\dot{\gamma}^{(\alpha)} = \dot{a} \text{sgn}(\tau^{(\alpha)}) \left\{ \left| \frac{\tau^{(\alpha)}}{g^{(\alpha)}} \right| \right\}^n \quad (3.57)$$

where  $\dot{a}$  and  $n$  are the reference strain rate and rate sensitivity exponent, respectively and  $g^{(\alpha)}$  is the slip system strain hardness.  $g^{(\alpha)}$  is related to the plastic slip rates in the lattice through:

$$\dot{g}^{(\alpha)} = \sum_{\beta=1, N} h^{\alpha\beta} |\dot{\gamma}^{(\beta)}| \quad (3.58)$$

where  $h^{(\alpha\beta)}$  are a collection of self and latent strain hardening moduli and  $N$  is the number of slip systems. For simulations of FCC crystals in this study Taylor isotropic hardening is assumed and all self and latent hardening moduli are given

### 3. Theory

by [82]:

$$h^{(\alpha\alpha)} = h^{(\alpha\beta)} = h(\bar{\gamma}) = \frac{dg(\bar{\gamma})}{d\bar{\gamma}} = h_0 \operatorname{sech}^2 \left| \frac{h_0 \bar{\gamma}}{g_\infty - g_0} \right| \quad (3.59)$$

where  $g_0$  and  $g_\infty$  are the initial and maximum slip system hardness respectively and  $h_0$  is the initial slip system strain hardening modulus ( $\frac{\partial g}{\partial \bar{\gamma}}$  when  $\bar{\gamma} = 0$ ). The quantity  $\bar{\gamma}$  is the accumulated plastic slip over all  $N$  slip systems over time and is given by:

$$\bar{\gamma} = \sum_{\alpha=1, N} \int_0^t |\dot{\gamma}^{(\alpha)}| dt \quad (3.60)$$

For simulations of HCP crystals in this study the hardening moduli are given by [50]:

$$\begin{aligned} h^{(\alpha\alpha)} &= h(\bar{\gamma}) \\ h^{(\alpha\beta)} &= q^{(\alpha\beta)} h(\bar{\gamma}) \end{aligned} \quad (3.61)$$

where  $q^{(\alpha\beta)}$  are a set of interaction parameters whose values are given in Ch. 5. Depending on the slip system in question, the following hardening laws are used for the HCP crystals:

- linear hardening

$$h(\bar{\gamma}) = h_0 \quad (3.62)$$

- Voce hardening

$$h(\bar{\gamma}) = h_0 \left( 1 - \frac{g_0}{g_\infty} \right) \exp \left( -\frac{h_0 \bar{\gamma}}{g_\infty} \right) \quad (3.63)$$

### 3. Theory

- deformation twinning

$$h(\bar{\gamma}) = \begin{cases} h_0 & \text{for } \bar{\gamma} \leq \gamma_{ref} \\ h_0 \left( \frac{\bar{\gamma}}{\gamma_{ref}} \right)^{m-1} & \text{for } \bar{\gamma} > \gamma_{ref} \end{cases} \quad (3.64)$$

where  $\gamma_{ref}$  and  $m$  are parameters to be calibrated. To ensure twinning is only active under tensile loading the following condition is also enforced:

$$g^{(\alpha)} \rightarrow \infty \text{ for } \tau^{(\alpha)} \leq 0 \quad (3.65)$$

on the twinning slip systems.

Elasticity of the crystal is described using an elastic strain energy density potential, in particular it is assumed to be linear and isotropic in terms of finite deformation quantities (Cauchy stress and logarithmic strain). It can be described through Young's Modulus  $E$  and Poisson's ratio  $\nu$  using Eqns. 3.24 and 3.26, by replacing infinitesimal stresses and strains with the Cauchy stress and logarithmic strain. Based on the use of this elastic potential, the Jaumann stress rate on axes that rotate with the crystal lattice  $\overset{\nabla}{\boldsymbol{\sigma}}^*$  for a known elastic rate of deformation is [142]:

$$\overset{\nabla}{\boldsymbol{\sigma}}^* + \boldsymbol{\sigma} (\mathbf{I} : \mathbf{D}^*) = \mathbf{K} : \mathbf{D}^* \quad (3.66)$$

This is related to the Jaumann stress rate through:

$$\overset{\nabla}{\boldsymbol{\sigma}} = \overset{\nabla}{\boldsymbol{\sigma}}^* - (\mathbf{W} - \mathbf{W}^*) \cdot \boldsymbol{\sigma} + \boldsymbol{\sigma} \cdot (\mathbf{W} - \mathbf{W}^*) \quad (3.67)$$

Two convenient quantities defined on each slip system are the Schmid factor  $\boldsymbol{\mu}^{(\alpha)}$

### 3. Theory

and  $\boldsymbol{\omega}^{(\alpha)}$ :

$$\begin{aligned}\mu_{ij}^{(\alpha)} &= \frac{1}{2} \left[ s_i^{*(\alpha)} m_j^{*(\alpha)} + s_j^{*(\alpha)} m_i^{*(\alpha)} \right] \\ \omega_{ij}^{(\alpha)} &= \frac{1}{2} \left[ s_i^{*(\alpha)} m_j^{*(\alpha)} - s_j^{*(\alpha)} m_i^{*(\alpha)} \right]\end{aligned}\quad (3.68)$$

The plastic parts of the rate of deformation and spin tensors can then be written as:

$$\mathbf{D}^p = \sum_{\alpha=1,N} \boldsymbol{\mu}^{(\alpha)} \dot{\gamma}^{(\alpha)} \quad (3.69)$$

and

$$\mathbf{W}^p = \sum_{\alpha=1,N} \boldsymbol{\omega}^{(\alpha)} \dot{\gamma}^{(\alpha)} \quad (3.70)$$

Substituting Eqns. 3.54 and 3.66 into Eqn. 3.67 gives:

$$\overset{\nabla}{\boldsymbol{\sigma}} = \mathbf{K} : \mathbf{D} - \mathbf{K} : \mathbf{D}^p - \mathbf{W}^p \cdot \boldsymbol{\sigma} + \boldsymbol{\sigma} \cdot \mathbf{W}^p - \boldsymbol{\sigma}(\mathbf{I} : \mathbf{D}) + \boldsymbol{\sigma}(\mathbf{I} : \mathbf{D}^p) \quad (3.71)$$

Substituting Eqns. 3.69 and 3.70 into Eqn. 3.72 then completes the description of the material constitutive behaviour:

$$\overset{\nabla}{\boldsymbol{\sigma}} = \mathbf{K} : \mathbf{D} - \boldsymbol{\sigma}(\mathbf{I} : \mathbf{D}) - \sum_{\alpha=1,N} \dot{\gamma}^{(\alpha)} \left[ \mathbf{K} : \boldsymbol{\mu}^{(\alpha)} + \boldsymbol{\omega}^{(\alpha)} \cdot \boldsymbol{\sigma} - \boldsymbol{\sigma} \cdot \boldsymbol{\omega}^{(\alpha)} \right] \quad (3.72)$$

The crystal plasticity constitutive behaviour is implemented by means of a user material subroutine (UMAT) for Abaqus, originally developed by Huang [140] and modified in this work to allow HCP crystals to be modelled.

## 3.4. The Finite Element Method

The numerical solution of continuum mechanics problems in this study is achieved using the FEM, as implemented in the Abaqus commercial FE codes (DS SIMU-

### 3. Theory

LIA, USA). The subsequent overview of the FEM continues from the overview of continuum mechanics in Section 3.2. More detailed discussions of the FEM relevant to the implementation in this work are available in Belytschko *et al.* [135], Dunne and Petrinic [137] and the Abaqus Theory Manual (DS SIMULIA, USA). To facilitate the discussion of the FEM, matrix/vector notation (Voigt notation [135]) is employed for this section.

#### 3.4.1. The Finite Element Method in Structural Problems

In the FEM, a solid body is divided into discrete volumes or elements, which are interconnected at nodes, as shown in Fig. 3.4. Quantities such as displacements  $\mathbf{u}$  can be interpolated throughout the body based on discrete values at the element nodes according to:

$$\mathbf{u} = \mathbf{N}^{(e)} \mathbf{u}^{(e)} \quad (3.73)$$

where  $\mathbf{N}^{(e)}$  is a matrix of shape functions in an element  $e$  and  $\mathbf{u}^{(e)}$  is a column vector of element nodal displacements. For the elements used in this thesis velocities and accelerations can be interpolated in a similar manner, e.g. :

$$\ddot{\mathbf{u}} = \mathbf{N}^{(e)} \ddot{\mathbf{u}}^{(e)} \quad (3.74)$$

where  $\ddot{\mathbf{u}}^{(e)}$  is a column vector of element nodal accelerations. Using this approach the rate of deformation associated with the spacial gradient in the velocity  $\mathbf{v}$  is interpolated by:

$$\mathbf{D} = \mathbf{B}^{(e)} \mathbf{v}^{(e)} \quad (3.75)$$

where  $\mathbf{B}^{(e)}$  is a matrix of spacial gradients of the shape functions and  $\mathbf{v}^{(e)}$  is a column vector of element nodal velocities.

### 3. Theory

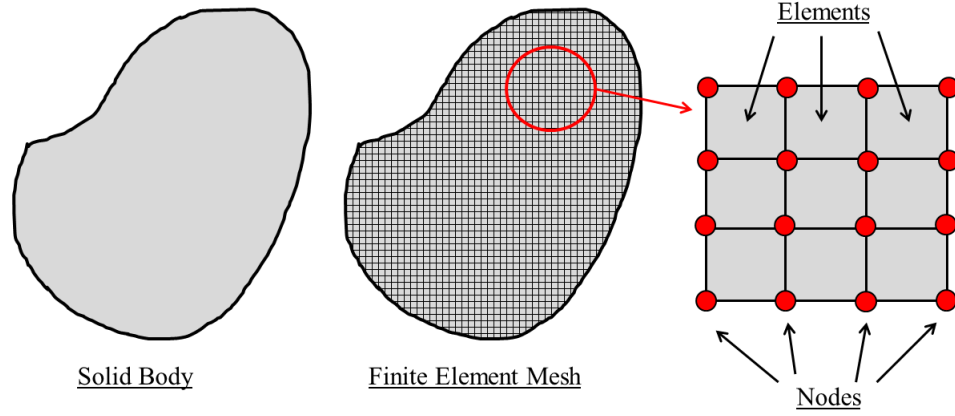


**Figure 3.4.:** In the FEM the geometry of a body is subdivided into discrete regions known as elements. The elements are interconnected at points known as nodes.

Similarly, the virtual velocity  $\delta \mathbf{v}$  and virtual rate of deformation  $\delta \mathbf{D}$  can be interpolated according to:

$$\delta \mathbf{v} = \mathbf{N}^{(e)} \delta \mathbf{v}^{(e)} \quad (3.76)$$

and

$$\delta \mathbf{D} = \mathbf{B}^{(e)} \delta \mathbf{v}^{(e)} \quad (3.77)$$

where  $\delta \mathbf{v}^{(e)}$  is a column vector of element nodal virtual velocities.

It is useful for present purposes to rewrite the principle of virtual work (Eqn. 3.23) in matrix/vector (Voigt) notation:

$$\int_{\Omega} \delta \mathbf{D}^T \boldsymbol{\sigma} d\Omega = \int_{\partial\Omega} \delta \mathbf{v}^T \mathbf{t} d\partial\Omega - \int_{\Omega} \delta \mathbf{v}^T \rho \ddot{\mathbf{u}} d\Omega \quad (3.78)$$

where the components of  $\delta \mathbf{D}$ ,  $\boldsymbol{\sigma}$  and  $\mathbf{t}$  are organised in column vector format. The finite element approximation of the principle of virtual work can be constructed by substituting Eqns. 3.74, 3.76 and 3.77 into Eqn. 3.78:

$$\begin{aligned} \sum_e \int_{\Omega^{(e)}} \delta \mathbf{v}^{(e)T} \mathbf{B}^{(e)T} \boldsymbol{\sigma} d\Omega &= \sum_e \int_{\partial\Omega^{(e)}} \delta \mathbf{v}^{(e)T} \mathbf{N}^{(e)T} \mathbf{t} d\partial\Omega \\ &\quad - \sum_e \int_{\Omega^{(e)}} \rho \delta \mathbf{v}^{(e)T} \left( \mathbf{N}^{(e)T} \mathbf{N}^{(e)} \right) \ddot{\mathbf{u}}^{(e)} d\Omega \end{aligned} \quad (3.79)$$

### 3. Theory

where the summations are over all element in the mesh,  $\Omega^{(e)}$  is the element volume and  $\partial\Omega^{(e)}$  is the part of the element surface that resides on the bounding surface of the body,  $\partial\Omega$ .

Performing the summation, which in effect means assembling elemental quantities into corresponding global quantities and eliminating the arbitrary virtual velocity terms, one obtains the following global system of equations:

$$\int_{\Omega} \mathbf{B}^T \boldsymbol{\sigma} d\Omega = \int_{\partial\Omega} \mathbf{N}^T \mathbf{t} d\partial\Omega - \int_{\Omega} \rho (\mathbf{N}^T \mathbf{N}) \ddot{\mathbf{u}} d\Omega \quad (3.80)$$

where  $\ddot{\mathbf{u}}$  is now the global nodal acceleration vector for the whole mesh.

In general for non-linear constitutive laws, the Cauchy stress is a non-linear function of the displacement and for large deformation kinematics the quantities  $\rho$ ,  $\mathbf{B}$  and  $\mathbf{N}$  on the current configuration  $\Omega$  are functions of the displacement. Hence, from Eqn. 3.80 one can define the global out of balance force vector:

$$\begin{aligned} \mathbf{G}(\mathbf{u}, \ddot{\mathbf{u}}) &= \int_{\Omega} \mathbf{B}^T(\mathbf{u}) \boldsymbol{\sigma}(\mathbf{u}) d\Omega - \int_{\partial\Omega} \mathbf{N}^T(\mathbf{u}) \mathbf{t} d\partial\Omega \\ &+ \int_{\Omega} \rho(\mathbf{u}) (\mathbf{N}^T(\mathbf{u}) \mathbf{N}(\mathbf{u})) \ddot{\mathbf{u}} d\Omega \end{aligned} \quad (3.81)$$

where  $\mathbf{u}$  is now the global nodal displacement vector for the whole mesh.

To generate a solution to the continuum mechanics problem, the remaining task in general is to determine  $\mathbf{u}$  and  $\ddot{\mathbf{u}}$  such that:

$$\mathbf{G}(\mathbf{u}, \ddot{\mathbf{u}}) = \mathbf{0} \quad (3.82)$$

at any point in time. Methods applied to achieve this, relevant to this thesis, are summarized in the next section.

### 3. Theory

Eqn. 3.81 can be written as:

$$\mathbf{G}(\mathbf{u}, \ddot{\mathbf{u}}) = \int_{\Omega} \mathbf{B}^T(\mathbf{u})\boldsymbol{\sigma}(\mathbf{u})d\Omega - \int_{\partial\Omega} \mathbf{N}^T(\mathbf{u})t d\partial\Omega + \mathbf{M}\ddot{\mathbf{u}} \quad (3.83)$$

where the quantity  $\mathbf{M} = \int_{\Omega} \rho(\mathbf{u}) (\mathbf{N}^T(\mathbf{u})\mathbf{N}(\mathbf{u})) d\Omega$  is known as the consistent mass matrix. All dynamic simulations in this work use a lumped mass matrix  $\tilde{\mathbf{M}}$  in place of the consistent mass matrix, which is obtained by adding each row of the consistent mass matrix  $\mathbf{M}$  onto its diagonal. The lumped mass matrix is easily inverted and is constructed such that the momentum of the system using  $\tilde{\mathbf{M}}$  is equivalent to that of the system using  $\mathbf{M}$ , see Belytschko *et al.* [135].

Practically, integrals are evaluated on an element by element basis using Gaussian quadrature based numerical integration.

#### 3.4.2. Implicit and Explicit Solution Schemes

In this study quasi-static problems (problems with negligible inertial force contributions) are solved using the Abaqus/Standard implicit solver, which uses Newton's method to iteratively solve Eqn. 3.82. Quasi-static problems are also solved using the Abaqus/Explicit dynamic solver (in the sense that kinetic energy is kept small relative to internal energy in the system), which uses a central difference integration rule.

For the implicit solver, displacements are applied incrementally over time steps  $\Delta t$ . In moving from time  $t$  to  $t + \Delta t$ , Eqn. 3.82 is solved iteratively. For a given iteration,  $i$ ,  $\mathbf{u}^{(i)}$  and  $\mathbf{c}^{(i+1)}$  are, respectively, an approximation to the solution of Eqn. 3.82 and the difference between the approximate and exact solutions.  $\mathbf{c}^{(i+1)}$  can be approximated through the solution of the following linear system of

### 3. Theory

equations:

$$\frac{\partial \mathbf{G}(\mathbf{u}^{(i)})}{\partial \mathbf{u}} \mathbf{c}^{(i+1)} = \mathbf{G}(\mathbf{u}^{(i)}) \quad (3.84)$$

which requires the determination and inversion of the Jacobian matrix,  $\frac{\partial \mathbf{G}(\mathbf{u}^{(i)})}{\partial \mathbf{u}}$ .

Once  $\mathbf{c}^{(i+1)}$  is known, the next approximation to the solution is obtained:

$$\mathbf{u}^{(i+1)} = \mathbf{u}^{(i)} + \mathbf{c}^{(i+1)} \quad (3.85)$$

Iterations continue until the components of  $\mathbf{G}(\mathbf{u}^{(i)})$  and  $\mathbf{c}^{(i+1)}$  are sufficiently small, with the solution at time  $t + \Delta t$  being  $\mathbf{u}^{(i+1)}$ .

For the explicit solver, Eqn. 3.82 is solved incrementally using small increments in time,  $\Delta t$ . For each increment  $j$  the vector of nodal accelerations is determined as:

$$\ddot{\mathbf{u}}^{(j)} = \tilde{\mathbf{M}}^{-1} \cdot \left( - \int_{\Omega} \mathbf{B}^T \boldsymbol{\sigma} d\Omega^{(j)} + \int_{\partial\Omega} \mathbf{N}^T \mathbf{t} d\partial\Omega^{(j)} \right) \quad (3.86)$$

This allows the determination of the displacement at the next increment through:

$$\mathbf{u}^{(j+1)} = \mathbf{u}^{(j)} + \Delta t^{(j+1)} \dot{\mathbf{u}}^{(j+\frac{1}{2})} \quad (3.87)$$

where mid-increment velocities are determined according to the following central difference operation:

$$\dot{\mathbf{u}}^{(j+\frac{1}{2})} = \dot{\mathbf{u}}^{(j-\frac{1}{2})} + \frac{\Delta t^{(j+1)} + \Delta t^{(j)}}{2} \ddot{\mathbf{u}}^{(j)} \quad (3.88)$$

For simulations in this study  $\dot{\mathbf{u}}^{(-\frac{1}{2})} = 0$  and the maximum size of the time increment is limited by i) the time taken for a stress wave to pass through an element and ii) the ratio of kinetic to internal energy in the system.

### 3.4.3. Strain Measures in Abaqus

In Abaqus the strain rate is defined as the rate of deformation tensor, as per Eqn 3.10. As per Eqn. 3.11 this strain rate returns the logarithmic strain when integrated over time when the principal axes of straining remain fixed with respect to the material coordinates. In Abaqus, for more general deformations the strain is constructed by integrating the strain rate approximately over an increment in time using the central difference algorithm. In Abaqus/Standard the strain at the start of an increment is also rotated to approximately account for rigid body motion during the increment using the Hughes-Winget method [143].

Defining  $\mathbf{x}_{t+\frac{\Delta t}{2}} = \frac{1}{2}(\mathbf{x}_t + \mathbf{x}_{t+\Delta t})$ , where  $\mathbf{x}$  is the global nodal position vector, the central difference integration of the rate of spin is:

$$\Delta \mathbf{W} = \text{asym} \left( \frac{\partial \Delta \mathbf{u}}{\partial \mathbf{x}_{t+\frac{\Delta t}{2}}} \right) \quad (3.89)$$

where  $\Delta \mathbf{W}$  is the increment in spin and  $\Delta \mathbf{u}$  is the increment in nodal displacement. This is used to approximate the increment in average material rotation  $\Delta \mathbf{R}$  using the Hughes-Winget method [143] by:

$$\Delta \mathbf{R} = \left( \mathbf{I} - \frac{1}{2} \Delta \mathbf{W} \right)^{-1} \cdot \left( \mathbf{I} + \frac{1}{2} \Delta \mathbf{W} \right) \quad (3.90)$$

The increment in the rate of deformation tensor is given by the following central difference formula:

$$\Delta \mathbf{D} = \text{sym} \left( \frac{\partial \Delta \mathbf{u}}{\partial \mathbf{x}_{t+\frac{\Delta t}{2}}} \right) \quad (3.91)$$

This allows the strain at time  $t + \Delta t$  to be found based on the strain at time  $t$ :

$$\boldsymbol{\varepsilon}_{t+\Delta t} = \Delta \mathbf{R} \cdot \boldsymbol{\varepsilon}_t \cdot \Delta \mathbf{R}^T + \Delta \mathbf{D} \quad (3.92)$$

Further details on the calculations of strain in Abaqus are given in the Abaqus Theory Manual (DS SIMULIA, USA).

## 3.5. ALE Adaptive Meshing

In this study the ALE adaptive meshing capability in the Abaqus/Standard solver is used. This type of analysis combines features of typical Lagrangian and Eulerian analysis techniques. In a typical Lagrangian analysis nodes are fixed within the material of the structure. Elements, which are always full of material, deform as the material deforms. In an Eulerian analysis, node positions are independent of the underlying material and material flows through an element.

In an ALE analysis in Abaqus/Standard, discussed in detail in the Abaqus Analysis Manual (DS SIMULIA, USA), for each analysis increment the Lagrangian problem is first solved to obtain solution equilibrium, through solution of equations similar to Eqn. 3.82. Following this, nodes on the boundary of the domain of interest are moved with prescribed velocities, independently of the underlying material, using an Eulerian approach. Mesh smoothing is then applied by iteratively sweeping through all non-constrained nodes in the analysis domain and minimizing their displacement relative to a projection of the deformed FE mesh back to the original mesh. This step reduces element distortion due to the movement of boundary nodes. The final step uses an advection process to map material point and nodal quantities from the mesh at the beginning of the Eulerian stage to the new mesh. The advection equation is solved using an explicit second order accurate Lax-Wendroff scheme [144]. A typical Lax-Wendroff advection scheme is illustrated here for the 1-D linear advection of a quantity  $q$ ,

### 3. Theory

with:

$$\frac{\partial q}{\partial t} + a \frac{\partial q}{\partial x} = 0 \quad (3.93)$$

approximated by:

$$q_{t+\Delta t}^i = q_t^i - \frac{a\Delta t}{2\Delta x}(q_t^{i+1} - q_t^{i-1}) + \frac{(a\Delta t)^2}{2\Delta x^2}(q_t^{i+1} - q_t^i + q_t^{i-1}) \quad (3.94)$$

where  $i$  is the material point number and  $a$  is the advection velocity [145].  $\Delta t$  and  $\Delta x$  are respective increments in time and space.

Following the Eulerian stage in the ALE analysis increment, the global solution is not necessarily in equilibrium. Equilibrium is only achieved again following the solution of the Lagrangian stage in the subsequent analysis increment.

A verification of the applicability of the scheme used in Abaqus for problems of interest in this work is performed in Appendix A.2.

## 3.6. Optimization Methods

In design, optimization refers to approaches which involve judiciously modifying the values of design variables, such as the dimensions of a component, such that a component with optimal performance can be identified. Design optimization methods are an important part of work carried out in Ch. 7 of this thesis.

Optimization problems in this work can be formally expressed as follows, assum-

### 3. Theory

ing matrix notation:

$$\begin{aligned} & \text{minimize : } f(\mathbf{x}) \\ & \text{subject to : } g(\mathbf{x}) < g_U \text{ and } \mathbf{x}_L \geq \mathbf{x} \leq \mathbf{x}_U \end{aligned} \quad (3.95)$$

The solution of the optimization problem is a set of values of the  $n$  - dimensional vector  $\mathbf{x}$  (where  $n$  is the number of design variables) which gives a minimum value of the objective function  $f(\mathbf{x})$  while satisfying a set of constraints,  $g(\mathbf{x}) < g_U$ . The components of the vector  $\mathbf{x}$  are the design variables, where  $\mathbf{x}_L$  and  $\mathbf{x}_U$  correspond to a set of upper and lower bounds that the corresponding values in  $\mathbf{x}$  can take. Values of  $\mathbf{x}$  within the bounds  $\mathbf{x}_L$  and  $\mathbf{x}_U$  constitute the design space.

To introduce the concept of optimization in design, a simple example of its application is given here. Consider the cantilever beam of length  $L$  and thickness  $b$  in Fig. 3.5, under an end load  $P$ . The beam height  $h$  is to be chosen such that there is a suitable trade-off between minimizing the beam volume  $V(h) = bhL$  and minimizing the beam deflection  $w(h) = \frac{4PL^3}{Ebh^3}$ , where  $E$  is Young's Modulus. In this case, the beam height is the only design variable, so  $n = 1$  and  $x_1 = h$ . If there are practical limits on the beam height, such that the height is less than  $x_{U,1} = h_U$  and greater than  $x_{L,1} = h_L$ , then the design space is  $h_L > h > h_U$  or  $x_{L,1} > x_1 > x_{U,1}$ . If there is a practical limit on the highest bending stress in the beam  $\sigma(h) = \frac{6PL}{bh^2}$ , this amounts to the constraint  $\sigma(h) < \sigma_{max}$ , so that  $g(\mathbf{x})$  in Eqn. 3.96 becomes  $\sigma(h)$  and  $g_U$  becomes  $\sigma_{max}$  for this problem.

There is a number of methods for formalizing the trade-off problem. One simple approach is to define a function that is a weighted sum of the performance metrics of interest, in this case  $V$  and  $w$ . This function is known as the objective function (OF) and its value depends on the value of  $h$ . The goal of the optimization

### 3. Theory

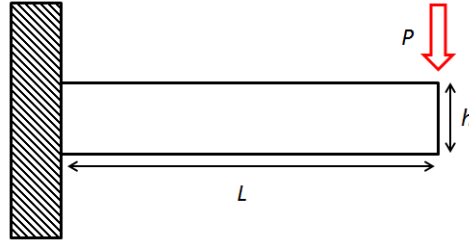


**Figure 3.5.:** A cantilever beam of length  $L$  thickness  $b$  and consisting of material with Young's modulus  $E$  is subject to a point load  $P$ . Applying Euler beam theory and neglecting self-weight, a given value of  $h$  gives the beam a certain volume  $V$  and deflection  $w$ . An objective function can be identified as a weighted sum of  $w$  and  $V$ .

problem is to find the value of  $h$  that minimizes the OF. For example, for the beam the optimization problem is:

$$\begin{aligned} \text{minimize : } f(h) &= bhL + \frac{4PL^3}{Ebh^3} \\ \text{subject to : } g(h) &= \frac{6PL}{bh^2} < \sigma_{max} \text{ and } h_L > h > h_U \end{aligned} \quad (3.96)$$

Fig. 3.6 shows how the OF varies with  $h$  for the cantilever beam problem in Fig. 3.5, with arbitrary values assumed for the other parameters. A minimum value for the OF can easily be identified, corresponding to the optimal choice of  $h$ .

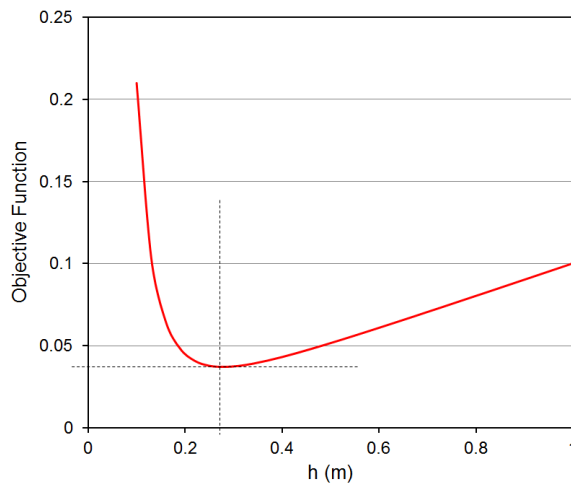


**Figure 3.6.:** The dependence of the OF on the beam height,  $h$ .

When designing more complex components it may be possible to change the value of many design variables when seeking an optimal design. Also, the exact

### 3. Theory

dependence of the OF on the design variables may not be known and may be computationally expensive to determine, even for a single value of a single design variable. This has led to the development of optimization algorithms that seek the optimal design through approximating the value of the OF over the entire design space, which may be multi-dimensional, based on a limited number of evaluations of the objective function for a number of judiciously chosen design variable values, or sample points.

There are many ways to approximate the OF over the design space. For example a linear regression may be used, which for the simple case of the cantilever beam amounts to assuming the objective function  $f(\mathbf{x})$  varies linearly between its known values at certain sample points, as shown in Fig. 3.7.

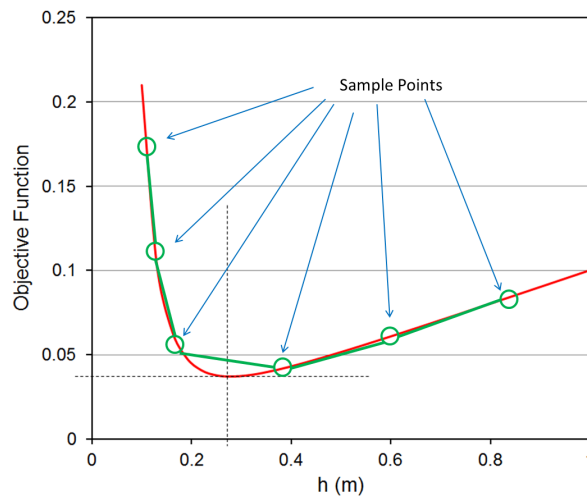


**Figure 3.7.:** The OF is approximated using a simple linear fit based on known values at the sample points.

A more powerful approximation of the OF, which is also known as a surrogate model, is the use of a Gaussian Process (GP) model [146]. In this case, predicted values of the OF between known values at sample points are described with a normal distribution, rather than simply with a single value. This means that each predicted value of  $f(\mathbf{x})$  has a certain variance, or uncertainty, which is correlated with the distance between the sample points. As shown in Fig. 3.8, this accounts for the greater uncertainty in the predicted value of the OF in regions of the

### 3. Theory

design space further from the sample points. The advantage of such a model is that it allows for optimization algorithms to be developed that not only search for optimal designs in regions of the design space that have promising OF values, but also in regions where there is relatively large uncertainty in the predicted OF values. One such algorithm is the EGO algorithm [134].

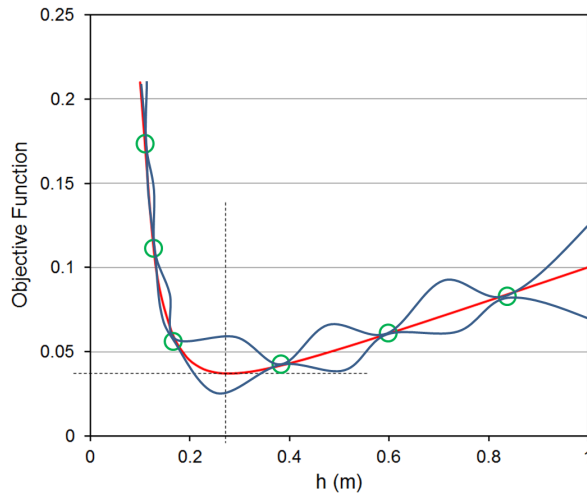


**Figure 3.8.:** The OF is approximated using a Gaussian Process model based on known values at the sample points. There is greater uncertainty in the fit in regions further from sample points.

The EGO algorithm is specifically developed for computational studies with expensive OF evaluations. It uses a GP based surrogate model to globally approximate the OF throughout the design space, based on a limited number of expensive function evaluations. The method used to explore the design space is based on the concept of an expected improvement function (EIF). Through the use of an EIF, the EGO algorithm trades off between exploiting regions of the design space with promising values and exploring regions where there is higher uncertainty in the approximation.

In this study the open-source optimization library DAKOTA (Sandia Laboratories, USA) is used to implement the EGO algorithm. The implementation of the algorithm is discussed in detail in the DAKOTA User Manual (Sandia Laboratories, USA) and in brief here. The algorithm works by:

### 3. Theory

1. Calculating  $f(\mathbf{x})$  for a number of initial sample points (values of  $\mathbf{x}$ ) in the design space.
2. Fitting a GP surrogate model to the sample points.
3. Calculating the EIF from the GP model.
4. Choosing a new sample point  $\mathbf{x}$  based on the EIF, from which a new value of  $f(\mathbf{x})$  is calculated.
5. Generating an updated GP model with the new sample point.

Stages 3-5 are repeated iteratively until the EIF reaches a tolerance signifying sufficient certainty that a global minimum has been identified or, as is the case in this study, for a suitable number of iterations.

For the construction of the GP surrogate model it is assumed that  $f(\mathbf{x})$  in all points in the design space can be described by [147]:

$$f(\mathbf{x}) = \mathbf{h}(\mathbf{x})^T \boldsymbol{\beta} + Z(\mathbf{x}) \quad (3.97)$$

where  $\mathbf{h}$  is known as the trend (which takes the form of a column vector of dimension  $n$ , i.e. the number of design variables in the optimization problem) and  $\boldsymbol{\beta}$  is a column vector of trend coefficients of dimension  $n$ .  $Z(\mathbf{x})$  is a stationary Gaussian Process (see Shi [146]) with zero mean. The covariance of  $Z$  for two points,  $\mathbf{a}$  and  $\mathbf{b}$ , can be defined as:

$$\text{Cov}[Z(\mathbf{a}), Z(\mathbf{b})] = \sigma_Z^2 \exp \left[ - \sum_{i=1}^n \theta_i (a_i - b_i)^2 \right] \quad (3.98)$$

where the  $\theta_i$  are scaling parameters and  $\sigma_Z^2$  is the process variance.

### 3. Theory

The GP surrogate model in DAKOTA approximates  $f(\mathbf{x})$  in Eqn. 3.97 throughout the design space by assuming that each point can be described by a normal distribution with a mean (expected) value  $\mu_G(\mathbf{x})$  and a variance  $\sigma_G(\mathbf{x})$ . Formally this can be written as:

$$\hat{f}(\mathbf{x}) \sim N[\mu_G(\mathbf{x}), \sigma_G(\mathbf{x})] \quad (3.99)$$

where  $\hat{f}(\mathbf{x})$  is the GP model prediction of  $f(\mathbf{x})$ . In DAKOTA  $\mu_G(\mathbf{x})$  and  $\sigma_G(\mathbf{x})$  are assumed to take the following form:

$$\begin{aligned} \mu_G(\mathbf{x}) &= \mathbf{h}(\mathbf{x})^T \boldsymbol{\beta} + \mathbf{r}(\mathbf{x})^T \mathbf{R}^{-1}(\mathbf{g} - \mathbf{F}\boldsymbol{\beta}) \\ \sigma_G^2(\mathbf{x}) &= \sigma_Z^2 - \begin{bmatrix} \mathbf{h}(\mathbf{x})^T & \mathbf{r}(\mathbf{x})^T \end{bmatrix} \begin{bmatrix} \mathbf{0} & \mathbf{F}^T \\ \mathbf{F} & \mathbf{R} \end{bmatrix}^{-1} \begin{bmatrix} \mathbf{h}(\mathbf{x}) \\ \mathbf{r}(\mathbf{x}) \end{bmatrix} \end{aligned} \quad (3.100)$$

where  $\mathbf{r}(\mathbf{x})$  is the column vector of covariance between  $\mathbf{x}$  and each of the  $p$  sample points (as defined in Eqn. 3.98), which has dimension  $p$ . The trend  $\mathbf{h}$  is assumed to be a column vector of constants, each with the same value, and  $\boldsymbol{\beta}$  is a column vector with entries given by the mean of the OF values over the  $p$  sample points.  $\mathbf{R}$  is a  $p \times p$  matrix containing the correlation between each pair of sample points and  $\mathbf{g}$  is a column vector of sample point OF values of dimension  $p$ .  $\mathbf{F}$  is a  $p \times n$  matrix with  $p$  rows, with each row containing the vector  $\mathbf{h}(\mathbf{x}_p)^T$  for each sample point  $p$ .

The determination of  $\mu_G(\mathbf{x})$  and  $\sigma_G(\mathbf{x})$  requires a knowledge of  $\sigma_Z^2$  and  $\theta_i$  (through Eq. 3.98). These terms are identified through a process of maximum likelihood estimation in DAKOTA. Once  $\mu_G(\mathbf{x})$  and  $\sigma_G(\mathbf{x})$  have been found, the EIF at a point is subsequently determined through the numerical integration of:

$$EIF(\hat{f}(\mathbf{x})) = \int_{-\infty}^{\hat{f}_*} (\hat{f}_* - G) \hat{f}(\mathbf{x}) dG \quad (3.101)$$

where  $\hat{f}_*$  is the current optimal solution determined at the sample points.

# **4. An Assessment of the Mechanical Performance of Permanent and Absorbable Metal Stents**

## **4.1. Chapter Summary**

Modern trends in permanent stent development are towards reduced strut thickness. Reducing strut thickness naturally leads to reductions in the mechanical integrity of the stent. It is important to assess the extent to which reducing strut thickness reduces stent integrity, both in terms of radial scaffolding performance and resistance to longitudinal compression.

Given the inferior mechanical performance of bioabsorbable metals relative to 316L and L605, and the requirement for stents consisting of these materials to match the scaffolding performance of permanent stents, it is also important to compare the mechanical performance of stents consisting of bioabsorbable materials to that of modern, permanent stents.

#### 4. The Mechanical Performance of Permanent and Absorbable Metal Stents

In this chapter the mechanical performance of stents consisting of a range of permanent and bioabsorbable alloys are compared in the deployment phase, using simulated bench-testing. In addition, the role of stent geometry, including the use of thinner struts, on device mechanical performance is assessed. This chapter gives insights into how the use of thinner struts and bioabsorbable metals affects stent mechanics. It also serves as a baseline for subsequent chapters. Ch. 5 builds on the results of this chapter by assessing strut deformations in more detail, using micromechanics approaches. Chs. 6 and 7 build on this chapter by including the effects of corrosion when assessing AMS performance and by simulating *in-vivo* deployment when making scaffolding performance predictions.

## 4.2. Introduction

Given that the mechanical performance of currently available bioabsorbable alloys is inferior to that of alloys used in permanent stents, as shown in Table 4.1 and Fig. 4.1, it is important that the consequences of such differences on overall device mechanical performance are known. In this chapter the mechanical performance of AMS's and permanent stents is compared through simulated bench testing. Simulated bench testing, based on the use of FEA, is commonly used in contrasting the performance of different permanent stents [148, 149, 20]. This study employs a similar approach in investigating the ability of AMS's to match the performance of permanent stents over metrics such as radial strength, recoil and flexibility. To the author's knowledge, this is the first study in which the performances of magnesium alloy, iron and permanent stents have been directly contrasted on a common stent geometry over a range of performance metrics, such as radial strength and flexibility. Also, to the author's knowledge, this is the first computational study in which stent resistance to longitudinal compres-

#### 4. The Mechanical Performance of Permanent and Absorbable Metal Stents

sion is compared over a range of materials, with the ability of coronary stents to resist longitudinal compression recently emerging as a concern in thin-strut stents [150].

**Table 4.1.:** Mechanical properties for each material considered in this study. Iron-T1 and Iron-T2 denote pure iron with two different heat treatments.

Material	Young's Modulus (GPa)	Yield Strength (MPa)	UTS (MPa)	Elongation (%)	Source
Stainless Steel 316L	193	380	750	51	[35]
Cobalt Chromium L605	243	629	1147	46	[32]
Magnesium Alloy WE43	45	216	298	18	[7]
Magnesium Alloy AZ31	44	138	245	17	Ch. 6
Iron - T1	211	138	282	25	[151]
Iron - T2	211	170	270	36	[8]

The adoption of a common geometric platform across materials in this study allows a direct comparison of a material's performance in a stent application with that of established stent materials. However, given that AMS designs used in *in-vivo* studies to date [114, 40] differ somewhat from the common geometry used here, and that some may be designed based on the mechanical properties of a specific alloy, it is useful to also consider the performance of designs representative of those tested *in-vivo*, alongside that of the common geometry.

As such, the specific goals of this chapter are: 1) to assess the effects of using thinner struts on radial and longitudinal stent scaffolding performance, 2) to compare AMS and permanent stent performance using: i) a common stent geometry and ii) representative stent geometries, through FE modelling, and 3) to identify current design challenges facing AMS development, based on model predictions.

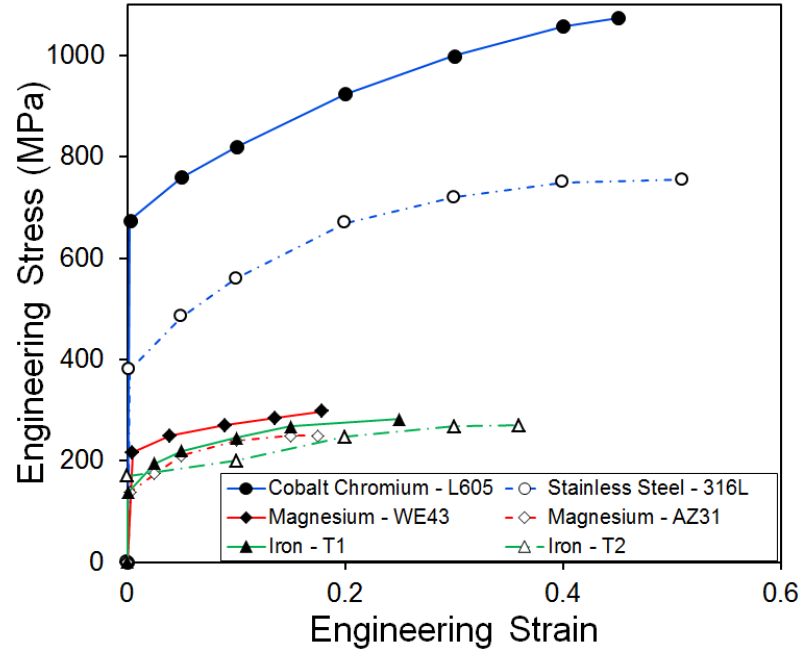


**Figure 4.1.:** Engineering stress-strain curves for each material modelled in this study. The source of each stress-strain curve is shown in Table 4.1. Iron-T1 and Iron-T2 denote pure iron with two different heat treatments.

### 4.3. Methods

Stent bench-testing is simulated using the Abaqus/Explicit code (DS SIMULIA, USA). The performances of candidate bioabsorbable alloys are assessed on a generic stent geometry (geometry A in Fig. 4.2), allowing a direct comparison of material performance across a common geometric platform, and also on geometries representative of those used in previous *in-vivo* experiments on magnesium alloy stents [40] and iron stents [114]. Information on the studied geometries is given in Fig. 4.2 and Table 4.2.

Six stent materials are studied in each bench-test. Conventional stent materials 316L and L605 are studied on generic geometry A, with L605 also studied on geometry A1, which has the same underlying design as geometry A, but strut dimensions similar to those of many modern ‘thin-strut’ stents. Magnesium alloys AZ31 and WE43, which is the alloy used in the clinical trials of Erbel *et al.* [40],

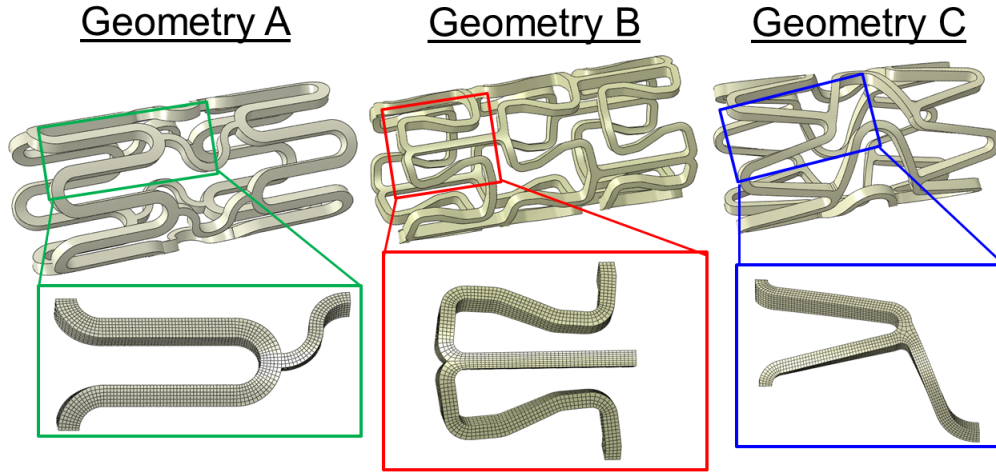


**Figure 4.2.:** Stent geometries used in this study and corresponding finite element meshes. Geometry details are given in Table 4.2

**Table 4.2.:** Stent geometries used in this study. Each geometry has a pre-deployment outer diameter  $D$  of 1.5 mm and is meshed using reduced integration 3-D linear brick elements (C3D8R).

Stent	Similar to:	Source	Strut Width ( $\mu\text{m}$ )	Strut Thickness ( $\mu\text{m}$ )	Length (mm)	FE Mesh (Elements)
A	Generic	[22]	120	120	3.30	66 000
A1	Generic	[22]	80	80	3.26	108 000
B	MAGIC Stent	SEM Images [40]	80	140	3.18	76 000
C	PUVA Stent	Microscope Images [114]	80	120	2.70	61 500

#### 4. The Mechanical Performance of Permanent and Absorbable Metal Stents

are studied using generic geometry A and also geometry B, which is representative of the MAGIC stent geometry used in the trial of Erbel *et al.* [40]. Two forms (denoted T1 and T2) of annealed pure iron, which has been used in the *in-vivo* studies of Peuster *et al.* [114], are considered in this study, with different mechanical properties arising from different annealing heat treatments. The performance of the pure iron is assessed on the generic geometry A and geometry C, which is representative of the PUVA stent used in the study of Peuster *et al.* [114].

Stress-strain data for each material are taken from the literature, as detailed in Table 4.1 and Fig. 4.1. Each material is modelled using a rate-independent elastic-plastic material description, with elasticity assumed linear in terms of finite deformation quantities, in particular Cauchy stress and logarithmic strain and plasticity described using  $J_2$  flow theory with non-linear isotropic hardening. The FE meshes used to discretise each geometry, shown in Fig. 4.2, are chosen based on the results of preliminary solution mesh dependence studies. In order to ensure a negligible influence of inertial effects when using the Abaqus/Explicit code, the ratio of kinetic energy to internal energy of less than 0.05 is maintained in all simulations.

Four bench-tests are simulated for each material and geometry, as detailed in Fig. 4.3. In the first test, stent deployment and recoil are simulated through the expansion to 3.0 mm and subsequent contraction of a rigid cylindrical shell, as shown in Fig. 4.3. This approach has been used in a number of previous studies [152, 132] and has been shown by De Beule *et al.* [153] to give an accurate prediction of the final, deployed stent geometry for unconfined, straight stent expansions relative to that achieved in more computationally expensive wrapped balloon simulations, such as those of Mortier *et al.* [20]. For this study the extra control over final stent diameter afforded by cylinder deployment for each

material and geometry is also advantageous.

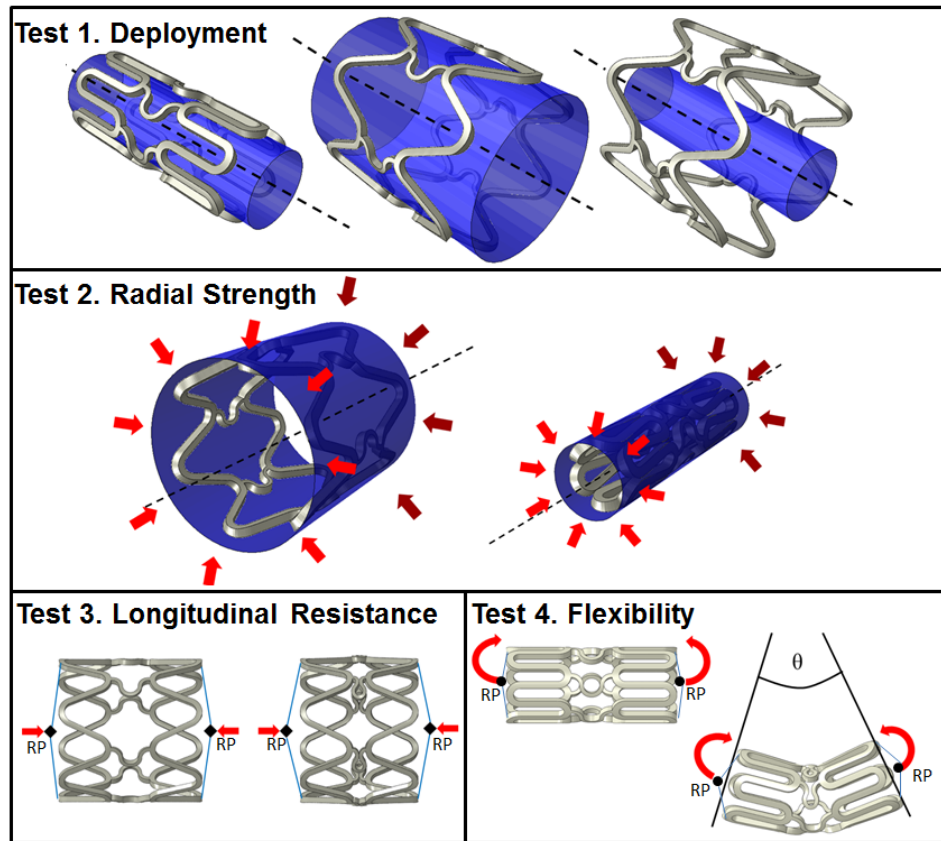


**Figure 4.3.:** Schematic representation of the test cases simulated. Test 1 is stent deployment with an inner cylinder. Test 2 is stent crimping with an outer cylinder. Test 3 is stent longitudinal compression. Nodes on each end of the stent are tied to two reference points (RP) using rigid beams. The reference point on the right is moved toward the fixed point on the left. Test 4 is stent flexibility testing. Again, nodes are tied to two reference points, with the right point rotated about the fixed left point through an angle  $\theta$ .

The quantities of interest in the first test are peak von Mises stresses  $\sigma_e$ , max principal logarithmic strains  $\varepsilon_{mp}$  and stent recoil. Von Mises stresses are chosen as a simple measure of maximum device stress in this case, given the ductile nature and large plastic deformations of the metals considered in this study, with alternative measures such as maximum principal stresses also giving similar overall trends in terms of device performance. In order to facilitate a comparison of peak stresses and strains across each material, an appropriate comparative indicator is required. For this study a straight-forward approach is chosen in comparing materials, through the definition of respective stress and strain based

#### 4. The Mechanical Performance of Permanent and Absorbable Metal Stents

factors of safety,  $\eta_\sigma$  and  $\eta_\epsilon$ . In determining each factor of safety, predicted peak stresses and strains in the stent are compared with estimates of true stress and strain at the point of UTS in each material's engineering stress-strain curve. A conventional conversion of engineering to true stress and logarithmic strain measures [154] is used, based on UTS and strain at UTS data ( $\sigma_{UTS}$  and  $\epsilon_u$ ) for each material, given in Table 4.1. This gives the following factor of safety definitions:

$$\begin{aligned}\eta_\sigma &= \frac{(1 + \epsilon_u)\sigma_{UTS}}{\sigma_e} \\ \eta_\epsilon &= \frac{\ln(1 + \epsilon_u)}{\epsilon_{mp}}\end{aligned}\quad (4.1)$$

In quantifying stent recoil a conventional approach is taken [149], with recoil given by:

$$\text{Recoil} = \frac{D_1 - D_2}{D_1} \times 100\% \quad (4.2)$$

where  $D_1$  is the stent internal diameter at max expansion and  $D_2$  is the stent internal diameter following rigid cylinder contraction.

To assess the ability of the two ring geometries used in this study to capture the  $\eta_\sigma$  and  $\eta_\epsilon$  values and overall recoil behaviour of each material in a longer stent, a preliminary deployment simulation of a four ring generic stent, half of which was modelled due to longitudinal symmetry, with a wrapped balloon is performed. Results are compared to those from a cylinder deployment of a two ring generic stent. It is observed that the final stent configurations are very similar, as shown in Fig. 4.4, with only a 1.1% higher peak von Mises stress and a 0.09% lower stent recoil magnitude predicted for the wrapped balloon simulation. Such differences result in minor over-estimations in  $\eta_\sigma$  (1.1%) and recoil (0.09%) values for the cylinder deployment method, but these over-estimations are small relative to the range of values each metric takes over the different materials tested in this study.

#### 4. The Mechanical Performance of Permanent and Absorbable Metal Stents

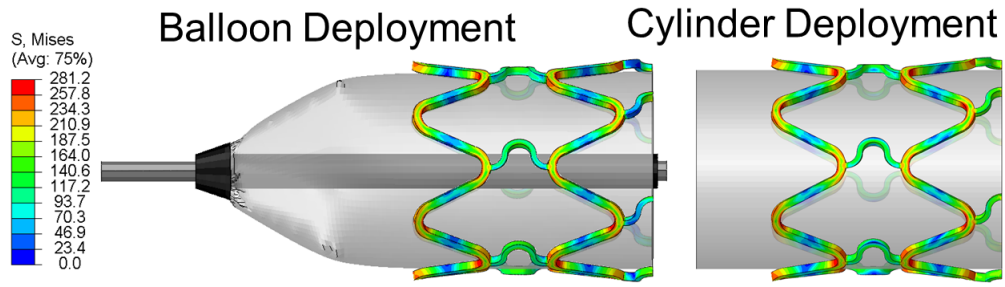


**Figure 4.4.:** A comparison of von Mises stresses in MPa in the magnesium alloy stent following expansion by balloon deployment and a rigid cylinder.

In the second test, stent radial strengths are predicted for each material. Radial compression of each stent is simulated by introducing a thin elastic sheath over the deployed stent, as shown in Fig. 4.3. An inward pressure is applied to the outer surface of the sheath and transferred to the stent by contact. The sheath is sufficiently compliant as to not support a significant inward pressure by itself (Young's Modulus,  $E = 0.1$  GPa; Poisson's Ratio,  $\nu = 0.4$ ) and is constrained to only deform radially with respect to the stent's longitudinal axis. The collapse behaviour of the stent is quantified through the determination of a pressure-diameter curve, with the stent outer diameter  $D$  determined for a given applied pressure. Due to there being no obvious point of global collapse, the pressure for 10% diameter loss, relative to the unloaded stent outer diameter  $D_0$  is taken as a measure of stent radial strength in this study. This diameter loss corresponds to a clear deviation from linear behaviour in the pressure-diameter curve for all stents.

The third test predicts stent resistance to longitudinal compression. All nodes on each end of the deployed stent geometry are fixed to control nodes (RP) by means of multi-point constraints, as shown in Fig. 4.3. The right control node is then moved toward the left control node, which is fixed in all directions, under displacement control. The resulting reaction force on the right node is taken as a measure of resistance to a given amount of stent longitudinal compression, consistent with the measure used in the experiments of Prabhu *et al.* [150].

#### 4. *The Mechanical Performance of Permanent and Absorbable Metal Stents*

The final test predicts the stent's flexibility, in terms of both elastic and plastic deformations. The approach taken is similar to that commonly used in FE stent flexibility studies [155, 156, 22] and allows a direct comparison with previous experimental studies [157]. Similar to the previous bench-tests, only two circumferential rings of the stent are modelled for stents A and C and three for stent B. This simplification, which allows improved computational efficiency, gives a good approximation of the flexibility of a longer stent with the same repeating unit [155]. In the present study, each end of the stent is fixed in all directions to two control nodes via multi-point-constraints, the right control node is then rotated about the left control node through an angle  $\theta$ , as shown in Fig. 4.3. In an approach similar to that of the previously mentioned FE studies, stent flexibility is determined in terms of the resulting moment-curvature curve, with the moment given by the reaction moment on the right-control node and the curvature  $\kappa$  given by:

$$\kappa = \frac{\theta}{L_U} \quad (4.3)$$

where  $L_U$  is the length of the stent unit. Stent flexibility is quantified as the inverse slope of the linear (elastic) portion of the moment-curvature curve, allowing a comparison of model predictions with the experiments of Mori and Saito [157].

Simulations are performed using the Abaqus/Explicit code on two Intel Xeon hexa-core processors on an SGI Altix HPC cluster at the Irish Centre for High Performance Computing. Each simulation requires approximately 50 CPU hours.

## 4.4. Results

Figs. 4.5a and 4.5b show the respective  $\eta_\sigma$  and  $\eta_\epsilon$  values for each material and geometry. It is predicted that all studied magnesium alloy stents have significantly lower  $\eta_\sigma$  and  $\eta_\epsilon$  values than the CoCr and 316L stents at maximum expansion. The iron stents are predicted to generally have  $\eta_\sigma$  and  $\eta_\epsilon$  values closer to those of the permanent stents, with the iron T2 generic stent having comparable values to the permanent stents. Predicted recoil for the 316L stent (3.9%), as shown in Fig. 4.5c, is in good agreement with that measured experimentally for the CYPHER stent (3.4% [158]), while the higher recoil predicted in the thin CoCr stent (6.7%) is consistent with experimental measurements of higher recoils in modern thin-strut stents, for example the MULTILINK VISION stent (5.9% [159]). The relatively high recoils predicted in the magnesium alloy stents (4.7% - 8.6%) are in agreement with reported stent recoil of under 8% for the Biotronik MAGIC magnesium alloy stent [40], while the relatively low recoils predicted for the iron stents (0.9% - 1.6%) are in agreement with the experimental studies of Peuster *et al.* [114], who reported a recoil of 2.2%.

Figs. 4.6a and 4.6a show the predicted pressure-diameter curves for selected stents and the pressure required for 10% diameter loss for all stents. Agrawal *et al.* [160] have suggested a minimum collapse pressure of 0.04 MPa for coronary stents. Modern CoCr stents have typical collapse pressures of just over 0.1 MPa [161], with some older 316L stents having collapse pressures as high as 0.21 MPa [162]. This range shows good agreement with the stent radial strength predictions in this study of 0.08 - 0.15 MPa for 10 and 50% diameter loss in the 80  $\mu\text{m}$  CoCr stent and 0.16 - 0.25 MPa for the 316L stent. The lower radial strengths of the magnesium alloy stents predicted in this study (0.06 - 0.14 MPa for 10 and 50% diameter loss) are in good agreement with the reported collapse pressure of 0.08 MPa for the Biotronik MAGIC magnesium alloy stent [40].

#### 4. The Mechanical Performance of Permanent and Absorbable Metal Stents

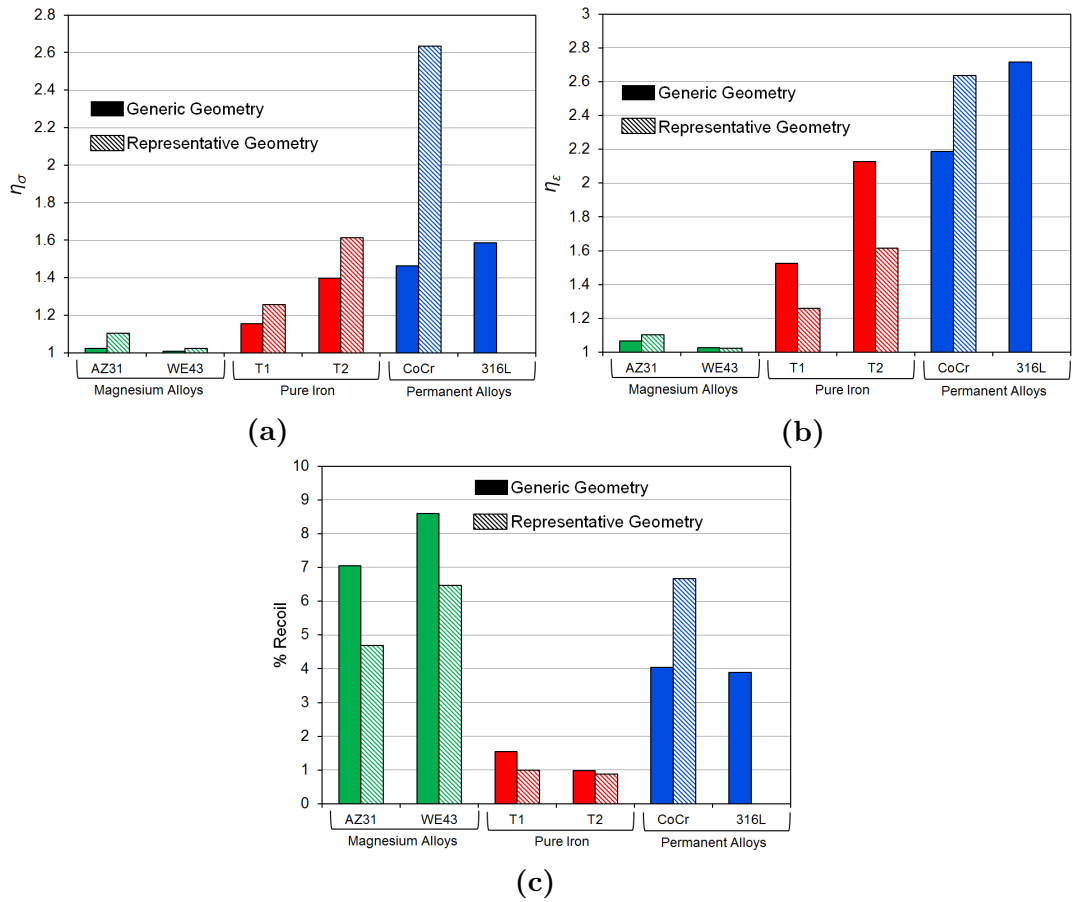


**Figure 4.5.:** Predicted factors of safety, (a)  $\eta_\sigma$  and (b)  $\eta_\epsilon$  for each stent material and geometry. (c) Predicted elastic recoil for each stent.

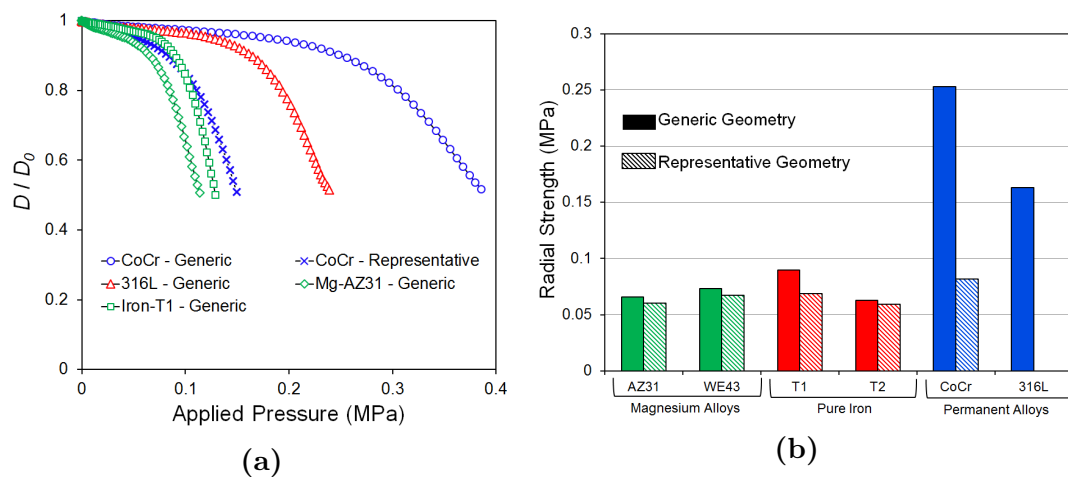


**Figure 4.6.:** (a) Predicted loss in stent outer diameter  $D$  relative to its unloaded diameter  $D_0$  due to an external applied pressure for selected stents. (b) The applied pressure required to give a 10% stent diameter reduction for all materials and stents, which is taken as a measure of radial strength.

#### 4. The Mechanical Performance of Permanent and Absorbable Metal Stents

As shown in Fig. 4.7a, it is predicted that the AMS's have greater flexibility than the permanent stents, including the 80  $\mu\text{m}$  CoCr stent. However, as shown in Fig. 4.7b, the curvatures at which the AMS's reach a  $\eta_\epsilon$  value of 1.0 are somewhat lower than those of the permanent stents. Moment-curvature predictions for the 316L stent in this study show good qualitative and quantitative agreement with those of Pant *et al.* [22], who simulated flexure in a similar stent geometry. Also, considering only the linear portion of the moment-curvature behaviour, predicted flexibility for the 316L stent ( $0.0062 \text{ N}^{-1} \text{ mm}^{-2}$ ) falls within the range of 316L stent flexibilities experimentally investigated by Mori and Saito [157] of  $0.0053 - 0.024 \text{ N}^{-1} \text{ mm}^{-2}$ .

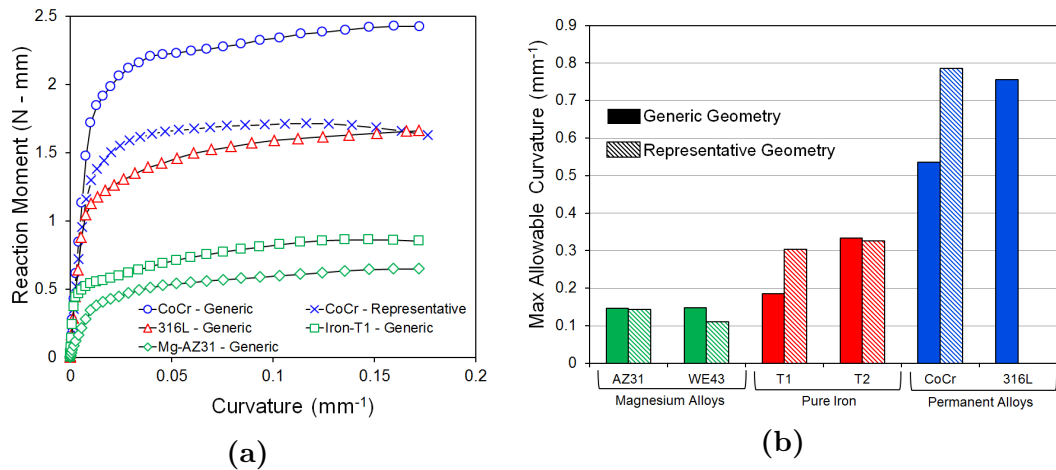


**Figure 4.7.:** (a) Predicted moment-curvature curve for selected stents. (b) Predicted stent curvature when the  $\eta_\epsilon$  value first reaches a value of 1.0 in an element for all stents and materials.

Figs. 4.8a and 4.8b show the predicted resistance of selected stents to an applied longitudinal compression and the reaction force required for 10% compression of all stents. The predicted force of 2.8 N required for a 6.5% compression of the 316L stent differs from the force of 0.5 N for the same compression of the CYPHER stent observed experimentally in Prabhu *et al.* [150]. This difference is possibly due to the different connecting section geometries of the stent studied here and the CYPHER stent, with stent geometry contributing significantly to device compressive resistance [150]. Insufficient resistance to stent longitudinal compression is undesirable as it increases the risk of stent-artery malapposition

#### 4. The Mechanical Performance of Permanent and Absorbable Metal Stents

if the stent comes into contact with the delivery system following deployment. In this study, it is predicted that the AMS's have a significantly lower resistance to longitudinal compression than the permanent stents. It is also predicted that reducing the strut dimensions from 120 to 80  $\mu\text{m}$  in the CoCr stent resulted in a significant reduction in resistance to longitudinal compression, which is in-keeping with clinical observations of poor resistance to longitudinal compression of certain thin-strut CoCr stents [150].

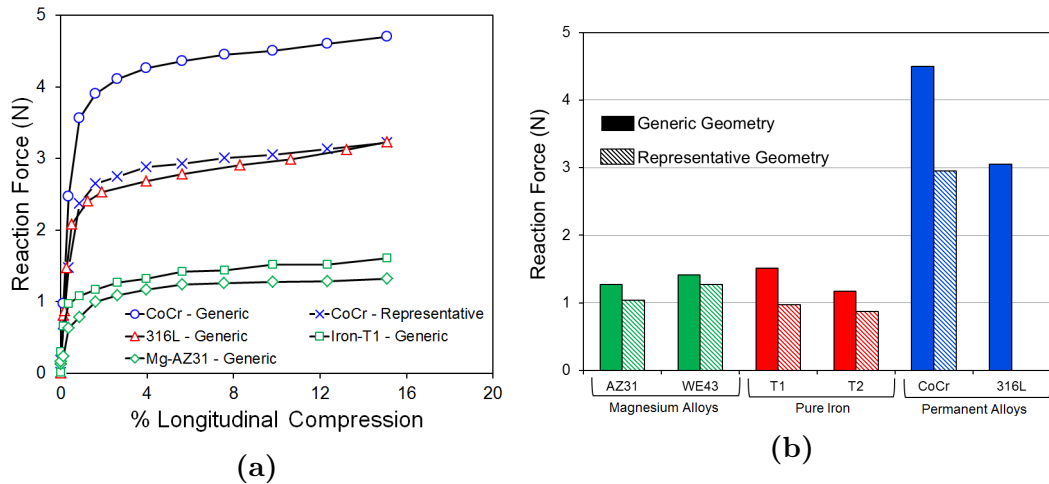


**Figure 4.8.:** (a) Prediction of the resulting reaction force for a given longitudinal compression for selected stents. (b) The force required for a 10% stent longitudinal compression for all materials and stents.

## 4.5. Discussion

The very low  $\eta_\epsilon$  values ( $< 1.1$ ) predicted in this study for both magnesium alloys and the generic and representative magnesium stent designs, relative to those of the modern CoCr and 316L stents ( $> 2.6$ ), suggest that considerable effort is required in terms of both device and alloy design to ensure a comparable fracture risk with modern, permanent stents. Addressing such a risk is of particular importance considering the nature of the relatively undemanding tests considered here, where additional deformations due to arterial curvature or irregular lumen geometry were not considered. Alloy specific device design, through geometric

#### 4. *The Mechanical Performance of Permanent and Absorbable Metal Stents*

parameter studies and shape optimization based on FEA seem necessary in the further development of such stents. Early applications of such an approach have shown promise [131]. A more detailed investigation into the use of optimization for addressing limitations in bioabsorbable alloy performance in AMS's is performed in Ch. 7 of this thesis.

Despite the promise of optimization methods, given the large gap in predicted  $\eta_\epsilon$  values between the magnesium and permanent stents, it is likely that improved alloy ductility relative to the AZ31 and WE43 alloys studied here is necessary before comparable performance in this regard can be achieved. In terms of the pure iron, it is predicted that  $\eta_\epsilon$  values more comparable with permanent stents are achievable (up to 2.1), with it likely that similar performance is possible for this metric through careful stent design.

The low maximum curvatures predicted for both magnesium stent designs and alloys ( $< 0.15 \text{ mm}^{-1}$ ) relative to the modern, permanent stents ( $< 0.75 \text{ mm}^{-1}$ ) also suggest that significant effort is required in terms of improved stent design to ensure strains in stent connecting links are minimized, and improved alloy design in terms of increased ductility. This is particularly important considering typical natural arterial curvatures of up to  $0.066 \text{ mm}^{-1}$  in 90% of the population [163], with variations of  $0.025 - 0.18 \text{ mm}^{-1}$  reported during the cardiac cycle [164]. In the case of iron stents, maximum curvatures of up to  $0.33 \text{ mm}^{-1}$  were predicted, which gives an improved performance over the magnesium stents, but may still require careful design of stent connecting links to allow comparable performance with permanent stents.

In terms of recoil, a reasonable performance is predicted for the magnesium stents, (4.7 - 8.6%) relative to the thin CoCr stent (6.7%), however it is important to note the larger strut cross-sections of the simulated magnesium stents (0.0144 -

#### 4. The Mechanical Performance of Permanent and Absorbable Metal Stents

0.0154 mm<sup>2</sup>) relative to the CoCr stent (0.006 mm<sup>2</sup>). Interestingly, the recoil performance of the iron stents (1.6%) is predicted to be significantly better than even the permanent stents. In terms of radial strength, similar performance is noted for the magnesium (0.06 - 0.073 MPa), iron (0.06 - 0.09 MPa) and thin CoCr stents (0.082 MPa), again noting the larger cross-sectional areas of the AMS's. These recoil and radial strength results suggest that the studied materials have sufficient Yield Strengths (138 - 216 MPa) and UTS (245 - 298 MPa) to achieve comparable scaffolding ability with permanent stents, albeit through the use of designs with larger strut dimensions.

It is noted in these comparisons that the iron stents show good potential in terms of achieving comparable performance with permanent stents across most metrics. However, in the future development of iron stents it is of interest to reduce strut dimensions insofar as possible, in order to compensate for the relatively low rate of iron degradation *in-vivo* [112]. In allowing for such a reduction it appears, based on model predictions, that device radial strength is the limiting performance metric. As such, the development of higher strength (Yield and UTS) iron alloys would be highly beneficial in the future development of iron stents, with newly developed alloys such as Fe35Mn [112] showing much promise in this regard. Such reductions in device dimensions would also prove beneficial in terms of improvements in device fracture risk and maximum curvature. Despite the future promise of iron and iron alloys for AMS applications, its relatively low corrosion rate [113] and concerns regarding the accumulation of corrosion products [165] mean that the majority of AMS research thus far has focused on magnesium alloys. As a result, the remainder of this thesis focuses on magnesium based AMS's, however methodologies developed in subsequent chapters, such as corrosion modelling approaches, can also be applied to studying iron stents.

For the thin-strut stent, there were expected increases in device flexibility relative

#### 4. The Mechanical Performance of Permanent and Absorbable Metal Stents

to the CoCr stent with 120  $\mu\text{m}$  strut thickness. In addition, there was a lower predicted fracture risk in the thin-strut stent than in the 120  $\mu\text{m}$  CoCr stent and a similar predicted fracture risk to the 316L stent. The thin-strut stent had reduced radial strength relative to the 316L stent, although it is still well above the lower-limit proposed by Agrawal *et al.* [160], and has not been widely reported as a clinical concern. The lower longitudinal strength of the thin-strut stent has been reported as a clinical concern [150], however, and may dictate a lower limit on device strut thickness.

The prediction of device fracture risk used in this study is based on predicted  $\varepsilon_{mp}$  in the stent hinge. Using this measure, the thin-strut CoCr stent was predicted to have a lower fracture risk than the 120  $\mu\text{m}$  CoCr stent. However, due to the use of continuum plasticity theory in the simulations of this chapter, the role of statistical size effects, and in particular the possibility of reduced ductility with reduced number of grains through strut dimensions, is not considered. This is addressed in Ch. 5 by assessing the mechanical performance of both permanent and bioabsorbable stent struts undergoing large plastic deformations, allowing for more detailed, microstructure sensitive, predictions of fracture risk to be made. This more detailed prediction is important for both thin-strut stents and bioabsorbable stents, which are predicted to have relatively high fracture risks in this study. Thus, stent fracture risks determined using conventional modelling approaches in this chapter can be directly compared with risks calculated using more detailed micromechanics based approaches, based on the results of Ch. 5.

When considering the mechanical performance of bioabsorbable stents, corrosion will naturally play an important role following deployment in the body. In order to assess the performance of AMS's in more detail it is necessary to include the effects of corrosion on device mechanical integrity. To address this, a corrosion model for AMS's is developed in Ch. 6, and is experimentally calibrated and

#### 4. The Mechanical Performance of Permanent and Absorbable Metal Stents

validated with respect to immersion experiments on bioabsorbable alloy foils. This enhances the interpretation of the results of this chapter, as the performance of corroding AMS's can then be compared directly to the performance of a number of modern and older generation (316L) permanent stents.

Only *in-vitro* device performance is considered in this chapter. A more detailed comparison between bioabsorbable and permanent stent performance can be made by predicting *in-vivo* device performance. This is addressed in Ch. 7 by simulating the delivery, balloon expansion, recoil and corrosion of stents in stenosed arterial geometries. A useful comparison can then be made between the predictions of the relatively straight-forward and computationally inexpensive simulations in this chapter and the highly detailed simulations in Ch. 7. This comparison will help to determine which aspects of stent performance require the use of detailed *in-vivo* simulations in their assessment.

## 4.6. Conclusions

This study presents a computational investigation into the role of material choice and strut thickness on coronary stent performance for magnesium alloy, iron, steel and cobalt chromium stents, based on generic and alloy specific geometric platforms. Stent performance was assessed through simulated bench-testing, using modelling techniques that have either been well established in the literature or have predictions that can be readily compared with the results of *in-vitro* experiments. The following are some key conclusions from this work:

- A significantly higher device fracture risk was predicted in deployment for the magnesium stents than the permanent or iron stents. A lower fracture

#### 4. *The Mechanical Performance of Permanent and Absorbable Metal Stents*

risk was predicted for the thin-strut CoCr stent than the 120  $\mu\text{m}$  CoCr stent.

- Respective maximum allowable device curvatures in the magnesium and iron stents were predicted to be less than 20% and 50% of those of the permanent stents. The thin-strut CoCr stent was predicted to have greater flexibility and maximum curvature than the 120  $\mu\text{m}$  CoCr stent.
- Resistances to longitudinal compression in the magnesium and iron stents were predicted to be less than 50% of those of the permanent stents. The reduction in strut thickness from 120 to 80  $\mu\text{m}$  for the CoCr stent was also predicted to lead to a significant reduction in resistance to longitudinal compression.
- The struts of the magnesium and iron stents studied here require cross-sectional areas 2.4 and 1.5 times greater, respectively, than the modern CoCr stent for comparable performance in terms of radial strength and recoil. The use of an 80 rather than 120  $\mu\text{m}$  strut thickness for the CoCr stent lead to a significant reduction in predicted radial strength, however this reduction has not been reported as a clinical concern in these devices to date.
- In terms of magnesium alloy stent development, the results presented indicate that alloy ductility needs to be increased by a factor of up to 3 for comparable performance with modern stents, vis-a-vis predicted fracture risk, with it strongly recommended that the ductility of alloys proposed for AMS application at least matches that of the AZ31 and WE43 alloys studied here.

#### 4. *The Mechanical Performance of Permanent and Absorbable Metal Stents*

- For iron stents, future research should focus on the development of higher strength iron alloys, allowing smaller strut dimensions that are more accommodating of the low *in-vivo* corrosion rates of iron and that are comparable to those of modern, permanent stents.
- Despite the promise of iron stents in terms of their mechanical performance, concerns regarding corrosion rate and biocompatibility [113, 165] mean that, overall, magnesium stents are currently the most promising form of AMS. For this reason the focus of the remainder of this thesis is on the use of magnesium and magnesium alloys in AMS's.

# 5. Microscale Mechanics of Permanent and Absorbable Metal Stents

## 5.1. Chapter Summary

It was predicted in Ch. 4 that magnesium stents have a significantly higher fracture risk than permanent stents, based on the use of classical plasticity theory. In order to allow for more accurate predictions of fracture risks in both permanent and absorbable stents and to account for size effects discussed in Ch. 2, microscale modelling approaches are required. In this chapter the influence of SSE's on the mechanics of permanent and absorbable metal stents is predicted using crystal plasticity theory. SSE's are investigated in FCC metals in Section 5.3 and in magnesium in Section 5.4. The outcome of this chapter is an improved understanding of the influence of SSE's on stent mechanics and an improved appreciation of limits on minimum strut thicknesses and maximum grains sizes in permanent and absorbable metal stents.

## 5.2. Introduction

The influence of SSE's on coronary stent strut performance is predicted: i) across a range of different materials, ii) in struts with a range of thicknesses and lengths for a fixed grain size, iii) for regular and random microstructures, and iv) for alloy microstructures with and without precipitates. The influence of SSE's is predicted for both tensile and bending loading conditions, consistent with typical stent loading conditions in deployment. Since coronary stent struts are often subject to large plastic deformation in service, SSE's are investigated in struts undergoing deformation up to, and beyond, the point of  $\epsilon_u$  (strain at maximum supported load [166]).

## 5.3. Statistical Size Effects in FCC Materials

### 5.3.1. Methods

A comprehensive set of simulations is performed to characterise the influence of SSE's on the deformation of thin struts. Struts are represented using a 2-D geometry due to the previously documented computational expense of 3-D modelling of aggregates using single crystal plasticity theory [167], and the confirmed predictive capability of similar 2-D polycrystal models [78, 80], relative to the experiments of Murphy *et al.* [35]. A generalized plane-strain behaviour is assumed in the out of plane dimension, as per Harewood and McHugh [168]. Despite the use of a 2-D geometry, each metallic grain is assigned a uniformly distributed random 3-D lattice orientation in all simulations (i.e. the plastic slip computation at each integration point considers slip on all twelve slip planes, each of which

## 5. Microscale Mechanics of Permanent and Absorbable Metal Stents

can be orientated in 3-D), resulting in a texture-less microstructure. While texture will, in general, strongly influence SSE's, it is assumed that the annealing process, which coronary stent tubing undergoes during manufacture [5], removes textures introduced during prior cold-working treatments. Although relatively little has been reported on textures in annealed stents, this assumption is based on reports of 'weak' textures in annealed stent tubing [169] and the possibility of attaining 'weak' textures in 316L with appropriate annealing conditions [170].

The simulations performed in this study are divided into a number of sets, as detailed in Table 5.1. Within these sets, SSE's are characterised for struts: i) loaded in tension, ii) loaded in bending, and iii) with different microstructure morphologies. In all cases the Abaqus/Standard solver is used (DS SIMULIA, USA).

**Table 5.1.:** Details of each set of FE simulations performed in this study over a range of strut lengths  $l$ , thicknesses  $t$  and grain diameters  $d$ .

Set	Material	$\frac{l}{d}$	$\frac{t}{d}$	Loading	Precipitates	Grain Geometry
1	316L, A, B	1.7, 5, 16.8, 33.6, 67.2, 134.5	1.5, 5, 10, 16.8, 25.2	Tension	No	Regular
1	L605	134.5	1.5, 5, 10, 16.8, 25.2	Tension	No	Regular
2	316L	2 - 50	1.5, 5, 10, 16.8	Bending	No	Regular
3	316L	134.5	1.5, 5, 10, 16.8, 25.2	Tension	No	Random
3	316L	16.8	1.5, 5, 10, 16.8	Tension	Yes	Regular

The required geometries, microstructures and associated FE meshes for each set are generated using a custom-written Python script, with a flowchart for the generation procedure shown in Fig. 5.1. The script allows the automated generation and meshing of strut geometries with a range of lengths  $l$  and thicknesses  $t$  (see Fig. 5.2a) and with varying degrees of microstructure uniformity, following the method of Fritzen *et al.* [171]. For the random microstructures, Voronoi tessella-

tion vertex co-ordinates are obtained for a given random point seed distribution using the QHULL software package [172].

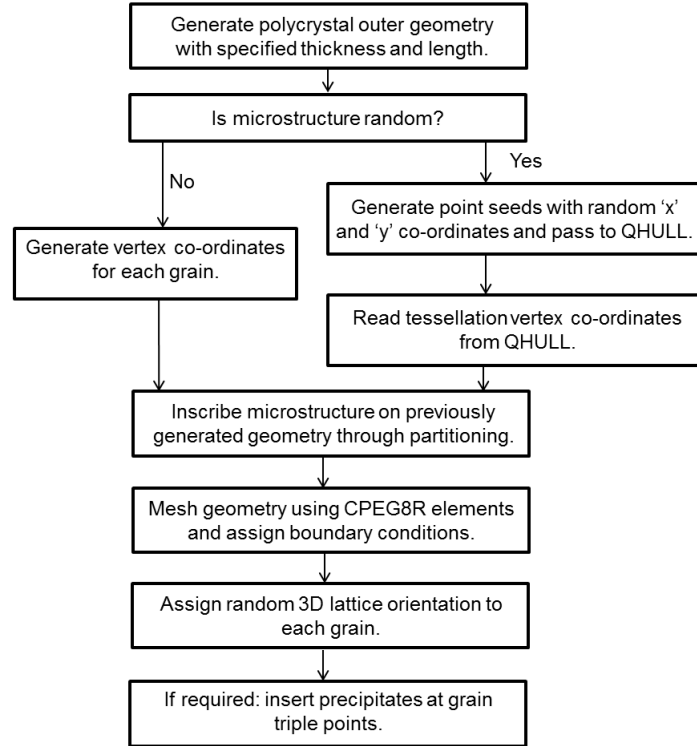


**Figure 5.1.:** Algorithm for the automated generation of meshed microstructure geometries using the Abaqus/CAE geometry kernel.

Two degrees of microstructure uniformity are considered, a highly regular microstructure, with grain geometries taking the form of hexagons, and a random microstructure, based on a Poisson-Voronoi tessellation. The tessellation is obtained by generating point seed coordinates using a uniform distribution random number generator, without constraint on the minimum distance between two neighbouring point seeds. For both random and regular microstructures the grain diameter  $d$ , shown in Fig. 5.2c, is determined from the average grain area  $G_a$  according to:

$$d = \frac{2G_a}{3\sqrt{3}} \quad (5.1)$$

which corresponds to the side length of a regular hexagon with area  $G_a$ . Resulting strut geometries and microstructures are shown in Figs. 5.2a and 5.2b, with a typical grain diameter distribution for the random microstructure shown in

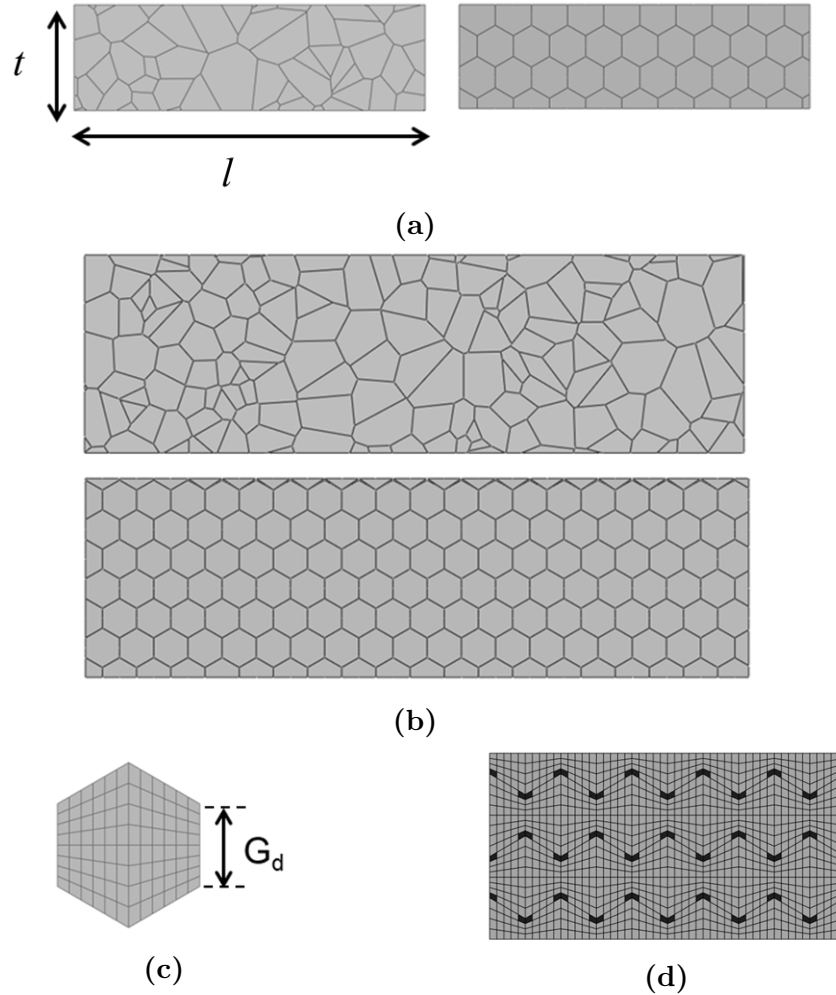


**Figure 5.2.:** (a) 2-D representations of the polycrystals with random and regular microstructures. Thickness  $t$  is  $30\ \mu\text{m}$  and length  $l$  is  $100\ \mu\text{m}$ . (b) Polycrystals with random and regular microstructures with thickness  $60\ \mu\text{m}$  and length  $200\ \mu\text{m}$ . (c) A single hexagonal grain of diameter  $d$  showing the FE mesh used in this study. (d) Precipitate distribution in the FE mesh. Precipitates are shown in black and are included at all grain triple points.

Fig. 5.3. This distribution arises naturally when no constraints are placed on point seed distances in the generation process and is not specifically representative of any experimentally observed microstructure.

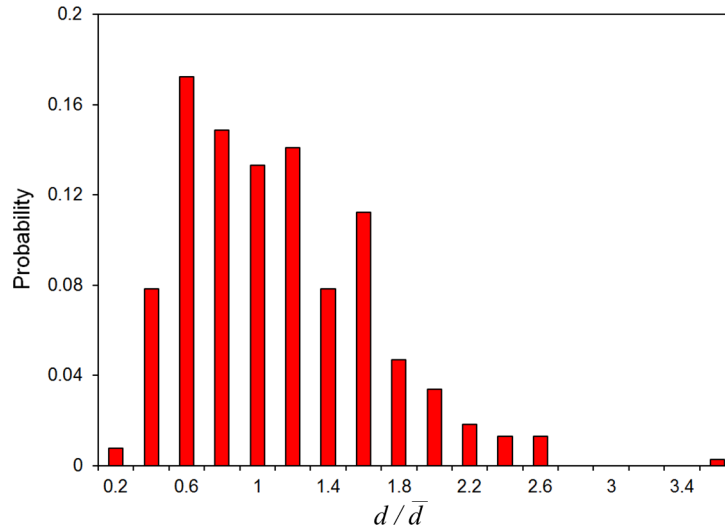


**Figure 5.3.:** Grain diameter  $d$  probability distribution for a typical random microstructure used in this study.  $\bar{d}$  is the mean grain diameter and is equal to  $5.95 \mu\text{m}$ .

Each strut is meshed using reduced integration quadratic generalized plane strain elements (CPEG8R, four integration points and eight nodes) with an average of 96 elements per grain, as shown in Fig. 5.2c. The resulting ratio of element size to grain size is equivalent to that of Harewood and McHugh [168], who have shown its suitability in predicting  $\epsilon_u$  in a mesh dependence study based on crystal plasticity simulations similar to the type performed here.

As part of the generation procedure, precipitates are inserted at grain triple points for some of the generated geometries, as shown in Fig. 5.2d. The area fraction (4.2%) and size ( $1 \times 2 \mu\text{m}$ ) of the precipitates are within the range of those reported in annealed L605 stent tubing [5]. Since no details of precipitate spacing distributions are given in that study, a regular dispersion is assumed by placing precipitates at grain triple-points only.

Two different loading conditions are considered, uniaxial tension and pure bend-

ing. Tensile loading of each strut is simulated as shown in Fig. 5.4a. All nodes on the left-most edge of each strut are fixed in  $x$  direction, resulting in a symmetry condition on this edge, while the bottom left and right nodes are fixed in the  $y$  direction. To simulate uniaxial tension all nodes on the right edge are displaced an equal distance in the  $x$  direction through the use of linear equation constraints. Bending of the struts is simulated as shown in Fig. 5.4b. The left edge of the strut is fixed in the  $x$  direction, while the bottom left node is fixed in the  $y$  direction. A reference node, R1, is rotated about point R2 in Fig. 5.4b with the rotation of the node transferred to the strut through its connection via rigid beams to all nodes on the right edge.

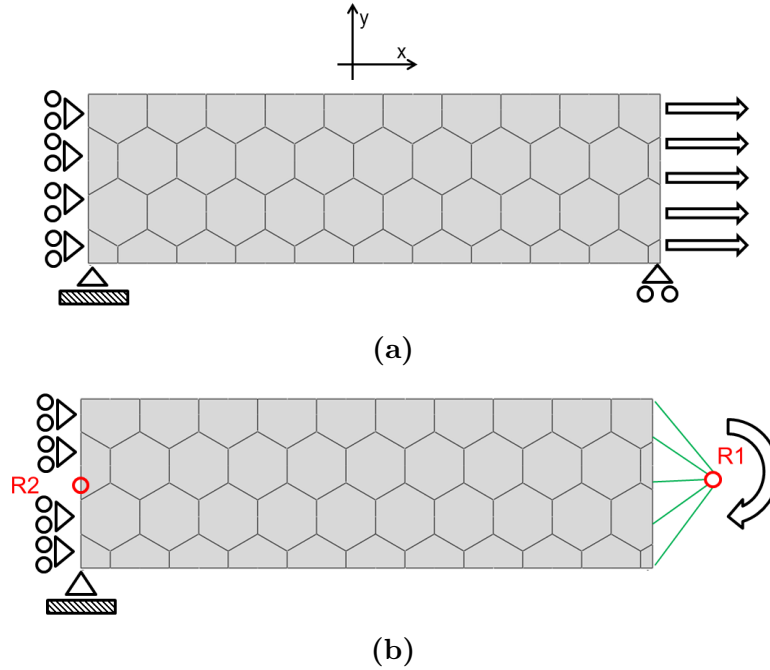


**Figure 5.4.:** Boundary conditions used for (a) uniaxial tension and (b) pure bending. In (a) and (b) left and right polycrystal edges are kept straight through the application of boundary conditions and linear multi-point constraints. In (a) a displacement in the  $x$  direction is applied to the right edge to simulate a tensile test. In (b) a clock-wise rotation is applied to control node R1 about point R2 to simulate pure bending.

SSE's are investigated for four different materials, namely stainless steel 316L, cobalt chromium L605, and two comparator materials, A and B. Materials A and B are arbitrary materials which have similar elastic properties, Yield Strength and UTS to 316L, but have lower and higher  $\epsilon_u$  respectively. The inclusion of

## 5. Microscale Mechanics of Permanent and Absorbable Metal Stents

these materials allows the investigation of the dependence of SSE's on single crystal strain hardening behaviour.

All studied materials are assumed to have a FCC crystal structure with material behaviour described using rate dependent crystal plasticity theory, as described in Ch. 3. For the FCC crystal all 12 slip systems  $\{111\}\langle 011\rangle$  are potentially active (reverse slips are not considered to be independent slip systems). The crystal plasticity theory is implemented in Abaqus by means of the UMAT of Huang [140], discussed in Ch. 3. A reference strain rate  $\dot{a}$  of  $0.0106 \text{ s}^{-1}$  and rate sensitivity exponent  $n$  of 50 are assumed in Eqn. 3.57 for describing the rate dependence of the plasticity of each material. These values are the same as those used in the study of Harewood and McHugh [80] for 316L struts and lead to a relatively rate-independent material behaviour. This is consistent with the room-temperature behaviour of most metals and also ensures a reasonable computational expense. The elastic constants used for each material are given in Table 5.2. Due to a lack of experimental data on the composition of precipitates in L605 tubing, their behaviour is assumed to be linear elastic, with a Young's Modulus of 700 GPa, consistent with that of tungsten carbide [173].

**Table 5.2.:** Elastic properties and single crystal hardening parameters for materials A and B, 316L, L605, and tungsten carbide precipitates.

Material	$E$ (GPa)	$\nu$	$g_0$ (MPa)	$g_\infty$ (MPa)	$h_0$ (MPa)
Material A	190	0.28	140	300	440
Material B	190	0.28	140	800	150
316L	190	0.28	140	380	260
L605	243	0.3	200	660	400
Precipitates	700	0.3	-	-	-

Calibration of the material constants for the crystal plasticity model requires a knowledge of the parameters  $g_0$ ,  $g_\infty$  and  $h_0$  in Eqn. 3.57. These parameters are determined by matching predicted Yield Strength, UTS and  $\epsilon_u$  with those reported by Murphy *et al.* [35] for stent struts of thickness 150  $\mu\text{m}$  and length

## 5. Microscale Mechanics of Permanent and Absorbable Metal Stents

4.0 mm. In order to replicate the geometry of the these samples as closely as possible, calibration is carried out using struts with the largest thickness (150  $\mu\text{m}$ ) and length (0.8 mm) permitted by available computational resources. Grains are modelled as regular hexagons of diameter 5.95  $\mu\text{m}$ , based on grain size data in Murphy *et al.* [35].

The resulting values of  $g_0$ ,  $g_\infty$  and  $h_0$  are shown in Table 5.2, with the final engineering stress-strain curves of the model and experiment observed to be in excellent agreement, as shown in Fig. 5.5a and Table 5.3. In addition to 316L, a similar calibration is carried out for L605, based on macroscopic stress-strain data presented in Teague *et al.* [174]. A grain diameter of 10.0  $\mu\text{m}$  is used in this case, consistent with that reported in Teague *et al.* [174]. The predicted stress-strain curve and the experimentally observed stress-strain data are shown for L605 in Fig. 5.5a and Table 5.3.

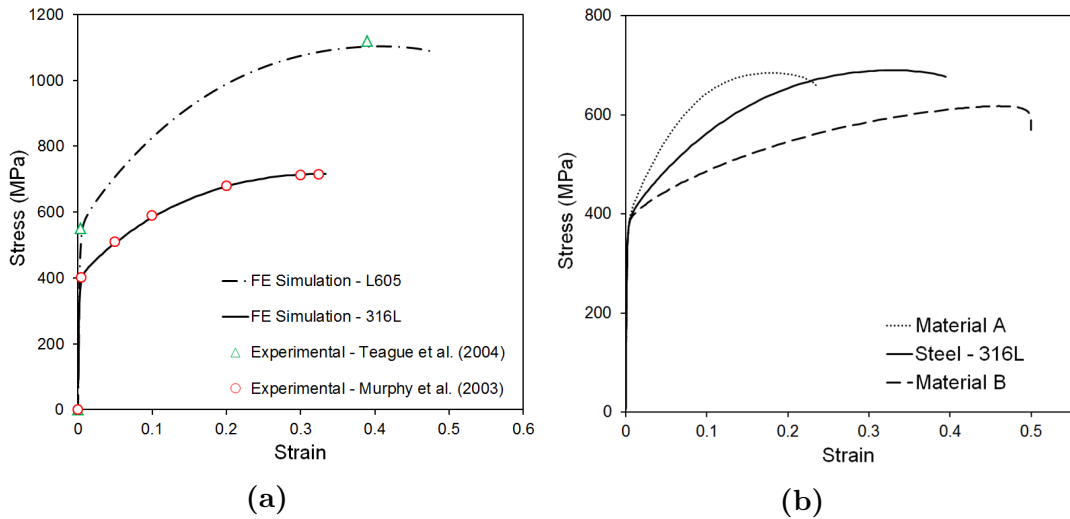


**Figure 5.5.:** (a) Selected points from stress-strain curves for 150  $\mu\text{m}$  thick 316L struts as tested by Murphy *et al.* [35] and data for L605 rods tested by Teague *et al.* [174]. Calibrated FE model stress-strain curves are also shown for each material. (b) Stress-strain curves for 316L and two comparison materials, A and B, given by simulated tensile testing of 150  $\mu\text{m}$  thick and 800  $\mu\text{m}$  long polycrystals.

Following calibration, two further material behaviours A and B are generated based on an appropriate choice of  $g_0$ ,  $g_\infty$  and  $h_0$ , leading to materials with,

## 5. Microscale Mechanics of Permanent and Absorbable Metal Stents

**Table 5.3.:** Predicted and experimentally observed yield stress, UTS and  $\epsilon_u$  values based on simulations performed here and experiments on 316L struts and L605 rods by Murphy *et al.* [35] and Teague *et al.* [174] respectively.

Material	Yield Strength (MPa)	UTS (MPa)	$\epsilon_u$	Yield Strength (MPa)	UTS (MPa)	$\epsilon_u$
	Predicted			Experimental		
316L	400	716	0.33	400	713	0.33
L605	550	1103	0.4	550	1118	0.39

respectively, lower and higher  $g_0$ ,  $g_\infty$  and  $h_0$  than 316L. Stress-strain curves for each material are compared to that of 316L in Fig. 5.5b, while the adopted values of  $g_0$ ,  $g_\infty$  and  $h_0$  parameters for all the materials studied are shown in Table 5.2.

Three sets of simulations are used to characterise SSE's in the studied struts, as detailed in Table 5.1. In Set 1, SSE's are investigated in struts loaded in tension and consisting of each of four materials, 316L, L605, A and B. In these simulations, strut lengths range from 0.01 mm to 0.8 mm and thicknesses range from 9  $\mu\text{m}$  to 150  $\mu\text{m}$ , with a subset of these dimensions used for L605, as detailed in Table 5.1. The average grain diameter for struts consisting of 316L, A and B is 5.95  $\mu\text{m}$ , with a diameter of 10.0  $\mu\text{m}$  used for the L605 struts. In this set, and all others, five simulations are performed for each material and combination of thicknesses and lengths, corresponding to five different random lattice orientations.

In Set 2, SSE's are investigated for 316L struts subject to pure bending. The simulated struts have lengths from 0.2 mm to 0.6 mm, thicknesses from 60 to 150  $\mu\text{m}$ , and thickness to grain diameter ratios of 1.5 to 10.0. In Set 3 the influence of microstructure morphology on SSE's is investigated for a subset of the 316L strut dimensions simulated in Set 1, see Table 5.1. Simulations are conducted for microstructures with regular and random morphologies, with and without precipitates.

## 5. *Microscale Mechanics of Permanent and Absorbable Metal Stents*

In total 650 simulations are performed over the three sets considered. Simulations are performed on between one and six Intel Xeon hexa-core processors on an SGI Altix HPC cluster at the Irish Centre for High Performance Computing, requiring over 50 000 CPU hours.

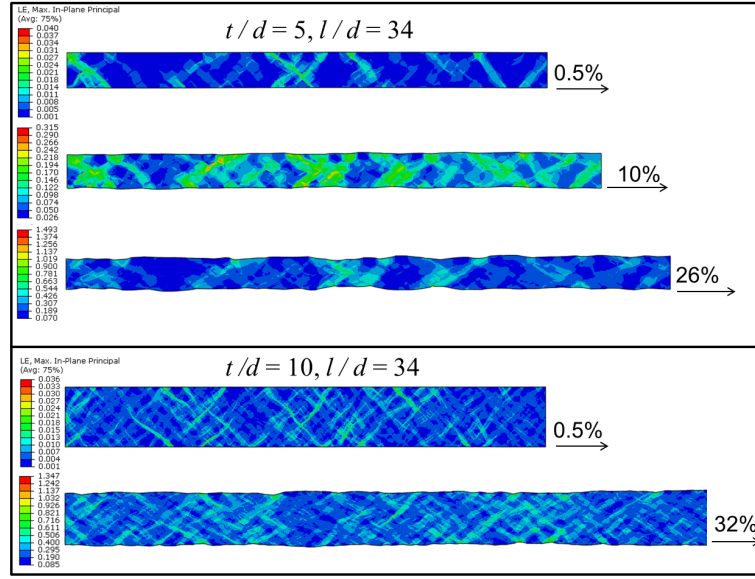
### 5.3.2. Results

#### 5.3.2.1. Set 1 - SSE's in Uniaxial Tension

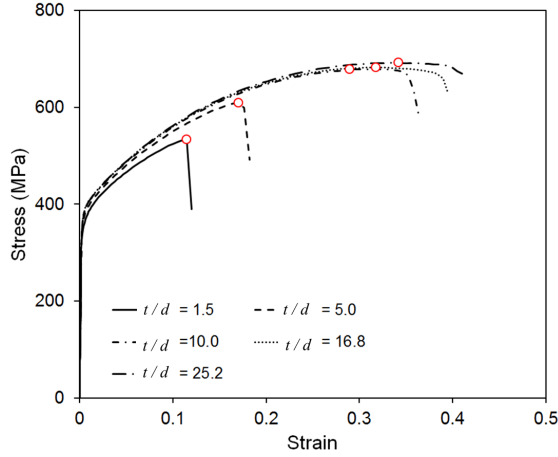
Figs. 5.6a, 5.6b and 5.6c show the predicted influence of the number of grains through the dimensions of a 316L strut on its mechanical behaviour in tension. In Fig. 5.6a FE contour plots of maximum principal logarithmic strain  $\epsilon_{mp}$  are shown for struts of the same length and grain size but different thickness in tension. The formation of shear bands is evident in both struts. The development of necking is more pronounced in the thinner strut at  $\epsilon_u$  (26% and 32% in the thinner and thicker struts respectively). Fig. 5.6b shows a selection of predicted engineering stress-strain curves for struts of the same length and grain size. Both UTS and  $\epsilon_u$ , circled, are reduced with decreasing thickness. Fig. 5.6c shows the predicted reduction in  $\epsilon_u$  in struts of fixed grain size and with increasing length and decreasing thickness. Saturation, or ‘levelling-off’ in  $\epsilon_u$  values is evident for each thickness with increasing length.

Figs. 5.7a and 5.7b show the predicted influence of single crystal strain hardening behaviour on the deformation of struts with different numbers of grains through their dimensions. Fig. 5.7a shows FE contour plots of  $\epsilon_{mp}$  in struts consisting of material A, which has a relatively low ‘bulk’  $\epsilon_u$ , see Fig. 5.5b, and material B, which has a relatively high ‘bulk’  $\epsilon_u$ . Necking is more pronounced in material B at  $\epsilon_u$  (13% for A and 37% for B). Fig. 5.7b shows the predicted dependence of  $\epsilon_u$

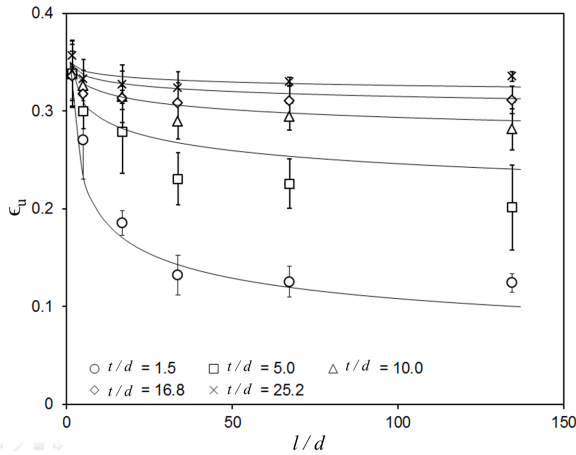
5. Microscale Mechanics of Permanent and Absorbable Metal Stents



(a)



(b)



(c)

**Figure 5.6.:** (a) FE contour plots of max principal logarithmic strain in polycrystals of the same length  $l$  with five and ten grains through their thickness  $t$ . (b) Predicted engineering stress-strain curves for polycrystals with increasing number of grains through the thickness and a length of 0.8 mm. UTS and  $\epsilon_u$  are circled. (c)  $\epsilon_u$  for polycrystals with increasing numbers of grains through their thickness and length. Error bars represent one standard deviation, with five polycrystals simulated for each data point. Fit lines are given by Eqn. 5.2.

## 5. Microscale Mechanics of Permanent and Absorbable Metal Stents

on thickness and length in struts with a fixed grain size, for different materials. The  $\epsilon_u$  of material B has a greater dependence on both thickness and length than it does in materials A and 316L, shown in Fig. 5.6c. The degree of scatter in  $\epsilon_u$  (given by the size of error bars on each data point) predicted for material B is somewhat greater than that in materials A and 316L for a given strut size.

In order to aid in the interpretation of results shown in Fig. 5.6c and Fig. 5.7b it is useful to describe the predicted SSE's in terms of the following power-law model:

$$\bar{\epsilon}_u = \bar{\epsilon}_{u,0} \left( \frac{d}{l} \right)^{\left( \frac{\beta d}{t} \right)} \quad (5.2)$$

where  $\bar{\epsilon}_u$  is the mean value of  $\epsilon_u$  for struts of a given size, taken over a number different lattice orientations (five in this study),  $\bar{\epsilon}_{u,0}$  is the mean value of  $\epsilon_u$  for single crystals ( $\frac{l}{d} = 1.0$ ,  $\frac{t}{d} = 1.0$ ) of the material, again taken over a number different lattice orientations, and  $\beta$  is a fitting parameter.

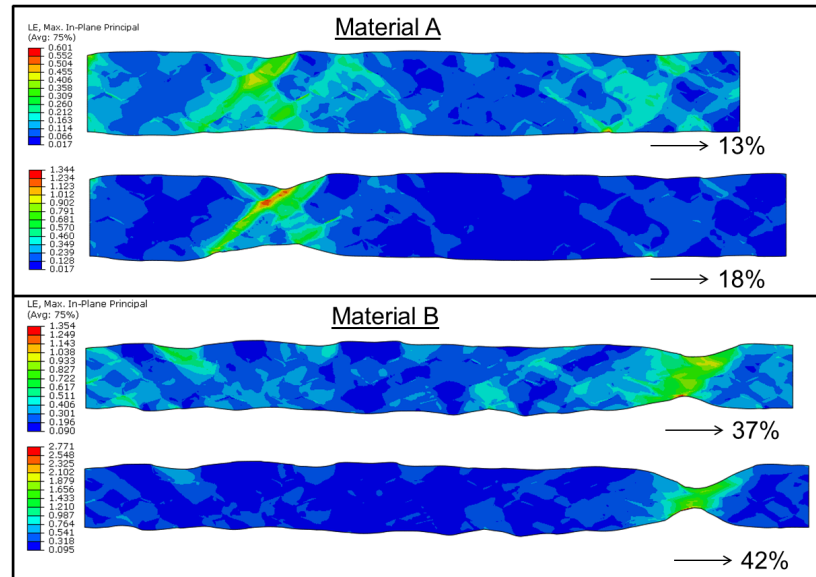
In using this model to describe the results shown in both Figs. 5.6c and 5.7b, a suitable value for  $\beta$  can be found by the following averaging:

$$\beta = \frac{\sum_{j=1}^3 \sum_{i=1}^n \left[ \log \left( \frac{d_i}{l_i} \right) \left( \frac{\bar{\epsilon}_{u,i}}{\bar{\epsilon}_{u,0,j}} \right) \right] \left( \frac{t_i}{d_i} \right)}{3n} \quad (5.3)$$

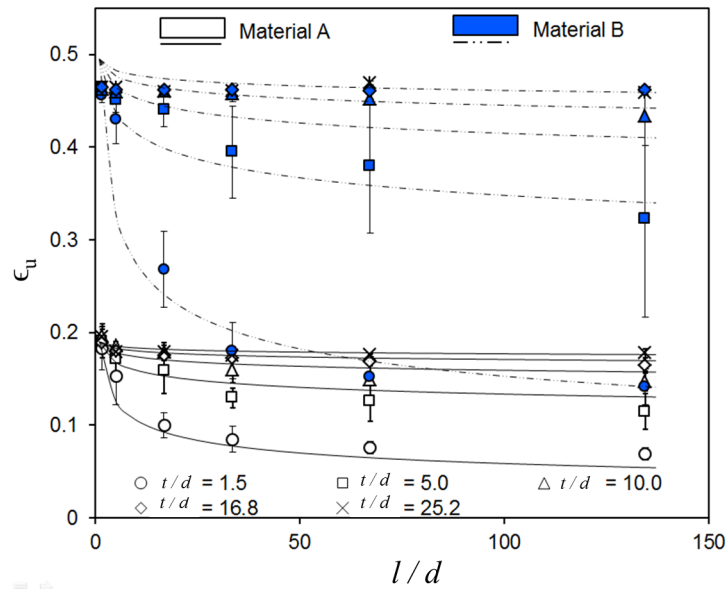
where summation is over the  $n$  data points for each of the three materials  $j$  in Figs. 5.6c and 5.7b. The resulting predictions from Eqn. 5.2 are shown in Figs. 5.6c and 5.7b, based on a value of  $\beta = 0.37$ . The  $R^2$  coefficient for the fit of Eqn. 5.2 to the data (0.946) is determined conventionally, as follows:

$$R^2 = 1 - \frac{\sum_{i=1}^n n(y_i - f_i)^2}{\sum_{i=1}^n n(y_i - \bar{y})^2} \quad (5.4)$$

where  $y$  and  $f$  are the respective  $\bar{\epsilon}_u$  predictions from the FE simulations and Eqn. 5.2 and  $\bar{y}$  is the mean of all  $\bar{\epsilon}_u$  predictions shown in Figs. 5.6c and 5.7b.



(a)



(b)

**Figure 5.7.:** (a) FE contour plots of max principal logarithmic strain in polycrystals with the same dimensions and grain diameters but consisting of materials A and B. (b)  $\epsilon_u$  for polycrystals with increasing numbers of grains through their thickness and length for materials A and B. Error bars represent one standard deviation, with five polycrystals simulated for each data point. Fit lines are given by Eqn. 5.2.

## 5. Microscale Mechanics of Permanent and Absorbable Metal Stents

Due to its simplicity and accuracy, Eqn. 5.2 gives a number of insights into the synergistic roles of modifying strut thickness and length for a fixed grain size on  $\epsilon_u$ . In particular, Eqn. 5.2 shows that increasing the length reduces  $\epsilon_u$  according to a power-law type behaviour, with the extent of this reduction scaling linearly with  $\bar{\epsilon}_{u,0}$ . This is evident in Fig. 5.7b, where material B is subject to somewhat more pronounced SSE's than material A. Eqn. 5.2 also shows that as the thickness increases and the strut behaviour tends towards that of a 'bulk' sample, the dependence of  $\epsilon_u$  on length is quickly diminished.

Fig. 5.8 shows a direct comparison of the predicted reduction in  $\epsilon_u$  with decreasing thickness for 316L and L605. This comparison is of interest in the context of coronary stent design, as it allows a comparison of the performance of both materials for a given strut thickness, while also taking their different average grain diameters into account. A very similar quantitative and qualitative dependence of  $\epsilon_u$  on strut thickness is predicted for both materials in this case.

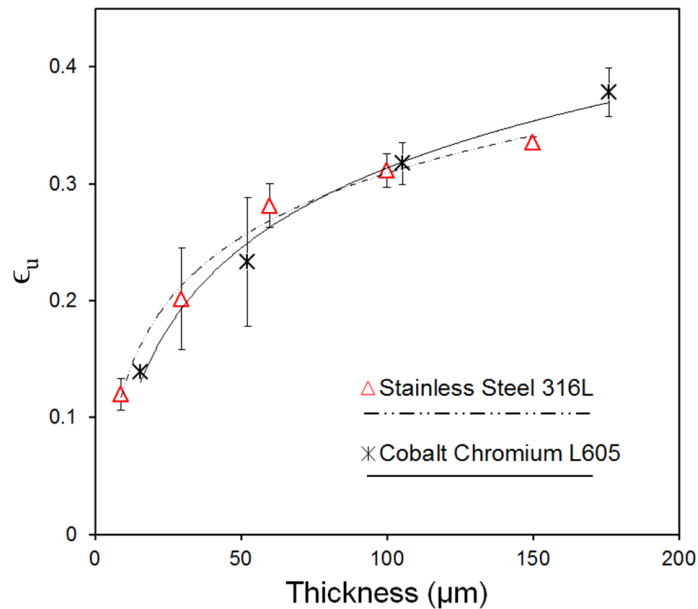


**Figure 5.8.:**  $\epsilon_u$  in polycrystals of increasing thickness and with material properties and microstructures that are representative of 316L and L605. Error bars represent one standard deviation, with five polycrystals tested for each data point. Power law best fits are included for illustrative purposes.

**5.3.2.2. Set 2 - SSE's in Bending**

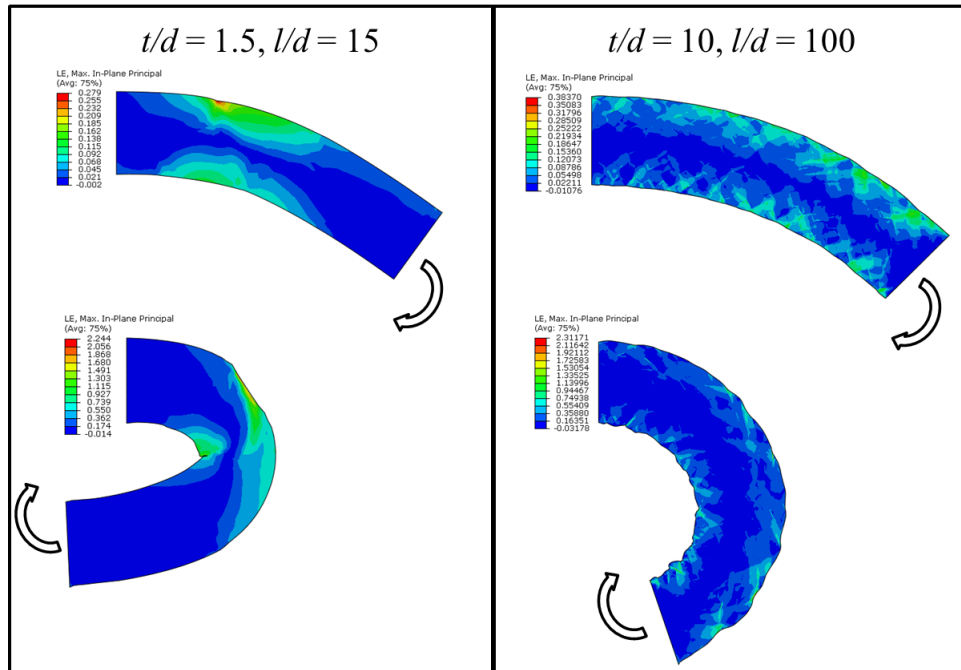
Figs. 5.9a and 5.9b show simulation results for struts in bending. Fig. 5.9a shows FE contour plots of  $\varepsilon_{mp}$  in struts of the same thickness and length but different grain sizes loaded in pure bending. In the struts with 1.5 grains through the thickness the deformation is quite inhomogeneous, deviating considerably from the typical constant curvature arc taken by a beam of homogeneous material. However, in the strut with 10 grains through the thickness, the bending deformation is far more regular. Shear bands are predicted to form on the inner and outer edges of the latter strut, but not in the former.

Fig. 5.9b shows a selection of moment-curvature curves for struts of increasing thickness and with two different grain sizes. Moment refers to the reaction moment on RP1 in Fig. 5.4b, while curvature,  $\kappa$ , is given by:

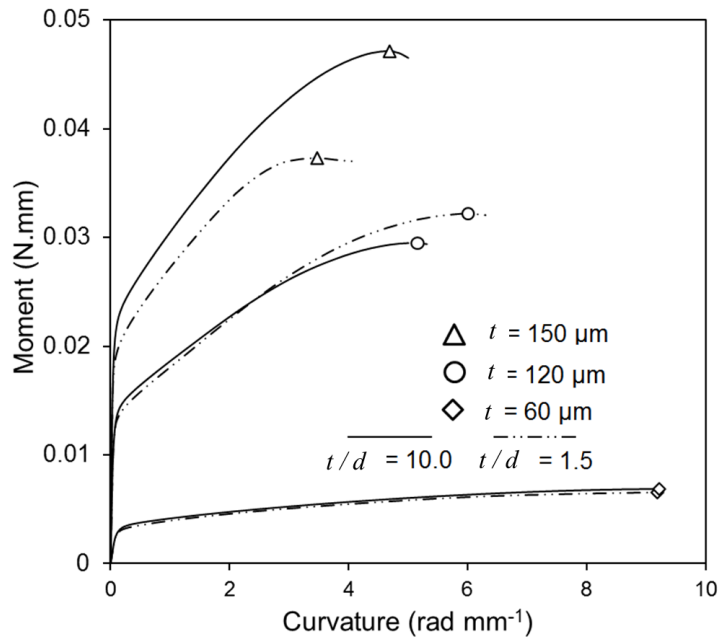
$$\kappa = \frac{\theta}{l} \quad (5.5)$$

where  $\theta$  is the angle of rotation of RP1 about RP2. This curvature measure is analogous to that used in Eqn. 4.3 in Ch. 4 in describing the bending of the entire stent. For the individual struts this can be regarded as a measure of average curvature along the length of the strut; however as shown in Fig. 5.9a, due to the inhomogeneous deformation of some struts, local curvatures may deviate from this value somewhat. Fig. 5.9b shows that, as expected, thicker struts support greater moments and have lower curvatures at maximum moment  $\kappa_u$ .

Fig. 5.10a shows predicted  $\kappa_u$  for struts of increasing thickness and increasing number of grains through the thickness. As thickness is increased a corresponding reduction in  $\kappa_u$  is predicted. This result shows good agreement with that previously reported in the simulations of Harewood and McHugh [80] for 316L



(a)



(b)

**Figure 5.9.:** (a) FE contour plots of max principal logarithmic strain polycrystals of the same dimensions but different grain diameter  $d$  subject to pure bending. (b) Predicted moment-curvature curves for a selection of polycrystals of increasing thicknesses and with two different grain diameters.

## 5. Microscale Mechanics of Permanent and Absorbable Metal Stents

struts in bending. However, as seen in Fig. 5.10a, the influence of SSE's in bending is not immediately apparent, with similar  $\kappa_u$  values predicted for each strut of a given thickness, regardless of grain diameter. This is due to  $\kappa_u$  predictions being heavily influenced by a geometrical effect, brought about by changing the strut's thickness to length ratio. This continuum effect is not due to changes in specimen to grain size ratio, but is solely due to the use of curvature as a measure of deformation. When results are instead considered in terms of maximum surface strain  $\epsilon_s$ , given by:

$$\epsilon_s = \frac{\kappa_u t}{2} \quad (5.6)$$

the results no longer depend on the ratio of strut thickness to length and the influence of SSE's becomes apparent, as shown in Fig. 5.10b.

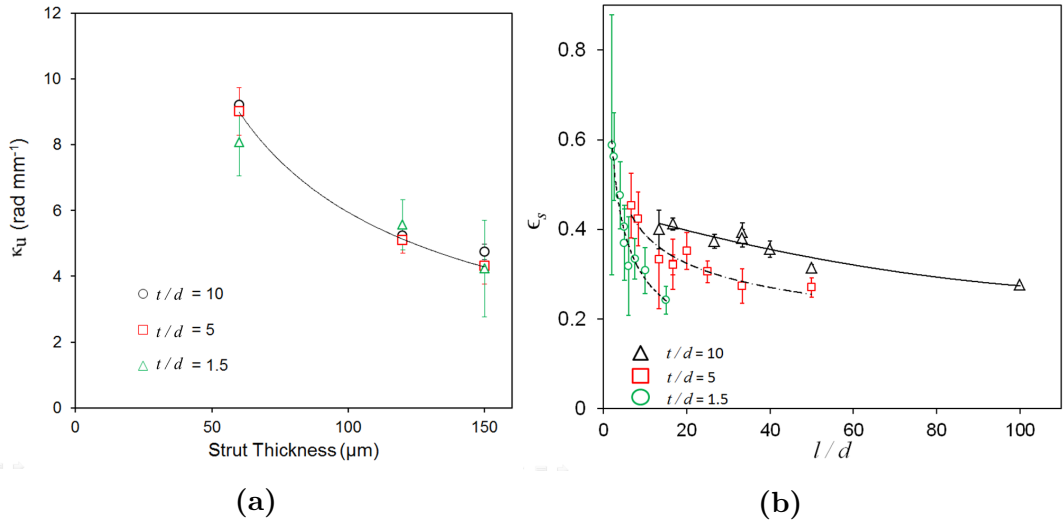


**Figure 5.10.:** Predicted  $\kappa_u$  for (a) polycrystals with increasing thickness and grain diameters, with a fixed length of 0.6 mm, and (b)  $\epsilon_s$  in polycrystals with increasing thickness and lengths and fixed grain diameter. Error bars represent one standard deviation, with five polycrystals tested for each data point shown. Power law best fits are included for illustrative purposes.

Fig. 5.10b shows predicted  $\epsilon_s$  for a combination of strut lengths, thicknesses and grain sizes. Similar SSE's are predicted in bending to those observed in tension, with  $\epsilon_s$  decreasing with increasing length and increasing with increasing thickness, for a given grain size. The magnitude of the predicted SSE's in bending is somewhat less than in tension and considerable scatter in  $\epsilon_s$  is predicted for

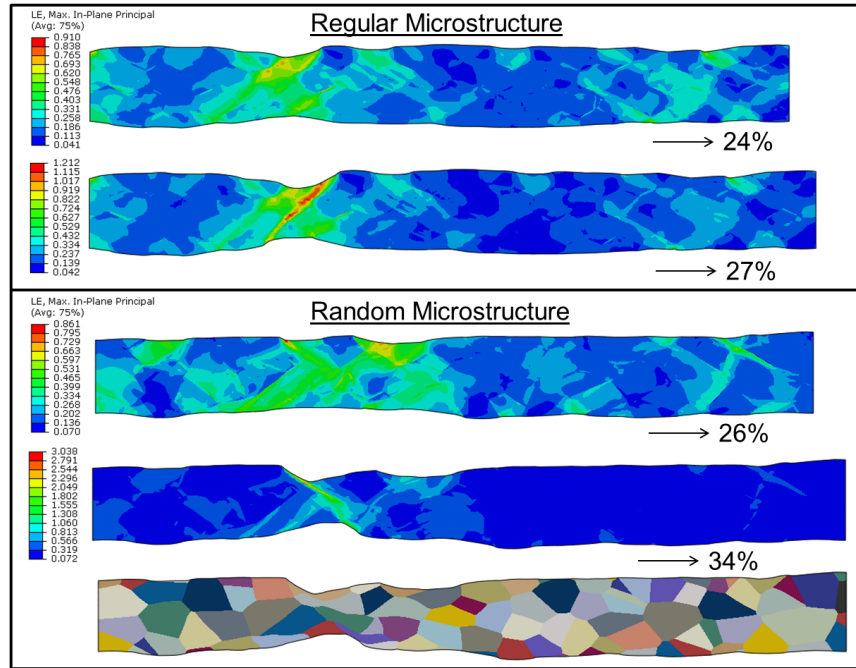
struts with few grains through their dimensions.

### 5.3.2.3. Set 3 - Influence of Microstructure Morphology on SSE's

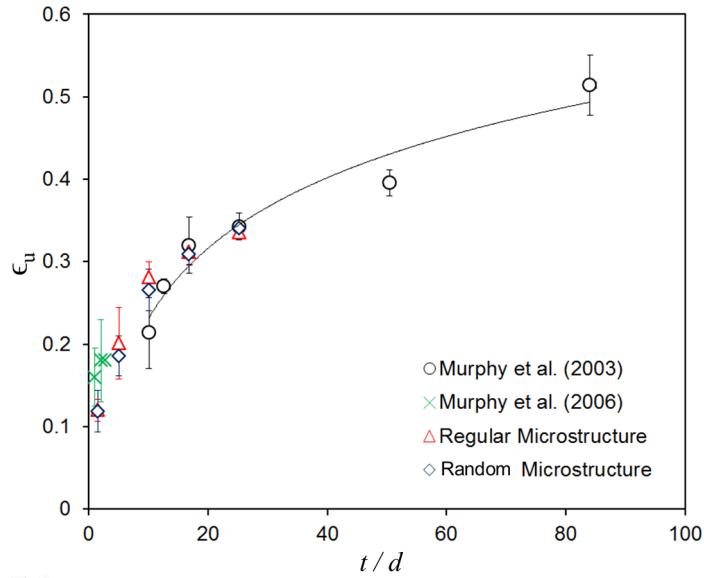
FE contour plots of  $\varepsilon_{mp}$  are shown in Fig. 5.11a for struts with the same thickness and length but with regular and random microstructures of the same average grain diameter. Similar degrees of necking are noted in both microstructures at  $\epsilon_u$  (24% and 26% in the respective regular and random microstructures), although a more pronounced post -  $\epsilon_u$  necking is observed in the random microstructure.

The dependence of  $\epsilon_u$  on thickness for each microstructure type is shown in Fig. 5.11b. Both microstructures lead to very similar  $\epsilon_u$  for a given thickness, both in terms of magnitude and scatter. In addition, model predictions for both sets of microstructures show good qualitative and quantitative agreement with the experimental results of Murphy *et al.* [35] based on tensile testing of thin 316L struts of fixed grain diameter and decreasing thickness. Predictions are also in general agreement with the results of Murphy *et al.* [79] although mean  $\epsilon_u$  values are underestimated. This may be due differences in absolute grain sizes between the two experiments or the over-estimation of the extent of SSE's due to the use of a 2-D rather than 3-D modelling approach, as discussed subsequently.

FE contour plots of  $\varepsilon_{mp}$  are shown in Fig. 5.12a for struts of the same thickness, length and lattice orientations but for microstructures with, and without, precipitates. The addition of precipitates is predicted to lead to more pronounced necking following  $\epsilon_u$  for a given applied strain. Fig. 5.12b shows the predicted influence of precipitate inclusion on the dependence of  $\epsilon_u$  on thickness for a given grain size. The inclusion of precipitates leads to a reduction in the predicted magnitude of  $\epsilon_u$ , however a similar dependence of  $\epsilon_u$  on thickness is evident in



(a)



(b)

**Figure 5.11.:** (a) FE contour plots of  $\epsilon_{mp}$  in polycrystals with the same dimensions and grain diameters but with regular and random grain geometries. (b)  $\epsilon_u$  for increasing thickness to grain diameter ratio for both random and regular microstructures. The experimental results of Murphy *et al.* [35] and Murphy *et al.* [79] are also included. A power law best fit for the data from Murphy *et al.* [35] is included for illustrative purposes.

both microstructures.

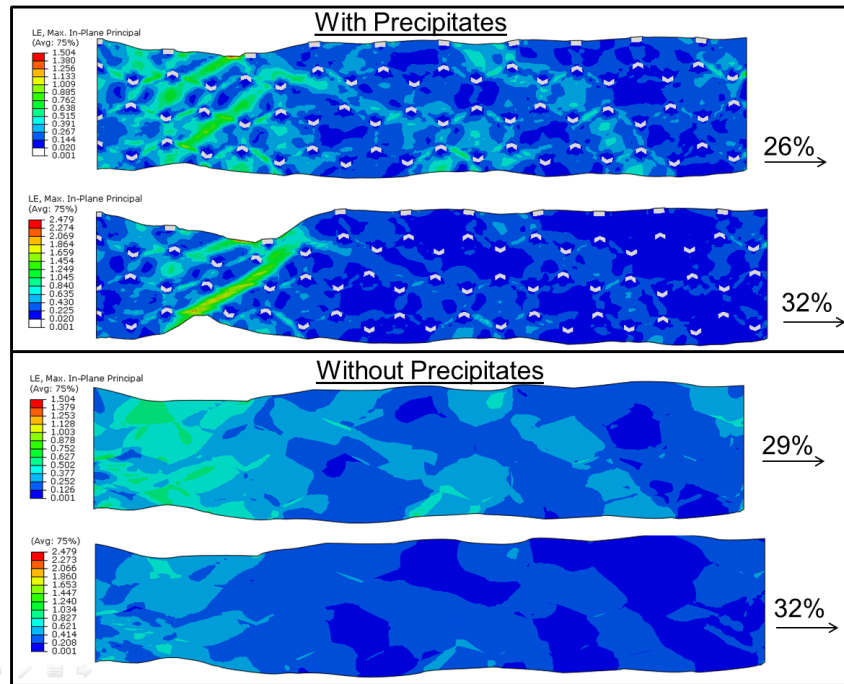
### 5.3.3. Discussion

A comprehensive numerical investigation of SSE's in 2-D struts is performed over a range of strut sizes, microstructures and materials. Results are discussed in terms of: i) the roles of  $\frac{t}{d}$  and  $\frac{l}{d}$  ratios in SSE's, ii) the role of bulk material properties in SSE's, iii) the role of SSE's in bending, and iv) morphology and UTS.

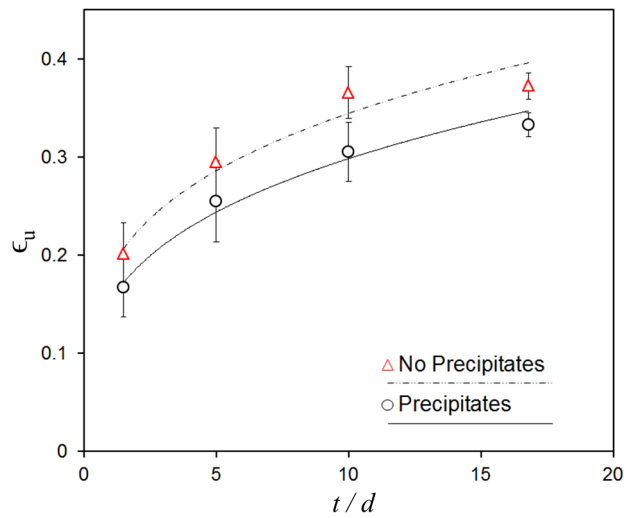
#### 5.3.3.1. The role of $t/d$ and $l/d$ ratios in SSE's

This study gives a number of new insights into the role of SSE's in strut plasticity. While it has been shown in previous computational studies that for a fixed grain size decreasing the thickness of a strut reduces its  $\epsilon_u$  [78], the predictions of this study show that the strut's length also has an influence on  $\epsilon_u$ . It is predicted that the  $\epsilon_u$  of struts in tension decreases according to a power-law with an increasing number of grains along the strut length. For struts with single grains through the thickness the mechanism for this decrease is a 'weakest-link' effect, with the overall  $\epsilon_u$  of the strut depending largely on the strength and  $\epsilon_u$  of the grain most preferably orientated for slip along its length. Increasing the number of grains along the strut length increases the probability of there being a grain with low resistance to slip, until inevitably the strut is guaranteed to contain a grain with the smallest possible resistance to slip for a given set of material properties.

Although the mechanism for  $\frac{l}{d}$  ratio effects is conceptually simple, the identification of a power-law dependence of  $\epsilon_u$  on  $\frac{l}{d}$  ratio and a critical  $\frac{l}{d}$  ratio above which



(a)



(b)

**Figure 5.12.:** (a) FE contour plots of max principal logarithmic strain in polycrystals with the same dimensions and grain diameters but with and without precipitates. (b)  $\epsilon_u$  in polycrystals of increasing thickness and fixed grain diameter and length. Error bars represent one standard deviation, with five polycrystals tested for each data point. Power law best fits are included for illustrative purposes.

## 5. Microscale Mechanics of Permanent and Absorbable Metal Stents

these effects are negligible in this study is important. As shown in Fig. 5.6c, it is predicted that changing the  $\frac{l}{d}$  ratio from 20 to 40 leads to a 37% reduction in predicted failure strain for a  $\frac{t}{d}$  of 1.5, and a 21% reduction for a  $\frac{t}{d}$  ratio of 5.0. Similarly in bending, as shown in Fig. 5.10b, there is a clear dependence of maximum surface strain on  $\frac{l}{d}$  ratio for ratios up to 100.

These critical ratios are surprising, given that they are noticeably higher than  $\frac{l}{d}$  ratios used in many computational studies on size effects, e.g. Fülöp *et al.* [85], Murphy *et al.* [79], Harewood and McHugh [80], Hoefnagels *et al.* [88], Chan *et al.* [77] and even some experimental studies, e.g. Gau *et al.* [65]. This suggests that few computational studies are correctly accounting for the important effect of  $\frac{l}{d}$  ratio when attempting to predict  $\frac{t}{d}$  ratio effects or other microstructure related size effects. Based on the predictions of this study, it is recommended that in computational and experimental studies on size effects a minimum  $\frac{l}{d}$  ratio of 40 in tension and 100 in bending is used to negate  $\frac{l}{d}$  ratio effects in struts with few grains through their thickness.

As is evident from Fig. 5.6c, increasing the number of grains through the strut thickness is predicted to reduce the extent of the  $\frac{l}{d}$  ratio effect, again according to a power law behaviour. The mechanism for this change is that the average strength of several grains through the thickness, rather than that of a single grain, now controls the weakest-link effect. While again this concept is quite simple, it should be noted that: i) to the author's knowledge the individual contributions of  $\frac{l}{d}$  and  $\frac{t}{d}$  ratio effects to the overall SSE have not previously been identified, as is done here in Eqn. 5.2, and ii) it does not account for all features predicted by the single crystal models, such as increased necking prior to UTS in material with higher bulk  $\epsilon_u$ .

The importance of knowing the contributions of both  $\frac{t}{d}$  and  $\frac{l}{d}$  ratio effects is

evident in stent design. It is often the case that components of the stent geometry are small enough that both  $\frac{t}{d}$  and  $\frac{l}{d}$  ratio effects are apparent ( $\frac{t}{d} < 20$ ,  $\frac{l}{d} < 100$ ). If the grain size is changed for a fixed geometry, then both  $\frac{t}{d}$  and  $\frac{l}{d}$  ratios will change, and will do so to different extents. To account for this, the individual contributions of the  $\frac{t}{d}$  and  $\frac{l}{d}$  ratio effects to the overall SSE must be known. Hence, to the author's knowledge this is the first study that allows the effects of changing grain size on SSE's in stent components with low  $\frac{t}{d}$  and  $\frac{l}{d}$  ratios to be predicted.

### 5.3.3.2. The role of bulk material properties in SSE's

As shown in Fig. 5.7b and Eqn. 5.2, it is predicted that  $\epsilon_u$  scales linearly with bulk  $\epsilon_u$  for struts of a given size and microstructure. This means that the role of SSE's can be predicted for a wide range of FCC metals based on the results of this study and also implies that materials with similar bulk  $\epsilon_u$  are susceptible to similar SSE's, despite differences in bulk UTS. This implication is important in terms of stent design. The higher UTS of L605 has facilitated the development of struts with thicknesses significantly less than those typical in 316L stents. L605 stents with struts of thickness as low as 40  $\mu\text{m}$  have been developed, e.g. the Meril MITSU stent, while 316L struts have typically been on the order of 130-140  $\mu\text{m}$ , e.g. the Cordis CYPHER stent. Murphy *et al.* [35] have shown that for 316L such a reduction leads to >32% (relative) decrease in  $\epsilon_u$ . Since no similar experimental studies on size effects in L605 have been reported, the predictions of this study give an important insight into how such a reduction in dimensions may affect L605 strut performance. As shown in Fig. 5.8, it is predicted that L605 is susceptible to similar SSE's to 316L, despite its higher strength. Since SSE's are likely to be a major contributor to overall size effects for struts of this size and since L605 struts are thinner than 316L struts, this finding is of

importance in highlighting the need for further investigation of size effects in L605, as part of safe stent design. Overall, this suggests that care should be taken when using ‘bulk’ material data in the design of L605 stents to ensure conservatism under large plastic deformations due to tension and bending (see Harewood *et al.* [175]).

### 5.3.3.3. The role of SSE’s in bending

In this study, surface strain  $\epsilon_s$  has been identified as a quantity that gives new insights into the influence of SSE’s in bending. As shown in Fig. 5.10b, SSE’s in bending are predicted to lead to reductions in  $\epsilon_s$  with increasing  $\frac{l}{d}$  ratio and  $\frac{t}{d}$  ratio. In identifying the underlying mechanism of the SSE’s in bending, it remains unclear as to whether strut behaviour is controlled by an average of grain properties through the thickness or whether it depends more strongly on the behaviour of surface grains. Due to the use of  $\epsilon_s$  in quantifying the role of SSE’s in bending, it is possible to identify the individual contributions of geometrical effects and SSE’s to changes in strut performance with changing dimensions. This identification of individual contributions is important in the analysis of stent performance.

As an example, decreasing the thickness of a 330  $\mu\text{m}$  long 316L strut with grain area 92  $\mu\text{m}^2$  from 120  $\mu\text{m}$  to 60  $\mu\text{m}$  leads to a 100% improvement in maximum curvature due to geometric effects, based on Eqn. 5.5. However, once the negative effects of SSE’s are included, based on Fig. 5.10b, the improvement drops to 74%. The ability to account for both geometric effects and SSE’s in this way makes the results of this study very useful in determining the trade-off in performance in bending between reducing absolute strut thickness and  $\frac{t}{d}$  ratio.

#### 5.3.3.4. Morphology and UTS

The similarity in predictions for both regular and random microstructures in terms of  $\epsilon_u$  in Fig. 5.11b is a somewhat surprising result, as the number of grains through the thickness in certain regions can be somewhat lower than those in the equivalent regular microstructure. However, this result is in agreement with the findings of Savage *et al.* [78] for struts with relatively many ( $> 12$ ) grains through their thickness. In explaining the observed similarity, it seems for the random microstructure there is a relatively low probability of a grain that is preferably orientated for slip coinciding with a region with relatively few grains through the thickness.

The introduction of precipitates to the microstructure, which is based on observations of precipitates in L605 stent tubing [5], albeit with simplified distribution, geometry and mechanical properties, leads to a reduction in predicted  $\epsilon_u$ , shown in Fig. 5.12b. This is attributed to the tendency of the precipitates to encourage the formation of early strain localization as shown in Fig. 5.12a. However, the introduction of the precipitates is observed to have relatively little effect on overall SSE's.

It is predicted that SSE's also influence strut UTS, although to a lesser extent than  $\epsilon_u$ . The results of Fig. 5.6b show that the effect on UTS is only noticeable when there are quite few ( $< 5.0$ ) grains through the strut thickness. This may explain the observations of Murphy *et al.* [35], who reported no significant reduction in UTS in struts with decreasing thickness and fixed grain size, as the minimum number of grains through the strut thickness in that study was 10.0.

## 5.4. Statistical Size Effects in Magnesium

### 5.4.1. Methods

A similar approach to characterising SSE's in magnesium is taken to the characterisation performed for FCC crystals. However, in this case Taylor isotropic hardening is not assumed in Eqn. 3.58. As per Graff *et al.* [50], slip in magnesium is assumed to take place on basal  $\{0001\}$  and prismatic  $\{1\bar{1}00\}$  planes in the  $\langle 11\bar{2}0 \rangle$  directions and in the pyramidal planes  $\{11\bar{2}2\}$  in the  $\langle 11\bar{2}3 \rangle$  directions. Tensile twinning is also represented as slip on the  $\{10\bar{1}2\}$  planes in the  $\langle 10\bar{1}1 \rangle$  directions. Hardening on the basal systems is assumed to follow Eqn. 3.62, hardening on the prismatic and pyramidal systems is assumed to follow Eqn. 3.63 and hardening on the twinning systems is assumed to follow Eqn. 3.64. These equations are repeated here in order of original appearance for clarity:

$$h(\bar{\gamma}) = h_0 \quad (5.7)$$

$$h(\bar{\gamma}) = h_0 \left( 1 - \frac{g_0}{g_\infty} \right) \exp \left( -\frac{h_0 \bar{\gamma}}{g_\infty} \right) \quad (5.8)$$

$$h(\bar{\gamma}) = \begin{cases} h_0 & \text{for } \bar{\gamma} \leq \gamma_{ref} \\ h_0 \left( \frac{\bar{\gamma}}{\gamma_{ref}} \right)^{m-1} & \text{for } \bar{\gamma} > \gamma_{ref} \end{cases} \quad (5.9)$$

The hardening parameter values for each slip system are given by Graff *et al.* [50], based on calibrating a similar crystal plasticity model from magnesium single crystal and polycrystal test data from Kelley and Hosford [176, 177]. The relevant values are shown in Table 5.4.

The interaction coefficients,  $q_{\alpha\beta}$  in Eqn. 3.61, are also given by Graff *et al.* [50], based on the same calibration as for the hardening coefficients. Eqn. 3.61 is re-

**Table 5.4.:** Hardening parameter values for magnesium single crystals from Graff *et al.* [50].

	Basal	Prismatic	Pyradmidal	Twinning
$g_0$ (MPa)	1	20	40	5
$g_\infty$ (MPa)	-	50	260	-
$h_0$ (MPa)	10	7500	7500	200
$\gamma_{ref}$	-	-	-	0.11
$m$	-	-	-	10

peated here for clarity and the relevant coefficient values are shown in Table 5.5:

$$\begin{aligned}
 h^{(\alpha\alpha)} &= h(\bar{\gamma}) \\
 h^{(\alpha\beta)} &= q^{(\alpha\beta)} h(\bar{\gamma})
 \end{aligned}
 \tag{5.10}$$

**Table 5.5.:** Latent hardening (interaction) coefficients  $q_{\alpha\beta}$  for magnesium single crystals, where the hardening on slip system  $\alpha$  depends on slip on slip system  $\beta$ . Values are from Graff *et al.* [50].

	Basal $\beta$	Prismatic $\beta$	Pyradmidal $\beta$	Twinning $\beta$
Basal $\alpha$	$q_{\alpha\beta}=0.2$	$q_{\alpha\beta}=0.5$	$q_{\alpha\beta}=0.5$	$q_{\alpha\beta}=0.5$
Prismatic $\alpha$	$q_{\alpha\beta}=0.2$	$q_{\alpha\beta}=0.2$	$q_{\alpha\beta}=0.2$	$q_{\alpha\beta}=0.5$
Pyradmidal $\alpha$	$q_{\alpha\beta}=1.0$	$q_{\alpha\beta}=1.0$	$q_{\alpha\beta}=0.2$	$q_{\alpha\beta}=0.25$
Twinning $\alpha$	$q_{\alpha\beta}=1.0$	$q_{\alpha\beta}=1.0$	$q_{\alpha\beta}=0.2$	$q_{\alpha\beta}=0.2$

In order to implement the aforementioned hardening behaviours in the UMAT of Huang [140], which was used in the FCC portion of the study, a number of modifications to the UMAT are required. These include the addition of: i) the hardening laws in Eqns. 3.62, 3.63 and 3.64, ii) the ability to model crystal lattices with different aspect ratios and iii) the ability to model more than three sets of active slip systems. To test the correct implementation of these modifications and the suitability of the calibration parameters of Graff *et al.* [50] for the model used in this study, the experiments of Kelley and Hosford [176, 177] are simulated. These experiments involved channel-die compression of single magne-

## 5. Microscale Mechanics of Permanent and Absorbable Metal Stents

sium crystals. In the experiments the crystals were loaded and constrained in a number of different directions such that deformation occurs on a small number of slip systems at a given time. To simulate these experiments the channel die compression of a single 8 noded linear brick element (C3D8) is performed in this study, as shown in Fig. 5.13. Loading and constraint directions, expressed in Miller-Bravais indices for each test, are shown in Table 5.6.

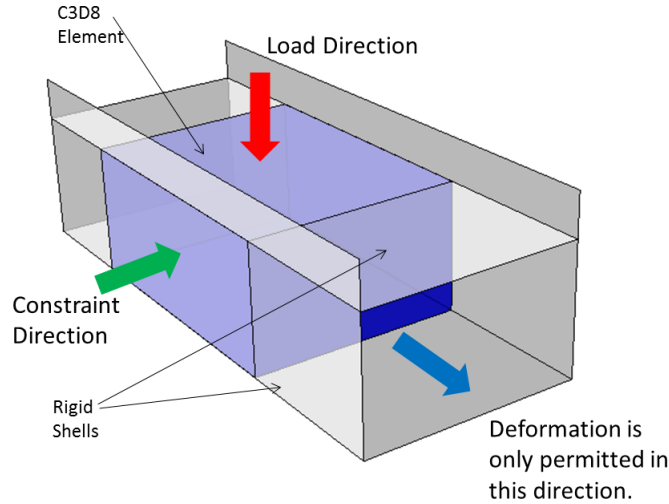


**Figure 5.13.:** Simulation of the channel die experiments of Kelley and Hosford [176, 177].

**Table 5.6.:** Loading and constraint directions for the simulation of the channel die experiments in Miller-Bravais indices.

Simulation	Load Direction	Constraint Direction
A	$[0001]$	$[10\bar{1}0]$
B	$[0001]$	$[1\bar{2}\bar{1}0]$
C	$[10\bar{1}0]$	$[0001]$
D	$[1\bar{2}\bar{1}0]$	$[1\bar{2}\bar{1}0]$
E	$[10\bar{1}0]$	$[10\bar{1}0]$
F	$[1\bar{2}\bar{1}0]$	$[10\bar{1}0]$

The resulting model predictions are shown relative to the experimental results of Kelley and Hosford [176, 177] in Fig. 5.14. Good agreement is observed between the model predictions and the experiment, given the large number of parameters required to calibrate the model. Further to this, similar calibration tests were performed in Graff *et al.* [50], which also show good agreement between their model predictions and the results of polycrystal channel die experiments.

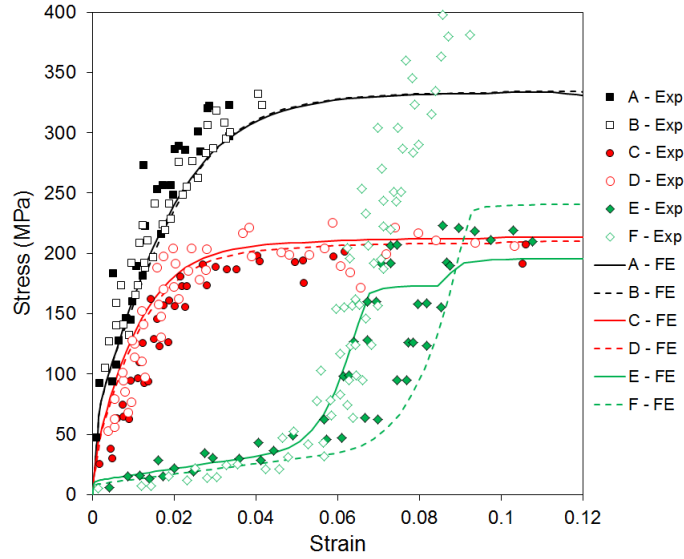


**Figure 5.14.:** Finite element model predictions compared to the experimental channel die test results of Kelley and Hosford [176, 177].

While it was assumed that due to annealing the FCC struts of the previous section were textureless, a typical processing route for magnesium stents has not been reported. One of the few studies that have reported a processing route for a magnesium stent has used extruded tubing [178]. It is reported in Vedani *et al.* [178] that the extrusion process results in the basal plane in the HCP lattice being favourably orientated to be parallel to the extrusion direction. To account for the effects of this preferred texture in simulations, a bias is introduced when assigning random crystallographic orientations, so that the  $a_4$  direction (normal to the basal plane) on the HCP lattice in Fig. 2.1b is preferentially aligned to be normal to a chosen ‘extrusion direction’.

The assumed orientations for textureless and extruded (textured) magnesium tubing are shown in the form of stereographic projections in Fig. 5.15a. The projections are generated by identifying the  $a_4$  direction from an arbitrary sample of lattice orientations obtained from the random orientation generator used in model generation, see Fig. 5.1. The out-of-plane direction on the plot corresponds to the tube axis/extrusion direction and the radial directions correspond to radial directions on the tubing. The effect of the bias introduced in the ran-

## 5. Microscale Mechanics of Permanent and Absorbable Metal Stents

dom orientation generator (see Graff *et al.* [50] for details) for textured tubing is manifested in the projections of Fig. 5.15a as the grouping of points towards the radial directions, which corresponds to the basal plane being preferentially orientated to be parallel to the extrusion direction. Fig. 5.15b shows the same extrusion and radial directions on a sample of stent tubing. A depiction of simulated test samples ‘cut’ from the tubing that are aligned with the extrusion and radial directions is also shown. Figs. 5.15c and 5.15d show the conditions for loading in tension and bending for these simulated samples aligned in the radial and extrusion directions. These radial and extrusion sample directions are chosen for the simulations in this work based on the confirmed predictive capability of a modelling approach, similar to that used here, for the loading of AZ31 rods in these directions by Graff *et al.* [50].

Given that a preferred grain size has not been established for magnesium stents, a size of 10.0  $\mu\text{m}$  is assumed here. This assumption has little impact on the results of the study, since single crystal data was used in the model calibration and since results are presented in a way that is independent of absolute grain size.

SSE’s are investigated in magnesium for a subset of the cases considered for the FCC crystals. Struts with hexagonal grains are subject to simulated tensile testing for an  $\frac{l}{d}$  ratio of 40.0 and  $\frac{t}{d}$  ratios of 1.5, 6.0, 12.0 and 25.5 and bending for an  $\frac{l}{d}$  ratio of 40.0 and  $\frac{t}{d}$  ratios of 6.0, 12.0 and 25.5.

Since the parameters of Graff *et al.* [50] were provided for C3D8 elements, struts are meshed with a single layer of these elements, with 72 elements per grain. To allow comparable results between the 3-D elements used here and the 2-D generalized plane strain elements used when simulating FCC crystals, equal ‘out-of-plane’ deformations are enforced for the 3-D models by constraining all nodes

5. Microscale Mechanics of Permanent and Absorbable Metal Stents

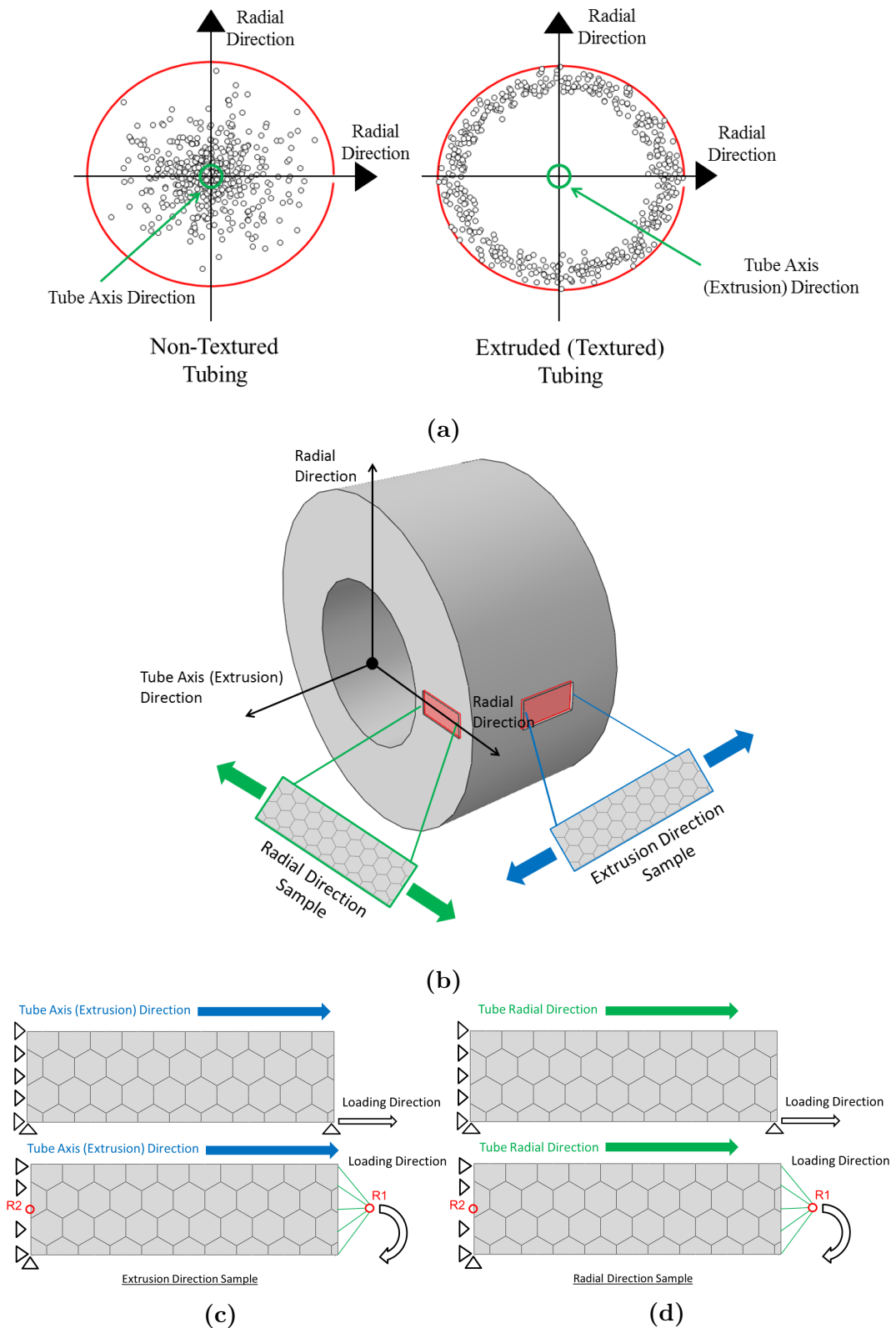


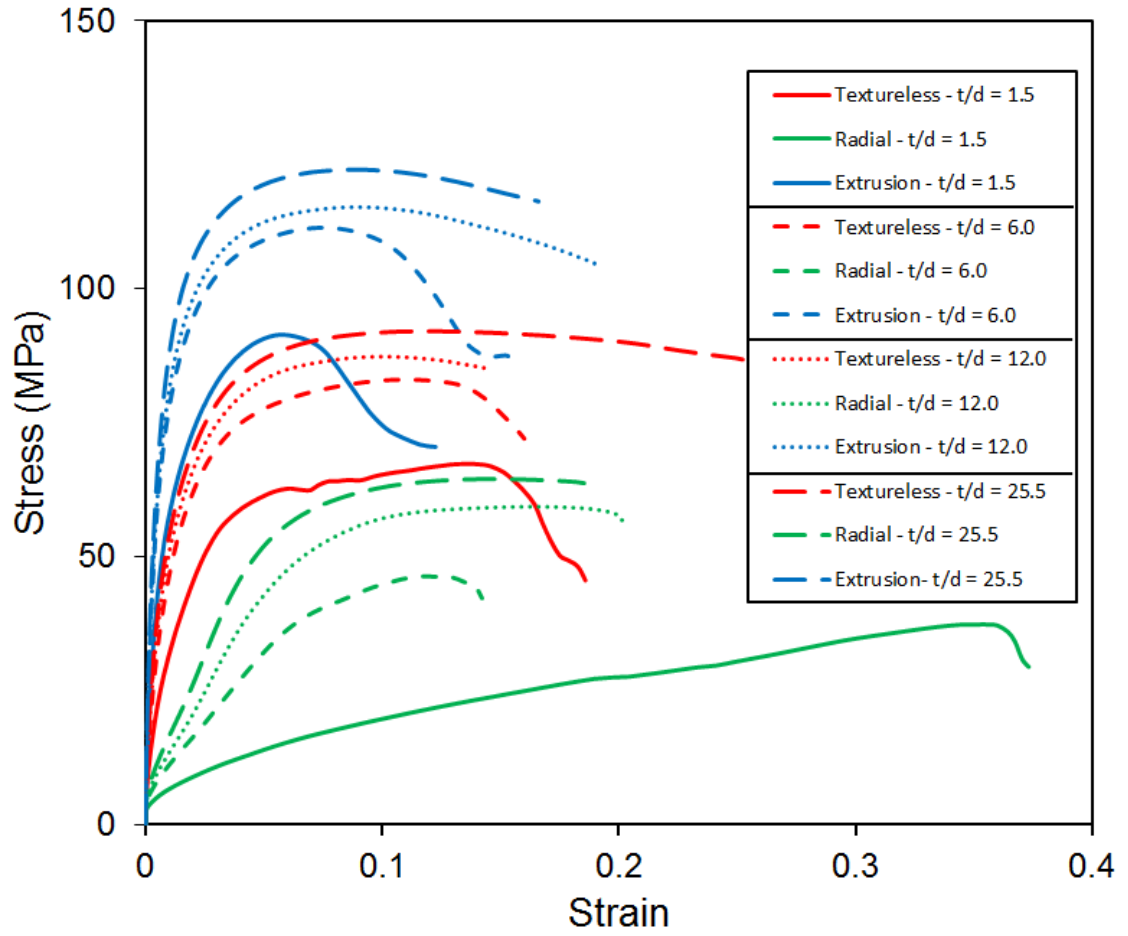
**Figure 5.15.:** (a) Stereographic projections showing assumed orientations of the  $a_4$  axis of the HCP lattice for texturless and textured microstructures. The tube axis/extrusion direction is the out-of-plane direction. (b) A depiction of the extrusion and radial directions on extruded stent tubing from which struts are cut. (c) A depiction of the loading directions for samples cut along the extrusion direction. (d) A depiction of the loading directions for samples cut along the radial direction.

to have equal displacements in the ‘out-of-plane’ directions. This is achieved using ‘Equation’ type constraints.

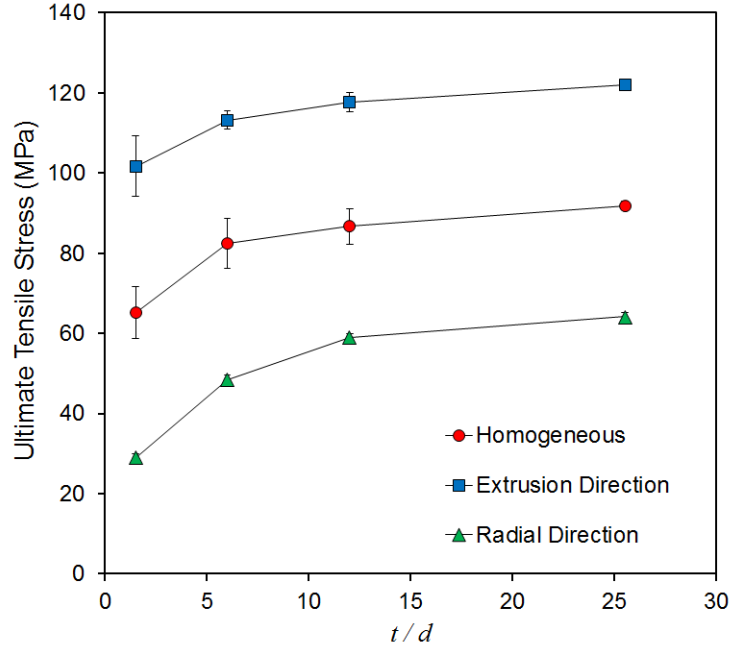
### 5.4.2. Results

Fig. 5.16 shows a set of representative stress-strain curves for the magnesium struts. A number of unusual features can be identified in these curves relative to those of the FCC crystals, shown in Fig. 5.6b. When the textured radial-aligned struts are loaded in tension they have a very low Yield Strength, hardening and UTS. However they have a relatively high  $\epsilon_u$ . With increasing number of grains through the thickness there is a marked increase in hardening rate and a corresponding decrease in  $\epsilon_u$ . The struts with no texture have a higher Yield Strength and UTS than the textured radial-aligned struts. Increasing the number of grains through the thickness leads to an increase in UTS and little change in  $\epsilon_u$  for these struts. Finally, the textured extrusion-aligned struts loaded in tension have the highest Yield Strength and UTS. As per the non-textured struts there is an increase in UTS and little change in  $\epsilon_u$  with increasing  $\frac{t}{d}$  ratio. Fig. 5.17 shows the change in UTS with increasing  $\frac{t}{d}$  ratio for all struts tested in tension.

Fig. 5.18 shows predicted changes in  $\epsilon_u$  for textured and non-textured struts loaded in uniaxial tension. The non-textured struts and textured extrusion-aligned struts loaded in tension exhibit an expected dependence of  $\epsilon_u$  on  $\frac{t}{d}$ . Little or no change in  $\epsilon_u$  for increasing  $\frac{t}{d}$  ratio is predicted for these struts, which is in agreement with the predictions of Eqn. 5.2. A more unexpected behaviour is predicted for the textured radial-aligned struts loaded in tension. In this case, struts with very few grains (1.5) through their dimensions have a relatively high  $\epsilon_u$ . The  $\epsilon_u$  quickly reduces as the  $\frac{t}{d}$  ratio is increased to 6.0, and then increases again with an increase in  $\frac{t}{d}$  ratio to 12.0. As shown in Fig. 5.16, the high  $\epsilon_u$



**Figure 5.16.:** Predicted engineering stress-strain curves for magnesium struts with different  $\frac{t}{d}$  ratios and with and without texture. Textured struts are aligned with the radial and extrusion directions, as depicted in Figs. 5.15c and 5.15d.



**Figure 5.17.:** Predicted changes in UTS with increasing  $\frac{t}{d}$  ratio for struts with and without texture in uniaxial tension. Textured struts are aligned with the radial and extrusion directions, as depicted in Figs. 5.15c and 5.15d.

value for the struts with a  $\frac{t}{d}$  ratio of 1.5 is associated with a very low rate of hardening.

As shown in Fig. 5.19, by the point UTS is reached, these struts have undergone a significant degree of necking, which is not evident in struts with more grains through their thickness at UTS. The difference between the point of UTS and the onset of necking may explain the high  $\epsilon_u$  in these struts relative to the others.

Figs. 5.20a and 5.20b show a selection of moment-curvature curves for textured and non-textured struts. For the textured microstructure there is a significant difference in the moment-curvature curves depending on the lalignment direction, with a lower moment supported by the struts aligned in the radial direction. In most cases the non-textured struts undergo a greater degree of curvature change before the maximum moment is reached.

In order to compare maximum supported moments across struts with different

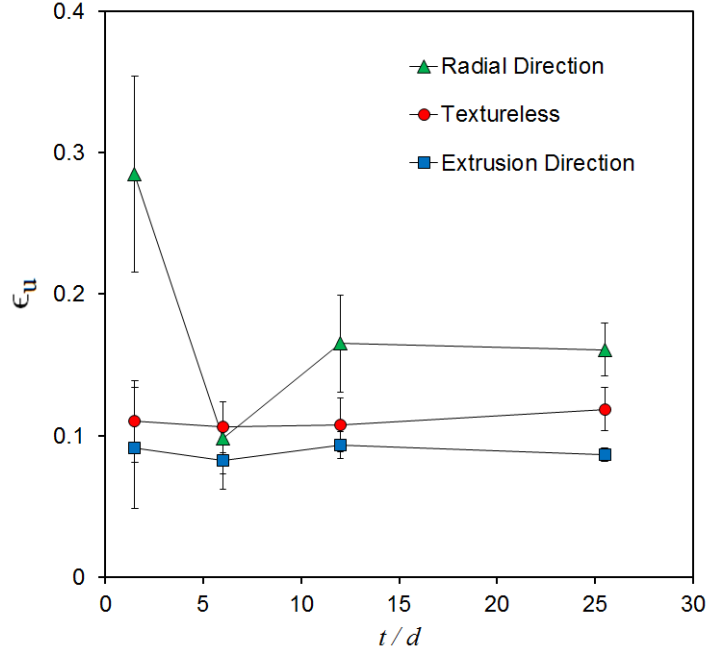


**Figure 5.18.:** Predicted changes in  $\epsilon_u$  with increasing  $\frac{t}{d}$  ratio for textured and non-textured struts in uniaxial tension. Textured struts are aligned with the radial and extrusion directions, as depicted in Figs. 5.15c and 5.15d.

thicknesses in bending, a bending stress is introduced according to the classical definition:

$$\sigma_b = \frac{6M}{t^2} \quad (5.11)$$

where  $M$  is the applied moment on the strut. Maximum bending stresses are shown for textured and non-textured struts with increasing  $\frac{t}{d}$  ratio in Fig. 5.21. The overall behaviour is similar to that of the struts loaded in uniaxial tension, namely highest stresses in the struts aligned with the extrusion direction and lowest stresses in those aligned with the radial direction. The modest increase in maximum stress with increasing  $\frac{t}{d}$  ratio is also similar to that predicted in tension.

Fig. 5.22 shows predicted  $\epsilon_s$  in struts in bending with increasing  $\frac{t}{d}$  ratio. For the textured struts there is little change in maximum surface strain with increasing  $\frac{t}{d}$  ratio. The surface strain in the non-textured struts is greater than that of the textured struts, but also has a greater degree of scatter. There is no significant

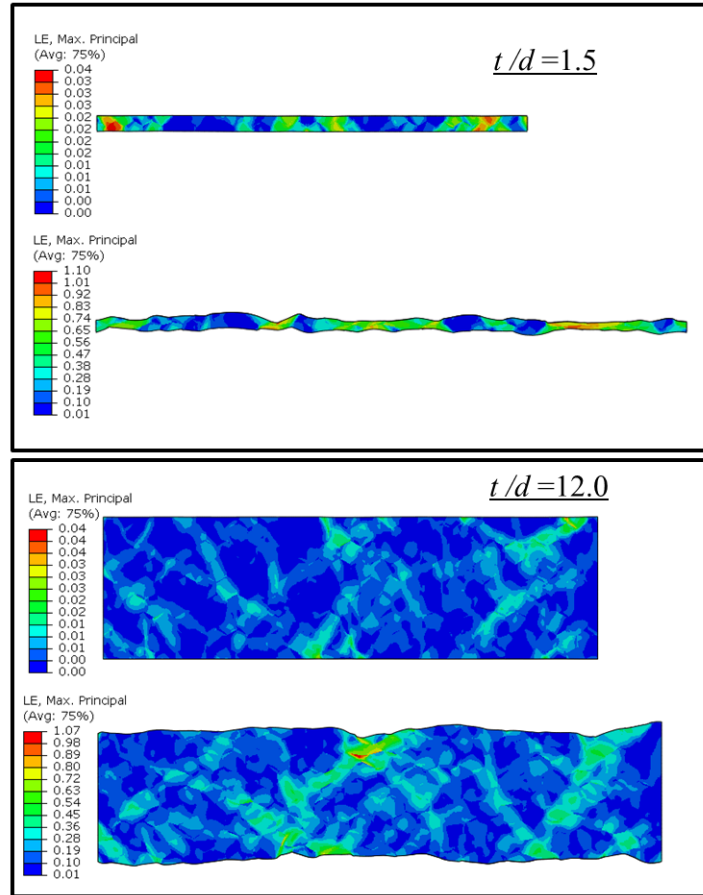


**Figure 5.19.:** Plot of maximum principal logarithmic strain in textured struts aligned with the radial direction at the onset of plastic slip and at UTS. The strut with a  $\frac{t}{d}$  ratio of 1.5 has undergone a significant degree of necking prior to UTS.

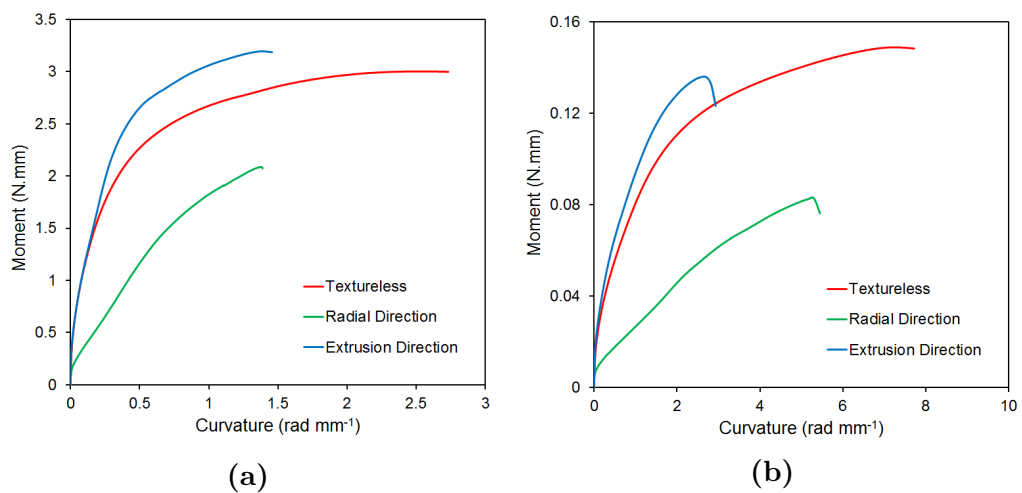


**Figure 5.20.:** A selection of predicted moment-curvature curves for textured and non-textured struts with (a) 6.0 and (b) 25.5 grains through the thickness. Textured struts are aligned with the radial and extrusion directions, as depicted in Figs. 5.15c and 5.15d.

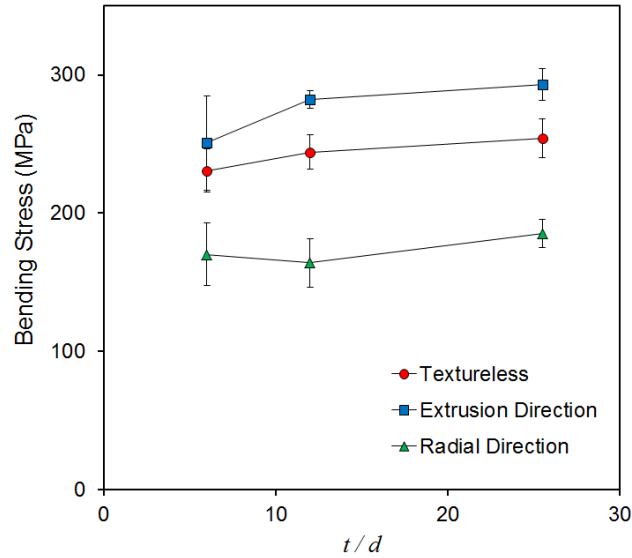


**Figure 5.21.:** Predicted changes in maximum bending stress with increasing  $\frac{t}{d}$  ratio for textured and non-textured struts in bending. Textured struts are aligned with the radial and extrusion directions, as depicted in Figs. 5.15c and 5.15d.

change in maximum surface strain predicted when  $\frac{t}{d}$  ratios increase from 6.0 to 25.5.

### 5.4.3. Discussion

The general outcome of this study on SSE's in magnesium struts is that in most circumstances increasing the number of grains through the strut thickness has relatively little influence on ductility and leads to modest increases in UTS. These findings are largely expected based on the predictions of the FCC models, which have shown that the extent of SSE's is largely governed by the ductility of the metal in question. Given that magnesium has a low ductility relative to 316L and L605, it is reasonable that SSE's have little influence.

Including the effects of texture in the analysis has produced a number of interesting findings. An unusual behaviour is predicted for textured struts aligned in the

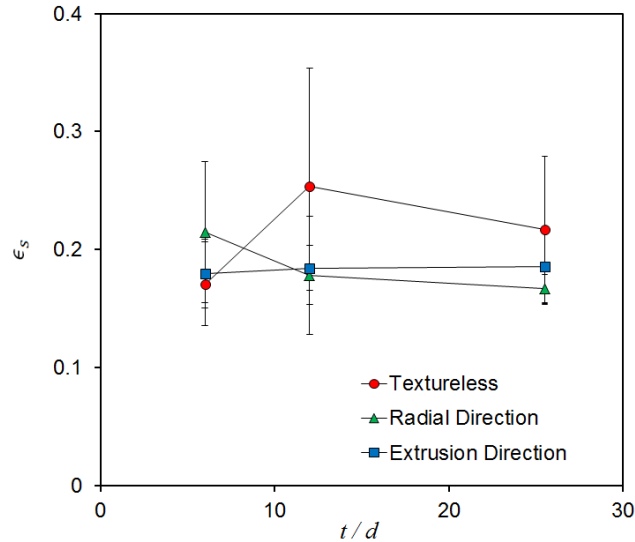


**Figure 5.22.:** Predicted changes in maximum surface strain with increasing  $\frac{t}{d}$  ratio for textured and non-textured struts in bending. Textured struts are aligned with the radial and extrusion directions, as depicted in Figs. 5.15c and 5.15d.

radial direction. With very few grains through the strut thickness, the struts can withstand a significant degree of necking before UTS. However, as the number of grains through the strut is increased, the  $\epsilon_u$  quickly decreases and then eventually increases again towards ‘bulk’ behaviour. This unusual behaviour warrants further study, given that it occurs over a range of  $\frac{t}{d}$  ratios that may be utilized in a stent.

In bending, texture appears to play an important role in deciding strut performance. The moments supported by struts aligned along the radial direction in bending are predicted to be significantly lower than those aligned along the extrusion direction or non-textured struts. This may have implications for magnesium stents, given that achieving adequate device radial stiffness and strength is a challenge in their design.

## 5.5. Accounting for Statistical Size Effects in Stent Design

An in depth investigation of SSE's in FCC and HCP materials has been performed in this chapter. It is now of interest to investigate how the predictions of these microscale simulations can be used in stent design and how they can add to the predictions of stent fracture risk from macroscale simulations in Ch. 4.

One useful approach for applying the results of this chapter is through the use of a *safe design chart* [80]. A *safe design chart* operates in a similar manner to a Goodman diagram. Tensile strains in a component are plotted on one axis and bending strains on another, as shown in Fig. 5.23a. The strain state in a component, such as a stent hinge, under mixed loading will correspond to a point in the tensile-bending strain-space. Based on the microscale tensile-test simulations in this chapter a point on the tensile strain axis can be identified that corresponds to the  $\epsilon_u$  of struts loaded in tension. Similarly, a point on the bending strain axis can be identified that corresponds to the  $\epsilon_s$  of the same strut in bending. A straight line can be constructed between these two points. Analogously to a Goodman diagram, any point beneath this line corresponds to a *safe* region of the strain-space, while any point above the line corresponds to an *un-safe* region.

Based on the results of this chapter, the *safe design chart* can be populated with data for struts consisting of different materials, such as 316L and Mg, and with different  $\frac{t}{d}$  and  $\frac{l}{d}$  ratios. This makes the design chart a powerful tool, as it can be used to assess *safe* performance for struts consisting of range of different materials, with different grain sizes, without the need to use involved microscale modelling. As an example, Fig. 5.23b shows a *safe design chart* for 316L and Mg

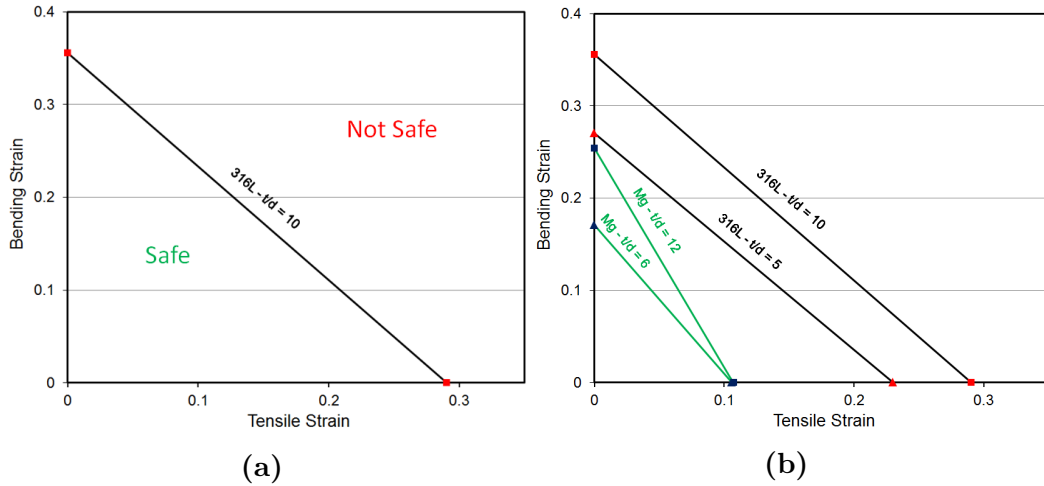


**Figure 5.23.:** (a) A *safe design chart* for a 316L strut with  $\frac{t}{d}$  ratio of 10. The strain-space is divided into *safe* and *un-safe* regions. (b) A *safe design chart* for 316L and Mg struts with different  $\frac{t}{d}$  ratios.

with two different  $\frac{t}{d}$  ratios, based on interpolated data from Figs. 5.6c, 5.10b, 5.18 and 5.22 (for textureless microstructures). It is immediately apparent that the *safe* region in the strain-space is considerably smaller for Mg than 316L, which is expected given its lower bulk ductility. However, it is also of interest to note that, in fact, the *safe* region for struts in bending dominated loading is quite similar for Mg and 316L. This is in stark contrast to the considerably lower  $\eta_c$  for Mg established in the macroscale simulations of Ch. 4, and reflects the loss in ductility in 316L struts due to SSE's in bending.

In addition to gaining insights into the relative behaviour of different materials, it is possible to use the design chart to combine the results of macroscale and microscale simulations. Considering the results of a macroscale simulation, for example that of Fig. 5.24, which is based on the stent deployment procedure described in Ch. 4, it is possible to identify critical regions on the stent where there may be a risk of failure. At these points measures of tensile strain and bending strain for the strut or hinge as a whole can be identified. Taking the approach of Harewood *et al.* [175], the tensile strain in the hinge can be found by determining the length of a midline along the hinge, calculating the change in length of the line as a result of stent deformation and dividing by the original

## 5. Microscale Mechanics of Permanent and Absorbable Metal Stents

hinge length. Similarly, bending strain can be found by identifying the change in angle subtended by the ends of the hinge during deformation and applying Eqns. 5.5 and 5.6, along with a knowledge of the hinge length, to find the resulting surface (bending) strain. Once these points in the strain-space are identified for critical regions of the hinge they can be used to assess, based on microscale predictions, the proximity of the point to the *safe* region of the design space (which could be taken as an alternate  $\eta_\epsilon$  to that used in Ch. 4).

To illustrate the above method, as a purely hypothetical example, considering Fig. 5.24 three arbitrary points (A, B, C) are identified in the strain-space. It is assumed, purely for the sake of illustration, that these three points correspond to the strain states in three regions in the deformed stent in Fig. 5.24. Point A corresponds to a region on the strain-space with high tensile and bending strains and is deemed to be *un-safe* for all materials. Point B corresponds to a region that is deemed *safe* for 316L stents, but *un-safe* for Mg stents and point C corresponds to a region, with predominantly bending loading, that is *safe* for all stents.

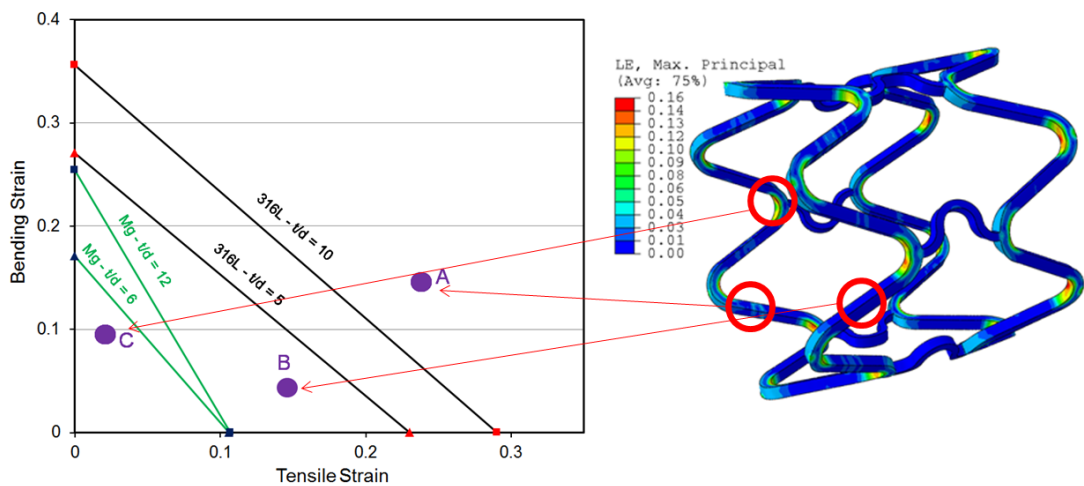


**Figure 5.24.:** Tensile and bending strains are determined at critical locations on the stent, determined by macroscale simulations. Failure risks can be determined by assessing the distance between these points and the *safe-un-safe* division on the *safe design chart*.

It is important to interpret predictions based on the use of the design chart in

a practical context. The *un-safe* region of the chart should most realistically be considered as an indication of potential failure risk, thereby allowing different designs to be compared in terms of relative failure risk. The design chart can be considered as an additional design aid, as part of the overall stent design process. In this sense, its use can be considered to be complimentary to other performance assessment methodologies, including standard macroscale FE simulations and, for example, comparisons of peak stresses with UTS, as per Ch. 4. In terms of specific usage possibilities, the design charts can be used to point the direction of design, for example toward reductions in tensile straining and toward bending, based on the example in Fig. 5.24. Moreover, given that it provides a quantitative comparator of fracture risk, the design chart can be used to drive optimization algorithms (discussed further in Ch. 7) toward the identification of optimal strut dimensions and grain sizes for different stents and different regions in the stent.

Further use and description of the *safe design chart* in stent design can be found in Harewood and McHugh [80] and Harewood *et al.* [175]. This includes the use of the *safe design chart* for assessing stent failure risks under significant device deformations undergone during bifurcation stenting treatments [175] and a demonstration of the conservative nature of failure risk predictions when the design chart is used for mixed tensile and bending loading of stent struts and hinges [80].

### 5.6. Study Limitations

This study focuses on 2-D microstructures, essentially with columnar grains extruded through the strut width  $w$ . However, the microstructure of coronary stent struts typically consists of equiaxed austenitic grains. It is likely that the use of

## 5. Microscale Mechanics of Permanent and Absorbable Metal Stents

a 2-D rather than 3-D representation of the stent strut microstructure, for the same single crystal elastic and plastic properties, will lead to differences in predicted  $\epsilon_u$  and UTS values due to: i) additional constraints on the deformation of grains arising from the use of generalized plane strain conditions and ii) the presence of fewer grains through  $w$  in 2-D simulations. An insight into the extent of such differences for a fixed grain size and one value of  $w$  can be found in McGarry *et al.* [167]. 2-D simulations were found to over-estimate UTS by 3.4% relative to 3-D simulations and underestimate  $\epsilon_u$  by 11.2% (in relative terms). 2-D simulations were also reported to undergo earlier shear-band formation and have greater dependence on crystallographic orientation.

Thus, for a given strut thickness the 2-D simulations of this study may over-estimate UTS values and under-estimate  $\epsilon_u$  relative to an equivalent 3-D simulation, that uses the same single crystal elastic and plastic properties. Notwithstanding differences due to additional constraints, 2-D simulations may also over-estimate the role of  $\frac{t}{d}$  ratio effects relative to 3-D simulations, as the total number of grains in the cross-section, and not just the thickness, will be important in the latter. However, such differences, if present, in  $\epsilon_u$  and the extent of SSE's are likely to decrease as the total number of grains through  $w$  in the 3-D simulations approaches one, which is the number inherently assumed by 2-D simulations. Based on the assumption that the total number of grains in the cross-section,  $\frac{d^2}{tw}$ , controls the extent of SSE's in 3-D, insights into any discrepancies that may be present between 2-D and 3-D predictions for different  $\frac{d}{w}$  ratios could be gained from Eqn. 5.2, by replacing the  $\frac{d}{t}$  term in the exponent with  $\frac{d^2}{tw}$  for the 3-D case.

This study focuses on 'first-order' [51] size effects in polycrystalline struts and does not account for higher order size effects resulting from changing absolute grain or specimen sizes, nor does it account for free surface effects. These effects can often play a significant role in determining the mechanical behaviour of com-

## 5. *Microscale Mechanics of Permanent and Absorbable Metal Stents*

ponents, which may exceed or act in synergy with the SSE's [51]. Accounting for such effects would require the use of a strain gradient based crystal plasticity models [89], which would be a very useful addition to what is presented in this work.

A detailed investigation into necking and post-UTS behaviours of the struts simulated in this study, such as that of Ghosh [179], is not presented here. However, such studies have been carried out in McGarry *et al.* [167] and Wang *et al.* [84], based on similar 2-D and 3-D crystal plasticity models. A more detailed investigation into the influence of SSE's on strut necking behaviour would be beneficial, and in particular would facilitate the implementation of explicit material failure models, such as the void growth model of Rice and Tracey [180]. This would be of particular relevance in the vicinity of precipitates [181].

Simulations of textured magnesium focused on loading of struts aligned in the radial and extrusion directions, based on the confirmed predictive capability of the adopted modelling framework for loading in these directions [50]. Although the tensile and bending loading simulations of struts aligned in the extrusion direction capture some of the more likely loading scenarios for stent hinges, it would also be useful to also consider loading of struts aligned with the tubing circumferential direction.

This study focuses on strut deformations associated with stent expansion and does not consider cyclic loading or fatigue. As was discussed in Ch. 2, failure risks during expansion may be of greater importance in next generation stents than the current generation, due to the use of thinner struts (resulting in a greater influence of SSE's) and lower ductility bioabsorbable alloys. Although the typical industrial practice for evaluating fracture risk in fatigue is based on macroscale simulations and the use of Goodman diagrams, recent studies by Sweeney *et*

*al.* [182, 183], which use a crystal plasticity based microscale simulation framework quite similar to that developed in this chapter, have developed a method to predict microstructure-sensitive fatigue failure of microscale components, including stent struts.

The work in the remainder of this thesis focuses primarily on the corrosion of bioabsorbable alloy stents. Although the ‘long-term’ performance of these stents is considered in subsequent simulations, failure risk due to fatigue loading is not assessed. The justification for this is that the life-time of bioabsorbable magnesium stents (2-6 months) is significantly shorter than the typical service life recommended for fatigue testing by the FDA ( $> 10$  years) [15] and that it is possible that the effects of corrosion on the integrity of the device structure may be of greater relevance than the effects of fatigue loading.

## 5.7. Conclusions

In this chapter, the influence of SSE’s on the mechanical behaviour of coronary stent struts in bending and tension is assessed through a comprehensive set of FE simulations based on single crystal plasticity theory. A range of strut thickness  $t$  and strut length  $l$  to grain diameter  $d$  ratios ( $\frac{t}{d}$  and  $\frac{l}{d}$ ) are considered for a range of materials. The primary findings of this study are as follows:

- As regards the effects of  $\frac{l}{d}$  ratio, in tension, increasing the  $\frac{l}{d}$  ratio is predicted to lead to a reduction in strain at UTS according to a power-law behaviour. Based on the predictions of this study it is recommended that computational and experimental studies use a minimum  $\frac{l}{d}$  ratio of 40 in tension and 100 in bending to negate  $\frac{l}{d}$  ratio effects in studies on size effects

## 5. *Microscale Mechanics of Permanent and Absorbable Metal Stents*

in struts with few grains through their thickness.

- For  $\frac{t}{d}$  and  $\frac{l}{d}$  ratios below 10.0 and 40.0 respectively in tension and 10.0 and 100.0 in bending it is important to establish the individual contributions of  $\frac{t}{d}$  and  $\frac{l}{d}$  ratios to the overall SSE. This is achieved in this study through the development of a simple power-law model in this study. Knowledge of these individual contributions is very useful in analysing stent components where both  $\frac{t}{d}$  and  $\frac{l}{d}$  ratios are usually quite low.
- The strain at UTS in tension for struts of a given  $\frac{t}{d}$  and  $\frac{l}{d}$  ratio is predicted to scale linearly with bulk strain at UTS. This finding makes the results of this study applicable to the study of SSE's in many FCC metals.
- L605 and 316L are predicted to be subject to similar size effects in tension, despite the higher UTS of L605. This finding is of interest in modern thin-strut stent design, and suggests that size effects are a concern in L605 stent design and development. For magnesium there is no significant increase in predicted strain at UTS with increasing  $\frac{t}{d}$  ratio.
- It is predicted that for FCC crystals in bending, increasing  $\frac{l}{d}$  ratios and reducing  $\frac{t}{d}$  ratios reduce maximum surface strain. Through the use of the measure 'surface strain' it is possible to compare the extents of geometric effects and SSE's for struts in bending. This makes the results of this study very useful in determining the trade-off in performance in bending between reducing absolute strut thickness and  $\frac{t}{d}$  ratio. For magnesium little change in maximum surface strain in bending is predicted with increasing  $\frac{t}{d}$  ratio.
- Precipitates and microstructure regularity have little influence on predicted size effects. This result is of significant interest for future modelling studies,

## 5. *Microscale Mechanics of Permanent and Absorbable Metal Stents*

as it facilitates the use of more easily constructed microstructure geometries.

- Predictions of this study can be used with frameworks previously established in Harewood and McHugh [80] to predict failure risks in a range of stent geometries, consisting of different materials and microstructures, subject to combined tensile and loading conditions.
- Texture is predicted to play an important role in dictating the mechanics of magnesium struts, with significant changes in moments supported by struts in bending possible, depending on their orientation in the extruded stent tubing. The modelling presented here is the first to investigate the effects of texture on magnesium stent performance.

# **6. A Phenomenological Corrosion Model for Magnesium Stents**

## **6.1. Chapter Summary**

In Ch. 2 it was noted that few studies on the effects of corrosion on the mechanical performance of AMS's have been performed. In this chapter the first experimentally validated model to predict the effects of corrosion on the mechanical integrity of magnesium alloy foils is developed. Immersion tests are first performed on foils to assess the effects of corrosion on foil integrity. A corrosion model is then developed and its predictions are validated with respect to the results of further immersion experiments. The corrosion model is applied in predicting the effect of corrosion on the mechanical performance of an AMS in the body. The outcomes of this chapter are an improved understanding of the effects of corrosion on thin bioabsorbable foils, a new method to model the corrosion of AMS's in the body and design recommendations for future bioabsorbable alloys.

## 6.2. Introduction

In order to characterise the behaviour of a bioabsorbable device in the body, and in particular coronary stents, it is important to consider not only the form and rate of corrosion observed, but also the effect that this corrosion process has on overall device mechanical integrity. It is noted that relatively few studies have been performed to this end for bioabsorbable metals *in-vitro*, with the study of Zhang *et al.* [184] on the reduction in bending strength of bioabsorbable alloy specimens following corrosion being the most applicable to date. Further to this, while a number of studies, such as that of Bobby Kannan *et al.* [109], have investigated the effects of mechanical loading on specimen corrosion behaviour, such studies have focused on corrosion behaviour in specimens with dimensions at least an order of magnitude larger than those of coronary stent struts.

The first objective of this chapter is the determination of the effects of corrosion on the mechanical integrity of bioabsorbable foil specimens in simulated physiological solution. Since the thickness of the foil samples is of the same order of magnitude as that of the struts used in AMS's, it is believed that such an approach may give a more appropriate indication of the effects of corrosion on AMS scaffolding support than that given in previous studies on larger samples. The second objective of this chapter is the determination of the effects of mechanical loading on the corrosion behaviour of the bioabsorbable alloy foil specimens. Again, it is believed that such an approach can give a more appropriate indication of the effects of mechanical loading on the corrosion behaviour of AMS's than tests on larger size samples.

In addition to experimental alloy characterisation, computational modelling of the corrosion process can give important insights into the fundamental corrosion mechanisms that lead to the gradual breaking down of an AMS in the body. Also,

such models can prove useful in the design of AMS's, through device assessment simulations and the optimization of device geometries for improved duration of structural integrity as corrosion progresses. Since the development of AMS's is a relatively new field, there are few computational approaches specifically developed for modelling the effects of corrosion and resulting reduction in mechanical integrity of the devices.

Hence, the third objective is the development of a phenomenological corrosion model that is detailed enough to give a better understanding of the corrosion behaviour of an AMS in the body, yet simple enough to allow the model to be calibrated through readily performed experiments and implemented for use with a commercial FE code. The approach taken is built on recent work by Gastaldi *et al.* [128], who developed what is to-date the only direct application of a corrosion model in a stent assessment application. In Gastaldi *et al.* [128] the effects of corrosion on device mechanical integrity are represented through the evolution of a continuum damage parameter, allowing an assessment of overall stent damage as corrosion proceeds. While adopting this continuum damage parameter approach, this work focuses on the development and calibration of a corrosion damage model which has the added ability to capture the effects of heterogeneous corrosion behaviour on AMS scaffolding support over time.

### 6.3. Methods

#### 6.3.1. Alloy Characterisation

The corrosion behaviour of a bioabsorbable magnesium alloy (AZ31) was determined in a solution of modified Hank's balanced salts (H1387, Sigma-Aldrich,

## 6. A Phenomenological Corrosion Model for Magnesium Stents

USA). The AZ31 alloy was sourced in the form of 0.23 mm thick foil (Goodfellow, UK) from which test specimens of length 50.0 mm and width 4.65 mm were cut, as shown schematically in Fig. 6.1a. A 20.0 mm long test region was created at the centre of each specimen by reducing the foil thickness to 0.21 mm in this region, as shown in Fig. 6.1b. This was accomplished by mechanical polishing with 600-grit emery paper, resulting in a final average surface roughness of 0.2  $\mu\text{m}$  as measured using a profilometer (Surftest 211, Mitutoyo, USA). Prior to testing, samples were cleaned in anhydrous ethanol and left to dry for a period of 24 hours, allowing for a consistent oxidisation of all polished sample surfaces. Regions of the sample outside the test section were covered in a layer of petroleum jelly to restrict corrosion attack to the region of interest. For corrosion testing, specimens were immersed in the solution of modified Hank's balanced salts, with solution temperature maintained at 37 °C by means of a thermostatically controlled water-bath. The solution volume (ml) to surface area ( $\text{cm}^2$ ) ratio was maintained between 25:1 and 50:1 in all tests, with this range being deemed appropriate based on the work of Yang *et al.* [185], who showed that increasing the volume to area ratio beyond 6.7 had little influence on the corrosion behaviour of a similar bioabsorbable magnesium alloy in Hank's solution.

In order to comprehensively characterise the corrosion behaviour of the bioabsorbable alloy, three independent experiments were performed, as listed in Table 6.1. The first experiment, A, was used to determine the corrosion rate and primary corrosion process for a bioabsorbable alloy in simulated physiological fluid. In order to determine the alloy corrosion rate, five specimens were immersed in solution for a period of 72 hours. The volume of hydrogen gas evolved from each specimen was measured using the apparatus shown in Fig. 6.2a. Specimens were fixed in such a way that all four surfaces in the test region were exposed to solution. The alloy corrosion rate was inferred from the volume of evolved hydrogen gas, based on the chemical balance for the conversion of magnesium to corro-

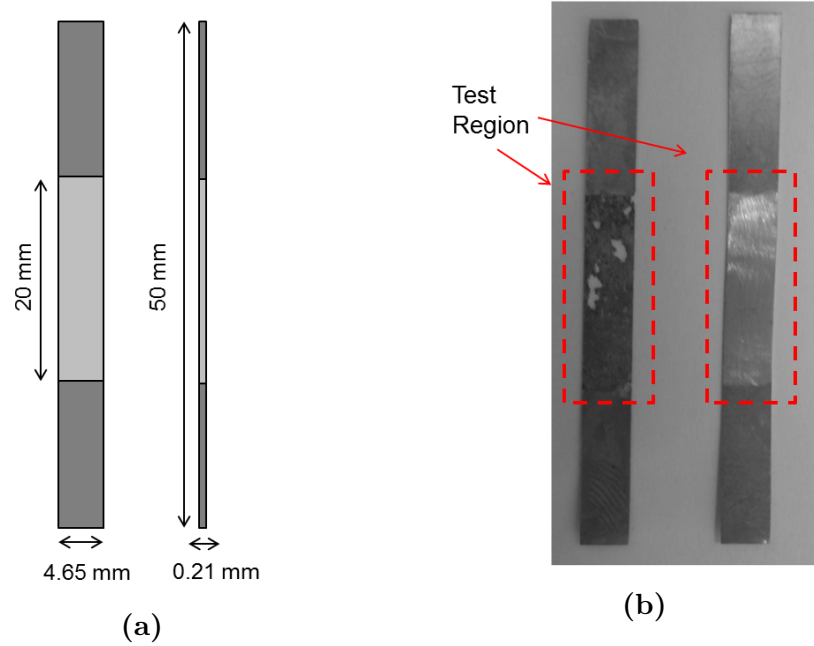


**Figure 6.1.:** (a) The AZ31 alloy foil specimen geometry used in Experiments A, B and C. (b) The polished test region in a corroded (left) and non-corroded (right) foil specimen.

sion product, using an approach described in Song *et al.* [91], which has shown good agreement with direct weight measurements [97] and has the advantage that corrosion rate can be determined without having to remove corrosion specimens from solution. In order to determine the primary form of corrosion, three further specimens were immersed in solution and removed at 3, 12 and 40 hours respectively. Specimens were cleaned in a solution of chromic acid for five minutes at 60 °C to remove corrosion products and the corrosion surfaces were viewed under SEM (S-4700, Hitachi, Japan). Samples subject to the cleaning process for a shorter period of time (partially cleaned) were also viewed under SEM, allowing the identification of precipitates in the corroded alloy micro-structure and the determination of their composition by energy-dispersive x-ray spectroscopy (EDX).

The second experiment, B, was used to determine the effects of corrosion on the mechanical integrity of the foil specimens. This was done by immersing 26 specimens in solution over a period of 90 hours. Specimens were removed at

**Table 6.1.:** List of experimental tests performed in this work.

Experiment	Description	No. of Samples	Results	Application
A	Determine specimen corrosion rate	5	Fig. 6.6	Model calibration
B	Determine effect of corrosion on specimen mechanical integrity	26	Fig. 6.9	Model calibration
C	Determine effect of mechanical loading on corrosion process	10	Fig. 6.10	Model validation

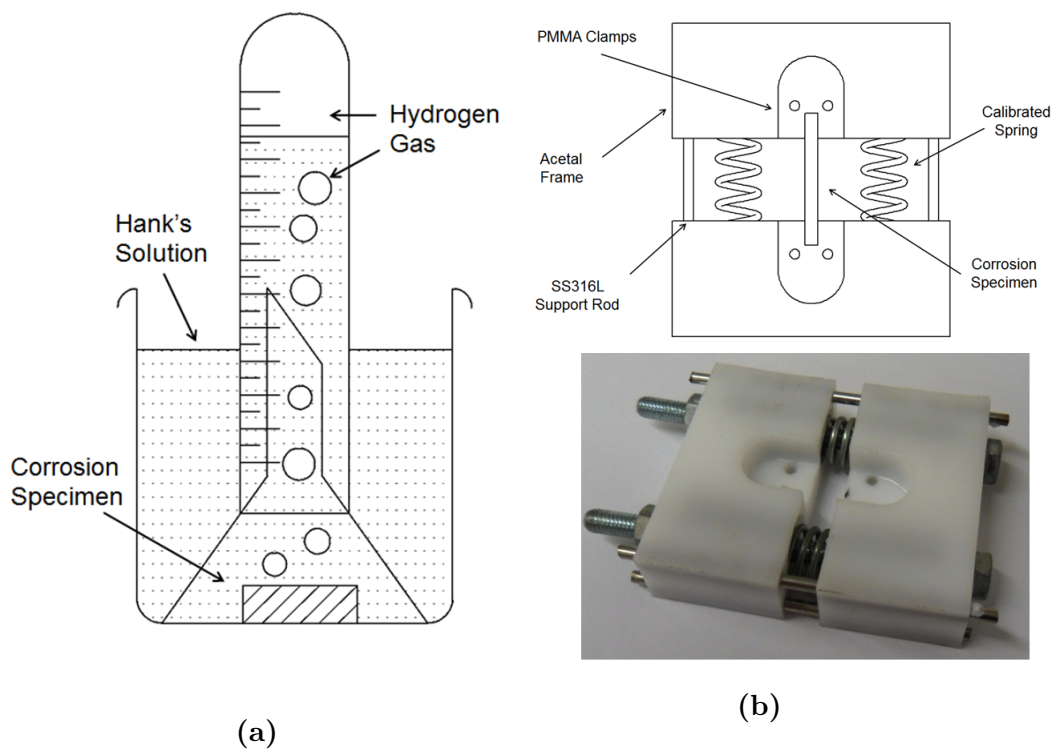


**Figure 6.2.:** (a) The hydrogen evolution apparatus used in Experiment A. (b) The constant load test rig used in Experiment B.

## 6. *A Phenomenological Corrosion Model for Magnesium Stents*

regular intervals, cleaned in a solution of chromic acid and weighed using a mass balance with a resolution of 0.1 mg. Specimens were then tested in uniaxial tension to fracture using a universal tensile tester (BZ 2.5 Zwick, UK) using a constant crosshead speed of  $0.005 \text{ mm s}^{-1}$ , with the polished test region taken as the gauge region. Due to the small size of the samples, tensile strains were measured using a non-contact video extensometer system (Messphysik GmbH, Germany). The maximum tensile load supported by the specimen was taken as a measure of mechanical integrity.

The final experiment, C, was used to determine the influence of tensile load on the corrosion behaviour of 10 specimens in solution. A near constant tensile load was applied to the specimens in solution by means of a custom built rig, shown in Fig. 6.2b. Two calibrated ( $2.73 \text{ N mm}^{-1}$ ) compression springs were used to apply the load to the samples by compressing them to a set length. This was done by tightening bolts that passed through their inner diameter, clamping the specimen in position and then loosening the bolts, allowing the sample to take the full load from the springs. Polymers were chosen for the frame and clamps to reduce the risk of galvanic corrosion, while stainless steel support rods were used to ensure that specimens were loaded purely in uniaxial tension. The time to fracture for each of ten samples subject to increasing uniaxial tensile stresses was determined using an electronic timing circuit attached to the test rig. The reduction in applied load due to gradual specimen elongation in solution was deemed to be less than 1.1 N (1.8 % of the lowest applied load), based on a maximum observed specimen elongation of 0.2 mm before fracture when measured using a LVDT (DC-EC, Schaevitz, USA) attached to the top of the test-rig.

### 6.3.2. Corrosion Model Development

A corrosion model has been developed for application in the Abaqus code (DS SIMULIA, USA), based on continuum damage theory [186]. The use of continuum damage theory allows the effects of corrosion induced microscale geometric discontinuities on overall specimen mechanical integrity to be accounted for, without explicitly modelling their progression. This is accomplished through the introduction of a scalar damage parameter  $D$  and an effective stress  $\bar{\sigma}_{ij}$ , as described in Lemaitre and Desmorat [187]. Briefly, the effective stress is given by:

$$\bar{\sigma}_{ij} = \frac{\sigma_{ij}}{1 - D} \quad (6.1)$$

In this work, the damage model is implemented in Abaqus/Explicit through the development of a user material subroutine (VUMAT). The temporal evolution of damage is considered on an element by element basis within the model. Considering the FE mesh shown in Fig. 6.3, corrosion is assumed to only take place for elements on external or exposed surfaces. The assumed evolution of the corrosion damage parameter for these surface elements is based on that given in Gastaldi *et al.* [128] for the case of perfectly uniform or homogeneous corrosion as:

$$\frac{dD_e}{dt} = \frac{\delta_U}{L_e} k_U \quad (6.2)$$

where  $k_U$  is a corrosion kinetic parameter of unit  $\text{h}^{-1}$  and  $\delta_U$  and  $L_e$  are respective material and FE model characteristic lengths of unit mm, as described in Gastaldi *et al.* [128]. In this study the material characteristic length is given a value of 0.017 mm, consistent with observed grain sizes for AZ31 alloy in the literature [96].

The damage evolution law in Eqn. 6.2 is enhanced in this work through the introduction of an element-specific dimensionless pitting parameter,  $\lambda_e$ . This

## 6. A Phenomenological Corrosion Model for Magnesium Stents

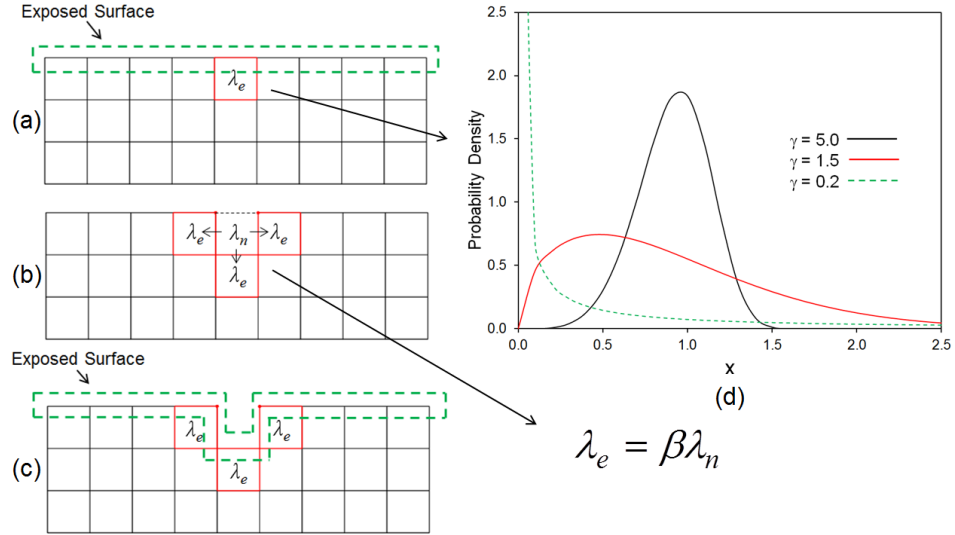


**Figure 6.3.:** (a) A sample FE mesh showing the elements along the exposed surface. Each exposed element is assigned a random value of  $\lambda_e$  from a Weibull distribution random number generator. (b) When an element is fully corroded it is removed from the FE mesh, neighbouring elements inherit its  $\lambda_e$  value. (c) The exposed corrosion surface is updated within the VUMAT subroutine. (d) The PDF for a standard Weibull distribution. Increasing  $\gamma$  leads to a more symmetric PDF and a more homogeneous corrosion.

parameter is used to introduce the capability of capturing the effects of heterogeneous or pitting corrosion to the modelling framework, through the following damage evolution law:

$$\frac{dD_e}{dt} = \frac{\delta_U}{L_e} \lambda_e k_U \quad (6.3)$$

Considering the FE mesh in Fig. 6.3, each element on the initial exposed surface is assigned a unique, random  $\lambda_e$  value through the use of a standard Weibull distribution-based random number generator. Hence, the probability of the value of  $\lambda_e$  lying in the range  $[a, b]$  for each element is given by:

$$\Pr[a \leq \lambda_e \leq b] = \int_a^b f(x) dx \quad (6.4)$$

where  $f(x)$  is the standard Weibull distribution probability density function, given as [188]:

$$f(x) = \gamma(x)^{\gamma-1} \exp^{-(x)^\gamma} \quad (6.5)$$

## 6. A Phenomenological Corrosion Model for Magnesium Stents

with the condition that  $x \geq 0$  and  $\gamma > 0$ , where  $\gamma$  is a dimensionless distribution shape factor. The use of such a distribution in describing the degree of heterogeneity of the corrosion process can be best described with reference to its probability density function, shown in Fig. 6.3, where increasing  $\gamma$  values lead to a more symmetric PDF. This in turn corresponds to a narrower range of  $\lambda_e$  values being assigned over the elements, giving a more homogeneous corrosion.

When  $D_e = 1$  in an element, the element is removed from the FE mesh. The corrosion surface is then updated in the VUMAT based on the use of an element connectivity map and a newly developed inter-element communication ability within the VUMAT code, described further in Appendix A.3. When the element is removed from the FE mesh, its neighbouring elements are assumed to inherit the value of its pitting parameter according to:

$$\lambda_e = \beta \lambda_n \tag{6.6}$$

where  $\lambda_n$  is the pitting parameter value in the recently removed element and  $\beta$  is a dimensionless parameter that controls the acceleration of pit growth within the FE analysis.

### 6.3.3. Corrosion Model Calibration and Validation

The corrosion model is calibrated based on the results of Experiments A and B. A representation of the test region in the foil is meshed with 56 000 linear reduced integration brick elements ( $L_e = 70 \mu\text{m}$ ), as shown in Fig. 6.4. In representing the deformation of the material in the FE corrosion model, finite deformation kinematics is assumed. The mechanical properties used are based on those of AZ31 foil samples with 0% mass loss, with representative experimental stress-

strain curves shown in Fig. 6.5.

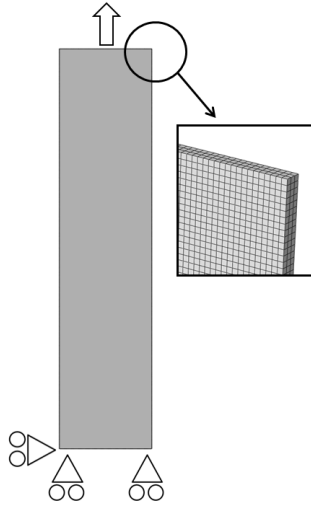


**Figure 6.4.:** Finite element representation of the tests region of the corroding foil samples. The region is loaded in uniaxial tension, with the mesh used shown in the outset.

Elasticity is considered linear and isotropic in terms of finite deformation quantities (Cauchy stress and logarithmic strain), with an experimentally determined Young's Modulus of  $E = 44$  GPa and a Poissons ratio of  $\nu = 0.35$  [189]. Plasticity is described using  $J_2$  flow theory with non-linear isotropic hardening, with a Yield Strength of 138 MPa and UTS of 245 MPa at an engineering strain of 17%. The mechanical properties of damaged elements are controlled through the evolution of the damage parameter  $D$  by reducing the stress returned for a given strain, according to Eqn. 6.1. A failure condition is also employed in which elements are removed if strains exceed those observed experimentally at UTS.

Experiment A is simulated by allowing corrosion to occur on all four exposed surfaces in the test region. The rate of mass loss over time is determined based on the average damage value over all of the model elements. Experiment B is simulated in a subsequent analysis step by simulating tensile loading of the test region. The maximum force withstood by the model is taken as a measure of loss in mechanical integrity and is compared to that observed experimentally.

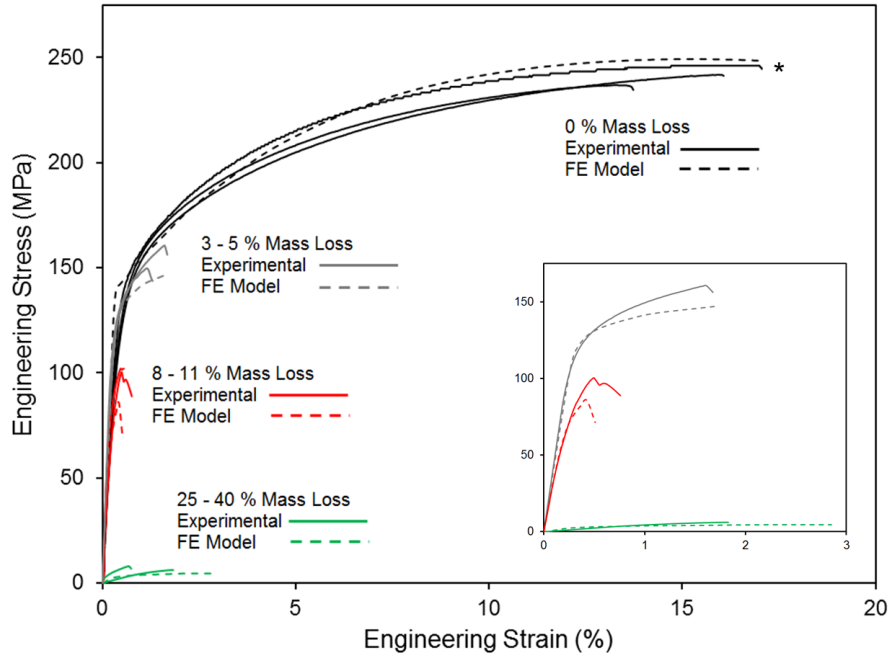


**Figure 6.5.:** Representative engineering stress-strain curves for corroded and non-corroded samples based on the results of Experiment B. FE model stress-strain curve predictions for similar amounts of corrosion induced mass loss are also included. The experimental curve used in describing the undamaged material properties used in the FE model is denoted with \*.

In calibrating the FE corrosion model, the values of the three independent model parameters,  $k_U$ ,  $\gamma$ , and  $\beta$  are determined for a given  $\delta_U$  and  $L_e$ , based on the simulation of Experiments A and B. These values are determined by imposing three conditions. First, the model should capture the experimentally observed reduction in specimen mechanical integrity with corrosion. Also, the predicted mass loss vs. time curve should qualitatively match that observed in Experiment A, shown in Fig. 6.6 to be largely linear. These conditions allow the determination of  $\gamma$  and  $\beta$  through an iterative calibration process. The third condition is that the simulated corrosion rate quantitatively matches that observed in Experiment A, allowing the parameter  $k_U$  to be readily determined for given values of  $\gamma$  and  $\beta$ .

In order to validate the predictive capabilities of the model for the calibrated parameters, Experiment C is simulated. Loading of the sample in uni-axial tension is simulated followed by the subsequent corrosion of the specimen under the

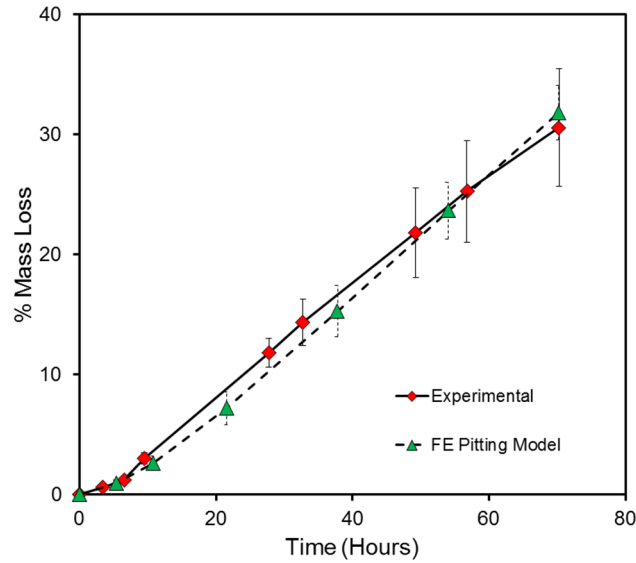


**Figure 6.6.:** Plot of percentage mass lost over time based on FE simulation predictions and the results of Experiment A. Error bars represent a single standard deviation from the mean ( $n = 5$ ).

constant applied load. The time to complete fracture of the specimen, given by the time at which the specimen force becomes 0.0, is then predicted, allowing a comparison with the results of Experiment C.

### 6.3.4. Stent Application

Once calibrated, the corrosion model is applied in predicting the performance of an AMS. A CAD approximation of the Biotronik MAGIC stent is generated based on SEM images in the literature [190]. The stent model geometry, which has a strut width of  $80\ \mu\text{m}$  and a strut thickness  $125\ \mu\text{m}$ , is shown mounted on a delivery system model in Fig. 6.7, with relevant dimensions given in Table 6.2. The geometry is meshed using reduced integration linear brick elements with an average element characteristic length of  $20\ \mu\text{m}$ , arrived at through a mesh convergence study, and which is accounted for in corrosion simulations through appropriate scaling of the corrosion model parameters. Stent material properties are taken to be the same as those used in the foil models, shown in Fig. 6.5.

## 6. A Phenomenological Corrosion Model for Magnesium Stents

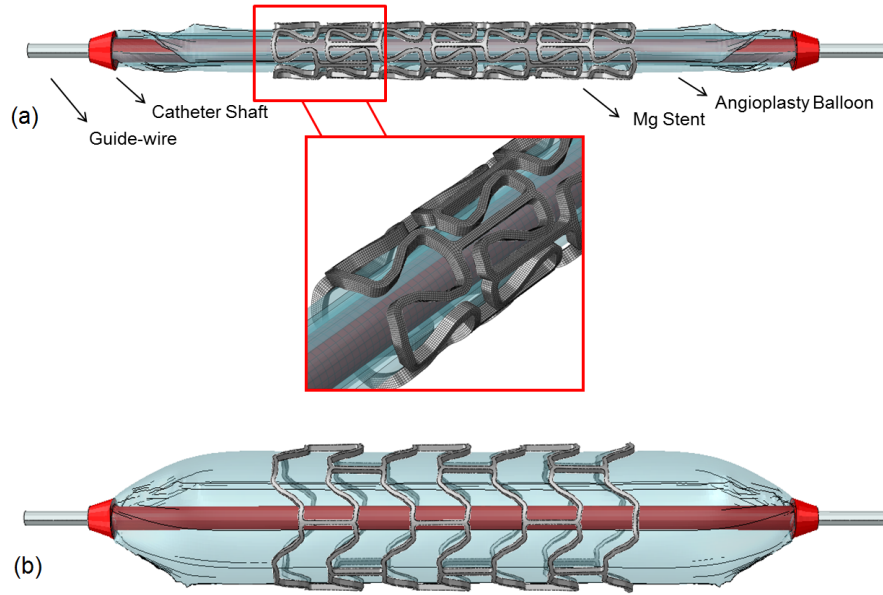


**Figure 6.7.:** The magnesium stent and delivery system FE model geometries (a) before and (b) after deployment. Deployment was carried out in an idealised artery and plaque geometry with a balloon inflation pressure of 20 atm. Model properties are given in Table 6.2.

**Table 6.2.:** Parameters for the stent, artery, plaque and delivery system models used in this work. Diameters before  $\theta_1$  and after  $\theta_2$  deployment are internal diameters for all cylindrical parts, with thickness  $t$  and length  $L$  measures taken before deployment.

Part	$\theta_1$ (mm)	$\theta_2$ (mm)	$t$ (mm)	$L$ (mm)	Material	FE Mesh (Elements)
Stent	1.15	2.76	0.15	8.0	AZ31: Elastic-Plastic, Fig. 6.5	130 000 C3D8R
Balloon	1.06	2.74	0.02	14.3	Nylon: $E = 0.85$ GPa, $\nu = 0.4$	21 000 M3D4R
Shaft	0.5	0.5	-	15.3	HDPE: $E = 1.0$ GPa, $\nu = 0.4$	8300 C3D8R
Wire	0.3	0.3	-	18.07	Nitinol: $E = 62.0$ GPa, $\nu = 0.3$	1800 C3D8R
Artery/ Plaque	1.76	3.01	1.40	18.0	Artery: Hyperelastic, Plaque: Hyperelastic	60 000 C3D8R

## 6. A Phenomenological Corrosion Model for Magnesium Stents

The deployment of the stent is simulated in a three layer artery of inner diameter 2.76 mm, with artery layer thicknesses taken from the work of Holzapfel *et al.* [139]. The artery is modelled using the strain energy density function in Eqn. 3.35, with model parameters taken from work by Gervaso *et al.* [152], based on experimental tissue testing by Holzapfel *et al.* [139]. The use of an isotropic artery material description, rather than a more physically representative anisotropic description, such as that of Holzapfel *et al.* [139], is considered acceptable in the case of this work, as the primary interest is the deformation and loading of the stent itself, rather than artery stresses. An idealised atherosclerotic plaque geometry of thickness 0.5 mm is included and is modelled using the same strain energy density function, with constants taken from work by Gastaldi *et al.* [21], based on experimental plaque testing by Loree *et al.* [191].

A tri-folded balloon geometry is constructed and secured to the delivery system, shown in Fig. 6.7, by means of tie constraints. In simulating stent deployment, the balloon is inflated through the application of a pressure of 20 atm (2.03 MPa) on its inner surface, giving a final stent inner diameter of 2.76 mm and a balloon to artery ratio of 1:1. Recoil is simulated through the removal of this applied pressure. Material properties and relevant dimensions for the balloon and delivery system are given in Table 6.2 and are based on those used in a similar delivery system model developed by Mortier *et al.* [20].

The general contact algorithm in Abaqus/Explicit is utilised for stent-artery contact, with the condition that all stent surfaces, internal and external, were considered to be potentially part of the contact domain. This allows the automatic re-definition of contact faces by the Abaqus solver following element removal (Abaqus Theory Manual, DS SIMULIA, USA) and the continued modelling of the stent-artery interaction as the device corrodes. A frictional coefficient of 0.2 is assumed for all tangential contact behaviour, with ‘hard’ contact defined for

normal contact behaviour.

As was the case in the study of De Beule *et al.* [153], Rayleigh damping ( $\alpha = 8000$ ) is employed for the balloon to prevent non-physical oscillations, with the average ratio of kinetic to internal energy for the analysis maintained below 5% [192]. Simulations are performed on a single Intel Xeon hexa-core processor on a SGI Altix HPC cluster at the Irish Centre for High Performance Computing, each requiring 600 CPU hours.

## 6.4. Results

### 6.4.1. Alloy Characterisation

The results of Experiment A, derived from the volume of hydrogen evolved from the surfaces of five corrosion specimens over time, are shown in Fig. 6.6. For the first six hours of immersion, the rate of mass loss is relatively low; however it quickly increases to give a steady rate of mass loss from which an average corrosion rate of  $0.084 \text{ mg cm}^{-2} \text{ h}^{-1}$  is derived. SEM images of the specimen corrosion surface are shown in Fig. 6.8. Microscopic pits are observed on the surface of the corrosion specimen after as little as three hours, shown in Fig. 6.8a. The maximum observed pit diameter in this case is approximately  $70 \text{ }\mu\text{m}$ . Pit growth is observed, with a maximum pit diameter of approximately  $400 \text{ }\mu\text{m}$  observed after 12 hours, shown in Fig. 6.8b. After 40 hours of immersion significant pit growth is observed, with macroscopic pits of diameter greater than  $2 \text{ mm}$  noted. In a number of cases, pits are observed to have progressed through the thickness of the specimen, shown in Fig. 6.8c. In addition to the observed pits, precipitates, whose composition was determined to be AlMn by EDX analysis, were observed

## 6. A Phenomenological Corrosion Model for Magnesium Stents

on the corrosion surface of partially cleaned samples when viewed under SEM, as shown in Fig. 6.8d. Based on these SEM images it is concluded that localized pitting corrosion is the primary form of corrosion attack in this case.

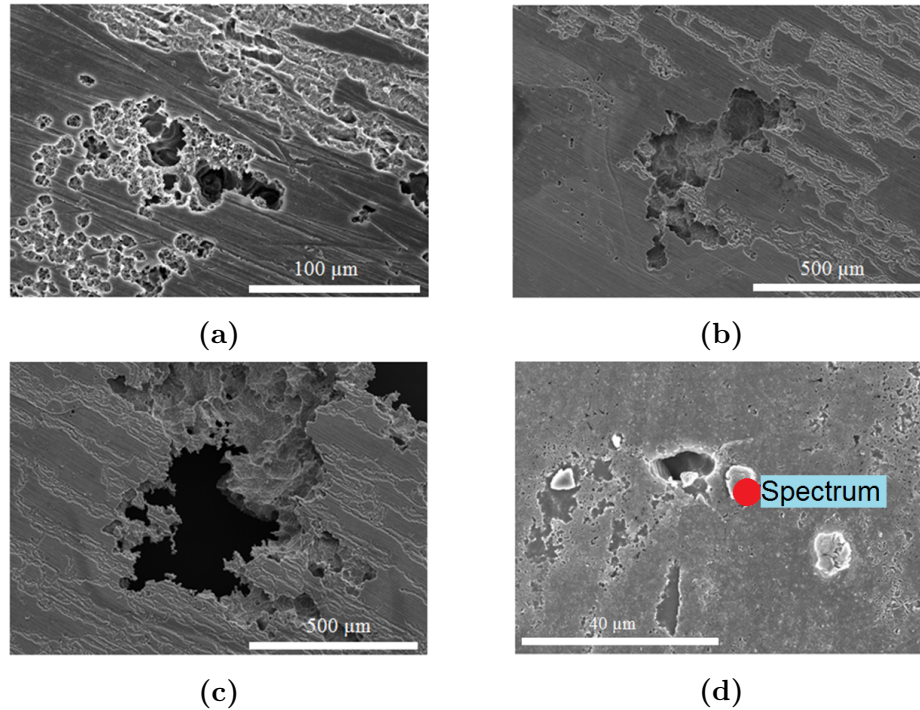


**Figure 6.8.:** SEM images of the AZ31 alloy corrosion surface following (a) 3 hours, (b) 12 hours and (c) 40 hours of immersion in solution. Pitting corrosion is noted to be significant in all cases. (d) SEM image of a corrosion pit and precipitates on a partially cleaned corrosion sample. EDX analysis was conducted at the point denoted ‘Spectrum’.

Representative engineering stress-strain curves for corroded and non-corroded specimens are shown in Fig. 6.5, based on the results of Experiment B. Specimen strength, as determined by dividing the maximum load withstood by the specimens in tension by the specimen cross-sectional area prior to corrosion, and engineering strain at the specimen strength are seen to decrease significantly with modest corrosion induced mass loss. Looking at the reduction in specimen strength with mass loss for all specimens in Fig. 6.9, a significant reduction in strength ( $> 25\%$ ) is noted for relatively small percentage mass losses ( $< 5\%$ ).

The results of Experiment C are shown in Fig. 6.10. The applied stress is taken as the ratio of applied load to original specimen cross-sectional area. It is ob-

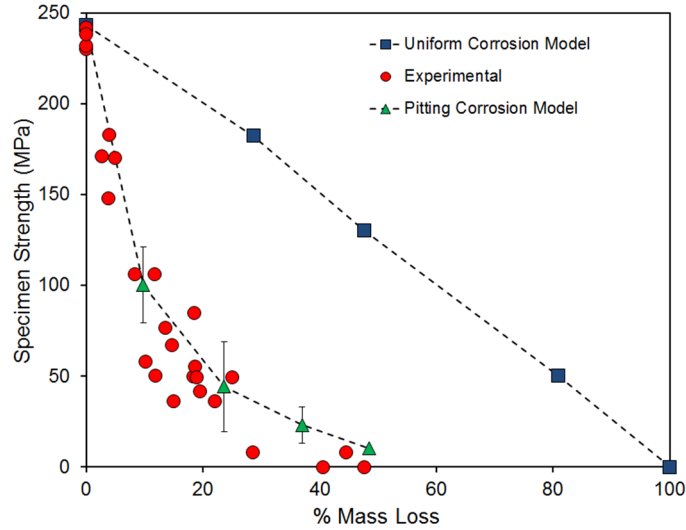


**Figure 6.9.:** Experimental results and FE simulation predictions for the reduction of specimen strength with corrosion mass loss, based on the results of Experiment B. Error bars represent a single standard deviation from the mean ( $n = 5$ ).

served that increasing applied stress leads to a significant reduction in the time to fracture for the specimen, with time to fracture halved when the applied stress is increased from 75 MPa to 150 MPa.

#### 6.4.2. Corrosion Model Calibration

The simulated corrosion of the foil test section is shown in Fig. 6.11. Macroscopic corrosion pits are seen to nucleate, grow and gradually coalesce through the removal of elements from the FE mesh. The parameters for the corrosion damage model, which were calibrated based on the results of Experiments A and B, are shown in Table 6.3. Parameters are shown for two cases, that of an idealised uniform corrosion model and that of the pitting model that most closely captures the experimentally observed corrosion behaviour.

The calibrated rate of mass loss from the FE pitting corrosion model is compared to that observed experimentally in Fig. 6.6. It can be seen that the FE pitting

## 6. A Phenomenological Corrosion Model for Magnesium Stents

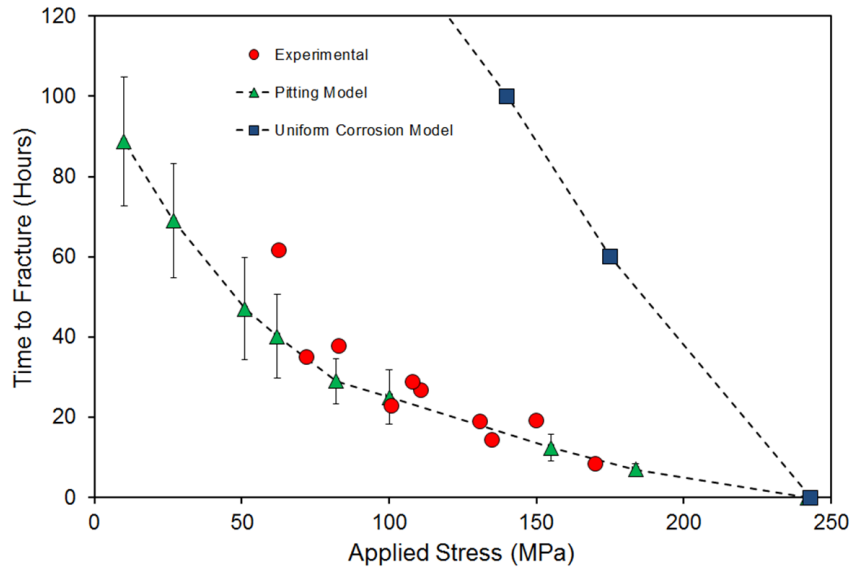


**Figure 6.10.:** Experimental results and FE simulation predictions for the effect of mechanical loading on specimen fracture time, based on the results of Experiment C. Error bars represent a single standard deviation from the mean ( $n = 5$ ).

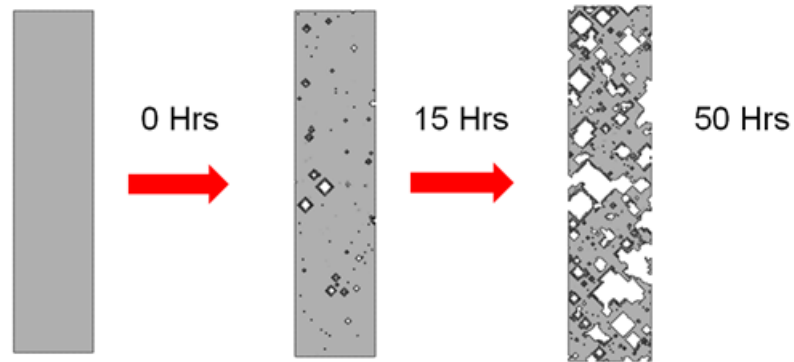


**Figure 6.11.:** The simulated corrosion of a foil specimen without loading. Pit growth is clearly observed.

**Table 6.3.:** Parameters used in the description of the corrosion damage models used in this work for the idealised case of uniform corrosion and for the case of pitting corrosion

Parameter	$L_e$ (mm)	$\delta_u$ (mm)	$k_u$ ( $\text{h}^{-1}$ )	$\gamma$	$\beta$
Uniform	0.07	0.017	0.026	inf	1.0
Pitting	0.07	0.017	0.00042	0.2	0.8

## 6. A Phenomenological Corrosion Model for Magnesium Stents

model is capable of capturing the experimentally observed rate of mass loss over time. Similar results are obtained in the case of the uniform corrosion model and as such are not included in the plot. The simulated results based on Experiment B are shown in Figs. 6.12a and 6.9. Again, the calibrated pitting corrosion model is able to capture the experimentally observed non-linear reduction in specimen strength with mass loss, whereas in this case, the uniform corrosion model fails to describe the observed trend.

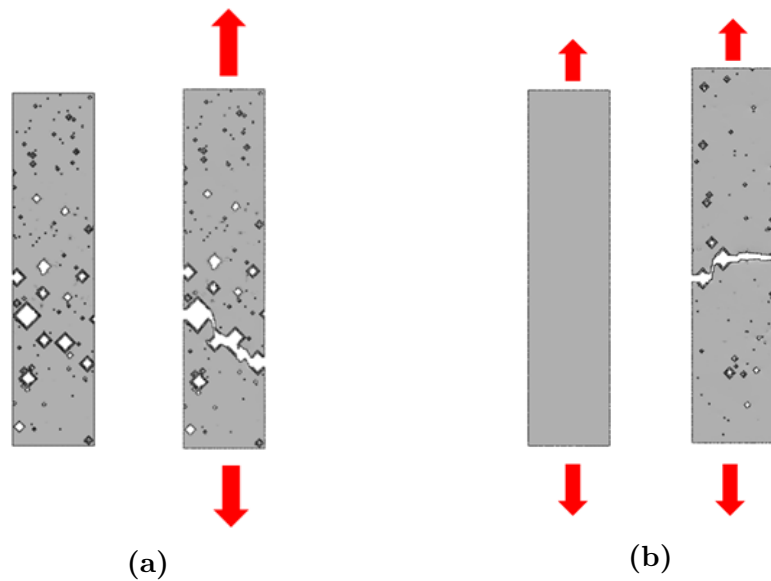


**Figure 6.12.:** (a) The simulated corrosion and subsequent tensile testing of a foil specimen. (b) A simulation of simultaneous foil loading and corrosion.

A simulation of Experiment C, the simultaneous loading and corrosion of a foil, is shown in Fig. 6.12b. The predictive capabilities of both pitting and uniform models are shown in Fig. 6.10, based on the results of Experiment C. It can be seen that the FE pitting model is able to qualitatively and quantitatively predict the influence of tensile stress on specimen fracture time, while the uniform corrosion model fails to describe this non-linear relationship. This result represents a first experimental verification of the predictive capabilities of the corrosion modelling framework developed in this work.

### 6.4.3. Stent Application

The simulated deployment and recoil of the MAGIC stent geometry in the idealised three layer artery model is shown in Fig. 6.13. A realistic balloon and stent ‘dog-bone’ profile can be seen during deployment, which shows agreement with experimentally observed stent geometries during the deployment phase [19]. The stent inner diameters pre- and post-recoil are 2.76 and 2.32 mm respectively.

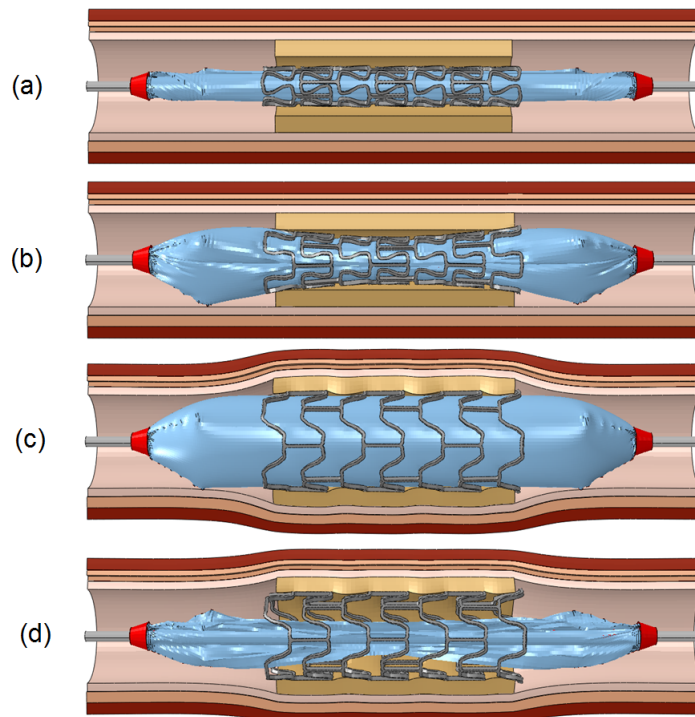


**Figure 6.13.:** FE simulation results for the balloon driven expansion and recoil of the AMS geometry including (a) insertion, (b) dog-boning mid deployment, (c) full deployment and (d) recoil stages.

Following deployment and recoil, the corrosion of the AMS geometry is simulated using both pitting and uniform corrosion models, as shown in Figs. 6.14a and 6.14b. It can be seen from Fig. 6.14a that pitting corrosion attack leads to a non-uniform breaking down of the AMS geometry, even in an idealised artery geometry, while the uniform model in Fig. 6.14b predicts a homogeneous corrosion attack.

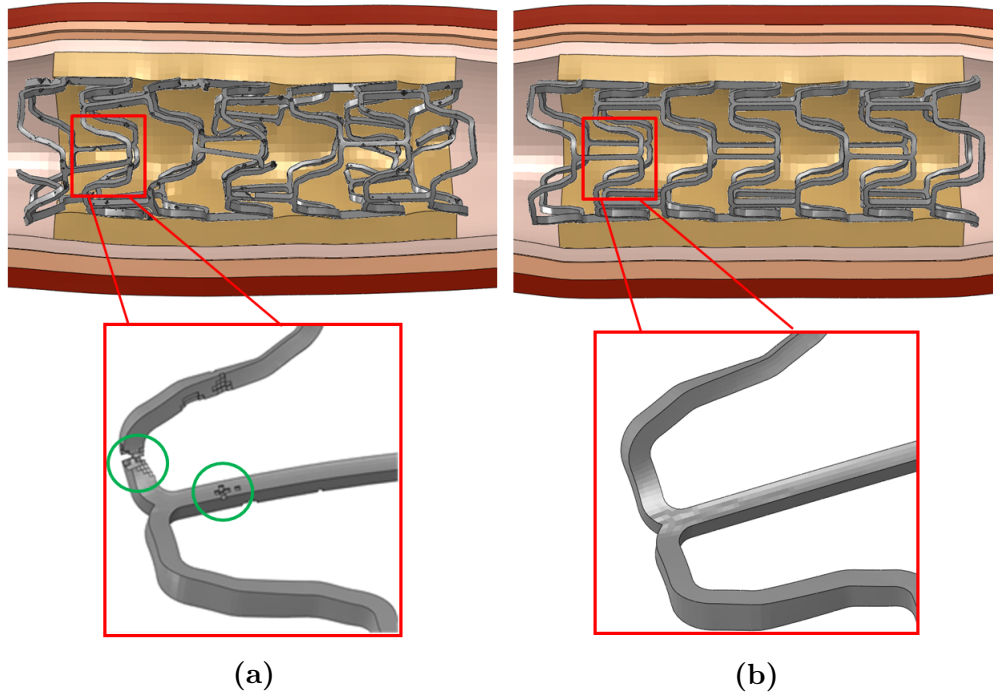


**Figure 6.14.:** FE simulation results for (a) pitting corrosion and (b) uniform corrosion processes in an AMS in an idealised artery geometry. It is observed that pitting corrosion attack leads to a non-uniform breaking down of the AMS geometry, with localized attack predicted to occur, as circled, in (a).

The predicted long-term stent recoil for each model is shown in Fig. 6.15, with stent recoil defined as per its use in Ch. 4:

$$\% \text{Recoil} = \frac{\theta_1 - \theta_2}{\theta_1} \times 100\% \quad (6.7)$$

where  $\theta_1$  and  $\theta_2$  are the respective stent inner diameters prior to, and during, device corrosion. It can be seen that the pitting corrosion model predicts a significant reduction in stent scaffolding support for a modest percentage mass loss, a highly undesirable trait for a magnesium based AMS's.

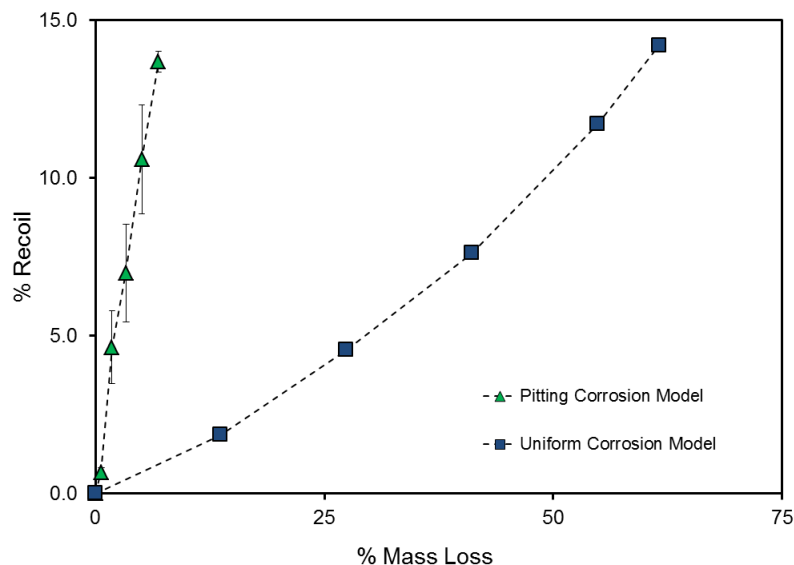


**Figure 6.15.:** FE prediction of % stent recoil due to corrosion. It is noted the pitting corrosion model predicts a significant loss of scaffolding support with relatively little mass loss compared to the uniform corrosion model. Error bars represent a single standard deviation from the mean ( $n = 3$ ).

## 6.5. Discussion

The average corrosion rate ( $0.084 \text{ mg cm}^{-2} \text{ h}^{-1}$ ) and localized pitting corrosion attack observed in this work are in agreement with those reported for similar alloy and solution compositions in the literature [42]. However, the gradual reduction in alloy corrosion rate due to the build-up of a layer of corrosion product reported in many other studies on larger samples [185, 184] was not observed for the thin foils studied in this work, where the corrosion rate remained largely constant, Fig. 6.6.

The significant corrosion-induced reduction in specimen mechanical integrity observed in Experiment B in this work, Fig. 6.9, is in agreement with results obtained in tests on larger samples in bending reported by Zhang *et al.* [184]. Since the corrosion model developed in this work is capable of capturing the observed results solely by accounting for the effects of specimen mass loss, Fig. 6.9, it is concluded that the primary factors for the observed reduction in specimen in-

## 6. A Phenomenological Corrosion Model for Magnesium Stents

tegrity are the non-uniform reduction in cross-section due to pit growth and the development of stress-concentrations in pitted regions.

While the results of Experiment C, Fig. 6.10, suggest a stress mediated corrosion attack on the foil samples, as has been observed in tests on larger samples with similar alloy and solution compositions [109], it is noted that the corrosion model developed in this work is capable of describing the observed dependence of fracture time on applied load solely through the simulation of localized pitting attack, with no explicit stress dependence included in the damage evolution law in Eqn. 6.3. This suggests that pit growth in the foil samples is the primary factor for the observed reduction in specimen fracture time with load.

When considering the observed corrosion behaviour, it should be noted that the sample processing employed here differs somewhat from that of coronary stents, which are typically laser cut and electrolytically polished. While the surface treatments employed in the processing of AMS's have not been reported in detail, it is likely, based on surface roughness studies on AZ31 and similar alloys in the literature [193, 98], that electro-polishing of the surface would lead to reduced corrosion rates and pitting susceptibility compared to those observed in this work. In addition, if anodizing treatments and surface coatings are employed this may also lead to reduced corrosion rates [99]. In terms of laser-cutting, little has been reported on the effects of this process on the corrosion behaviour of AMS's, although it has been shown that insufficient polishing can lead to preferential corrosion on laser-cut faces in conventional stents [48].

The observed localized corrosion behaviour is strongly linked with the microstructure of the AZ31 alloy used in this study. For example, Fig. 6.8d shows the presence of AlMn precipitates in the alloy microstructure, which, due to microgalvanic action with the surrounding matrix [194], can lead to preferential cor-

rosion in their vicinity and the eventual formation of corrosion pits. In addition, metallic grain size and twinning have been shown to influence the corrosion behaviour of AZ31 [97], with grain boundaries suggested to act as corrosion barriers, while mechanical twins have been suggested to act as corrosion initiation sites. As such, the observed corrosion behaviour in this work depends strongly on alloy processing conditions, with improved corrosion performance possible through careful control of precipitate concentration and grain size through appropriate alloy heat treatments [97].

In terms of the performance of the AMS's simulated in this work, it is predicted that heterogeneous corrosion leads to a significant reduction in stent scaffolding ability with relatively little corrosion induced mass loss when compared to the case of a perfectly homogeneous corrosion. The ability to make such a prediction is of particular relevance in the development of new alloys for AMS application, as it gives an indication of the degree of precedence that minimizing pitting susceptibility should have over other considerations in the alloy design, for example alloy ductility and tensile strength. In addition, the predictive capability afforded by the stent corrosion model allows improved AMS design through accounting for the effects of pitting corrosion in functionally critical regions, such as plastic hinges, in the design phase.

## **6.6. Limitations**

The model developed in this work has a number of limitations. Due to its phenomenological basis it does not physically capture the electrochemical processes and species evolution on the corrosion surface, meaning that its predictions are specific to a given alloy and solution composition. In addition, model predic-

## 6. A Phenomenological Corrosion Model for Magnesium Stents

tions are not motivated by alloy microstructure and as such, cannot be used in predicting the effects of precipitate inclusions or grain-size on corrosion. Due to a lack of experimental data on the effects of tissue coverage on alloy corrosion behaviour its effects are not included in the model, nor are the effects of dynamic loading on long-term AMS scaffolding ability.

Although the predictions of the corrosion model are specific to a given alloy microstructure, through re-calibration for each microstructure in consideration it can provide useful information into how a particular alloy microstructure would perform in a stent application in terms of long term radial strength and ductility. This can help in the selection of suitable alloy heat treatments, which by their nature can also modify alloy ductility and strength, without having to directly manufacture and corrode stent samples. In addition, through explicit modelling of an alloy microstructure, such as in Ch. 5 and the micro-galvanic corrosion process, the modelling framework developed here could be further extended to investigating the effects of precipitate concentration and grain size on an alloys corrosion behaviour.

In terms of tissue growth, the struts of an AMS have been found to be covered in a thin layer of neointima as few as six days after implantation in *in-vivo* tests [190]. While the corrosion behaviour of AMS's will depend on the degree of tissue coverage on strut surfaces, specific details on the relationship between tissue coverage and corrosion rates are not yet known. It is likely however, that increasing tissue coverage will reduce local corrosion rates through regulating the diffusion of hydrogen ions and corrosion product to and from the corrosion surface, and will certainly form a physical barrier in preventing flow enhanced corrosion [105] in the blood-stream. In terms of the model developed in this work, the framework exists which would allow different corrosion rates to be assigned to different surfaces or different individual elements. This feature may prove

useful in future analyses, where the effects of tissue coverage on device corrosion behaviour could be considered.

The effects of dynamic loading, which can lead to phenomena such as corrosion fatigue [7], on device performance were not considered in this work. Although it is likely that such a phenomenon would lead to a reduction in stent integrity over time [7], it is believed for the corrosion environment and alloy used in this study, that the influence of corrosion fatigue on stent integrity may be negligible compared to that of an aggressive, localized pitting attack. Nonetheless, the modelling framework developed here could be readily applied in considering the effects of dynamic loading on device corrosion through modelling of cyclic stent loading and the added dependence of the damage parameter on stress or strain amplitude and the number of loading cycles to which the stent has been subjected.

## **6.7. Conclusions**

A computational corrosion model is developed and implemented in Abaqus for application in absorbable metallic stent assessment and design. The model is calibrated based on the experimental determination of the corrosion behaviour of bioabsorbable magnesium alloy (AZ31) foils in simulated physiological fluid and is capable of describing the effects of mechanical loading on alloy corrosion.

The corrosion of the alloy is observed experimentally to be largely driven by a localized attack, which results in a significant reduction in foil mechanical integrity with relatively little mass loss. This behaviour is well described by the newly developed corrosion model, which captures both the experimentally observed

## *6. A Phenomenological Corrosion Model for Magnesium Stents*

corrosion rate and the resulting corrosion induced reduction in foil integrity.

Through combining experimental alloy characterisation and computational stent assessment, it is believed that this work provides new insights into the performance of an absorbable metallic stent, while also providing an experimental and computational methodology for future corrosion studies on the mechanical integrity of other candidate bioabsorbable alloys in corrosive physiological environments.

# 7. Designing an Optimum Bioabsorbable Metal Stent

## 7.1. Chapter Summary

It was shown in Ch. 4 that the design of magnesium stents is challenging due to limitations on strut dimensions imposed by the inferior mechanical performance of magnesium alloys relative to conventional stent materials. It was also suggested that accounting for device corrosion may further restrict possible strut dimensions. Optimization methods are a promising way to account for multiple, and sometime conflicting, requirements in identifying optimal AMS designs. In this chapter an optimization strategy for AMS's is developed that accounts for both the effects of limited alloy mechanical properties, identified in Ch. 4 and corrosion, discussed in Ch. 6. Through combining the outcomes of Chs. 4 and 6, the work in this chapter allows design recommendations to be made regarding the characteristics of optimal AMS geometries.

## 7.2. Introduction

Computer simulation has been used extensively in the development of permanent stents [148, 149, 20, 15]. While many existing simulation and design techniques for stents can be applied to the development of AMS's, new techniques are required to account for the significant degree of corrosion to which the devices are subject *in-vivo*. In this chapter, a new method for simulating device corrosion is developed which explicitly tracks the changing geometry of the stent as it corrodes, using adaptive meshing. The method is implemented in Abaqus/Standard (DS SIMULIA, USA), and is more computationally efficient than previously developed continuum damage techniques, which use the Abaqus/Explicit solver. This superior efficiency allows corrosion to be included in parameter and optimization studies which require a large number of simulations.

Optimization techniques have proven useful in the identification of stent designs with desirable attributes [195, 22]. Predictions in Ch. 4 have shown that the use of such techniques is of particular importance in AMS design, owing to limitations in the mechanical properties of currently available bioabsorbable alloys. Wu *et al.* [131] developed an optimization strategy for 2-D AMS geometries that used deployment simulations of single stent hinges, without corrosion. In the present study, a new optimization strategy for 3-D AMS design is developed which explicitly accounts for corrosion effects. This strategy, for the first time, enables the use of direct measures of long-term stent performance (i.e. long-term radial stiffness) in the optimization process. In addition, the strategy allows more accurate predictions of the stress and strain states in the device during deployment than previous studies; these measures are key constraints in the optimization process.

The premature loss of scaffolding due to corrosion has been reported to be a

primary reason for the relatively poor device efficacy in the first AMS clinical trial in coronary applications [40]. Since these reports, significant efforts have been made to improve device performance through the development of bioabsorbable alloys with improved mechanical properties and corrosion resistance, as reviewed by Moravej and Mantovani [113]. Despite this, the role of device design in determining long-term scaffolding behaviour has been largely overlooked and little has been reported on either the effects of corrosion on AMS mechanical behaviour or the extent to which device performance can be improved through design modifications.

In this chapter, existing and newly developed simulation and design techniques are used to investigate the effects of corrosion on the scaffolding ability of a range of stent unit-cell geometries. Results give new insights into: i) how corrosion affects scaffolding for a range of designs, loading scenarios and alloy mechanical and corrosion properties and ii) the extent to which modifying design can improve device performance.

### **7.3. Methods**

Finite deformation kinematics, overviewed in Ch. 3, is assumed in all simulations. A new method for simulating AMS corrosion based on ALE adaptive meshing is first presented. This ALE corrosion model is used in investigating the corrosion behaviour of a range of AMS designs, by means of parameter studies. A new optimization strategy is then presented, which uses the EGO algorithm [134] and the ALE corrosion model. This strategy is used to identify features of AMS designs with favourable long-term performance.

## 7. Designing an Optimum Bioabsorbable Metal Stent

Following this, the deployment of a number of AMS designs in physiologically representative vessel geometries is simulated to investigate how predictions of *in-vitro* AMS performance are related to *in-vivo* performance predictions. The Abaqus/Explicit solver and the continuum damage model developed in Ch. 6 are used to simulate device corrosion in this case, due to their favourable robustness in the treatment of simultaneous large deformations, intermittent large sliding contact and corrosion.

### 7.3.1. ALE Corrosion Model

Corrosion is simulated using the ALE adaptive meshing capability in Abaqus/Standard, discussed in Ch. 3. This capability allows the boundaries of the FE mesh to be moved independently of the underlying material between analysis increments. This simulates the effects of material removal, as any material outside of the FE mesh in an increment does not contribute to mechanical behaviour (Abaqus Analysis Manual, DS SIMULIA, USA).

The ALE corrosion model uses a newly developed facet based approach to track the corrosion surface as it evolves over time, based on the use of 3-D linear reduced integration elements (C3D8R). This approach allows corrosion to be simulated on the complex geometrical features, such as corners and edges, present in the stent geometry. Here, facets are triangles whose vertices are given by nodes on intersecting element edges, as shown in Fig. 7.1a. As shown schematically in Fig. 7.1b, uniform corrosion is simulated by moving facets along their inward pointing normals,  $\mathbf{n}$ , at a velocity equal to the corrosion rate,  $v$  (in the form  $L.T^{-1}$ ). Using this approach, the position of a node on the corrosion surface at any time can be found by finding the intersection of its corresponding facets.

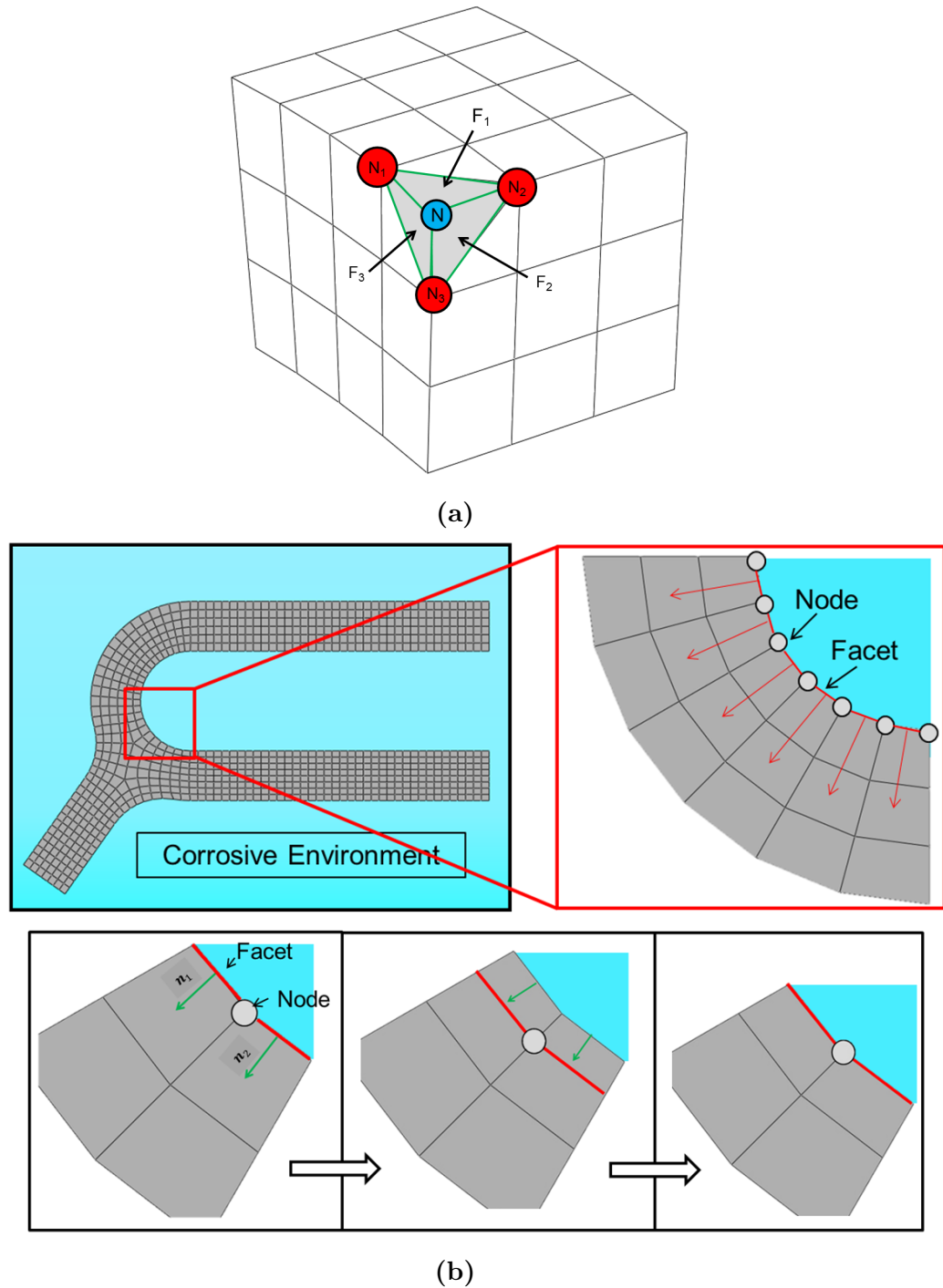


**Figure 7.1.:** (a) For each node in the FE mesh  $N$  its corresponding facets are the triangles generated by connecting it to pairs of nodes with which it shares element edges and which occupy the same element face. For example, the facet  $F_1$  is given by the nodes,  $N$ ,  $N_1$  and  $N_2$ . (b) Facets along the corrosion interface move inward along their normals,  $n_i$ , at constant velocity,  $v$ . The position of an exterior node at any time is given by the intersection of its facets.

## 7. Designing an Optimum Bioabsorbable Metal Stent

A number of custom-written Fortran user subroutines, including UMESHMOTION, are used to implement the ALE corrosion model in the Abaqus/Standard code. A flowchart detailing the implementation of the model is shown in Fig. 7.2. Based on the results of a mesh convergence study, all stent simulations use six C3D8R elements through the strut width.

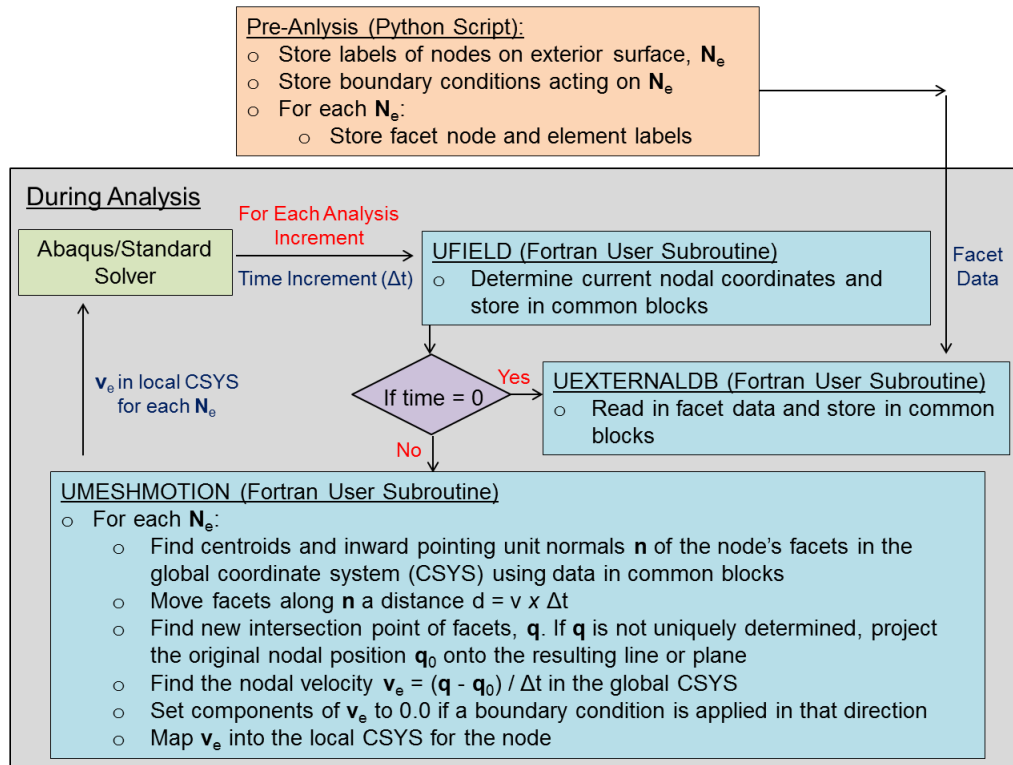


**Figure 7.2.:** A flowchart for the implementation of the ALE corrosion model with Abaqus/Standard

### 7.3.2. Effects of corrosion on AMS performance

It is of interest to determine: i) the effects of corrosion on AMS mechanical performance and ii) the extent to which long-term scaffolding performance depends on device design and alloy mechanical and corrosion properties. These are investigated through two parameter studies (P1 and P2) and an optimization study (O1). In all three studies, corrosion is simulated using the ALE corrosion model.

### 7.3.2.1. Parameter Study 1 (P1)

Parameter study P1 focuses on a simple, sinusoidal stent hinge profile with a number of different cross-sections, shown in Fig. 7.3a. The deformation and corrosion of the hinges is simulated as shown in Fig. 7.3b.

The quantity of interest in terms of hinge performance is radial stiffness, which is calculated as follows:

$$R_k = \frac{F_2 - F_1}{L_T(D_2 - D_1)} \quad (7.1)$$

where  $F_i$  and  $D_i$  are points on the stent's force  $F$  diameter  $D$  curve during crushing, shown in Fig. 7.4, and  $L_T$  is total hinge length.

Three elastic-plastic magnesium alloy behaviours are adopted for the hinges, shown in Tables 7.1 and 7.2, based on properties of AZ31 alloy, WE43 alloy and MZX alloy. The latter two alloys have been used in *in-vivo* AMS experiments in Erbel *et al.* [40] and Deng *et al.* [43], respectively. Elastic-plastic properties of iron are also considered, based on its use in early *in-vivo* AMS experiments [114]. The specific goals of this study are to investigate: i) the extent to which hinges consisting of different materials lose mechanical integrity with corrosion and ii) the extent to which hinges of different cross-sectional areas lose mechanical integrity with corrosion.

### 7.3.2.2. Parameter Study 2 (P2)

Parameter study P2 uses a similar approach to study P1, but rather than investigating a single sinusoidal hinge profile, a range of hinge profiles that are more reflective of those used in commercial AMS's, namely the DREAMS stent [39]

## 7. Designing an Optimum Bioabsorbable Metal Stent

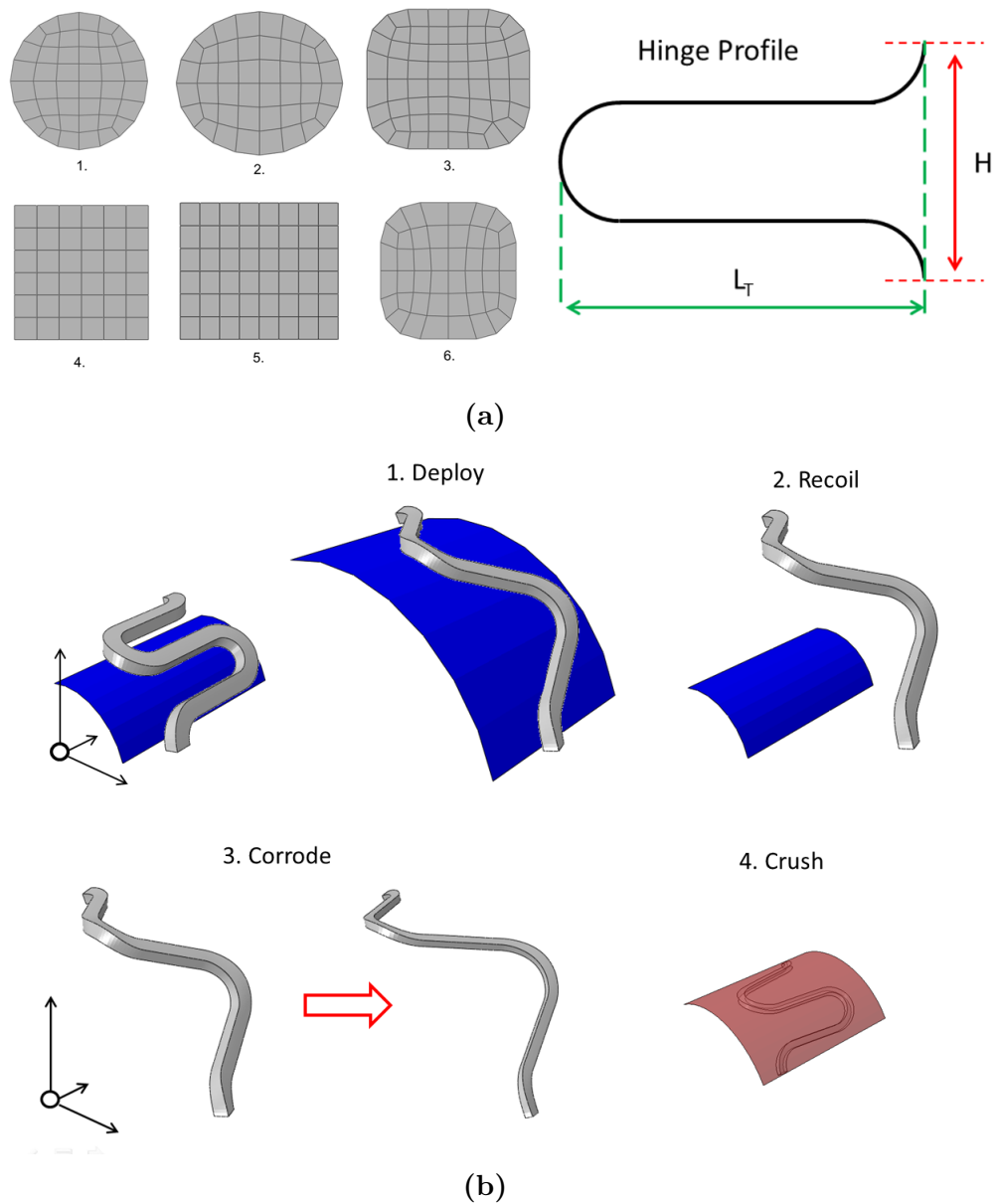


**Figure 7.3.:** (a) Hinge cross-sections and FE meshes and a schematic of the hinge profile are shown. All cross-sections have a radial thickness of 0.12 mm. Cross-sections 1, 4 and 6 have a circumferential width of 0.12 mm while the others have a width of 0.14 mm. The hinge profile has length  $L_T$  equal to 1.1 mm and height  $H$  equal to 0.785 mm. (b) Deployment and corrosion simulations for the hinges. The hinge is deployed by expanding a semi-rigid inner cylinder. It then undergoes recoil and corrosion and is subsequently crushed using an outer cylinder. Symmetry boundary conditions are used so only quarter of the stent unit is modelled.

7. Designing an Optimum Bioabsorbable Metal Stent

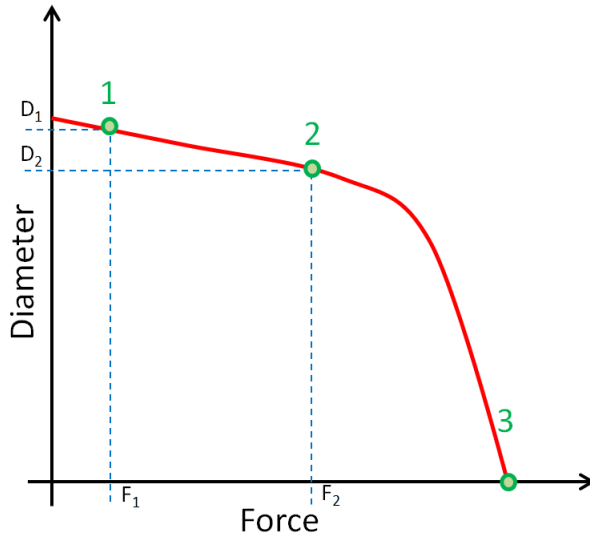


**Figure 7.4.:** Radial stiffness is taken as the slope of the stent’s force-diameter curve between points ‘1’ and ‘2’ during crushing. Maximum radial force is given by point ‘3’ .

**Table 7.1.:** Engineering stress-strain data used in this study.

Material	E (GPa)	Yield Strength (MPa)	UTS (MPa)	Strain at UTS	Source
PtCr (M1)	203	480	834	44.8%	[6]
WE43 (M2)	44	216	298	18.5%	[7]
MZX (M3)	44	184	287	23.0%	[43]
Iron (M4)	211	170	270	36.0%	[8]

**Table 7.2.:** True stress-strain data for AZ31 alloy used in this study, from Ch. 6.

Stress (MPa)	Plastic Strain
138	0.000
170	0.009
192	0.020
231	0.054
271	0.111
288	0.157

## 7. Designing an Optimum Bioabsorbable Metal Stent

are investigated. In this study the dimensions of the device are allowed to vary within a specified design space, shown in Fig. 7.5.

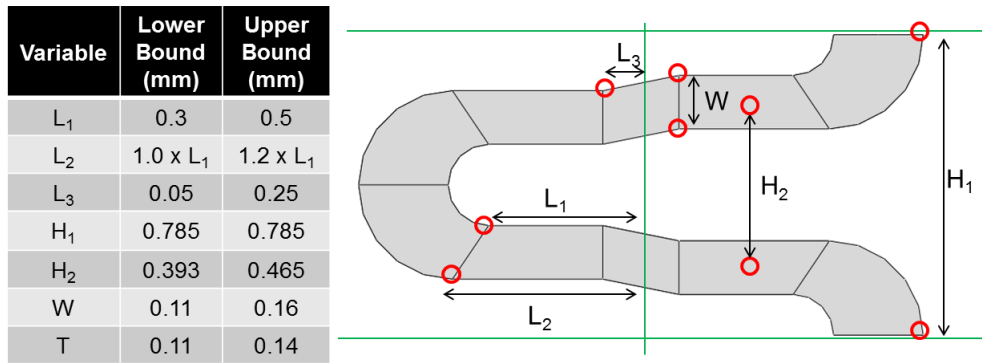


**Figure 7.5.:** Schematic of the stent design used in the parameter and optimization studies. The profile has a fixed overall height  $H_1$ , corresponding to an outer diameter of 1.5 mm, and is extruded through an out-of-plane thickness  $T$ .

The upper bounds on the design space are due to geometrical limitations for device construction or, in the case of thickness, the desire to not increase strut thickness beyond that of early generation permanent stents (e.g. the CYPHER stent). Lower bounds correspond to hinge dimensions below which optimal designs are deemed unlikely to be found. A structured meshing technique with exactly six elements maintained through the strut width is used to ensure consistent mesh characteristics for all designs. The goals of this study are to: i) investigate the extent to which hinges with a range of different profiles lose mechanical integrity with corrosion and ii) identify a set of baseline designs to be compared with a design from a subsequent optimization study over the same design space. In the present study a Monte-Carlo based sampling method is used to generate stent designs within the design space, based on a uniformly distributed random selection of dimensions. The mechanical behaviour of AZ31 alloy, shown in Table 7.2, is adopted for all simulations. Only designs with predicted maximum strains during deployment below 80% of strain at UTS are considered.

**7.3.2.3. Optimization Study (O1)**

In optimization study O1 a strategy is developed to maximize the long-term scaffolding performance of a candidate AMS design by explicitly considering the effects of corrosion on device performance. The approach used incorporates the EGO algorithm [134], which is implemented in the open-source DAKOTA optimization toolkit (Sandia National Laboratories, USA). The implementation of the EGO algorithm in DAKOTA is detailed in the Dakota Theory Manual (Sandia National Laboratories, USA) and in Ch. 3.

For the purposes of this study, the goal is to maximize hinge radial stiffness, as defined in Eqn. 7.1, after a specific amount ( $vt=10 \mu\text{m}$ , where  $t$  is immersion time) of corrosion. Optimizations are performed using the same design space as was used in study P2, shown in Fig. 7.5. The objective function to be minimized is:

$$OF(\mathbf{x}) = 1 - AR_k(\mathbf{x}) \quad (7.2)$$

where  $\mathbf{x}$  is a vector with the values of the six design variables ( $L_1, L_2, L_3, H_2, W, T$ ) as its components and  $A$  is a scaling parameter. A penalty condition similar to that used in previous stent optimization studies [196], is used in the present study to ensure that the objective function value is relatively high when strains in a candidate hinge exceed a desired limit. The penalty condition is enforced by assigning the objective function the following value:

$$OF(\mathbf{x}) = 1 + \varepsilon_{mp}(\mathbf{x}) \quad (7.3)$$

if  $\varepsilon_{mp}$ , for a hinge exceeds 80% of the strain at UTS. For the present study a value of 0.15 for the scaling parameter  $A$  in Eqn. 7.2 is found to be suitable for ensuring that only designs with maximum strains below the prescribed limit are identified as optimal.

## 7. Designing an Optimum Bioabsorbable Metal Stent

As shown in Fig. 7.6, the optimization can be described in five steps. Prior to the optimization, 28 initial values of  $\mathbf{x}$  are randomly generated using a Latin Hypercube [197] based sampling technique. This step, which corresponds to ‘Step 0’ in Fig. 7.6, is proposed for starting the EGO algorithm in Bichon *et al.* [198]. For each  $\mathbf{x}$  a stent geometry and FE model are automatically generated using Python scripting and the Abaqus/CAE pre-processor in ‘Step 1’. The deployment, corrosion and crimping simulations shown in Fig. 7.3b are performed for each model in ‘Step 2’ and the objective function is evaluated using Eqns. 7.2 and 7.3 and passed to DAKOTA in ‘Step 3’. In ‘Step 4’, DAKOTA uses a best-fit model (Gaussian Process surrogate model; see Ch. 3 for details and Pant *et al.* [22] for an application of this model in stent optimization) to attempt to describe OF throughout the entire design space based on known discrete values of the function at previously sampled points  $\mathbf{x}$  (for the first iteration the 28 initial sample points are used). A new value of  $\mathbf{x}$  is identified that maximises the value of an expected improvement function (EIF, as defined in Ch. 3), by using the best fit model and its prediction of OF. This new  $\mathbf{x}$  corresponds to a promising region of the design space or a region that warrants further exploration. The optimization algorithm iterates by passing this value of  $\mathbf{x}$  back into ‘Step 1’ and calculating the exact value of OF at this point, which is used to update the best-fit model for the next iteration. As the algorithm iterates, the uncertainty (see Ch. 3) in the OF predictions by the best-fit model through the design space, and the associated EIF value, reduce and an optimal set of values of  $\mathbf{x}$  is identified.

In the present study the optimization is performed for a fixed number of iterations (150), rather than using a specific convergence criterion. This approach is found to be a suitable trade-off for obtaining a significantly improved performance over the baseline design without the additional computational expense, and diminishing returns, of specifically identifying a globally optimal solution. For the present study, the optimization process is conducted five times, in each

## 7. Designing an Optimum Bioabsorbable Metal Stent

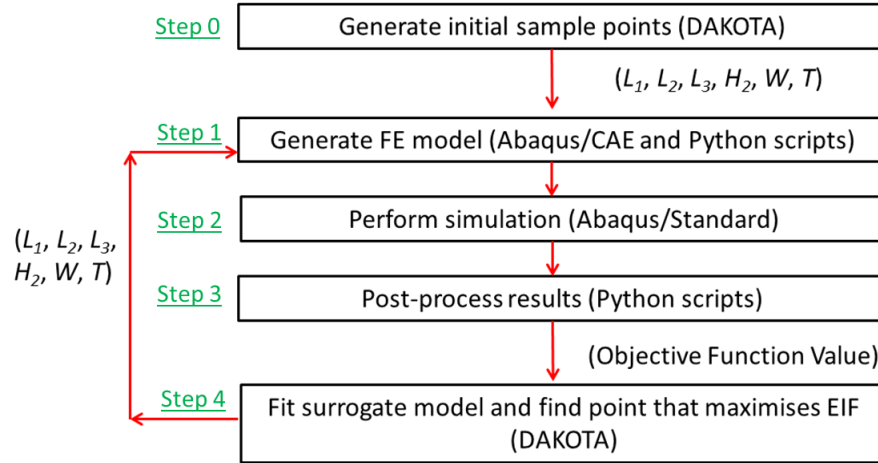


**Figure 7.6.:** The five-step optimization strategy developed in this study.

case with a different set of twenty eight initial points. The optimal design is identified as the one with the lowest objective function value from the five optimizations. Optimizations are performed autonomously on a HPC cluster, each requiring approximately 120 CPU hours.

### 7.3.2.4. Effects of corrosion on in-vivo AMS performance

It is of interest to investigate how improvements in AMS performance identified in study O1 translate to improvements in *in-vivo* performance. It is also of interest to predict and compare the performances of different AMS designs and a permanent stent *in-vivo*. To this end, the performance of the optimized design is compared to that of: i) a baseline design from study P2, ii) an approximation of a commercial AMS design (MAGIC Stent, Biotronik) and iii) an approximation of a commercial permanent stent design (OMEGA Stent Platform, Boston Scientific), in stenosed vessel geometries. The approximations of the commercial AMS and permanent stent are shown in Fig. 7.7a. The baseline design is chosen as the design with an  $R_k$  value closest to the mean of all of those found in study P2. All AMS designs are assumed to consist of AZ31 alloy, while the permanent stent material is modelled as PtCr, with mechanical properties shown in Tables 7.1

and 7.2.

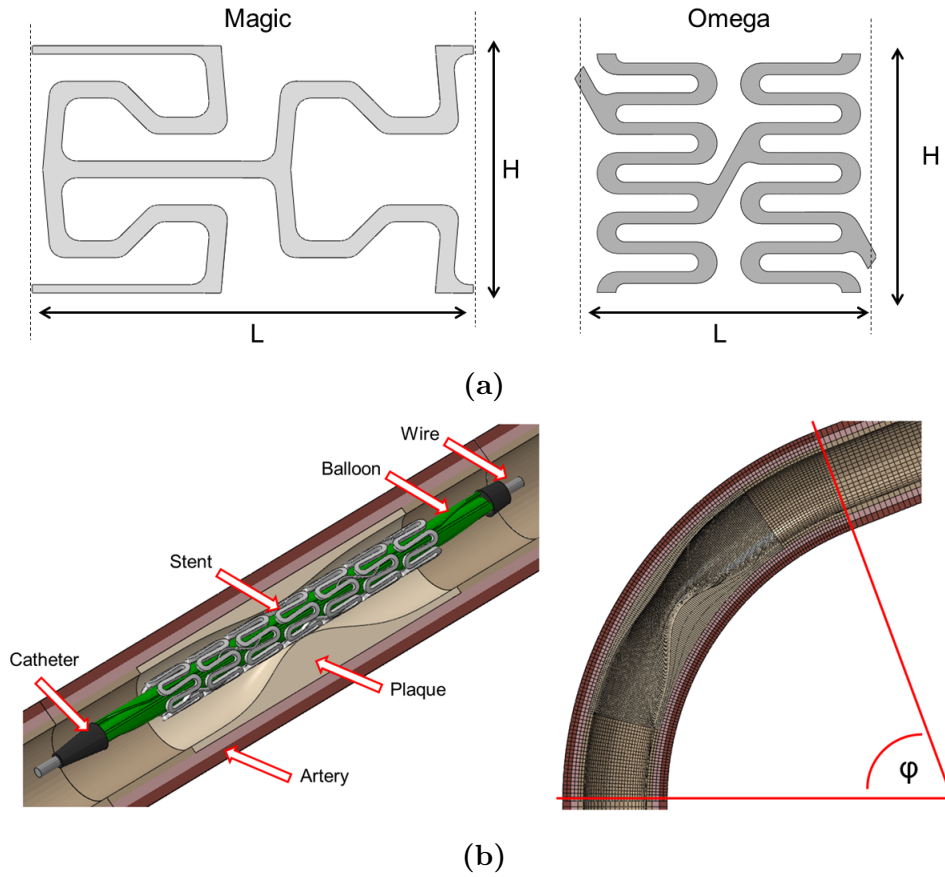


**Figure 7.7.:** (a) Designs for the MAGIC and OMEGA stent approximations used in this study. For the MAGIC stent,  $H = 1.18$  mm and  $L = 2.1$  mm. Strut width is 0.08 mm and thickness is 0.16 mm. For the OMEGA stent  $H = 2.03$  mm and  $L = 2.25$  mm. Strut width is 0.1 mm and thickness is 0.08 mm. (b) Stent deployment model in straight and curved arterial configurations.

Following the recommendations of Conway *et al.* [23] with regard to the representation of vessel curvature and the inclusion of a lesion in stent deployment simulations, two vessel configurations are used to simulate deployment and corrosion, shown in Fig. 7.7b. For the curved artery, the angle  $\phi$  in Fig. 7.7b corresponds to that recommend by the FDA [15] for computational studies on stents (radius of curvature = 15 mm). The delivery system, shown in Fig. 7.7b, consists of a HDPE catheter, nitinol guide-wire and folded nylon angioplasty balloon. Important dimensions and material properties for each component are listed in Table 7.3.

## 7. Designing an Optimum Bioabsorbable Metal Stent

**Table 7.3.:** Information on the components of the stent delivery system used in this study. Material properties are taken from Mortier *et al.* [20].

	Dimension	Material	FE Mesh (Num Elements: Element Type)
Balloon	Length = 16.0 mm	Nylon, $E = 750$ MPa, $\nu = 0.4$	14 400: M3D4R
Wire	Diameter = 0.34 mm	Nitinol, $E = 62$ GPa, $\nu = 0.3$	4000: C3D8R
Catheter		HDPE, $E = 1$ GPa, $\nu = 0.4$	3440: C3D8R

The folded angioplasty balloon geometry is created by drawing the geometry shown in Fig. 7.8a and mapping it into a cylindrical configuration. This method of construction is more straightforward than previously used techniques [199] and allows greater flexibility in choosing the balloon design. The dimensions ( $b_1$ ,  $b_2$ ,  $c$ ) of the balloon are chosen to produce an inflated diameter of 3.00 mm at an internal pressure of 1.2 MPa.

Arteries are assumed to consist of three layers; intima, media and adventitia. Each layer is modelled using a rate independent anisotropic hyperelastic material model, which captures the effects of helically wound collagen fibres in the tissue. The material model, whose application in a similar type of analysis is discussed in detail in Mortier *et al.* [20], uses the strain energy density function in Eqn. 3.40. Values for all parameters ( $\mu$ ,  $k_1$ ,  $k_2$ ,  $\rho_f$  and  $\alpha_f$ ) and artery layer thicknesses are included in Table 7.4, from Holzapfel *et al.* [139]. The value of  $\kappa$  is determined for each layer through numerical experiments. The model is implemented using the VUANSIOHYPER subroutine in the Abaqus/Explicit solver.

An atherosclerotic plaque is included in the vessel, whose material behaviour is described through a reduced order polynomial hyperelastic equation with the strain energy density function in Eqn. 3.35. Material parameters are taken from Gastaldi *et al.* [21] and shown in Table 7.4, based on experimental plaque characterisation by Loree *et al.* [191]. As per Gastaldi *et al.* [21] and Conway *et al.* [23],

7. Designing an Optimum Bioabsorbable Metal Stent

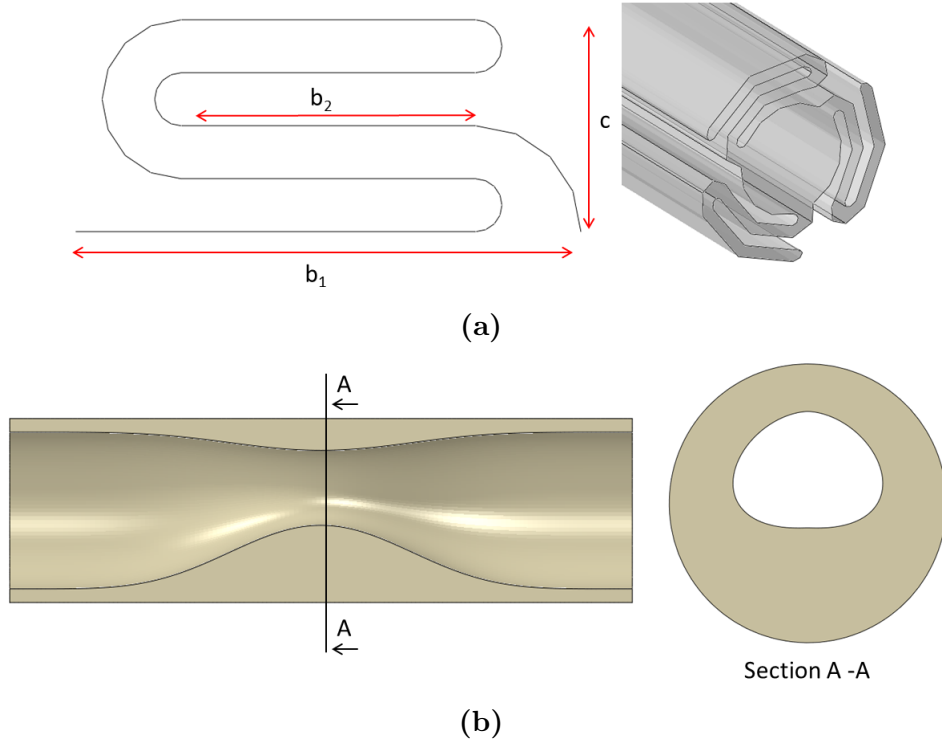


**Figure 7.8.:** (a) Schematic showing the construction of the folded angioplasty balloon used in this study. The balloon’s tapered ends are constructed by reducing  $b_2$  appropriately using the ‘Loft’ command in Abaqus/CAE. (b) Schematic of the plaque geometry used in this study. The centre of the lumen varies eccentrically along the plaque length according to a Hickeys-Henne bump function [22]. The shape and area of the lumen gradually transition from circular to oval along the length, according to the same bump function.

**Table 7.4.:** Information on the components of the tissue used in this study. Thicknesses and constants  $\mu$ ,  $k_i$ ,  $\rho_f$  and  $\alpha_f$  are given by Holzapfel *et al.* [139]. The plaque constants are given by Gastaldi *et al.* [21].

Artery Layer	Thickness (mm)	$\kappa$ (kPa)	$\mu$ (kPa)	$k_1$ (kPa)	$k_2$	$\rho_f$	$\alpha_f$ (deg)	FE Mesh (Num Elements: Element Type)
Intima	0.24	70.0	28.62	124.01	180.43	0.55	69.5	16 000: C3D8R
Media	0.32	1063.8	0.94	13.28	10.81	0.25	21.0	16 000: C3D8R
Adventitia	0.34	247.5	4.04	32.50	103.63	0.65	72.7	16 000: C3D8R
		$\kappa$ (kPa)	$C_{10}$ (kPa)	$C_{20}$ (kPa)	$C_{30}$ (kPa)	$C_{40}$ (kPa)	$C_{50}$ (kPa)	$C_{60}$ (kPa)
Plaque	4762	2.38	189	-388	3730	-2540	573	53 000: C3D8R

## 7. Designing an Optimum Bioabsorbable Metal Stent

perfect plasticity is assumed for the plaque once von Mises stresses reach 0.4 MPa. The geometry of the plaque is shown in Fig. 7.8b and consists of an eccentric, oval shaped lumen. The eccentricity, shape and area of the lumen change along the plaque length according to a Hicks-Henne bump function [200], following a generalisation of the method outlined in Pant *et al.* [22]. The shape of the lumen corresponds to a maximum stenosis of 67% by area, which is similar to that used in the studies of Pant *et al.* [22] (64%) and Conway *et al.* [23] (50 to 60%).

The length of the modelled arterial segment is 54.0 mm. Each end of the segment is fixed throughout the simulation. For the straight vessels the guide-wire is fixed in position and deployment is achieved through the application of a pressure to the inner surface of the balloon. For the curved vessel, the catheter, balloon and stent are first tracked through the vessel, followed by the application of a pressure to the inner surface of the balloon. The guide-wire is fixed at the proximal end only in this case.

Following device deployment and recoil, the AMS geometries undergo corrosion using the uniform and pitting continuum damage corrosion models developed in Ch. 6 and discussed in the next section. Deployment and recoil simulations require approximately 800 CPU hours each in straight vessels and 1300 CPU hours in curved vessels, while the corrosion stages require approximately 400 CPU hours each. Simulations are performed on a SGI-Altix HPC cluster at the Irish Centre for High Performance Computing.

### 7.3.3. Corrosion Damage Model

For the uniform corrosion model the parameter  $\lambda_e$  in Eqn. 6.3 is set equal to 1.0, and it is possible to replace the product  $\delta_U k_U$  with  $v$  (which is equivalent to the

## 7. Designing an Optimum Bioabsorbable Metal Stent

corrosion rate parameter used in the ALE corrosion model). Since  $L_e$  is simply a property of the FE mesh, this allows the uniform corrosion damage model to be calibrated with a single parameter,  $v$ . The predictions of the ALE corrosion model and the uniform corrosion damage model can then be presented in terms of the quantity  $vt$  which is the input corrosion rate multiplied by the immersion time and can be considered to be an equivalent one-dimensional ‘corrosion distance’. Using this quantity means that results are applicable for any uniformly corroding alloy (not just AZ31), once the corrosion rate for that alloy is known. A further advantage of using this quantity is that results expressed in this form are applicable even when the input corrosion rate is not constant in time (if  $vt$  is interpreted as  $\int_0^t v(t)dt$  in that case).

For the pitting corrosion model, the parameter  $\beta$  in Eqn. 6.6 is scaled for meshes of characteristic length  $L_e$  by:

$$\beta = \beta_0^{\frac{L_e}{L_{e,0}}} \quad (7.4)$$

where  $\beta_0 = 0.8$  and  $L_{e,0} = 0.07$  are reference values from the calibrated model in Ch. 6. The parameters  $k_U = 0.00042 \text{ h}^{-1}$ ,  $\delta_U = 0.017 \text{ mm}$  and  $\gamma = 0.2$  are also taken from Ch. 6. Random  $\lambda_e$  values are assigned by placing a virtual grid with cuboidal cells of side length  $L_{e,0}$  over the mesh in a pre-processing step. Each cell is assigned a random  $\lambda_e$  value from a standard Weibull distribution with shape parameter  $\gamma$  and each element of the mesh within that cell assumes its  $\lambda_e$  value.

## 7.4. Results

### 7.4.1. Parameter and Optimization Studies

Fig. 7.9a shows a series of force - diameter curves for a corroding hinge as it is crimped, based on study P1. It is observed that all curves maintain a similar shape following various degrees of corrosion. Fig. 7.9b shows the predicted reduction in  $R_k$  and maximum radial force in a hinge due to corrosion. The reductions in stiffness and force with time follow similar trends and are somewhat linear. Fig. 7.9c shows the initial  $R_k$  of hinges with a variety of cross-section profiles. As is expected, wider struts have greater radial stiffness. Fig. 7.9d shows predicted stiffness retention, or the stiffness of the device during corrosion  $R_k$  divided by the stiffness before corrosion  $R_{k,0}$  for a variety of hinge profiles and materials. The stiffness retention is quite similar in each hinge, regardless of underlying material. However, there is slightly greater stiffness retention in hinges with larger circumferential widths.

Fig. 7.10a shows the loss in  $R_k$  with corrosion for a sample of the geometries considered in parameter study P2 ( $n = 25$ ) and the optimized design from optimization study O1 (denoted Opt 5 in Table 7.5). The optimization process leads to a design with significantly higher  $R_k$  than is predicted in the designs assessed in parameter study P2, before and during corrosion. Fig. 7.10b shows the stiffness retention for the optimized design and the sample geometries from study P2. The optimized design is predicted to retain its initial stiffness better than the parameter study designs for most of the corrosion process. The reason for the improved performance of the optimized design can be seen when the device dimensions, shown in Table 7.5, and the results shown in Figs. 7.9c and 7.9d are considered. From Table 7.5, a general feature of the optimal designs identified

7. Designing an Optimum Bioabsorbable Metal Stent

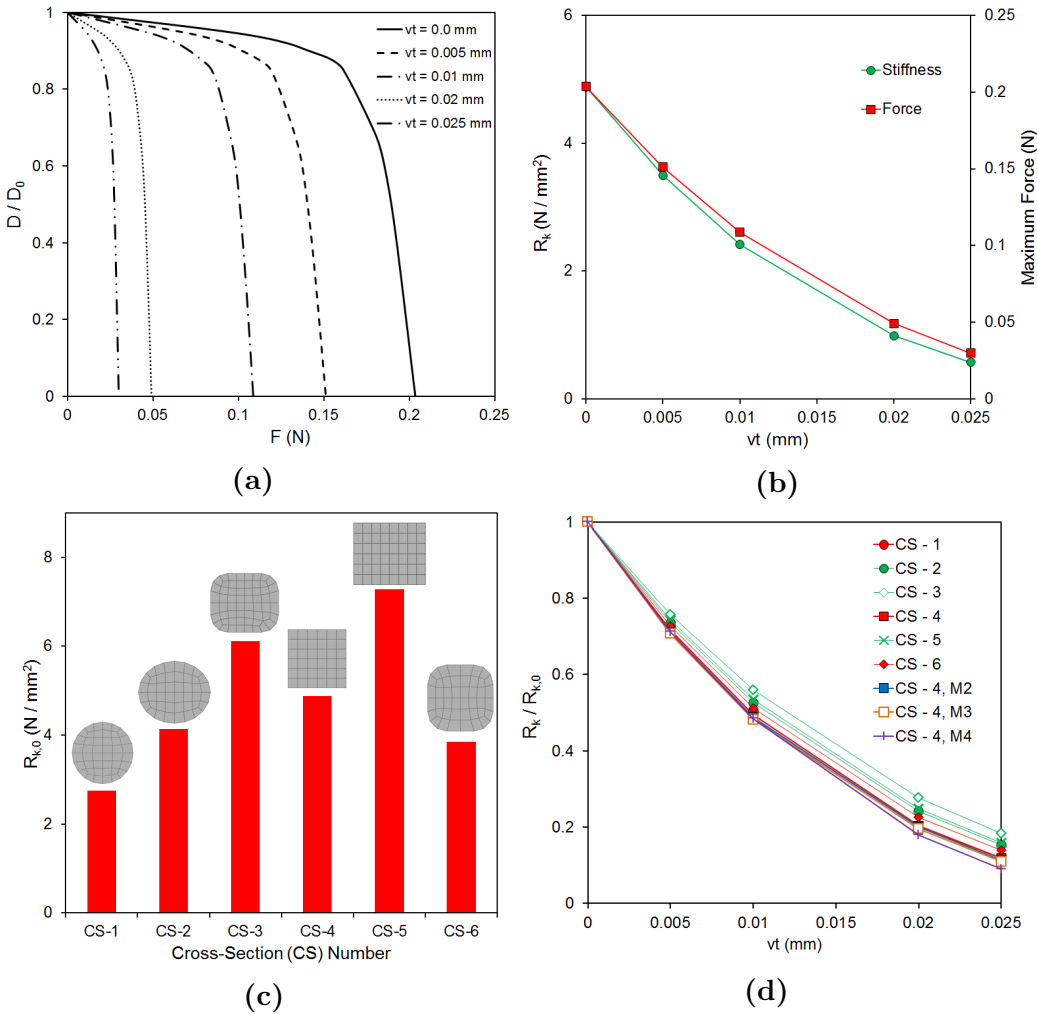


**Figure 7.9.:** (a) Sample force  $F$  diameter  $D$  curves for an elastic-plastic hinge during crushing, following corrosion. (b) Reduction in  $R_k$  and maximum force in a hinge due to corrosion. (c)  $R_k$  values for a selection of hinge profiles before corrosion. (d)  $R_k$  values for a selection of hinge profiles (CS 1-6 in Fig. 7.9c) and materials (M 2-4 in Table 7.1) during corrosion.

in each of the five optimizations performed, and in particular the overall optimal design (Opt 5), is that strut widths are significantly greater than those of the baseline design (143 vs. 114  $\mu\text{m}$  for Opt 5). Fig. 7.9c indicates that struts with greater width have greater initial radial stiffness and Fig. 7.9d shows that struts with greater width have greater stiffness retention. Thus, greater AMS strut width is expected to give better scaffolding performance before and during corrosion. It is noted that the improvement in stiffness retention in the optimal design over the baseline is smaller than the variation in Fig. 7.9d. This is because no limitation on maximum hinge strain is adopted in study P1 while there is a limitation in the optimization study, thus limiting the range of allowable hinge profiles.

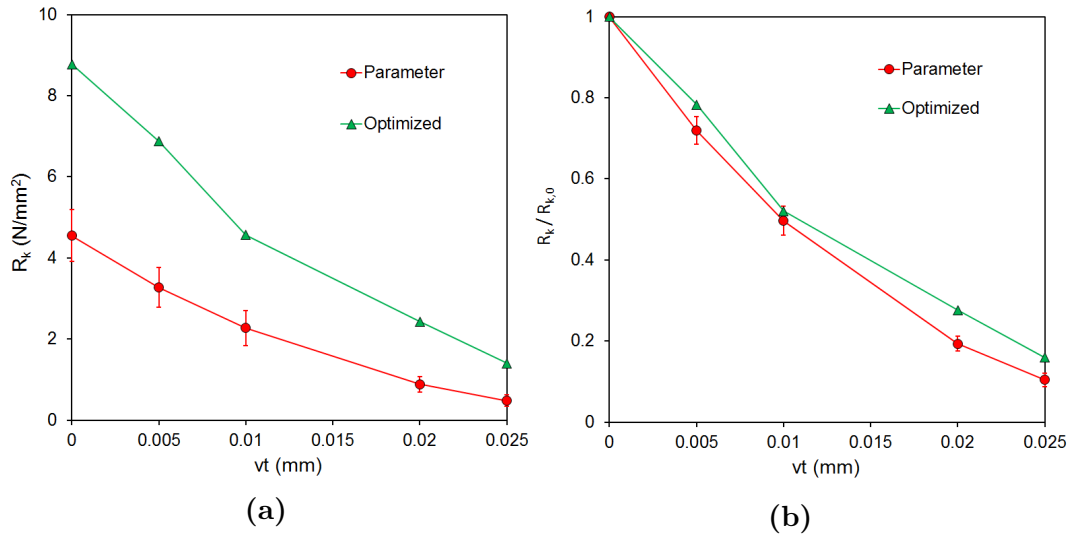


**Figure 7.10.:** (a) Predicted changes in  $R_k$  during corrosion for the optimized design and the designs in the parameter study P2. (b) The fraction of the radial stiffness before corrosion,  $R_{k,0}$ , that is maintained as the stents corrode. Error bars signify one standard deviation from the mean, based on a sample of 25 stent geometries.

### 7.4.2. In-Vivo Deployment Simulations

Fig. 7.11a shows the simulated deployment of a stent in a straight arterial configuration. A realistic ‘dog-bone’ stent profile is noted during balloon inflation.

## 7. Designing an Optimum Bioabsorbable Metal Stent

**Table 7.5.:** Optimized and baseline device dimensions, based on the geometry in Fig. 7.5. The result of the fifth optimization (Opt 5) is taken as the overall optimal design.

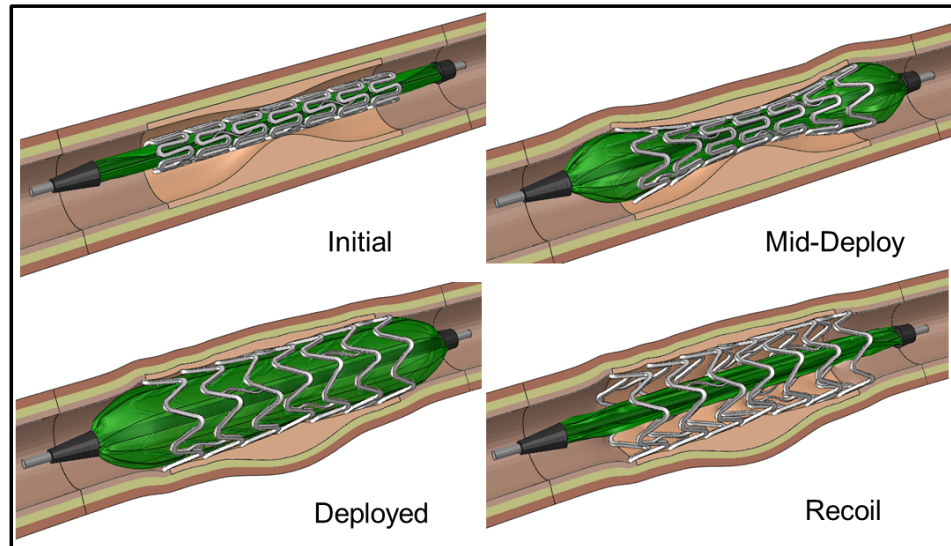
	$L_1$	$L_2$	$L_3$	$H_1$	$H_2$	$W$	$T$	Objective Function
Opt 1	0.406	1.036	0.100	0.785	0.435	0.131	0.137	0.714
Opt 2	0.410	1.044	0.374	0.785	0.421	0.132	0.140	0.682
Opt 3	0.456	1.031	0.456	0.785	0.442	0.139	0.140	0.697
Opt 4	0.408	1.033	0.106	0.785	0.410	0.133	0.136	0.683
<b>Opt 5</b>	0.451	1.053	0.500	0.785	0.393	0.143	0.140	0.670
<b>Baseline</b>	0.319	1.100	0.184	0.785	0.431	0.114	0.117	

Fig. 7.11b shows the simulated tracking of a stent and catheter through a curved stenosed vessel. Straightening of the vessel following stent deployment is shown to be captured by the simulation.

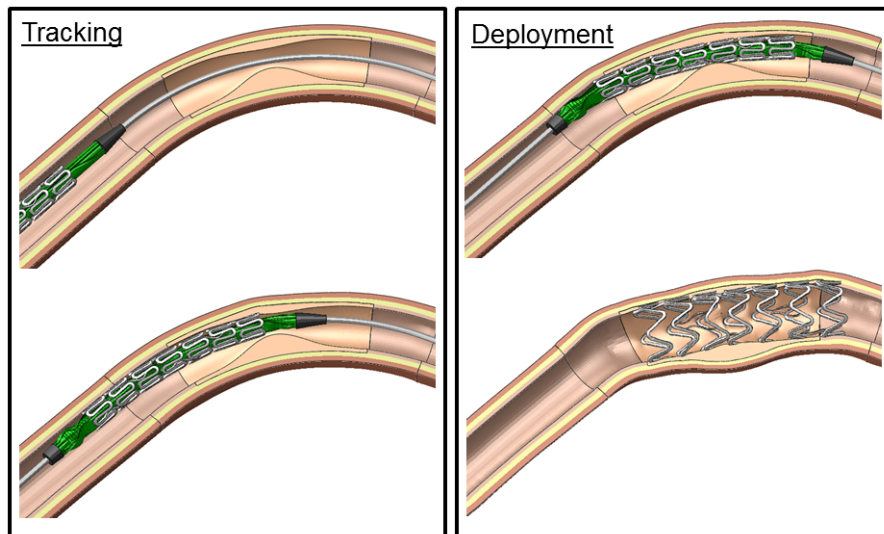
Fig. 7.12a shows cross-sections of predicted stent configurations before and after uniform corrosion for  $vt=37.5 \mu\text{m}$ . It is evident that the optimized AMS maintains greater minimum lumen area (MLA) than the commercial AMS after corrosion. Device collapse is, expectedly, most notable in regions with the highest degree of initial occlusion. To quantify these observations, Fig. 7.12b shows a profile of lumen area along the length of the plaque before stenting, at maximum balloon inflation and after device recoil and corrosion. From this figure it is observed that the optimized AMS and the commercial permanent stent have similar predicted acute recoils. Fig. 7.12c shows predicted reductions in MLA with corrosion for each AMS design. For uniform corrosion, the MLA maintained by the optimized AMS is predicted to be greater than that of the baseline geometry and commercial geometry. Fig. 7.12d shows mass loss for the uniformly corroding stents for the same input corrosion rate,  $v$ . The optimized stent is predicted to lose less mass than the baseline and commercial device for a given immersion time.

Fig. 7.13a compares cross-sections of stented arteries for uniform and pitting corrosion of the baseline geometry for a case where both have lost 15% of their

7. Designing an Optimum Bioabsorbable Metal Stent



(a)



(b)

**Figure 7.11.:** (a) Stent deployment simulation in a straight arterial configuration. (b) Catheter tracking and stent deployment simulation in a curved arterial configuration.

## 7. Designing an Optimum Bioabsorbable Metal Stent

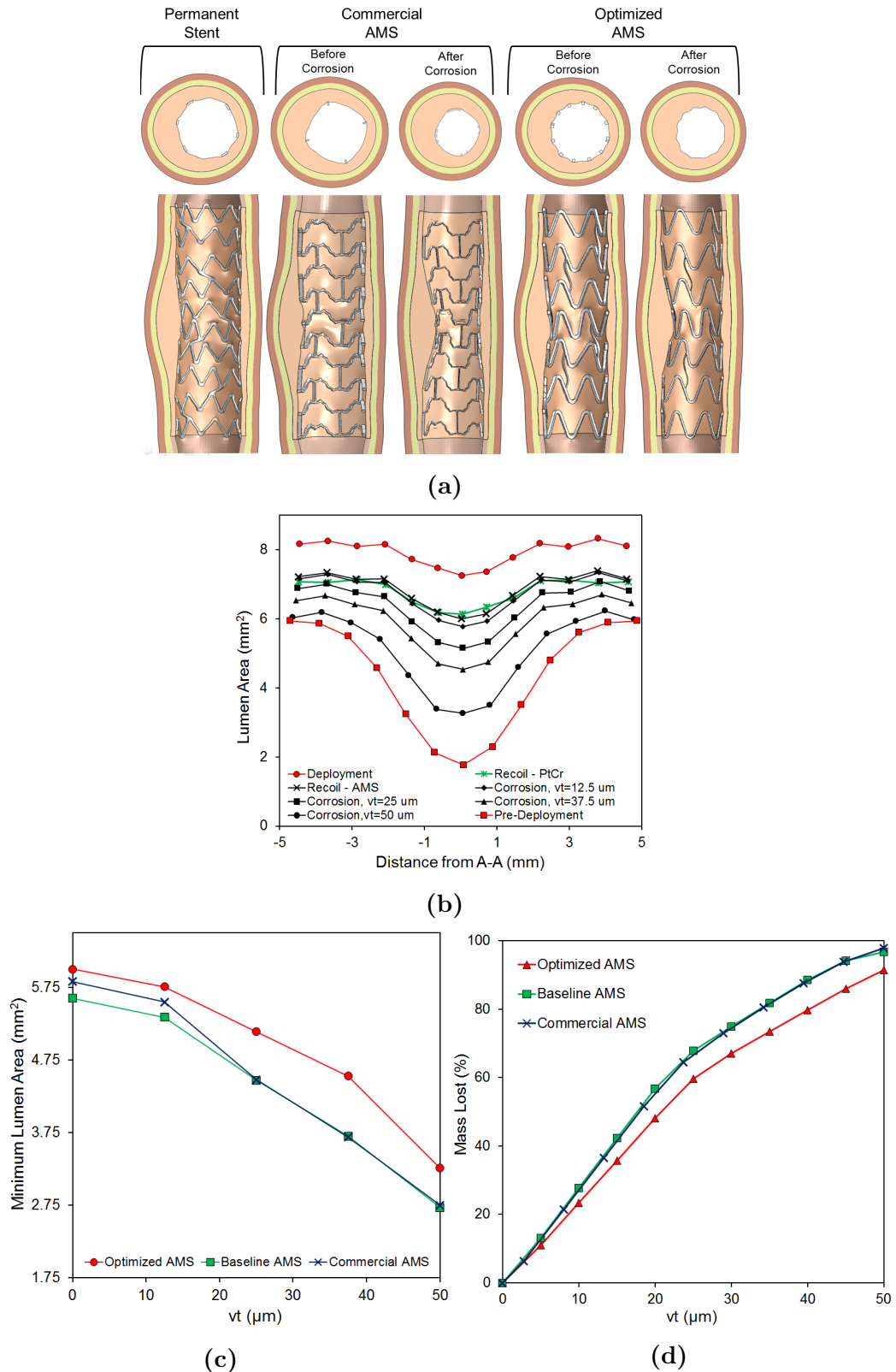


**Figure 7.12.:** (a) Cross-sections of predicted stent configurations before and after uniform corrosion (for  $vt = 37.5 \mu\text{m}$ ). (b) Lumen area profiles for the optimized AMS and OMEGA stent during corrosion of the former. (c) Change in MLA for the optimized, baseline and commercial AMS's undergoing uniform corrosion in a straight vessel. (d) Loss in mass with time for a given input corrosion rate for the optimized, commercial and baseline designs in a straight vessel.

## 7. Designing an Optimum Bioabsorbable Metal Stent

original mass. In this case it is clear that lumen loss is significantly higher in the stent undergoing pitting corrosion. Mass loss, rather than  $vt$ , is a more suitable quantity for presenting the results of the pitting model, as the predictions of this model are not uniquely specified by the quantity  $v$ , given that they also depend on the characteristics of pit initiation and growth ( $\gamma$  and  $\beta$ ). Fig. 7.13b shows predicted lumen loss for stents undergoing uniform and pitting corrosion, with three different random pitting assignments. It is predicted that for a given amount of mass loss, lumen loss is significantly greater for all stents undergoing pitting corrosion than for those undergoing uniform corrosion. A general improvement in lumen retention is predicted for the optimized stent undergoing pitting corrosion over the baseline stent, however the extent of the improvement is small relative to the variation in scaffolding performance for different initial random pit assignments. Fig. 7.13c shows the predicted times at which chronic recoil of the device due to corrosion leads to a 25% stenosis by area, considering the corrosion rates of a number of typical candidate magnesium alloys. The plot allows the extent of performance improvements due to design optimization and improvements due to using different alloys to be compared. It is noted that both optimized and baseline AZ31 alloy stents undergoing pitting corrosion are predicted to reach the critical level of chronic recoil approximately 20 times faster than the same stents undergoing uniform corrosion.

Figs. 7.14a and 7.14b show lumen area profiles for the permanent stent and optimized AMS following deployment in the curved vessel. Similar lumen areas are predicted for both stents to those obtained in straight vessels, shown in Fig. 7.12b, along with similar lumen losses with uniform corrosion for the AMS. Fig. 7.14c shows the change in lumen curvature with stenting for the same stents. The measure of curvature used is the distance between the lumen centroid and a straight line joining the lumen centroids at each end of the plaque. Straightening of the vessel is shown during deployment, with some return to the original curvature

## 7. Designing an Optimum Bioabsorbable Metal Stent

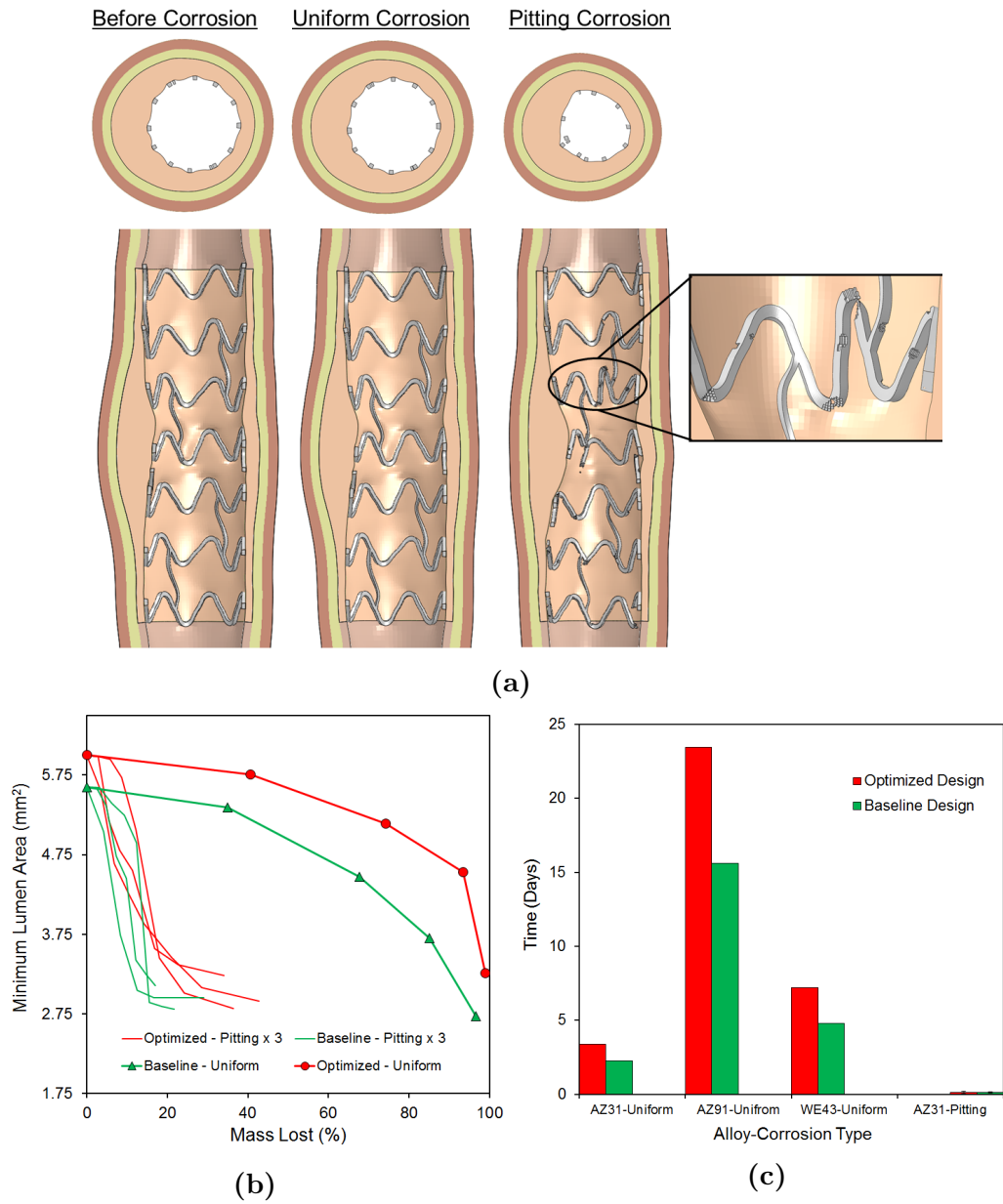


**Figure 7.13.:** (a) Artery cross-section showing predictions for uniform and pitting corrosion of the baseline geometry for 15% mass loss (b) Losses in lumen area due to stent corrosion for uniform and pitting cases. Each of the three curves for the pitting models represents a simulation of the same stent design undergoing pitting with three different random initial pit assignments. (c) Predicted immersion times required for a return to 25% stenosis by area due to corrosion, assuming AZ31 alloy ( $v = 11.0 \mu\text{m d}^{-1}$  from Ch. 6), AZ91 alloy ( $v = 1.6 \mu\text{m d}^{-1}$  from Kirkland *et al.* [42]) and WE43 alloy ( $v = 5.2 \mu\text{m d}^{-1}$  from Li *et al.* [201]) corrosion rates and uniform corrosion. The immersion time for AZ31 alloy undergoing pitting corrosion is also included.

evident following balloon deflation. As the AMS corrodes the curvature of the vessel is predicted to approach that of the original configuration.

## **7.5. Discussion**

### **7.5.1. ALE Corrosion Model**

In this study a novel method for simulating the effects of uniform corrosion on stent scaffolding is developed, based on adaptive meshing. The approach is more efficient than previously developed damage approaches [128] and, since it does not rely on element removal, less sensitive to mesh resolution. The model developed in this study can be easily calibrated, relying only on a knowledge of corrosion rate, and can be applied to corrosion studies on other implants, in particular orthopaedic implants where large deformations are not typical. Due to the explicit tracking of the corrosion surface, the model developed here can also be easily extended to model corrosion in a more physical manner than previous methods. In particular, since the velocity of surface facets is explicitly controlled through a user subroutine, it can depend on, for example, species concentrations and fluxes at the corrosion surface and volume averaged material stresses and strains in the vicinity of the corrosion surface. A limitation of the adaptive meshing approach is that it is difficult to account for complex geometric interactions, for example the merging of corrosion pits.

## 7. Designing an Optimum Bioabsorbable Metal Stent

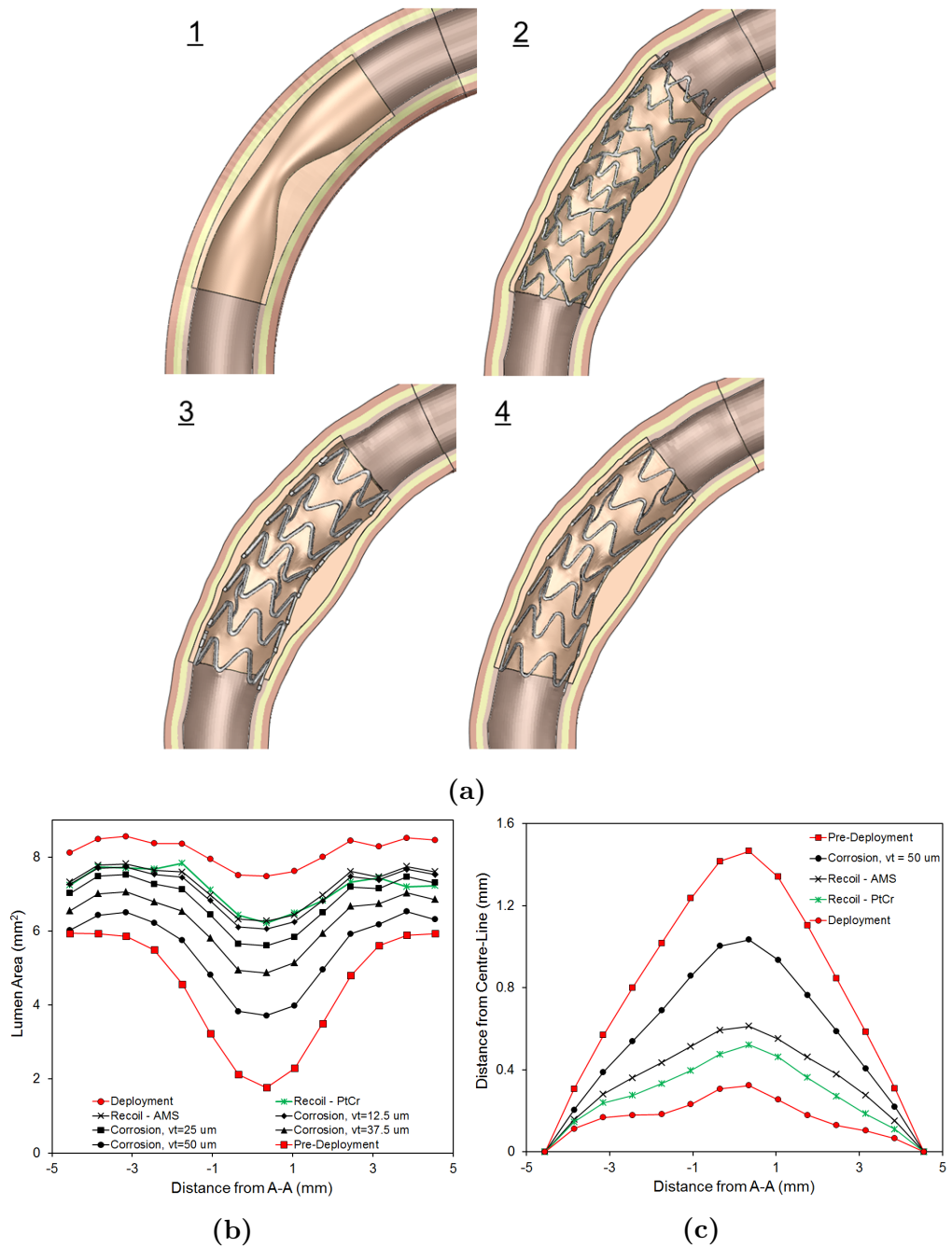


**Figure 7.14.:** (a) Cross-sections of arterial segments: (1.) pre-stenting, (2.) post-stenting with the Omega stent, (3.) post-stenting with the optimized AMS and (4.) following corrosion of the AMS. (b) Lumen area profiles for the permanent and AMS during corrosion of the latter. (c) Change in vessel curvature following stenting, as measured by the distance between the lumen centroid and a straight line (centre-line) joining the lumen centroids at each end of the plaque.

### 7.5.2. Parameter and Optimization Studies

A strong link between the initial and long term radial stiffness and maximum radial forces of AMS's undergoing uniform corrosion is identified, based on predictions in Figs. 7.9b and 7.9d. Results suggest that there is a largely linear loss in radial stiffness and maximum force with uniform corrosion ( $vt$ ) in AMS hinges, with the rate of loss depending mostly on hinge circumferential width and with little dependence on alloy mechanical properties or strut cross-section shape (circular, square, rounded). This means that: i) when assessing a candidate alloy or stent design for AMS application, radial stiffness and maximum force evaluations before corrosion give a reasonable indication of long term performance, ii) a 'first-pass' optimization of an AMS design can simply seek to maximise radial stiffness and force without accounting for corrosion and iii) the rate of loss of stiffness and force for many stent designs and alloys due to uniform corrosion can be approximated from Figs. 7.9d and 7.10b.

The optimization strategy developed in this study goes beyond previous AMS optimization studies [131] in that it implicitly accounts for the effects of corrosion in identifying an optimal stent geometry and uses a 3-D simulation of stent deployment for objective function evaluations. As shown in Fig. 7.10a, the optimization strategy leads to significantly improved long-term device radial stiffnesses relative to designs identified through a Monte-Carlo approach, for a similar computational expense. A particularly important feature of the optimized design is large strut width (143  $\mu\text{m}$ ), as shown in Table 7.5. This large width leads to a favourable initial radial stiffness and is also likely, from Fig. 7.10b, to have contributed to favourable retention of stiffness during corrosion. Based on these predictions (Figs. 7.9d and 7.10b) the use of struts with large widths, which interestingly weren't used in the commercial MAGIC stent (strut width is less than 100  $\mu\text{m}$  based on SEM images [190]), are particularly encouraged for

AMS's. It is noted, however, that the ability to identify designs with both large widths and suitable maximum deployment strains is not straight-forward, due to the limited ductility of currently available magnesium alloys (as shown in Ch. 4), and is only made possible through the use of optimization methods in this study. High strut thicknesses are also encouraged, however: i) they do not contribute to increases in radial stiffness or stiffness retention to the same degree as similar increases in width and ii) feasible values of strut thickness are likely to be limited by other metrics, such as their influence on vessel haemodynamics and device deliverability [31].

### **7.5.3. In-Vivo Deployment Simulations**

Through deployment simulations in stenosed vessels a number of insights into AMS performance is gained. First, the results in Figs. 7.12c, 7.9b and 7.10a give an appreciation of how long-term stent radial stiffness is related to lumen loss over time. This is useful as many AMS designs are likely to have radial stiffnesses that fall between those of the baseline and optimized designs in this study. Second, the predicted improvements in scaffolding duration with stent optimization, shown in Fig. 7.12c, can be directly compared to improvements gained through using alloys with different corrosion rates, which can vary over orders of magnitude [42], and through potential improvements through slowing corrosion rates through coating and surface treatment [101]. A third insight is in relation to the relative performances of AMS's and permanent stents. In Ch. 4 it was predicted that AMS's can match the short-term scaffolding performance of permanent stents based on the results of relatively simple deployment and crimping simulations, similar to those shown in Fig. 7.3b. In this study it is verified in Figs. 7.12b and 7.14b that, with careful design, the performance of a magnesium AMS can match the short-term scaffolding performance of a modern,

permanent stent in complex arterial configurations, albeit with somewhat larger strut cross-sectional area.

## 7.6. Limitations

Corrosion is treated in a phenomenological manner in this study, with a focus on its effects on device mechanical integrity. In reality, the corrosion of devices in the body is a highly complex phenomenon and can depend on alloy microstructure, surface condition, residual and cyclic stresses, stent processing and transport conditions in the vessel. Uniform corrosion is the target behaviour for AMS alloys, as it leads to predictable device performance, and as shown in Fig. 7.13b, generally results in greatest retention of scaffolding for a given amount of mass loss. If uniform corrosion is maintained *in-vivo*, the results of this study remain applicable, even if vessel transport conditions or surface conditions lead to time dependent corrosion rates.

If uniform corrosion is not applicable, predicted stent radial stiffnesses for a given amount of mass loss may be over-estimated in this study. The extent of this over-estimation can be appreciated based on the results in Fig. 7.13b. The pitting model used in this study is calibrated based on the results of experiments in a reasonably aggressive corrosion environment and its predictions are in good agreement with observed *in-vitro* stent behaviour in a similar environment [202]. It is likely, however, that the pitting results in Fig. 7.13b (and the relevant experiments) under-estimate *in-vivo* stent scaffolding duration somewhat. Thus, it is likely that general AMS *in-vivo* corrosion behaviour falls between predictions shown in Fig. 7.13b for the ideal uniform corrosion behaviour and the more aggressive pitting corrosion behaviour.

In this study the time-dependent behaviour of coronary tissue is not considered. Following deployment, the tissue will gradually adapt to the presence of the stent which may reduce inward radial pressure on the device. Accounting for this behaviour is important in future predictions of AMS performance and may lead to an increase in predicted lumen area for a given corrosion time. Despite this limitation, it is noted that the deployment simulations in vessels performed in this study are the most detailed of those performed on AMS's to date.

## **7.7. Conclusions**

- A new method for modelling stent corrosion is developed based on adaptive meshing. The method is easily calibrated, is more efficient than previously developed damage based methods and, since it does not use element removal, is less sensitive to mesh resolution.
- The radial stiffness and maximum radial force in stents undergoing uniform corrosion are predicted to decrease as an approximately linear function of the quantity 'corrosion rate multiplied by immersion time'. The rate of decrease is predicted to primarily depend on circumferential strut width and is reasonably independent of alloy mechanical properties or strut cross-section shape.
- Large AMS strut widths are recommended based on predictions of increased short-term radial stiffness and force and favourable retention of both during corrosion.
- An AMS optimization strategy is developed and used to identify an AMS

## *7. Designing an Optimum Bioabsorbable Metal Stent*

design with favourable strut width, while also accounting for the limited mechanical properties of currently available magnesium alloys.

- The short-term scaffolding performance of an optimized AMS design is predicted to match that of a modern permanent stent in a stenosed vessel. A favourable return to a natural vessel curvature is also predicted for the AMS as it corrodes.
- An optimized AMS design is predicted to maintain lumen patency approximately 1.5 times longer than a commercial design and a baseline design.

# 8. Physical Modelling of AMS

## Corrosion

### 8.1. Chapter Summary

Corrosion was modelled using a phenomenological approach in Chs. 6 and 7. In this chapter a physical corrosion model for AMS's is developed, based on the ALE adaptive meshing model introduced in Ch. 7. The model is used to simulate the corrosion of an AMS repeating unit in a situation where the diffusion of magnesium ions in the corrosive environment is the limiting factor on the corrosion rate. Model predictions in terms of mass loss rate and loss in device mechanical integrity with time are compared to the phenomenological models developed in Ch. 7.

### 8.2. Introduction

As discussed in Ch. 2, most physical corrosion models developed to date have focused on particular features in 2-D geometries, such as single corrosion pits or

bimetallic interfaces. In order to develop a physical corrosion model for coronary stents, the complex 3-D geometry of the device must be accounted for. This introduces difficulties, as it requires the solution of a 3-D moving boundary problem. The ALE corrosion model and facet based approach developed in Ch. 6 allows the complex moving boundary problem to be solved in a straightforward and efficient manner. The previously developed model is enhanced in this chapter, such that the velocity of the corrosion surface depends on the chemical state at the interface. The model developed here represents, to the author's knowledge, a first physical corrosion model for AMS's that accounts for the 3-D geometry of the device.

For the model developed in this chapter it is assumed that the corrosion rate is governed by the diffusion of magnesium ions in the corrosion environment. While this is a reasonably simple assumption, the model developed here can be easily extended to account for activation driven dissolution [203], or to have the corrosion rate depend on hydrogen ion diffusion or the formation rate of corrosion products on the corrosion surface [123].

### 8.3. Methods

The transport of a species  $I$  in solution can be generally described through the Nernst-Planck equation [121]:

$$\mathbf{N}_I = -D_I \nabla c_I + \mathbf{V} c_I - \frac{z_I D_I F c_I}{RT} \nabla \phi \quad (8.1)$$

where  $\nabla a = \frac{\partial a}{\partial x_i} \mathbf{e}_i$  is the gradient vector of the scalar field  $a$ ,  $\mathbf{N}_I$  is the species flux vector,  $D_I$  is the diffusion coefficient,  $c_I$  is the species concentration,  $\mathbf{V}$  is the solution velocity,  $\phi$  is the potential,  $z_I$  is the charge and  $F$ ,  $R$  and  $T$  are Faraday's

## 8. Physical Modelling of AMS Corrosion

constant, the universal gas constant and temperature respectively. This equation represents the flux of a species under diffusion, migration in a potential field and convection.

The conservation of flux for species  $I$  is then:

$$\frac{\partial c_I}{\partial t} = -\nabla \cdot \mathbf{N}_I \quad (8.2)$$

where  $\nabla \cdot \mathbf{a} = \frac{\partial a_i}{\partial x_i}$  is the divergence of the vector field  $\mathbf{a}$ . From Eqns. 8.1 and 8.2 it can be seen that the movement of ions through a solution is governed by the concentration gradient, the potential gradient and the fluid velocity. For the purposes of this study the fluid velocity and potential gradient are assumed to be zero. This may correspond to a case where movement of reactants is a largely diffusion controlled process. For AMS's, such a case may be relevant for stents with a thick polymer coating, stents with a quickly forming layer of corrosion product or stents embedded in tissue for cases where the transport of reacting species is largely diffusion controlled. In this case, Eqns. 8.1 and 8.2 reduce to Fick's law:

$$\frac{\partial c_I}{\partial t} = -\nabla \cdot (D_I \nabla c_I) \quad (8.3)$$

A further assumption in this study is that the transport and solubility of magnesium ions in solution govern the underlying rate of chemical reactions associated with the corrosion process, such that Eqn. 8.3 becomes:

$$\frac{\partial c_{Mg}}{\partial t} = -\nabla \cdot (D_{Mg} \nabla c_{Mg}) \quad (8.4)$$

where the subscript  $Mg$  pertains to magnesium ions and is omitted for the remainder of this chapter. As magnesium dissolves in solution, the corrosion surface moves, leading to a moving boundary problem. As the corrosion surfaces moves, mass must be conserved in the solid and solution. Assuming that the rate of

## 8. Physical Modelling of AMS Corrosion

dissolution is far greater than the rate at which ions diffuse from the corrosion surface leads to the following Rankine-Hugoniot condition on the moving corrosion surface (see Scheiner and Hellmich [203]):

$$\{-D\nabla c - (c_{sol} - c_{sat})\mathbf{v}\} \cdot \mathbf{n} = 0 \quad (8.5)$$

where  $c_{sol}$  is the concentration of magnesium ions in the solid,  $c_{sat}$  is the saturation concentration of magnesium ions in solution,  $\mathbf{v}$  is the corrosion surface velocity and  $\mathbf{n}$  is the corrosion surface normal. Eqns. 8.4 and 8.5 amount to a Stefan problem, for which analytical solutions have been derived for simple geometries [204].

To implement Eqns. 8.4 and 8.5 in Abaqus the ALE adaptive meshing strategy of Ch. 7 is employed. As part of this strategy it is necessary to identify the velocity of each facet  $\mathbf{v}$  along its inward pointing normal  $\mathbf{n}$ , shown in Fig. 7.1b. Based on Eqn. 8.5 this can be found as follows:

$$v = \frac{D(\nabla c \cdot \mathbf{n})}{c_{sol} - c_{sat}} \quad (8.6)$$

The identification of the quantity  $\nabla c \cdot \mathbf{n}$  is not trivial in this case. The approach taken here is shown in Fig. 8.1. The facet outward pointing normal is projected into the element containing the facet on the solution side of the interface. The concentration at the point of intersection of the outward normal and the element faces  $c_i$  is then found. The quantity  $\nabla c \cdot \mathbf{n}$  is given by  $c_i - c_{sat}$ .

To test the implementation of the newly developed model, predictions are compared to a 1-D analytical model based on similarity solutions to Stefan problems used by Javierre *et al.* [205] for solidification problems, and adopted here for the case of diffusion controlled corrosion. As shown in Fig. 8.2, the corrosion domain is split into two parts, solid and liquid. The initial length of the solid domain

## 8. Physical Modelling of AMS Corrosion

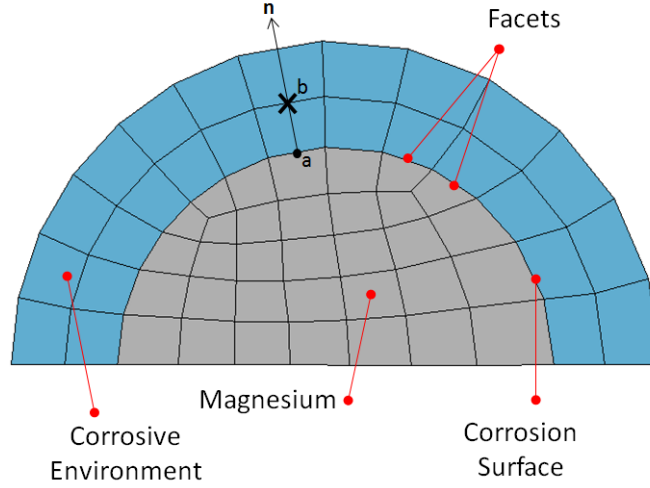


**Figure 8.1.:** The concentration gradient at the corrosion surface is approximated by projecting an outward normal  $\mathbf{n}$  from the centroid of each facet,  $a$ . The concentration in the corrosive environment is evaluated at point  $b$ , which is the intercept of the normal and the faces of element adjacent to the facet.

is 0.2 mm and the length of the liquid domain is 4.8 mm. The initial concentration of magnesium in solution  $c_0$  is  $0.0 \text{ kg m}^{-3}$ .  $c_{sol}$  is  $1735 \text{ kg m}^{-3}$ , which is the mass density of pure magnesium.  $c_{sat}$  is  $134.0 \text{ kg m}^{-3}$ , which is the solubility of magnesium chloride in water at  $25^\circ \text{C}$  [206]. The saturation concentration of magnesium ions in solution depends strongly on the temperature, pH and the availability of other ions, such as chlorine. For example, in the absence of chlorine ions, magnesium hydroxide is formed, which has a low solubility in water and leads to a  $c_{sat}$  value of  $0.0048 \text{ kg m}^{-3}$  [206]. The diffusivity  $D$  of magnesium in sea-water is taken as  $0.10575 \text{ mm}^2 \text{ h}^{-1}$  [207].

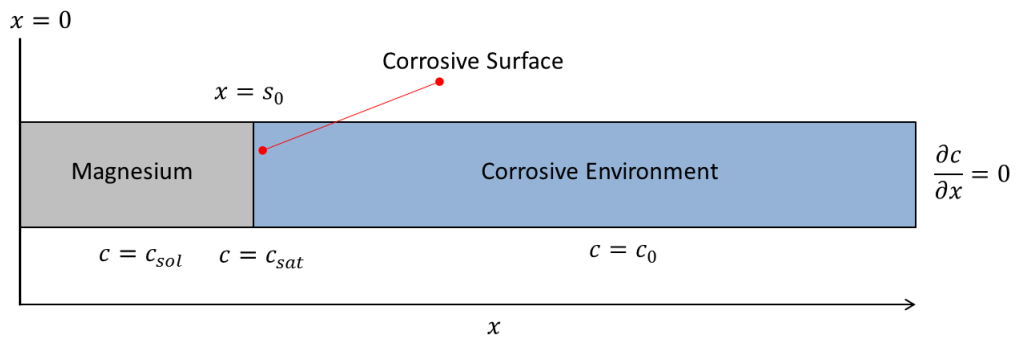


**Figure 8.2.:** A schematic of the 1-D corrosion problem solved analytically and using the ALE model in this chapter.

## 8. Physical Modelling of AMS Corrosion

The movement of the corrosion interface over time is given by:

$$s(t) = s_0 + 2\alpha\sqrt{t} \quad (8.7)$$

where  $s(t)$  and  $s_0$  are the current and initial interface positions respectively and  $\alpha$  is obtained through solving:

$$\alpha = \frac{c_0 - c_{sat}}{c_{sol} - c_{sat}} \sqrt{\frac{D}{\pi}} \frac{\exp\left(\frac{-\alpha^2}{D}\right)}{\operatorname{erfc}\left(\frac{-\alpha}{\sqrt{D}}\right)} \quad (8.8)$$

The concentration of magnesium in the solid and solution at position  $x$  is then:

$$c(x, t) = \begin{cases} c_{sol} & \text{if } x < s(t) \\ c_0 + \frac{(c_{sat} - c_0) \operatorname{erfc}\left(\frac{x - s_0}{2\sqrt{Dt}}\right)}{\operatorname{erfc}\left(\frac{-\alpha}{\sqrt{D}}\right)} & \text{if } x \geq s(t) \end{cases} \quad (8.9)$$

The corrosion of a stent repeating unit in solution is modelled using the ALE model and the Abaqus/Standard solver. The geometries of the stent and corrosion environment are shown in Fig. 8.3. Both the stent and surrounding environment are meshed using 3-D linear coupled temperature-displacement reduced integration brick elements (C3D8RT). The stent geometry is obtained through the simulated expansion of a stent unit with a stiff inner cylinder. The residual stress-state in the device is not considered during corrosion. The initial stent strut thickness and width are both 120  $\mu\text{m}$ . The coefficients used for the 1-D analytical model are adopted for the stent model.

The analyses in this chapter are performed to: i) assess the corrosion behaviour of an AMS geometry undergoing diffusion controlled corrosion in terms of mass loss rates and changes in device geometry, ii) assess the sensitivity of stent corrosion behaviour to changes in magnesium saturation concentration and diffusivity in the surrounding media, which is important since the saturation concentration and diffusivity of magnesium in human blood are not widely reported and iii) to assess

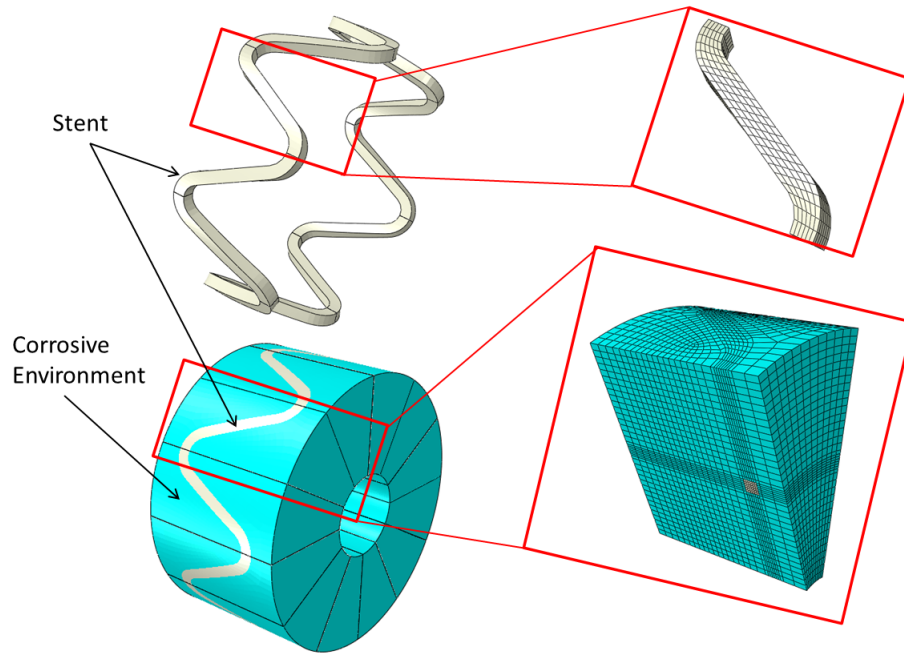


**Figure 8.3.:** Finite element model of a stent ring embedded in a corrosive environment. Due to the symmetry of the problem one 12th of the geometry is modelled. The corrosion environment is an annulus of length 1.47 mm and inner diameter 0.88 mm. The outer diameter is 4.88 mm. The stent length is 1.1 mm and outer diameter is 2.94 mm.

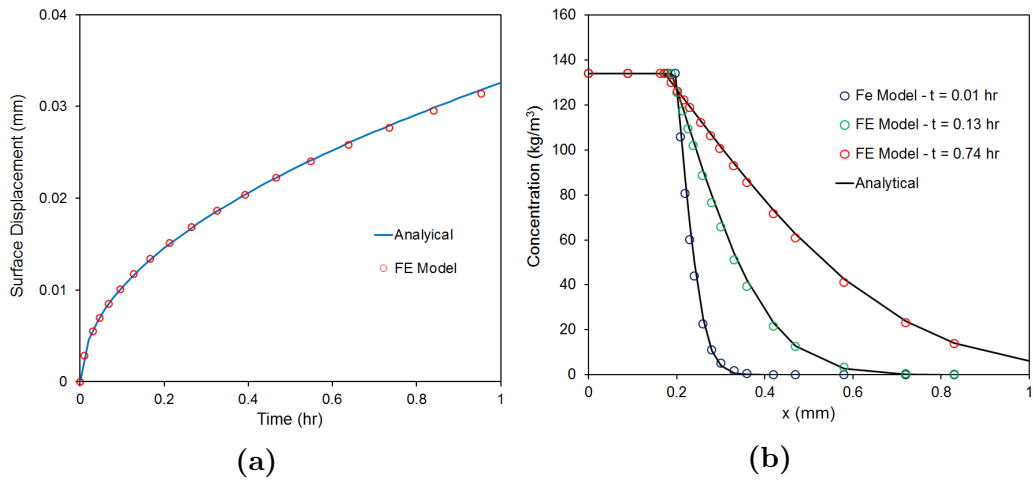
the differences in corroded device geometry and mechanical integrity predictions for the physical model of this chapter and the phenomenological ALE uniform corrosion model developed in Ch. 7. The final assessment is important as it allows the range of applicability of the more readily implemented phenomenological model to be assessed. Simulations in this chapter are performed on a single quad-core Intel i7 processor on a Dell XPS PC, each requiring approximately four CPU hours.

## 8.4. Results

Fig. 8.4a shows a comparison of corrosion surface displacement and Fig. 8.4b shows magnesium ion concentration predicted by the ALE corrosion model and given by the 1-D analytical model. There is good agreement between the models,

## 8. Physical Modelling of AMS Corrosion

verifying the applicability of the ALE adaptive meshing algorithm in Abaqus for Stefan problems of this type.



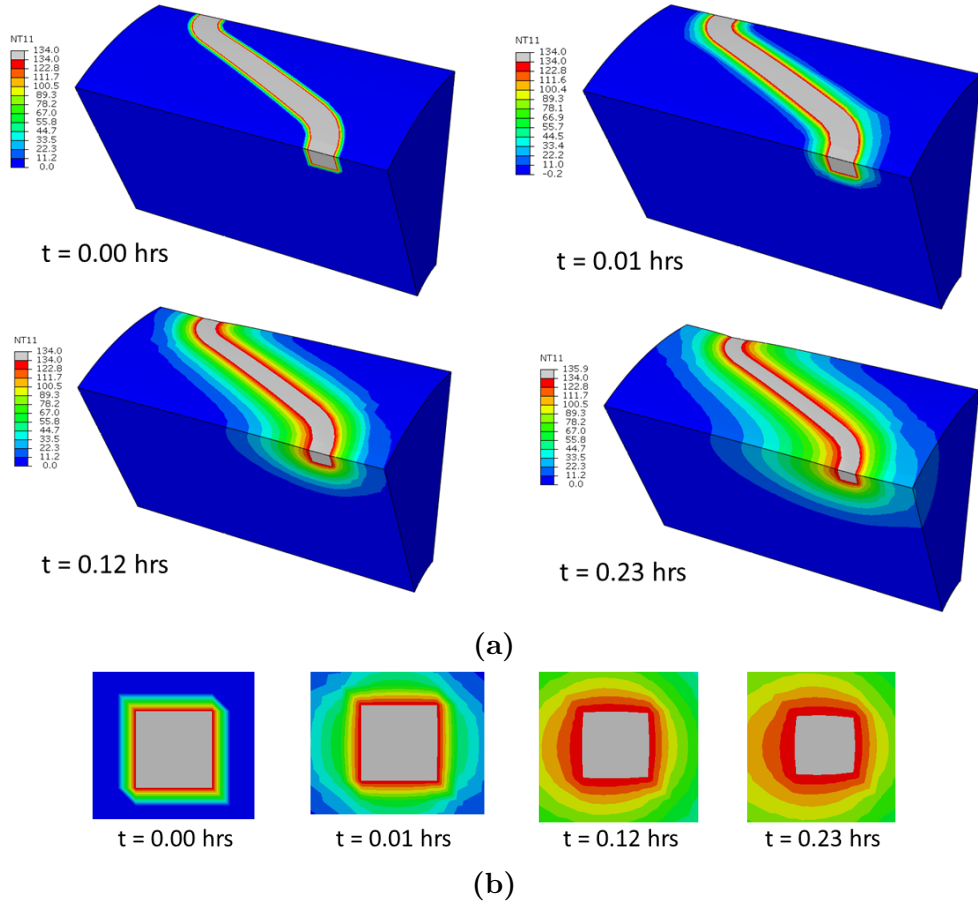
**Figure 8.4.:** A comparison of the predictions of the ALE corrosion model and the corresponding analytical solution to the Stefan problem. The predicted movement of the corrosion surface over time is shown in (a) and the predicted evolution of the concentration of magnesium ions in the solid and solution during corrosion is shown in (b).

Fig. 8.5a shows contour plots of predicted magnesium ion concentration in the corrosive environment over time. As the device corrodes its dimensions are reduced. The cross-section of the device takes on an expected ‘rounded’ appearance as corrosion progresses, shown in Fig. 8.5b.

Mass losses versus time profiles are shown in Figs. 8.6a and 8.6b for different magnesium saturation concentrations and diffusivities. It is observed that the mass loss is largely proportional to the square root of time in solution.

As shown in Fig. 8.7a, the constant of proportionality ( $A$  in Fig. 8.6b) is itself proportional to the saturation concentration. As shown in Fig. 8.7b, the slope of this second proportional relationship ( $B$  in Fig. 8.7a) increases with increasing diffusivity according to a power law. Using these findings it is possible to approximate the mass loss rate for the stent analysed here over a range of diffusivities

## 8. Physical Modelling of AMS Corrosion



**Figure 8.5.:** Contour plots of predicted magnesium ion concentration in  $\text{kg m}^{-3}$  in the corrosive environment over time. In (a) the upper half of the model has been removed for illustrative purposes. Grey regions correspond to non-corroded metal. (b) Illustration of the changing dimensions of a cross-section of the hinge as it corrodes.

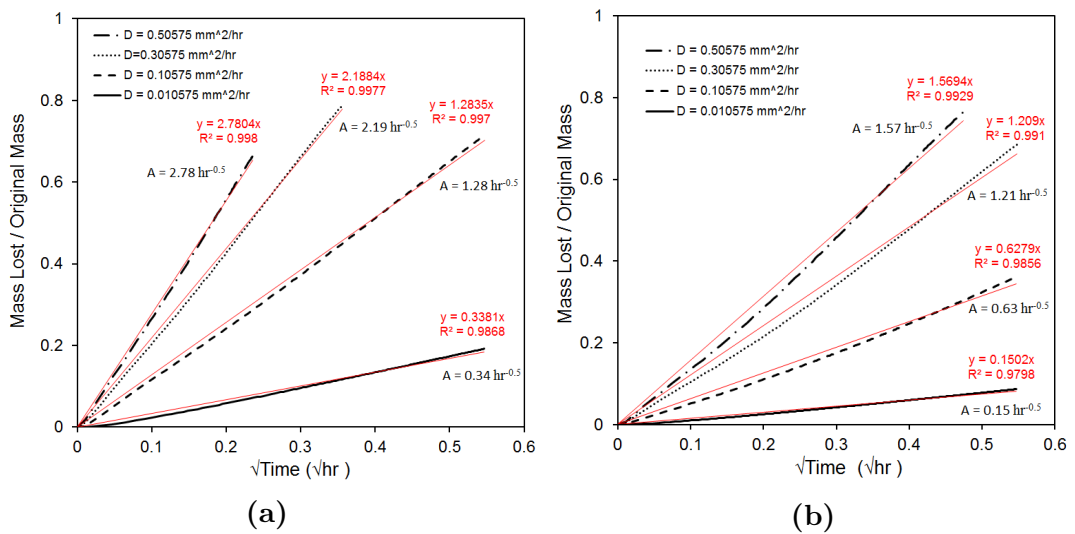


**Figure 8.6.:** Predicted loss in mass with time for a saturation concentration of (a)  $134.0 \text{ kg m}^{-3}$  and (b)  $13.4 \text{ kg m}^{-3}$ . Linear best fits of slope  $A \text{ hr}^{-0.5}$  are also shown in red for each set of data.

## 8. Physical Modelling of AMS Corrosion

and saturation concentrations through the following relationship:

$$\frac{dM}{dt} = \frac{\alpha D^\beta c_{sat}}{\sqrt{t}} \quad (8.10)$$

where  $M$  is the fraction of mass lost due to corrosion and  $\alpha$  and  $\beta$  are constants, equal to 0.017 and 0.57 respectively.

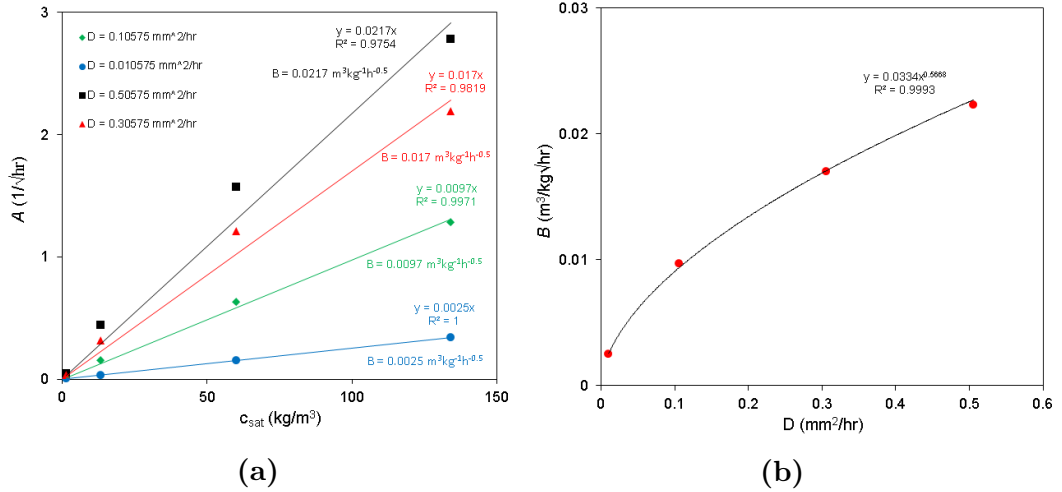


**Figure 8.7.:** (a) Predicted change in the constant of proportionality  $A$  from Figs. 8.6a and 8.6b with increasing saturation concentration. Linear best fits of slope  $B \text{ m}^3 \text{ kg}^{-1} \text{ hr}^{-0.5}$  are also shown for each set of data. (b) Predicted change in the constant of proportionality  $B$  from Fig. 8.7a with increasing diffusion coefficient.

Fig. 8.8a shows predicted mass loss versus time for the phenomenological and physical corrosion models. It is noted that the mass loss rate is largely constant for the phenomenological model due to the assumption of a constant corrosion rate. Although not performed here, it is noted that it is possible to modify the applied corrosion rate over time for the phenomenological model such that both the phenomenological and physical models have identical mass loss rates (for details on modifying time scales in the phenomenological model see Appendix A.4). Fig. 8.8b shows a comparison of the geometries of the AMS following corrosion with the physical and phenomenological models for the same  $\beta$  amount of mass loss. While the geometries are largely similar, the physical corrosion model expectedly predicts more rounded edges and also less corrosion in the inside of hinges, where there are lower concentration gradients and more corrosion on the

outside of hinges.

Figs. 8.9a and 8.9b show predicted losses in radial stiffness and strength with corrosion for the physical and phenomenological models, based on the definitions of these terms in Ch. 7. There is very close agreement between the predictions of both models, suggesting that the phenomenological model of Ch. 7 may be suitable for predicting the performance of AMS's undergoing diffusion controlled corrosion.

## 8.5. Discussion

A physical corrosion model is developed here for complex 3-D geometries, based on the use of ALE adaptive meshing. The model, implemented in the Abaqus commercial finite element solver shows good agreement with the analytical solution of a 1-D moving boundary diffusion corrosion problem and represents a first attempt at modelling the corrosion of AMS's using a physical, rather than phenomenological, approach. The verification performed here is also the first verification, to the author's knowledge, of the applicability of the ALE adaptive meshing algorithm in Abaqus for the solution of Stefan type problems.

The rounded appearance of struts following diffusion controlled corrosion is expected, and is commonly observed following electro-polishing treatments on stents. The dependence of mass loss on the square root of time in the stent, manifested in Eqn. 8.10, is likely to follow from the relationship between corrosion surface position and time for the 1-D corrosion problem, given in Eqn. 8.7 and shown in Fig. 8.4a. It is interesting that such a relationship holds, despite the complex geometry of the stent.

## 8. Physical Modelling of AMS Corrosion

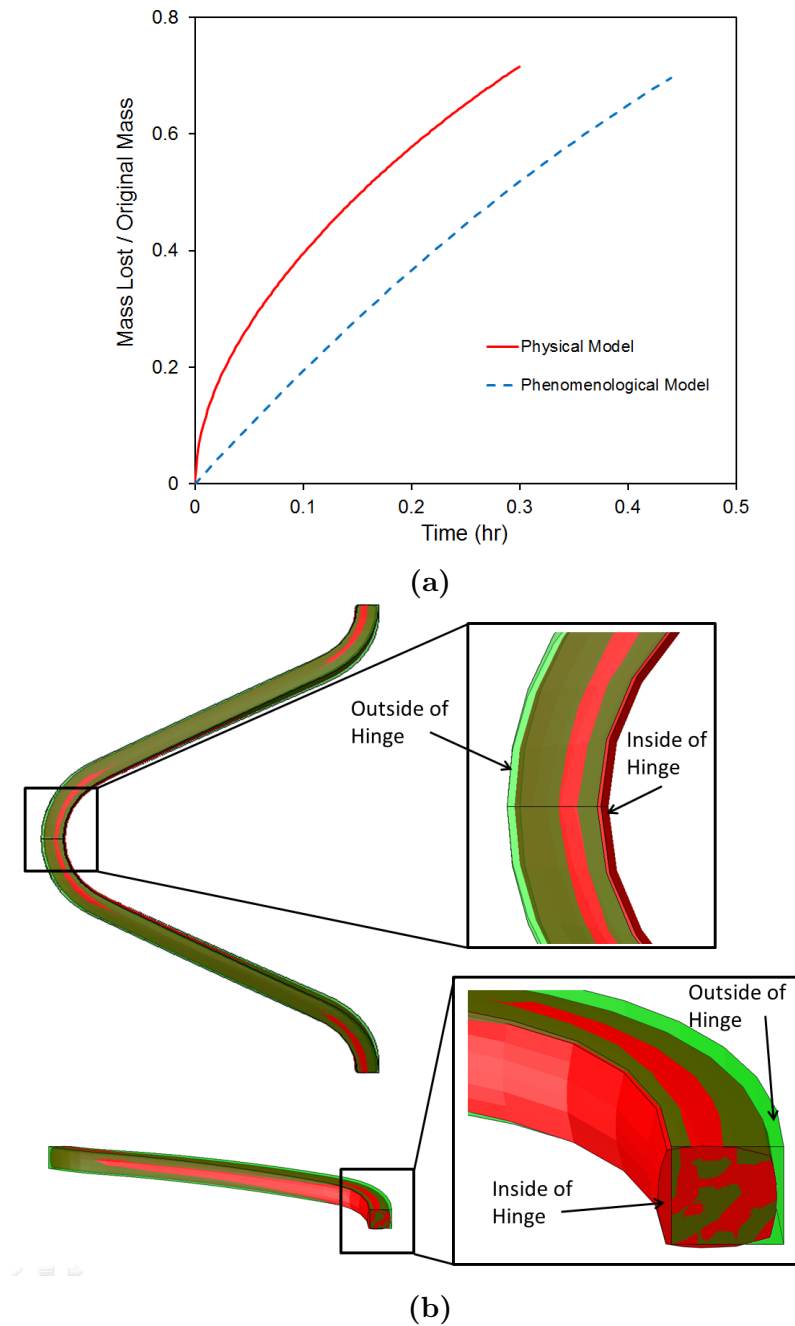


**Figure 8.8.:** (a) Comparison of mass lost over time predicted by the physical and phenomenological corrosion models. (b) Comparison of the stent geometry at 70% mass loss for both models. The physical corrosion model is shown in red and the phenomenological model is overlaid in transparent green. The physical model predicts greater mass loss on the outside of the hinge and less mass loss on the inside of the hinge than the phenomenological model.

## 8. Physical Modelling of AMS Corrosion

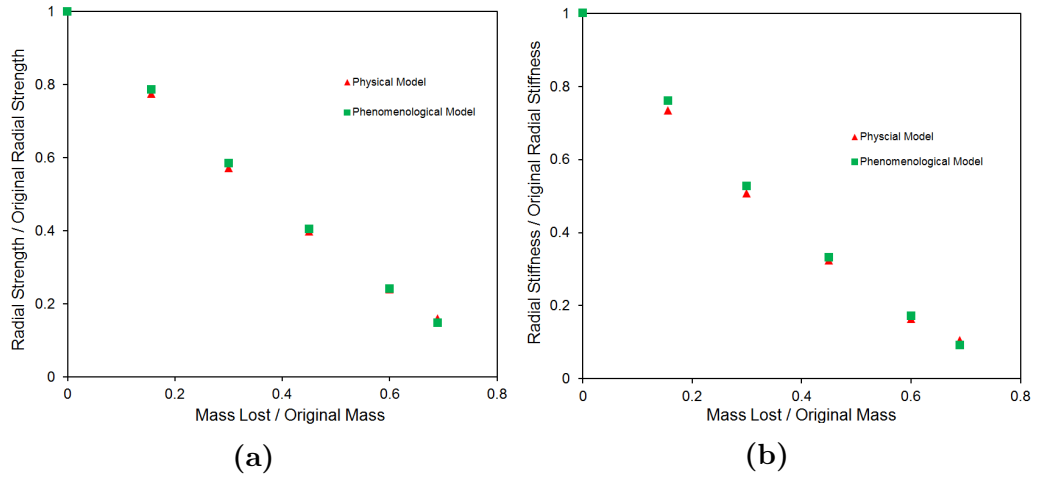


**Figure 8.9.:** (a) Predicted loss in radial strength with corrosion for the physical and phenomenological (ALE) corrosion models. (b) Predicted loss in radial stiffness with corrosion for the physical and phenomenological (ALE) corrosion models.

Eqn. 8.10 gives a number of useful insights into the corrosion of AMS's. It predicts that the mass loss rate is proportional to the saturation concentration of magnesium ions in solution. This facilitates predictions of corrosion rates in a variety of environments, which is of particular importance given that the solubility of magnesium ions depends strongly on the availability of chlorine ions in solution [92]. The dependence of mass loss rate on diffusivity is also of interest, given that a range of effective diffusivity values may be applicable depending on whether the device is embedded in polymer, tissue or corrosion product.

The physical and phenomenological corrosion models are in good agreement regarding predictions of device mechanical integrity for the same amount of mass lost, although as shown in Fig. 8.8a, the predicted amount of mass lost over time is different for both models. This difference can potentially be addressed through modifying the input corrosion rate for the phenomenological model, such that output mass loss rates are in agreement for both models. Based on this approach, this suggests that the phenomenological model developed in Ch. 7 is suitable for modelling at least diffusion controlled corrosion, where suitable input corrosion rates for the phenomenological corrosion model can be identified through the use

of the physical model and Eqn. 8.10.

## 8.6. Limitations

The physical corrosion model developed here gives a number of useful insights into AMS corrosion. However, the assumption of corrosion driven by magnesium diffusion alone limits its applicability. An obvious next step is to include the ability to explicitly model the reaction kinetics between magnesium and hydroxide ions at the corrosion surface, corrosion product deposition and ion migration under electric potential fields. The inclusion of these features would greatly extend the predictive capability of the existing model.

## 8.7. Conclusions

A physical corrosion model is developed for AMS's and its predictions are compared to those of the phenomenological model developed in Ch. 7. The following conclusions can be made:

- A physical model is developed that uses the ALE adaptive meshing method to model the corrosion of a 3-D stent geometry.
- Assuming that the corrosion rate is governed by the diffusion of magnesium ions in solution, it is predicted that the mass loss rate from the device is inversely proportional to the square root of immersion time.
- It is predicted that the mass loss rate is proportional to the saturation con-

## 8. *Physical Modelling of AMS Corrosion*

centration of magnesium ions in solution and is related to the diffusivity of magnesium ions in solution through a power law behaviour, where doubling the diffusivity increases the mass loss rate by a factor of approximately 1.47.

- The phenomenological corrosion model developed in Ch. 7 predicts a similar loss in mechanical integrity to the physical corrosion model for a given amount of mass loss.

# 9. Discussion and Conclusions

## 9.1. Chapter Summary

This chapter summarizes and discusses the outcomes of the work in this thesis. A brief summary of the outcomes of the individual chapters of the thesis is given in **Section 9.2**. Recommendations for the design of future stents based on the findings of the thesis are given in **Section 9.3**. Ideas for future studies and overall conclusions are given in **Sections 9.4** and **9.5** respectively.

## 9.2. Thesis Summary

New generations of coronary stents with thinner struts or consisting of bioabsorbable metals have the potential to significantly improve the clinical outcomes of coronary angioplasty. To ensure the safety and efficacy of these devices their mechanics should be well understood. The focus of this thesis is the application of numerical modelling in improving the understanding of the mechanics of next generation coronary stents.

The mechanical behaviour of absorbable metallic stents (AMS's) has not been

## 9. Discussion and Conclusions

widely reported. In Ch. 4 the mechanical performance of a range of AMS's was directly compared to that of conventional permanent stents for the first time using finite element analysis, across a range of important metrics such as radial stiffness and strength, recoil, flexibility and fracture risk. This comparison is important as it allows the identification of potential short-comings in the design of current bioabsorbable devices and materials and also gives designers and clinicians useful information regarding the degree to which current AMS's compare to conventional stents in terms of scaffolding performance. It was found that for a given geometry magnesium AMS's have inferior radial stiffness and strength to permanent stents and have relatively high recoil. However, through increasing strut dimensions within acceptable limits it was shown that magnesium AMS's can be developed with similar scaffolding performance to permanent stents. A finding of particular importance in this chapter was that magnesium AMS's are, in general, subject to significantly higher fracture risks than conventional stents. This finding is of importance given the existing occurrence and consequences of fracture for conventional stents [4].

Classical plasticity theories, which assume that material is homogeneous, are often used in the analysis and design of stents. These theories are not capable of capturing size effects, such as those arising from the small number of metallic grains through stent strut dimensions. In Ch. 5 a micromechanics approach was taken to study the deformation of stent components, using crystal plasticity theory. This study is important as it provides a far more precise design guide for stents than an existing rule of thumb, that no fewer than 8-10 grains should be maintained through the strut dimensions [34]. In the study a new relationship was established between the number of grains through a strut dimension and the overall ductility of the strut for a range of different materials. A finding of particular interest arising from the resulting equation was that cobalt chromium (L605) stents required a similar number of grains through their dimensions when

## 9. Discussion and Conclusions

compared to stainless steel (316L) stents to prevent significant losses in ductility, despite the superior bulk mechanical performance of L605 alloy. This finding is of interest in stent design since size effects in L605 have not been characterized experimentally and since this alloy is now being used in the development of stents with very thin struts [33]. Another finding of importance for future studies on stent strut micromechanics was that the number of grains along the strut length has an important influence on strut ductility. This finding has shown that a number of previous studies on the mechanics of microscale struts may not have adequately accounted for numbers of grains along the strut length when assessing statistical size effects. A number of recommendations were provided for future studies to ensure that an adequate number of grains along the length are maintained.

The corrosion of AMS's plays an important role in dictating their long-term device mechanics. An experimentally validated corrosion model for AMS's has not been previously developed. In Ch. 6 the effects of corrosion on the mechanical integrity of bioabsorbable alloy foils was investigated experimentally. The results of these experiments were used in the development, calibration and validation of a corrosion model for AMS's. The development of such a model is of great importance in the design of AMS's, allowing long-term device behaviour in the body to be better understood and allowing for the generation of improved device designs. It was found that bioabsorbable alloy foils in Hank's solution were subject to localized corrosion and quickly lost mechanical integrity with modest amounts of mass loss. The corrosion model captured this localized corrosion behaviour in a phenomenological way by randomly assigning pit locations and growth rates according to a Weibull distribution. An important finding in this chapter was that AMS's subject to the degree of localized corrosion observed in the experiments lost scaffolding ability an order of magnitude faster than AMS's subject to uniform corrosion, for a given mass loss rate. This finding is of interest

## 9. Discussion and Conclusions

since one of the primary limitations of current AMS's is their premature loss of scaffolding [40].

Ch. 4 compared the mechanical performance of AMS's to permanent stents using simulated bench testing. In order to better assess how AMS's perform in a clinical setting it is of interest to simulate device performance in the body and with the AMS's subject to corrosion. This comparison was performed in Ch. 7. In order to make a valid comparison, the AMS geometries used were a commercial geometry and a geometry obtained from a design optimization process developed especially for AMS's in Ch. 7. The device performance comparison and optimization process developed in this chapter are important as they give insights into: i) how AMS's perform relative to permanent stents in the body, ii) how AMS's perform as they corrode in the body and iii) the extent to which careful design can improve AMS performance in the body. It was found that the studied AMS's performed similarly to a modern permanent stent in straight and curved stenosed vessels prior to corrosion. It was also found that as the AMS's corroded, that natural curvature was restored in the curved vessels, which is a potential benefit of these devices over permanent stents [41]. A finding of particular importance was that it is possible, through making slight adjustments to the geometry of AMS's, to improve their duration of scaffolding in the body.

The corrosion models developed in Chs. 6 and 7 were phenomenological in nature. In order to obtain further insights into the rate and form of corrosion in a range of environments, it is of interest to develop a physical corrosion model. The implementation of physical corrosion models for complex 3-D structures, such as stents, is challenging and has not been previously attempted for AMS's. In Ch. 8 a physical corrosion model for AMS's was developed. A simple corrosion behaviour, namely diffusion controlled corrosion, was studied for a stent surrounded by a homogeneous corrosion environment. It was predicted that the rate of mass loss

for the stent was inversely proportional to the square root of immersion time and proportional to the saturation concentration of magnesium ions in the corrosion environment. It was also found that the loss in mechanical integrity of the AMS for a given amount of mass loss was very similar for the physical corrosion model and the phenomenological model developed in Ch. 7.

### 9.3. New Stent Design Recommendations and Insights

A number of new insights into the mechanics of AMS's have been gained as a result of the work in this thesis. It is evident from the findings of Ch. 4 and Ch. 7 that the width of the region acting as a plastic hinge in the stent strut plays an important role in the overall mechanics of the device, before and during corrosion. A high strut width improves radial stiffness and strength, reduces recoil and allows the use of thinner struts. Higher widths also lead to greater retention of device scaffolding during corrosion. Thus, a recommendation from this thesis is that in the design of AMS's, the width of the regions undergoing plastic deformation should be as high as possible. Although increasing strut widths usually leads to greater plastic strains and higher fracture risks, it has been demonstrated in Ch. 7 that this negative aspect of increasing strut width can be negated somewhat through optimization methods.

An interesting finding from Ch. 8 from the perspective of AMS design is that, for the case of diffusion control corrosion, material removal is focused on the outside of hinges (see 8.8b). This stands to reason, given that concentration gradients will be higher in this region than on the inside of hinges. This result gives useful indications into where strut width should be increased for maximum retention of

## 9. Discussion and Conclusions

device scaffolding performance during diffusion controlled corrosion.

Regarding the mechanical performance of AMS's during corrosion, a simple but useful finding from Ch. 7 is that for uniform corrosion the loss in radial stiffness and strength is largely linear with mass loss. The slope of this linear relationship is similar for a wide range of materials and device geometries. This means that an estimate in the loss in device integrity with mass loss can be very easily made based on the results in Ch. 7, without the need for finite element modelling techniques beyond those used in conventional stent design. Combining the predictions of Chs. 7 and 8, which suggests that mass loss depends on the square root of immersion time for diffusion controlled corrosion, it can also be predicted that the loss of radial stiffness is a function of the square root of immersion time for AMS's subject to diffusion controlled corrosion.

Based on the predictions of this thesis, the most important improvements in magnesium alloy performance are increasing their ductility and inhibiting pitting corrosion. Increasing alloy ductility will reduce fracture risks and will also facilitate the use of wider struts, which has many benefits for device performance. The terms localized or pitting corrosion when used in this thesis have referred to the preferential attack of certain regions of the magnesium alloy. It was predicted here that AMS's undergoing localized corrosion, similar to that observed in the experiments of Ch. 6, lose mechanical integrity an order of magnitude faster than the same device undergoing uniform corrosion. Thus, it is important that the extent of localized corrosion is minimized in the development of AMS's. It is important to also note, that what is often reported as 'uniform corrosion' for magnesium alloys based on observations of corrosion in relatively large samples, may in fact be manifested as localized corrosion in microscale components, such as stent struts. This is because what can be considered to be relatively small undulations in the corrosion surface on the larger sample can often be comparable

## 9. Discussion and Conclusions

in dimension to a coronary stent strut.

In terms of suitable microstructures for magnesium alloys in bioabsorbable stent applications, it is predicted that the number of grains through the strut dimensions does not strongly influence strut mechanics, apart from a slight decrease in UTS for struts with fewer than five grains through the thickness. Thus, the desire for small grain sizes for improved corrosion resistance [97] is predicted not to negatively influence mechanical performance from the perspective of statistical size effects. Based on the predictions of Ch. 5 the use of textured tubing in the development of magnesium AMS's requires care, however. Due to the textured HCP microstructure, certain regions of the device may have significantly less ductility or stiffness than similar regions in a corresponding device cut from annealed tubing.

Regarding statistical size effects in general, it is recommended, based on the findings of Ch. 5, that materials with ductility similar to 316L, such as L605 and PtCr should have similar numbers of grains through strut dimensions, regardless of differences in mechanical strength (Yield Strength and UTS). A straightforward and effective way to apply the results of Ch. 5 in device design is through the *safe design charts* of Harewood and McHugh [80], as discussed in Ch. 5. The use of such charts presents a powerful method of predicting failure risks across different materials and for different microstructures without relying on costly micromechanics simulations.

## 9.4. Future Work

The modelling of absorbable metal stents is a newly emerging field and presents many interesting challenges. The work in this thesis has presented a way to use relatively simple phenomenological approaches to model the effects of corrosion on stent performance. Far more insight can be gained through the application of physical corrosion models however.

The corrosion model developed in Ch. 8 represents an important first step toward the 3-D physical modelling of AMS corrosion. In Ch. 8 the corrosion rate was assumed to be controlled entirely by the diffusion of magnesium ions through a stagnant solution. Two important additions to the model in Ch. 8 are: i) the explicit inclusion of the alloy microstructure, which would allow for the microgalvanic processes that drive device corrosion to be accounted for, and ii) a faithful representation of corrosion product formation. The latter would allow: i) the availability of reactants at the corrosion surface to be modelled in a more realistic way and ii) comparisons to be made between predicted corrosion product compositions and formation rates and those observed *in-vitro* and *in-vivo*. The challenges associated with the inclusion of a microstructure and corrosion product layer in the FE model are mostly a result of the difficulty in dealing with numerous moving boundaries or interfaces, which can potentially merge and self-intersect. The adaptive meshing approach of Chs. 7 and 8 is not well suited to such complex moving boundary problems, while the damage model of Ch. 6 is not well suited to physical modelling, due to its approximate tracking of the corrosion surface. For future studies the author believes the X-FEM is ideally suited to this challenge, when combined with the use of level sets [208]. A precedent for the use of such methods in similar, albeit more straightforward, applications is evident in studies of solidification problems [208, 209].

Accurately identifying and modelling the properties of coronary tissues is an on-going challenge in the area of stent analysis. The behaviour of a corroding AMS will depend very much on the properties of the surrounding tissue, which may have viscous behaviours and be subject to remodelling. As such, accurately modelling tissue mechanics may have even greater importance when modelling AMS's, relative to permanent stents. An interesting and reasonably straightforward follow-on study to that presented here is to investigate the rate of lumen loss for AMS's in tissues with different mechanical properties.

There remain very few studies that have used micro-scale approaches in the study of stent mechanics. A number of improvements can be made to the study presented here. Experimental validation of model predictions for L605 is important, given the implications of size effects on this alloy for stent design. In addition, the use of 3-D strut geometries that are subject to 3-D loading conditions would give useful failure predictions in complex loading scenarios often seen in stent deployment.

### 9.5. Conclusions

The aim of this thesis was to improve the understanding of the mechanics of next generation coronary stents. To achieve this aim new phenomenological and physical corrosion models were developed based on the use of continuum damage mechanics and adaptive meshing approaches. Due to their generality these models will prove useful in future studies on the corrosion of both bioabsorbable stents and devices and larger-scale industrial components undergoing corrosion. A comprehensive investigation of size effects in micro-scale components was also performed to improve the understanding of the mechanics of devices with few

## 9. Discussion and Conclusions

grains through their dimensions, such as stent struts. This investigation will facilitate safer design of new generations of thin-strut stents. Based on the application of the corrosion models developed in this thesis and the investigation of size effects, the following specific predictions have been made:

- Cobalt chromium alloy (L605) is subject to similar losses in ductility with decreasing numbers of grains through device dimensions than stainless steel (316L).
- Magnesium ductility does not strongly depend on the number of grains through the device dimensions.
- Absorbable metal stents undergoing localized corrosion lose scaffolding ability an order of magnitude faster than devices undergoing uniform corrosion, for a given mass loss rate.
- Absorbable metal stents undergoing uniform corrosion have a largely linear loss in strength with mass lost.
- Strut width should be maximized in absorbable metal stent design.
- The mass loss rate of absorbable metal stents undergoing diffusion controlled corrosion is inversely proportional to the immersion time and is proportional to the saturation concentration of the diffusing magnesium ions.

# A. Appendices

## A.1. Soft Tissue Material Models

The anisotropic hyperelastic model of Holzapfel *et al.* [139] in Eqn. 3.40 is implemented using a VUANISOHYPER subroutine in this thesis. A flowchart for the implementation of this subroutine is shown in Fig. A.1.

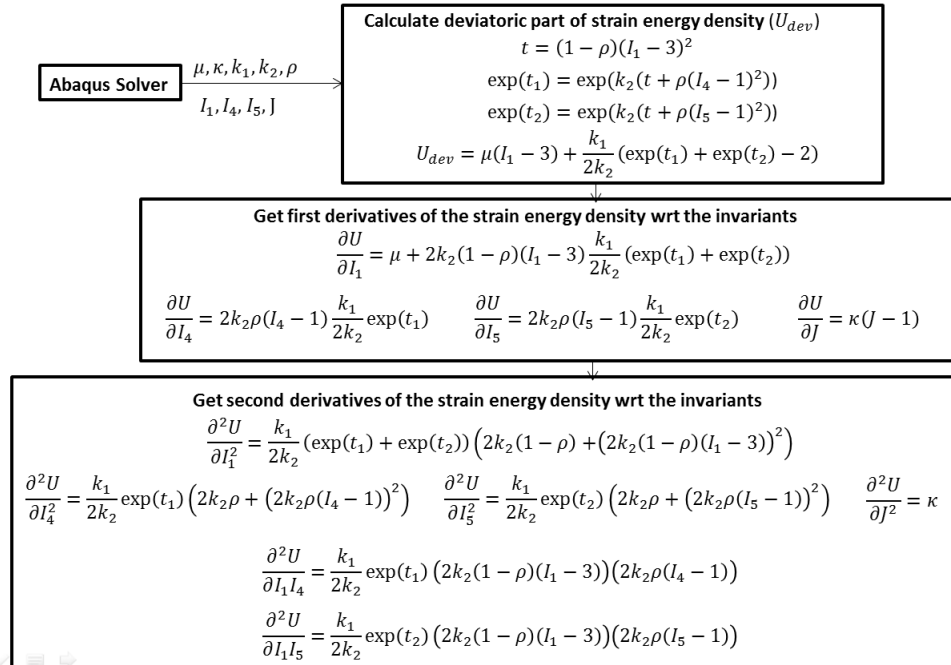


**Figure A.1.:** The VUANISOHYPER subroutine receives values of the invariants defined in Section 3.3 and returns the deviatoric part of the strain energy density and the derivatives of the strain energy density with respect to the invariants.

## A. Appendices

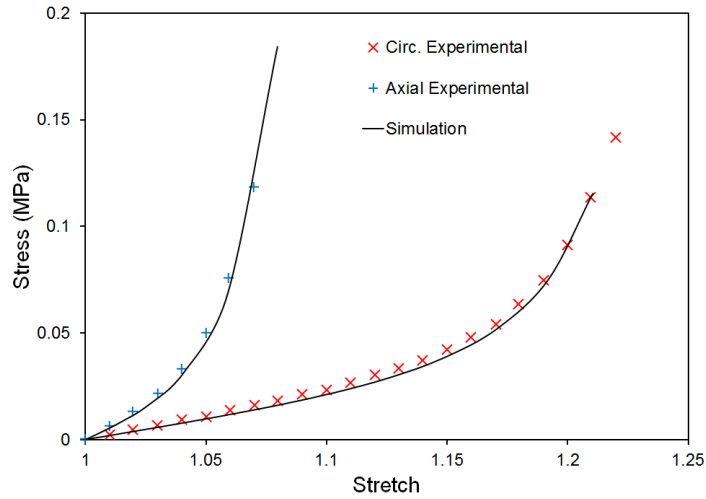
The subroutine is tested and suitable values for the constant  $\kappa$  are found by simulating the extension of a unit cube in directions corresponding to the axial and circumferential arterial directions. Model predictions are shown to be in good agreement with the experimental results of Holzapfel *et al.* [139] in Figs. A.2a, A.2b and A.2c.

The mechanical behaviour of plaques is modelled using a reduced order polynomial hyperelastic behaviour (Eqn. 3.35) with perfect plasticity enacted beyond a certain threshold stress (0.4 MPa). Plasticity is modelled using the Permanent Set model in Abaqus (DS SIMULIA, Abaqus Theory Manual), which is developed for problems with large elastic and plastic strains. Since many details on the implementation of this model are not available in the Abaqus manuals it is verified here that this model is suitable for implementing perfect plasticity at the desired threshold stress in the plaque. A unit cube is modelled undergoing tensile loading and unloading with the hyperelastic model in Eqn. 3.35 and the Permanent Set model. As shown in Fig. A.3 the model's stress-stretch behaviour falls within the range of plaque properties identified in Loree *et al.* [191] and perfect plasticity is enacted at the desired stress.

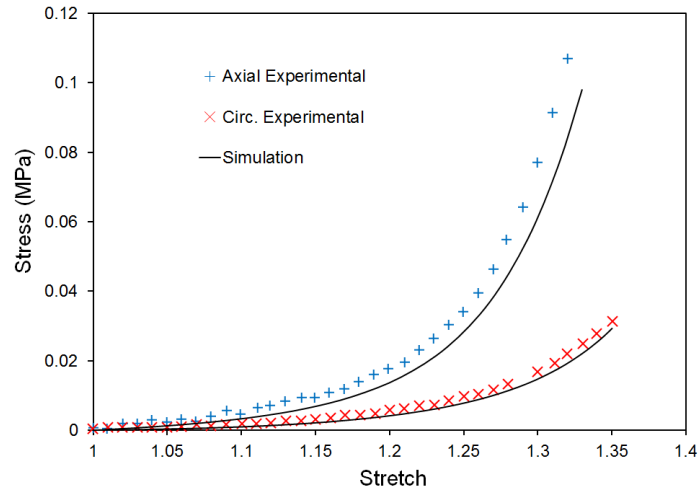
### A.2. Corrosion Model Verification

ALE adaptive meshing is a feature available in the Abaqus software, however there is little detail given in the Abaqus manuals regarding its implementation. In order to test the suitability of this feature for modelling corrosion, and to test the implementation of the ALE corrosion model subroutines described in Fig. 7.2, a number of tests cases are simulated. The implementation of the uniform corrosion damage model is also assessed with these tests.

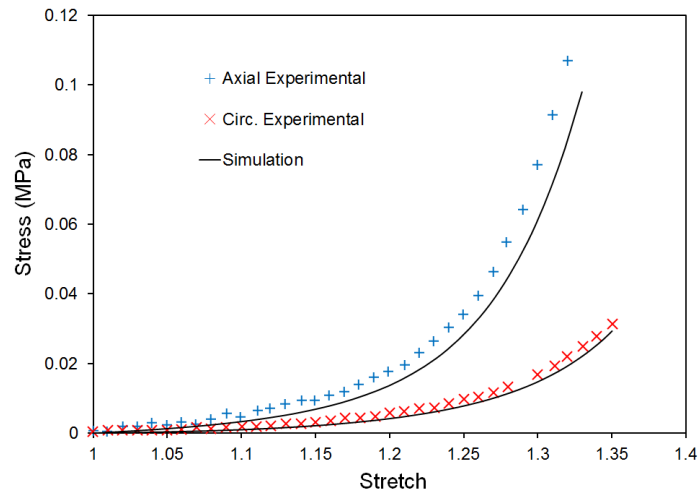
## A. Appendices



(a)



(b)



(c)

**Figure A.2.:** Comparison between finite element model predictions and the experiments of Holzapfel *et al.* [139] for uniaxial tension of (a) intima, (b) media and (c) adventitia arterial layers.

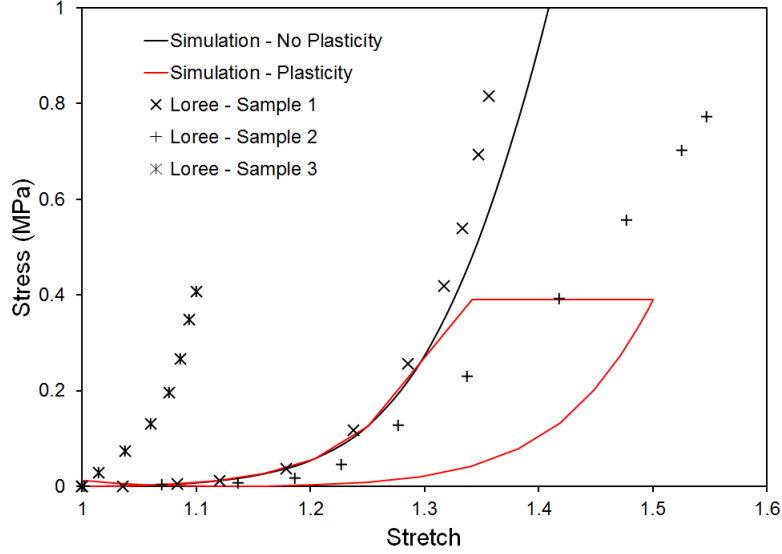


**Figure A.3.:** Comparison between finite element model predictions and experiments by Loree *et al.* [191] for uniaxial tension of a plaque with and without the assumption of perfect plasticity. The finite element models simulate one load-unload cycle.

The test cases are shown schematically in Fig. A.4. The first test assesses the ability of each corrosion model to capture the reduction in mechanical integrity of a corroding elastic-plastic rod, through a comparison with an analytical model. The rod is subject to longitudinal tensile strain of 0.08 and corrosion on its curved surface. The extent to which the force resisting the applied strain in the rod  $R_F$  reduces with corrosion can be determined analytically as:

$$\frac{R_F(t)}{R_{F,0}} = \frac{(r_0 - vt)^2}{r_0^2} = \left(1 - \frac{vt}{r_0}\right)^2 \quad (\text{A.1})$$

where  $R_{F,0}$  and  $r_0$  are the resisting force and rod radius at the onset of corrosion. The results of the first test are shown in Fig. A.5 in terms of the quantity  $\frac{vt}{r_0}$ . There is excellent agreement between the ALE corrosion model and the analytical solution, with good agreement for the corrosion damage model.

The second test assesses the ability of each model to accurately capture the changing inhomogeneous stress state in a corroding elastic annulus, shown in Fig. A.4. A quarter of the annulus is modelled using appropriate symmetry

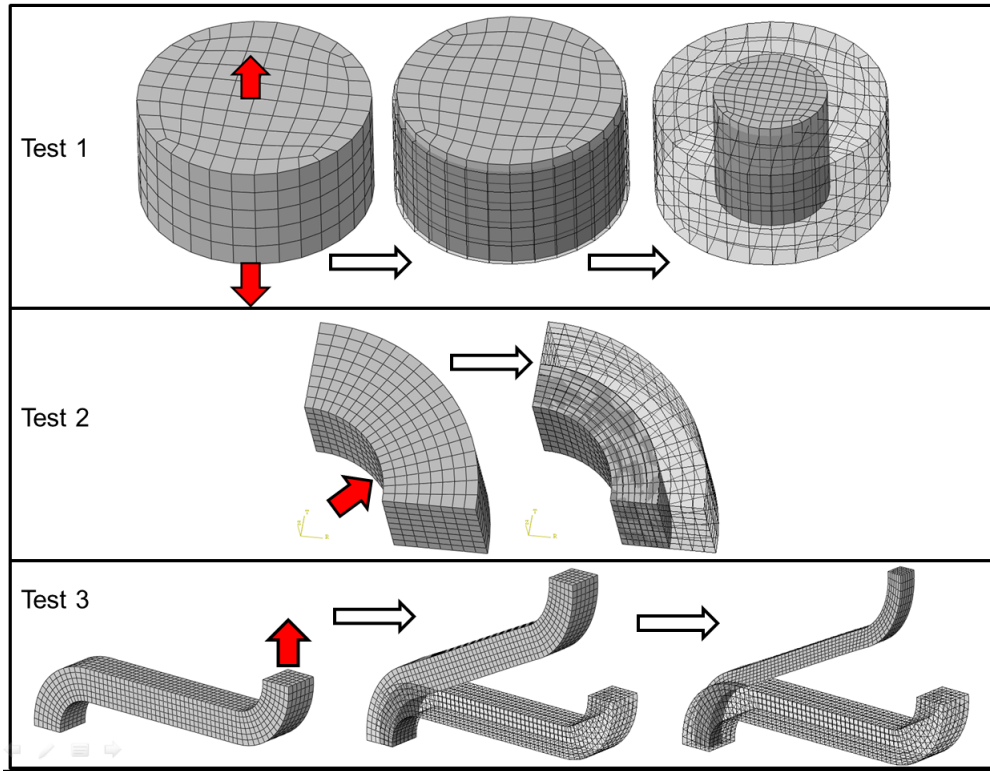


**Figure A.4.:** Schematic of the tests used to assess the implementation of the ALE corrosion model and the corrosion damage model.

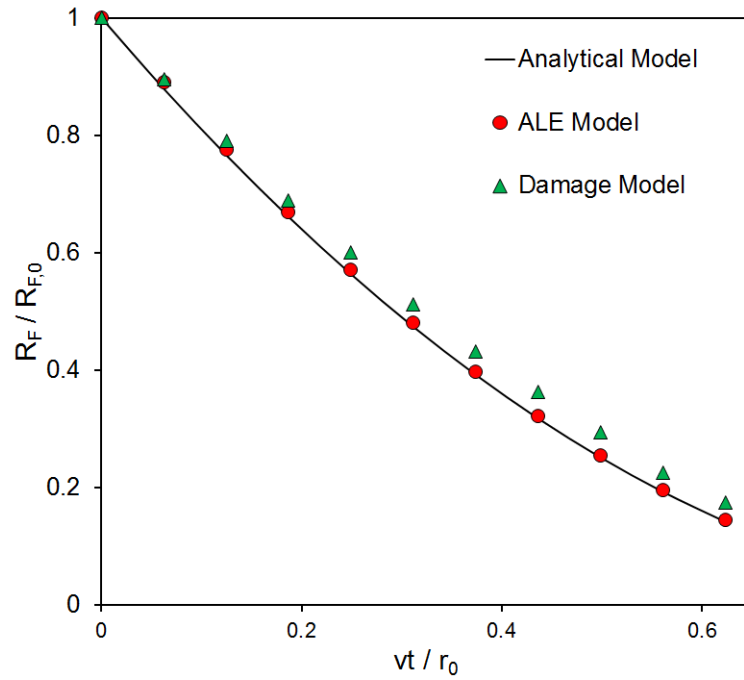


**Figure A.5.:** Comparison between the analytical solution and the ALE and corrosion damage models for Test 1.

## A. Appendices

boundary conditions, while the displacement in the longitudinal direction is fixed to replicate plane strain conditions. A displacement  $u$  of 0.1% of the annulus inner radius  $r_i$  is applied to the inside curved surface, while the outside curved surface corrodes. The changing stress state in the annulus at radius  $r$  during corrosion can be determined analytically for small strains based on Lamé's equations [210].

According to Lamé's equations for thick walled cylinders, the radial and circumferential stress distributions,  $\sigma_r$  and  $\sigma_\theta$  respectively, for a cylinder with internal pressure  $P$  are:

$$\begin{aligned}\sigma_r &= \frac{r_i^2 P}{(r_o^2 - r_i^2)} \left[ 1 + \frac{r_o^2}{r} \right] \\ \sigma_\theta &= \frac{r_i^2 P}{(r_o^2 - r_i^2)} \left[ 1 - \frac{r_o^2}{r} \right]\end{aligned}\quad (\text{A.2})$$

where  $r_o$  and  $r_i$  are respective external and internal radii. For a cylinder with an applied internal displacement  $u$  the internal pressure is:

$$P = \frac{u}{\frac{r}{E} \left( \frac{r_o^2 + r_i^2}{r_o^2 - r_i^2} + \nu \right)} \quad (\text{A.3})$$

giving the following stress distributions:

$$\begin{aligned}\sigma_r &= \frac{r_i^2 u E}{r(r_o^2(1 + \nu) + r_i^2(1 - \nu))} \left[ 1 + \frac{r_o^2}{r} \right] \\ \sigma_\theta &= \frac{r_i^2 u E}{r(r_o^2(1 + \nu) + r_i^2(1 - \nu))} \left[ 1 - \frac{r_o^2}{r} \right]\end{aligned}\quad (\text{A.4})$$

If the cylinder is corroding on its outer surface, its outer radius is reduced with a velocity,  $v$ . This gives rise to the following time dependent stress distributions:

$$\begin{aligned}\sigma_r &= \frac{r_i^2 u E}{r((r_o - vt)^2(1 + \nu) + r_i^2(1 - \nu))} \left[ 1 + \frac{(r_o - vt)^2}{r} \right] \\ \sigma_\theta &= \frac{r_i^2 u E}{r((r_o - vt)^2(1 + \nu) + r_i^2(1 - \nu))} \left[ 1 - \frac{(r_o - vt)^2}{r} \right]\end{aligned}\quad (\text{A.5})$$

## A. Appendices

where  $r_o$  is the outer radius of the annulus before corrosion. The results of the second test are shown in Fig. A.6a. There is good agreement between both the ALE and corrosion damage models and the analytical stress distributions from Eqn. A.5. Fig. A.6b shows the difference in predicted annulus geometry between the ALE corrosion model and the corrosion damage model after the same amount of corrosion.

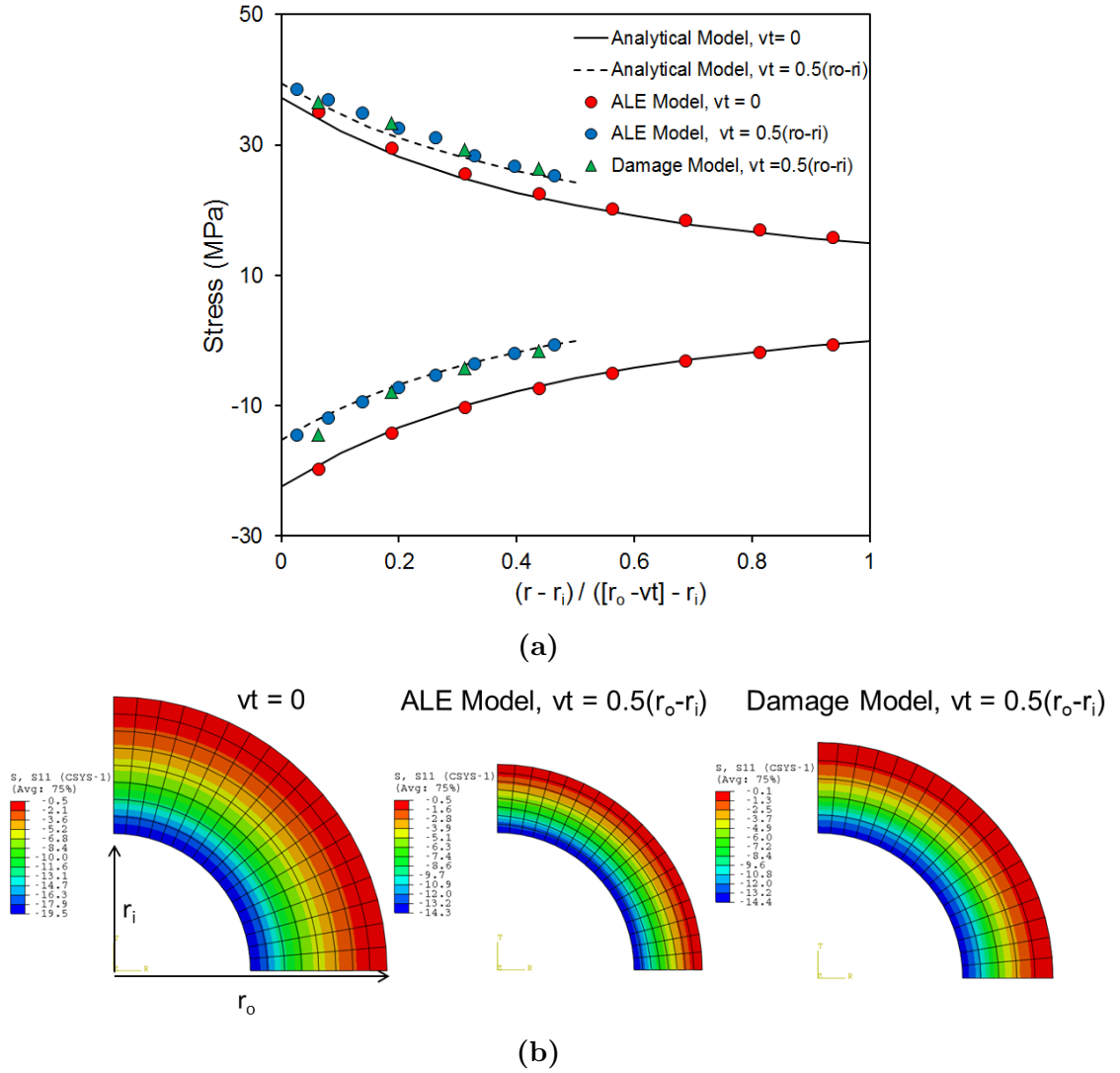


**Figure A.6.:** (a) Comparison between the analytical solution and the ALE and corrosion damage models for Test 2. The quantity  $\frac{r-r_i}{(r_o-vt)-r_i}$  can be considered to be a normalized radial position in the corroding annulus. The upper set of curves are circumferential stresses and the lower are radial stresses. (b) Radial stress distributions in MPa in the annulus before and during corrosion with the ALE and damage models.

The third test case compares the predictions and mesh sensitivity of both models

when applied to analysing an elastic-plastic stent hinge. As shown in Fig. A.4, the hinge is opened by applying a displacement to its top surface and fixing its bottom surface. The top surface is then held in position as the hinge is subject to corrosion on its non-fixed surfaces. The loss in resistive force to the applied displacement during corrosion is assessed for each model using meshes with four, six and eight elements through the strut width. The results of this test are shown in Figs. A.7a and A.7b. The ALE corrosion model is found to be relatively insensitive to the mesh used, with good agreement between the meshes with six and eight elements through the strut width. The corrosion damage model is observed to be more sensitive to the mesh used, however there is good agreement between the ALE and corrosion damage model predictions when six elements are maintained through the strut width, as shown in Fig. A.7a.

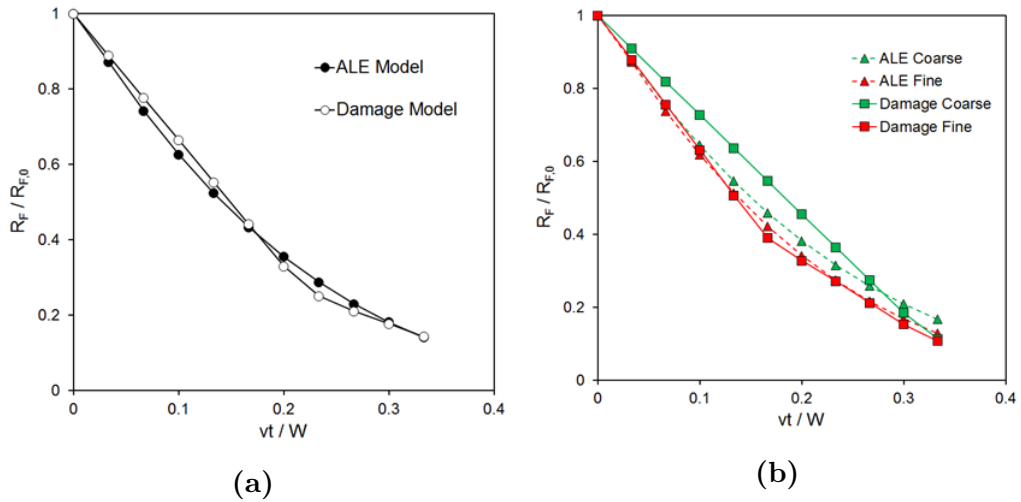


**Figure A.7.:** A comparison of predicted reduction in hinge reaction force  $R_F$  with corrosion for the ALE and damage corrosion models with (a) six and (b) four (coarse) and eight (fine) elements through the strut width  $W$ . The quantity  $R_{F,0}$  is reaction force before corrosion begins.

### A.3. Corrosion Damage Model Implementation

The corrosion model developed in this work consists of three components, a pre-processor which is executed prior to the main Abaqus analysis, a VUMAT which

is executed in conjunction with the Abaqus analysis and a DAMAGE subroutine which is called by the VUMAT.

The pre-processor prepares the input file for the main analysis by reading a dummy input file. Element connectivity is determined and also the elements on the initial corrosion surface. It subsequently generates random numbers for these surface elements. A flowchart for the pre-processor stage is shown in Fig. A.8.

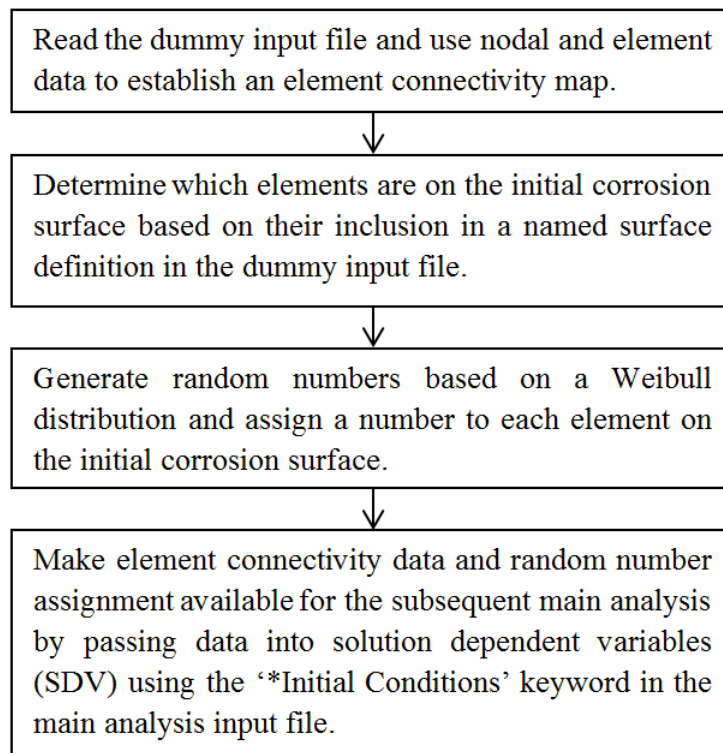


**Figure A.8.:** Flowchart for the corrosion model pre-processor stage.

The main Abaqus/Explicit analysis is performed using a VUMAT to describe the material constitutive behaviour. An elastic-plastic material model is employed to model the undamaged material behaviour along with the subroutine DAMAGE, which is used to update the value of the damage parameter  $D$ . This parameter in turn modifies the material constitutive behaviour to represent the effects of corrosion induced damage. A flowchart for the VUMAT is shown in Fig. A.9.

The subroutine DAMAGE is called by the VUMAT to update the value of the

## A. Appendices

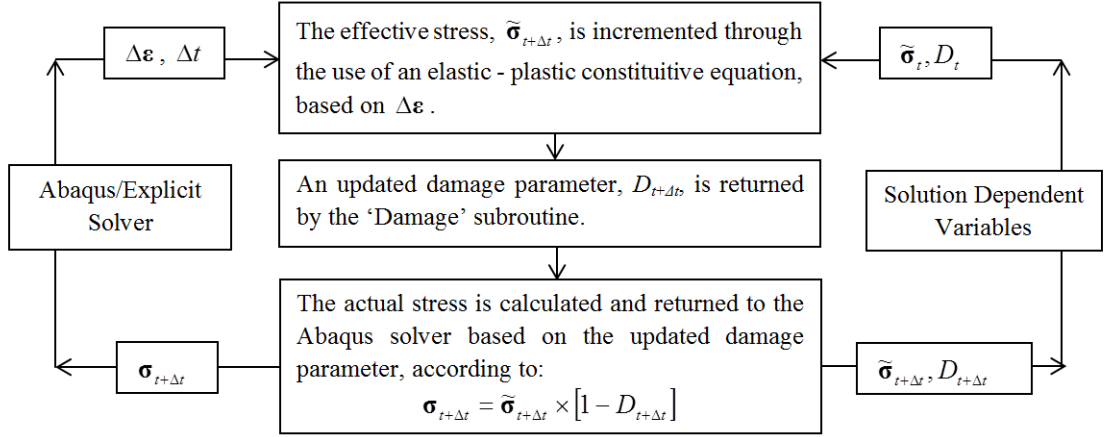


**Figure A.9.:** Flowchart for the corrosion model VUMAT.

damage parameter  $D$ . When elements are fully corroded or when the equivalent plastic strain  $\bar{\varepsilon}^{pl}$  reaches a critical value this subroutine sets an element removal flag for the Abaqus solver. Element random number assignments  $\lambda_e$  are stored in common blocks (detailed subsequently). Fig. A.11 shows a flowchart for the subroutine.

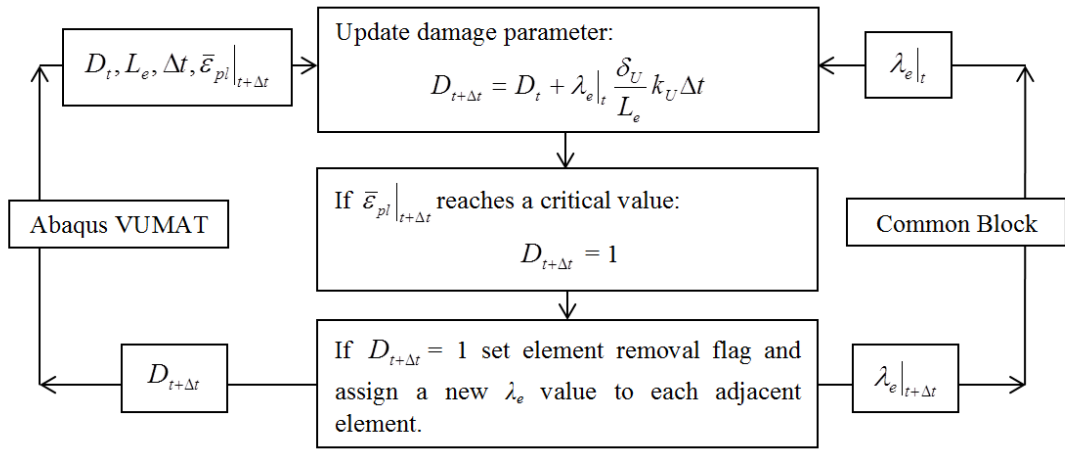


**Figure A.10.:** Flowchart for the DAMAGE subroutine.

Common blocks are a feature of the Fortran 77 language which allow for the use of shared or common memory. This shared memory allows data to be shared between blocks of elements in Abaqus/Explicit user subroutines, effectively allowing inter-element communication. However, care must be taken when used with multiple processors to ensure solution consistency. In order to ensure the solution is thread safe, separate arrays are used to receive element random number

assignments (Array A) and to output these assignments (Array B), as shown in Fig. A.11. As such, during an analysis increment, Array A can only be modified, while Array B can only be read from. At the end of an analysis increment, Array B assumes the values stored in Array A, in preparation for the next increment. This ensures that the solution does not depend on the number of processors used or the order in which they modify or read from the common block arrays. The use of common blocks in this way is only possible for *threads* mode in Abaqus, i.e. with a symmetric multiprocessing (SMP) environment.

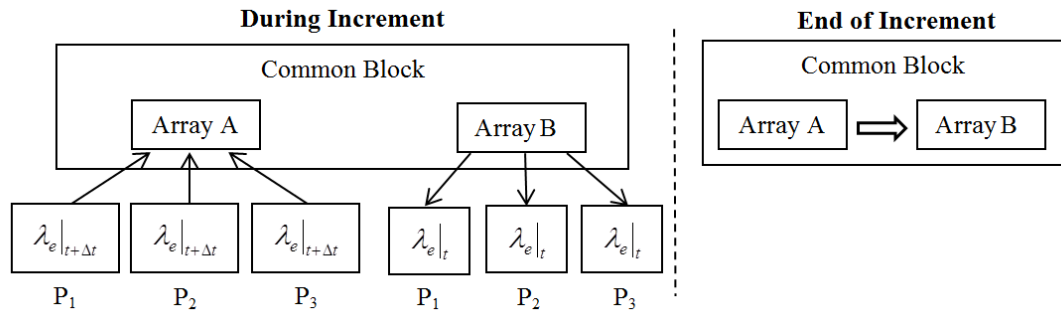


**Figure A.11.:** A condition is imposed in which common block arrays can only be either modified or read from during an analysis increment to ensure solution consistency over multiple processors ( $P_1$ – $P_3$ ).

## A.4. Time Scaling in the Corrosion Subroutines

The quantity  $v$ , which is the corrosion rate in units  $LT^{-1}$  (e.g.  $\text{mm h}^{-1}$ ), is a measure that is used extensively in Chs. 7 and 8 and the corrosion literature (see Roberge [211]). Physically, it can be interpreted as the rate at which the surface of a component undergoing 1-D (and uniform) corrosion moves, i.e. an equivalent 1-D corrosion speed.

Considering Fig. A.12,  $v$  can be related to the corrosion rate in units  $ML^{-2}T^{-1}$

## A. Appendices

(i.e.  $\text{mg cm}^{-2} \text{h}^{-1}$ ) through:

$$v = \frac{du}{dt} = \frac{A\dot{u}}{A} = \frac{\dot{m}}{A\rho} \quad (\text{A.6})$$

where  $A$  is the exposed cross-sectional area,  $\rho$  is the component density,  $m$  is the mass and  $u$  is the displacement of the corrosion surface. For example, the corrosion rate for AZ31 in Ch. 6 is  $0.084 \text{ mg cm}^{-2} \text{h}^{-1}$ . Given that the density of AZ31 alloy is approximately  $1900 \text{ mg cm}^{-3}$ ,  $v$  is:

$$v = \frac{0.084}{1 \times 1900} = 4.42 \times 10^{-5} \text{ cm hr}^{-1} \quad (\text{A.7})$$

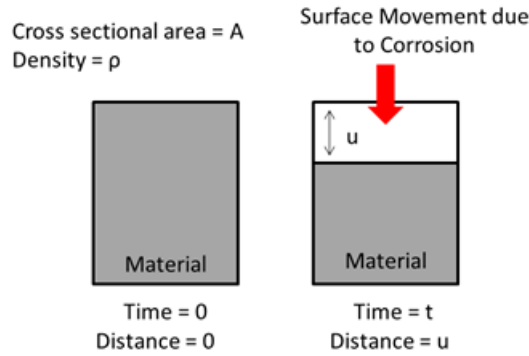


**Figure A.12.:** The 1-D corrosion of a block of material of cross-sectional area  $A$  and density  $\rho$ .

In the Abaqus/Explicit analyses in Chs. 6 and 7 mass scaling is used to attain reasonable solution times. The use of mass scaling restricts the suitable range of total analysis times, with an analysis time of approximately 1.0 found to be the most suitable for the stable time increment of  $1.0 \times 10^{-6}$  used in stent simulations in this work. For the modelling of corrosion it is thus necessary to scale the corrosion rate so that a desired amount of corrosion occurs in an analysis time of 1.0.

In order to scale the corrosion rate in the VUMAT it is necessary to identify the parameters in the corrosion model that can be scaled without affecting the

## A. Appendices

physics of the problem. It is also necessary to identify the relationship between *analysis time*  $t_a$  and *real time*  $t$  to allow for the interpretation of results. In general, if a corrosion rate  $v_c$  is used in an analysis in place of the real corrosion rate  $v$ , then the relationship between  $t_a$  and  $t$  is:

$$t = \frac{v_c}{v} t_a \quad (\text{A.8})$$

For the corrosion damage model used in this work the damage evolution in an element is given by:

$$\frac{dD_e}{dt} = \lambda_e \frac{\delta_U}{L_e} k_U \quad (\text{A.9})$$

The overall damage evolution in the model is then:

$$\frac{d\bar{D}}{dt} = \bar{\lambda} \frac{\delta_U}{\bar{L}} k_U \quad (\text{A.10})$$

where  $\bar{a}$  denotes an averaging of the quantity  $a_e$  over all elements in the mesh. Through Eqn. A.6 it can be shown that the rate of damage is related to the corrosion rate through:

$$v = \frac{d\bar{D}}{dt} \frac{m_0}{A\rho} \quad (\text{A.11})$$

where  $m_0$  is the initial mass of the component. Therefore Eqn. A.8 can be expressed as:

$$t = \frac{v_c}{v} t_a = \frac{\left[ \frac{d\bar{D}}{dt} \right]_c}{\frac{d\bar{D}}{dt}} t_a \quad (\text{A.12})$$

where  $\left[ \frac{d\bar{D}}{dt} \right]_c$  is an arbitrary corrosion damage rate chosen for convenience in the VUMAT.

The quantities  $\bar{\lambda}$  (average pitting parameter value) and  $\bar{L}$  (average element length) are fixed for a given mesh and choice of  $\gamma$  and  $\beta$  in Eqns. 6.5 and 6.6. Therefore

## A. Appendices

Eqn. A.14 becomes:

$$t = \frac{v_c}{v} t_a = \frac{\left[ \frac{d\bar{D}}{dt} \right]_c t_a}{\frac{d\bar{D}}{dt}} = \frac{\left[ \bar{\lambda} \frac{k_u \delta_u}{L} \right]_c t_a}{\bar{\lambda} \frac{k_u \delta_u}{L}} = \frac{\bar{\lambda} \left[ \frac{k_u \delta_u}{L} \right]_c t_a}{\bar{\lambda} \frac{k_u \delta_u}{L}} = \frac{[k_u \delta_u]_c t_a}{k_u \delta_u} \quad (\text{A.13})$$

This shows that as long as the scaling in Eqn. A.13 is used, arbitrary convenient values of  $k_u$  and  $\delta_u$  can be used in the VUMAT to scale the corrosion rate, without affecting the physics of the problem.

As an example of this scaling, in the VUMAT the quantities  $k_u$  and  $\delta_u$  are chosen for convenience such that  $[k_u \delta_u]_c = 0.05 \text{ mm hr}^{-1}$ . Using the real values of  $k_u$  and  $\delta_u$  for AZ31 alloy from Ch. 6,  $k_u \delta_u = 0.000442 \text{ mm hr}^{-1}$ . Therefore the relationship between the real time and the analysis time is:

$$t = \frac{0.05 \text{ mm hr}^{-1}}{0.000442 \text{ mm hr}^{-1}} t_a = 113 t_a \quad (\text{A.14})$$

# Bibliography

- [1] M Nichols, N Townsend, P Scarborough, R Luengo-Fernandez, J Leal, A Gray, and M Rayner. *European Cardiovascular Disease Statistics 2012*. European Heart Network, Brussels, European Society of Cardiology, Sophia Antipolis, 2012.
- [2] G Maluenda, G Lemesle, and R Waksman. A critical appraisal of the safety and efficacy of drug-eluting stents. *Clinical Pharmacology and Therapeutics*, 85(5):474–80, 2009.
- [3] D Baim. *Grossman’s Cardiac Catheterization, Angiography, and Intervention*. Lippincott Williams and Wilkins, Philadelphia, 2006.
- [4] S Garg and PW Serruys. Coronary stents: current status. *Journal of the American College of Cardiology*, 56(10 Suppl):S1–42, 2010.
- [5] P Poncin and J Proft. Stent tubing: understanding the desired attributes. In *Materials and Processes for Medical Devices Conference*, pages 253–259. ASM International, Boston, MA, US, September 2005.
- [6] BJ O’Brien, JS Stinson, SR Larsen, MJ Eppihimer, and WM Carroll. A platinum-chromium steel for cardiovascular stents. *Biomaterials*, 31(14):3755–61, 2010.

## Bibliography

- [7] XN Gu, WR Zhou, YF Zheng, Y Cheng, SC Wei, SP Zhong, TF Xi, and LJ Chen. Corrosion fatigue behaviors of two biomedical Mg alloys - AZ91D and WE43 - In simulated body fluid. *Acta Biomaterialia*, 6(12):4605–13, 2010.
- [8] MA Islam and NT Sato. Tensile and plane bending fatigue properties of pure iron and iron-phosphorus alloys at room temperature in the air. *Transactions of the Indian Institute of Metals*, 64(3):1693–97, 2011.
- [9] U Sigwart, J Puel, V Mirkovitch, F Joffre, and L Kappenberger. Intravascular stents to prevent occlusion and restenosis after transluminal angioplasty. *The New England Journal of Medicine*, 316(12):701–6, 1987.
- [10] PW Serruys, P de Jaegere, F Kiemeneij, C Macaya, W Rutsch, G Heyndrickx, H Emanuelsson, J Marco, V Legrand, P Materne, J Belardi, U Sigwart, A Colombo, J Goy, P van den Heuvel, J Delcan, and M Morel. A comparison of balloon-expandable-stent implantation with balloon angioplasty in patients with coronary artery disease. *New England Journal of Medicine*, 331(8):489–495, 1994.
- [11] DL Fischman, MB Leon, DS Baim, RA Schatz, MP Savage, I Penn, K Detre, L Veltri, D Ricci, M Nobuyoshi, M Cleman, R Heuser, D Almond, PS Teirstein, RD Fish, A Colombo, J Brinker, J Moses, A Shaknovich, J Hirshfeld, S Bailey, S Ellis, R Rake, and S Goldberg. A randomized comparison of coronary-stent placement and balloon angioplasty in the treatment of coronary artery disease. *New England Journal of Medicine*, 331(8):496–501, 1994.
- [12] DR Holmes, DJ Kereiakes, S Garg, PW Serruys, GJ Dehmer, SG Ellis, DO Williams, T Kimura, and DJ Moliterno. Stent thrombosis. *Journal of the American College of Cardiology*, 56(17):1357–65, 2010.
- [13] DJ Moliterno. Healing Achilles—sirolimus versus paclitaxel. *The New England*

## Bibliography

*Journal of Medicine*, 353(7):724–7, 2005.

- [14] C Stettler, S Wandel, S Allemann, A Kastrati, MC Morice, A Schömig, ME Pfisterer, GW Stone, MB Leon, JS de Lezo, JJ Goy, SJ Park, M Sabaté, MJ Suttorp, H Kelbaek, C Spaulding, M Menichelli, P Vermeersch, MT Dirksen, P Cervinka, AS Petronio, AJ Nordmann, P Diem, B Meier, M Zwahlen, S Reichenbach, S Trelle, S Windecker, and P Jüni. Outcomes associated with drug-eluting and bare-metal stents: a collaborative network meta-analysis. *Lancet*, 370(9591):937–48, 2007.
- [15] Food and Drug Administration. Non-Clinical Engineering Tests and Recommended Labeling for Intravascular Stents and Associated Delivery Systems. Technical report, available online: <http://www.fda.gov/MedicalDevices/DeviceRegulationandGuidance/PostmarketRequirements/QualitySystemsRegulations/MedicalDeviceQualitySystemsManual/ucm122416.htm>, 2013.
- [16] DM Martin and FJ Boyle. Drug-eluting stents for coronary artery disease: a review. *Medical Engineering and Physics*, 33(2):148–63, 2011.
- [17] S Morlacchi and F Migliavacca. Modeling Stented Coronary Arteries: Where We are, Where to Go. *Annals of Biomedical Engineering*, 41(7):1428–44, 2013.
- [18] C Dumoulin and B Cochelin. Mechanical behaviour modelling of balloon-expandable stents. *Journal of Biomechanics*, 33(11):1461–70, 2000.
- [19] F Migliavacca, L Petrini, V Montanari, I Quagliana, F Auricchio, and G Dubini. A predictive study of the mechanical behaviour of coronary stents by computer modelling. *Medical Engineering and Physics*, 27(1):13–8, 2005.
- [20] P Mortier, GA Holzapfel, M De Beule, D Van Loo, Y Taeymans, P Segers,

## Bibliography

- P Verdonck, and B Verhegghe. A novel simulation strategy for stent insertion and deployment in curved coronary bifurcations: comparison of three drug-eluting stents. *Annals of Biomedical Engineering*, 38(1):88–99, 2010.
- [21] D Gastaldi, S Morlacchi, R Nichetti, C Capelli, G Dubini, L Petrini, and F Migliavacca. Modelling of the provisional side-branch stenting approach for the treatment of atherosclerotic coronary bifurcations: effects of stent positioning. *Biomechanics and Modeling in Mechanobiology*, 9(5):551–61, 2010.
- [22] S Pant, NW Bressloff, and G Limbert. Geometry parameterization and multidisciplinary constrained optimization of coronary stents. *Biomechanics and Modeling in Mechanobiology*, 11(1-2):61–82, 2012.
- [23] C Conway, F Sharif, JP McGarry, and PE McHugh. A computational test-bed to assess coronary stent implantation mechanics using a population-specific approach. *Cardiovascular Engineering and Technology*, 3(4):374–387, 2012.
- [24] A Kastrati, J Mehilli, J Pache, C Kaiser, M Valgimigli, H Kelbaek, M Menichelli, M Sabaté, MJ Suttorp, D Baumgart, M Seyfarth, ME Pfisterer, and A Schömig. Analysis of 14 trials comparing sirolimus-eluting stents with bare-metal stents. *The New England Journal of Medicine*, 356(10):1030–9, 2007.
- [25] C Spaulding, J Daemen, E Boersma, DE Cutlip, and PW Serruys. A pooled analysis of data comparing sirolimus-eluting stents with bare-metal stents. *The New England Journal of Medicine*, 356(10):989–97, 2007.
- [26] H Roukoz, AA Bavry, ML Sarkees, GR Mood, DJ Kumbhani, MG Rabbat, and DL Bhatt. Comprehensive meta-analysis on drug-eluting stents versus bare-metal stents during extended follow-up. *The American Journal of Medicine*, 122(6):581–10, 2009.

## Bibliography

- [27] D Lloyd-Jones, R Adams, M Carnethon, G De Simone, TB Ferguson, K Flegal, E Ford, K Furie, A Go, K Greenlund, N Haase, S Hailpern, M Ho, V Howard, B Kissela, S Kittner, D Lackland, L Lisabeth, A Marelli, M McDermott, J Meigs, D Mozaffarian, G Nichol, C O'Donnell, V Roger, W Rosamond, R Sacco, P Sorlie, R Stafford, J Steinberger, T Thom, S Wasserthiel-Smoller, N Wong, J Wylie-Rosett, and Y Hong. Heart disease and stroke statistics—2009 update: a report from the American Heart Association Statistics Committee and Stroke Statistics Subcommittee. *Circulation*, 119(3):480–6, 2009.
- [28] S Garg and PW Serruys. Coronary stents: looking forward. *Journal of the American College of Cardiology*, 56(10 Suppl):S43–78, 2010.
- [29] JF LaDisa, LE Olson, I Guler, DA Hettrick, SH Audi, JR Kersten, DC Warltier, and PS Pagel. Stent design properties and deployment ratio influence indexes of wall shear stress: a three-dimensional computational fluid dynamics investigation within a normal artery. *Journal of Applied Physiology*, 97(1):424–30, 2004.
- [30] A Kastrati, J Mehilli, J Dirschinger, F Dotzer, H Schühlen, FJ Neumann, M Fleckenstein, C Pfaffert, M Seyfarth, and A Schomig. Intracoronary stenting and angiographic results : strut thickness effect on restenosis outcome (ISAR-STEREO) trial. *Circulation*, 103(23):2816–2821, 2001.
- [31] J Pache, A Kastrati, J Mehilli, H Schühlen, F Dotzer, J Hausleiter, M Fleckenstein, F Neumann, U Sattelberger, C Schmitt, M Müller, J Dirschinger, and A Schömig. Intracoronary stenting and angiographic results: strut thickness effect on restenosis outcome (ISAR-STEREO-2) trial. *Journal of the American College of Cardiology*, 41(8):1283–1288, 2003.
- [32] P Poncin, C Millet, J Chevy, and J Proft. Comparing and optimizing Co-Cr tubing for stent applications. In *Materials and Processes for Medical Devices Conference*. ASM International, Boston, MA, US, August 2004.

## Bibliography

- [33] A Seth. Interventional cardiology moving towards biomimicry - the development of the novel BioMime Sirolimus-eluting coronary stent system. *European Cardiology*, 6(2):78–82, 2010.
- [34] C Meyer-Kobbe and BH Hinrichs. The importance of annealing 316 LVM stents. *Medical Device Technology*, 14(1):20–5, 2003.
- [35] BP Murphy, P Savage, PE McHugh, and DF Quinn. The stress-strain behavior of coronary stent struts is size dependent. *Annals of Biomedical Engineering*, 31(6):686–691, 2003.
- [36] S Weiss, A Meissner, and A Fischer. Microstructural changes within similar coronary stents produced from two different austenitic steels. *Journal of the Mechanical Behavior of Biomedical Materials*, 2(2):210–6, 2009.
- [37] EO Hall. The deformation and ageing of mild steel: III discussion of results. *Proceedings of the Physical Society. Section B*, 64(9):747–753, 1951.
- [38] R Waksman. Promise and challenges of bioabsorbable stents. *Catheterization and Cardiovascular Interventions*, 70(3):407–414, 2007.
- [39] CV Bourantas, Y Zhang, V Farooq, HM Garcia-Garcia, and PW Onuma, Yand Serruys. Bioresorbable scaffolds: current evidence and ongoing clinical trials. *Current Cardiology Reports*, 14(5):626–34, 2012.
- [40] R Erbel, C Di Mario, J Bartunek, J Bonnier, B de Bruyne, FR Eberli, P Erne, M Haude, B Heublein, M Horrigan, C Ilsley, D Böse, J Koolen, TF Lüscher, N Weissman, and R Waksman. Temporary scaffolding of coronary arteries with bioabsorbable magnesium stents: a prospective, non-randomised multicentre trial. *Lancet*, 369(9576):1869–75, 2007.

## Bibliography

- [41] M Haude, R Erbel, P Erne, S Verheye, H Degen, D Böse, P Vermeersch, I Wijbergen, N Weissman, F Prati, R Waksman, and J Koolen. Safety and performance of the drug-eluting absorbable metal scaffold (DREAMS) in patients with de-novo coronary lesions: 12 month results of the prospective, multicentre, first-in-man BIOSOLVE-I trial. *Lancet*, 6736(12):1–9, 2013.
- [42] NT Kirkland, J Lespagnol, N Birbilis, and MP Staiger. A survey of bio-corrosion rates of magnesium alloys. *Corrosion Science*, 52(2):287–291, 2010.
- [43] CZ Deng, R Radhakrishnan, SR Larsen, DA Boismer, JS Stinson, AK Hotchkiss, EM Petersen, J Weber, and T Scheuermann. Magnesium alloys for bioabsorbable stents: a feasibility assessment. In *Magnesium Technology 2011*. Wiley, USA, March 2011.
- [44] MS Lee, D Jurewitz, J Aragon, J Forrester, RR Makkar, and S Kar. Stent fracture associated with drug-eluting stents: clinical characteristics and implications. *Catheterization and Cardiovascular Interventions*, 69(3):387–94, 2007.
- [45] S Lee, J Park, D Shin, Y Kim, G Hong, W Kim, and B Shim. Frequency of stent fracture as a cause of coronary restenosis after sirolimus-eluting stent implantation. *The American Journal of Cardiology*, 100(4):627–30, 2007.
- [46] J Aoki, G Nakazawa, K Tanabe, A Hoye, H Yamamoto, T Nakayama, Y Onuma, Y Higashikuni, S Otsuki, A Yagishita, S Yachi, H Nakajima, and K Hara. Incidence and clinical impact of coronary stent fracture after Sirolimus-eluting stent implantation. *Catheterization and Cardiovascular Interventions*, 69(3):380–6, 2007.
- [47] G Nakazawa, AV Finn, M Vorpahl, E Ladich, R Kutys, I Balazs, FD Kolodgie, and R Virmani. Incidence and predictors of drug-eluting stent fracture in hu-

## Bibliography

- man coronary artery a pathologic analysis. *Journal of the American College of Cardiology*, 54(21):1924–31, 2009.
- [48] DO Halwani, PG Anderson, BC Brott, AS Anayiotos, and JE Lemons. The role of vascular calcification in inducing fatigue and fracture of coronary stents. *Journal of Biomedical Materials Research. Part B, Applied Biomaterials*, 100(1):292–304, 2012.
- [49] D Askeland. *The Science and Engineering of Materials*. Cengage Learning, Stamford, CT, 2011.
- [50] S Graff, W Brocks, and D Steglich. Yielding of magnesium: From single crystal to polycrystalline aggregates. *International Journal of Plasticity*, 23(12):1957–1978, 2007.
- [51] MGD Geers. Size effects in miniaturized polycrystalline FCC samples : strengthening versus weakening. *International Journal of Solids and Structures*, 43(24):7304–7321, 2006.
- [52] PJM Janssen, THD Keijser, and MGD Geers. An experimental assessment of grain size effects in the uniaxial straining of thin Al sheet with a few grains across the thickness. *Materials Science and Engineering: A*, 419(1-2):238–248, 2006.
- [53] C Keller, E Hug, and X Feaugas. Microstructural size effects on mechanical properties of high purity nickel. *International Journal of Plasticity*, 27(4):635–654, 2011.
- [54] RW Armstrong. On size effects in polycrystal plasticity. *Journal of the Mechanics and Physics of Solids*, 9(3):196–199, 1961.

## Bibliography

- [55] A Jain, O Duygulu, DW Brown, CN Tom, and SR Agnew. Grain size effects on the tensile properties and deformation mechanisms of a magnesium alloy , AZ31B, sheet. *Materials Science and Engineering: A*, 486(1-2):545–555, 2008.
- [56] H Lim, MG Lee, JH Kim, BL Adams, and RH Wagoner. Simulation of polycrystal deformation with grain and grain boundary effects. *International Journal of Plasticity*, 27(9):1328–1354, 2011.
- [57] NA Fleck, GM Muller, MF Ashby, and JW Hutchinson. Strain gradient plasticity: theory and experiment. *Acta Metallurgica et Materialia*, 42(2):475–487, 1994.
- [58] JS Stölken and AG Evans. A microbend test method for measuring the plasticity length scale. *Acta Materialia*, 46(14):5109–5115, 1998.
- [59] MA Haque and MTA Saif. Strain gradient effect in nanoscale thin films. *Acta Materialia*, 51(11):3053–3061, 2003.
- [60] F Zhang, R Saha, Y Huang, W Nix, K Hwang, S Qu, and M Li. Indentation of a hard film on a soft substrate: strain gradient hardening effects. *International Journal of Plasticity*, 23(1):25–43, 2007.
- [61] E Arzt. Size effects in materials due to microstructural and dimensional constraints: a comparative review. *Acta Materialia*, 46(16):5611–5626, 1998.
- [62] C Keller, E Hug, R Retoux, and X Feugas. TEM study of dislocation patterns in near-surface and core regions of deformed nickel polycrystals with few grains across the cross section. *Mechanics of Materials*, 42(1):44–54, 2010.
- [63] M Klein, A Hadrboletz, B Weiss, and G Khatibi. The size effect on the stress-

## Bibliography

- strain ,fatigue and fracture properties of thin metallic foils. *Materials Science and Engineering: A*, 321:924–928, 2001.
- [64] LV Raulea, AM Goijaerts, LE Govaert, and FPT Baaijens. Size effects in the processing of thin metal sheets. *Journal of Materials Processing Technology*, 115(1):44–48, 2001.
- [65] J Gau, C Principe, and J Wang. An experimental study on size effects on flow stress and formability of aluminum and brass for microforming. *Journal of Materials Processing Technology*, 184(1):42–46, 2007.
- [66] M Lederer, V Gröger, G Khatibi, and B Weiss. Size dependency of mechanical properties of high purity aluminium foils. *Materials Science and Engineering: A*, 527(3):590–599, 2010.
- [67] TA Kals and R Eckstein. Miniaturization in sheet metal working. *Journal of Materials Processing Technology*, 103(1):95–101, 2000.
- [68] G Khatibi, A Betzwar-Kotas, V Groger, and B Weiss. A study of the mechanical and fatigue properties of metallic microwires. *Fatigue-Fracture of Engineering Materials and Structures*, 28(8):723–733, 2005.
- [69] XX Chen and AHW Ngan. Specimen size and grain size effects on tensile strength of Ag microwires. *Scripta Materialia*, 64(8):717–720, 2011.
- [70] G Kim. Modeling of the size effects on the behavior of Metals in microscale deformation. *Journal of Manufacturing Science and Engineering*, 129(3), 2007.
- [71] X Lai, L Peng, P Hu, S Lan, and J Ni. Material behavior modelling in

## Bibliography

- micro/meso-scale forming process with considering size/scale effects. *Computational Materials Science*, 43(4):1003–1009, 2008.
- [72] W Yun, D Peilong, X Zhenying, Y Hua, W Jiangping, and W Jingjing. A constitutive model for thin sheet metal in micro-forming considering first order size effects. *Materials and Design*, 31(2):1010–1014, 2010.
- [73] U Engel and R Eckstein. Microforming-from basic research to its realization. *Journal of Materials Processing Technology*, 125-126:35–44, 2002.
- [74] A Molotnikov, R Lapovok, CHJ Davies, W Cao, and Y Estrin. Size effect on the tensile strength of fine-grained copper. *Scripta Materialia*, 59(11):1182–1185, 2008.
- [75] Y Estrin, LS Tóth, A Molinari, and Y Bréchet. A dislocation-based model for all hardening stages in large strain deformation. *Acta Materialia*, 46(15):5509–5522, 1998.
- [76] LS Toth, A Molinari, and Y Estrin. Strain hardening at large strains as predicted by dislocation based polycrystal plasticity model. *Journal of Engineering Materials and Technology*, 124(1):71, 2002.
- [77] WL Chan, MW Fu, J Lu, and JG Liu. Modeling of grain size effect on micro deformation behavior in micro-forming of pure copper. *Materials Science and Engineering: A*, 527(24-25):6638–6648, 2010.
- [78] P Savage, BP O’Donnell, PE McHugh, BP Murphy, and DF Quinn. Coronary stent strut size dependent stress-strain response investigated using micromechanical finite element models. *Annals of Biomedical Engineering*, 32(2):202–11, 2004.

## Bibliography

- [79] B P Murphy, H Cuddy, F J Harewood, T Connolley, and P E McHugh. The influence of grain size on the ductility of micro-scale stainless steel stent struts. *Journal of Materials Science. Materials in Medicine*, 17(1):1–6, 2006.
- [80] FJ Harewood and PE McHugh. Modeling of size dependent failure in cardiovascular stent struts under tension and bending. *Annals of Biomedical Engineering*, 35(9):1539–53, 2007.
- [81] RJ Asaro and JR Rice. Strain localization in ductile single crystals. *Journal of the Mechanics and Physics of Solids*, 25(5):309–338, 1977.
- [82] D Peirce, RJ Asaro, and A Needleman. Material rate dependence and localized deformation in crystalline solids. *Acta Metallurgica*, 31(12):1951–1976, 1983.
- [83] J Cao, W Zhuang, S Wang, KC Ho, N Zhang, J Lin, and TA Dean. An integrated crystal plasticity FE system for microforming simulation. *Journal of Multiscale Modelling*, 1(1):107, 2009.
- [84] S Wang, W Zhuang, DS Balint, and J Lin. A crystal plasticity study of the necking of micro-films under tension. *Journal of Multiscale Modelling*, 1(3-4):331, 2009.
- [85] T Fülöp, WAM Brekelmans, and MGD Geers. Size effects from grain statistics in ultra-thin metal sheets. *Journal of Materials Processing Technology*, 174(1-3):233–238, 2006.
- [86] SI Liang-Ying, LU Cheng, K Tieu, and X Liu. Simulation of polycrystalline aluminum tensile test with crystal plasticity finite element method. *Transactions of the Nonferrous Metals Society China*, 17(6):1412–16, 2007.

## Bibliography

- [87] CJ Bayley, WAM Brekelmans, and MGD Geers. A three-dimensional dislocation field crystal plasticity approach applied to miniaturized structures. *Philosophical Magazine A*, 87:1361–1378, 2007.
- [88] JPM Hoefnagels, PJM Janssen, THD Keijser, and MGD Geers. First-order size effects in the mechanics of miniaturized components. *Applied Mechanics and Materials*, 14:183–192, 2008.
- [89] LP Evers, WAM Brekelmans, and MGD Geers. Scale dependent crystal plasticity framework with dislocation density and grain boundary effects. *International Journal of Solids and Structures*, 41(18-19):5209–5230, 2004.
- [90] C Keller, E Hug, AM Habraken, and L Duchene. Finite element analysis of the free surface effects on the mechanical behavior of thin nickel polycrystals. *International Journal of Plasticity*, 29:155–172, 2012.
- [91] G Song and A Atrens. Understanding magnesium corrosion: a framework for improved alloy performance. *Advanced Engineering Materials*, 5(12):837–858, 2003.
- [92] F Witte, N Hort, C Vogt, S Cohen, KU Kainer, R Willumeit, and F Feyerabend. Degradable biomaterials based on magnesium corrosion. *Current Opinion in Solid State and Materials Science*, 12(5-6):63–72, 2008.
- [93] A Atrens, M Liu, and NI Zainal Abidin. Corrosion mechanism applicable to biodegradable magnesium implants? *Materials Science and Engineering: B*, 176(20):1609–36, 2011.
- [94] LL Shreir, T Burnstein, and RA Jarman. *Corrosion 1. Metal/Environment Reactions*. Butterworth-Heinemann, Oxford, Boston, MA, 1994.

## Bibliography

- [95] B Liu and YF Zheng. Effects of alloying elements (Mn, Co, Al, W, Sn, B, C and S) on biodegradability and in vitro biocompatibility of pure iron. *Acta Biomaterialia*, 7(3):1407–20, 2011.
- [96] M Alvarez-Lopez, MD Pereda, JA del Valle, M Fernandez-Lorenzo, MC Garcia-Alonso, OA Ruano, and ML Escudero. Corrosion behaviour of AZ31 magnesium alloy with different grain sizes in simulated biological fluids. *Acta Biomaterialia*, 6(5):1763–71, 2010.
- [97] W Zhou, T Shen, and NN Aung. Effect of grain size and twins on corrosion behaviour of AZ31B magnesium alloy. *Corrosion Science*, 52(3):1035–1041, 2010.
- [98] R Walter and MB Kannan. Influence of surface roughness on the corrosion behaviour of magnesium alloy. *Materials and Design*, 32(4):2350–2354, 2011.
- [99] G Song. Control of biodegradation of biocompatible magnesium alloys. *Corrosion Science*, 49(4):1696–1701, 2007.
- [100] MB Kannan and L Orr. In vitro mechanical integrity of hydroxyapatite coated magnesium alloy. *Biomedical Materials*, 6(4):1–11, 2011.
- [101] HM Wong, KWK Yeung, KO Lam, V Tam, PK Chu, KDK Luk, and KMC Cheung. A biodegradable polymer-based coating to control the performance of magnesium alloy orthopaedic implants. *Biomaterials*, 31(8):2084–96, 2010.
- [102] Y Xin, T Hu, and PK Chu. In vitro studies of biomedical magnesium alloys in a simulated physiological environment: a review. *Acta Biomaterialia*, 7(4):1452–9, 2011.
- [103] R Rettig and S Virtanen. Time-dependent electrochemical characterization of

## Bibliography

- the corrosion of a magnesium rare-earth alloy in simulated body fluids. *Journal of Biomedical Materials Research. Part A*, 85(1):167–75, 2008.
- [104] A Yamamoto and S Hiromoto. Effect of inorganic salts, amino acids and proteins on the degradation of pure magnesium in vitro. *Materials Science and Engineering: C*, 29(5):1559–1568, 2009.
- [105] J Lévesque, H Hermawan, D Dubé, and D Mantovani. Design of a pseudo-physiological test bench specific to the development of biodegradable metallic biomaterials. *Acta Biomaterialia*, 4(2):284–95, 2008.
- [106] F Witte, V Kaese, H Haferkamp, E Switzer, A Meyer-Lindenberg, CJ Wirth, and H Windhagen. In vivo corrosion of four magnesium alloys and the associated bone response. *Biomaterials*, 26(17):3557–63, 2005.
- [107] L Xu, G Yu, E Zhang, F Pan, and K Yang. In vivo corrosion behavior of Mg-Mn-Zn alloy for bone implant application. *Journal of Biomedical Materials Research Part A*, 2007.
- [108] N Winzer, A Atrens, G Song, E Ghali, W Dietzel, KU Kainer, N Hort, and C Blawert. A critical review of the stress corrosion cracking (SCC) of magnesium alloys. *Advanced Engineering Materials*, 7(8):659–693, 2005.
- [109] M Bobby Kannan, W Dietzel, C Blawert, A Atrens, P Lyon, and M Bobbykannan. Stress corrosion cracking of rare-earth containing magnesium alloys ZE41, QE22 and Elektron 21 (EV31A) compared with AZ80. *Materials Science and Engineering: A*, 480(1-2):529–539, 2008.
- [110] MB Kannan. Influence of microstructure on the in-vitro degradation behaviour of magnesium alloys. *Materials Letters*, 64(6):739–742, 2010.

## Bibliography

- [111] MB Kannan and RKS Raman. In vitro degradation and mechanical integrity of calcium-containing magnesium alloys in modified-simulated body fluid. *Biomaterials*, 29(15):2306–14, 2008.
- [112] H Hermawan, A Purnama, D Dube, J Couet, and D Mantovani. Fe-Mn alloys for metallic biodegradable stents: degradation and cell viability studies. *Acta Biomaterialia*, 6(5):1852–60, 2010.
- [113] M Moravej and D Mantovani. Biodegradable metals for cardiovascular stent application: interests and new opportunities. *International Journal of Molecular Sciences*, 12(7):4250–4270, 2011.
- [114] M Peuster, P Wohlsein, M Brugmann, M Ehlerding, K Seidler, C Fink, H Brauer, A Fischer, and G Hausdorf. A novel approach to temporary stenting: degradable cardiovascular stents produced from corrodible metals results 6-18 months after implantation into New Zealand white rabbits. *Heart*, 86(5):563–569, 2001.
- [115] D Pierson, J Edick, A Tauscher, E Pokorney, P Bowen, J Gelbaugh, J Stinson, H Getty, CH Lee, J Drelich, and J Goldman. A simplified in vivo approach for evaluating the bioabsorbable behavior of candidate stent materials. *Journal of Biomedical Materials Research. Part B, Applied Biomaterials*, pages 1–10, 2011.
- [116] M Moravej, F Prima, M Fiset, and D Mantovani. Electroformed iron as new biomaterial for degradable stents: development process and structure-properties relationship. *Acta Biomaterialia*, 6(5):1726–35, 2010.
- [117] JX Jia, G Song, A Atrens, D St John, J Baynham, and G Chandler. Evaluation of the BEASY program using linear and piecewise linear approaches for the boundary conditions. *Materials and Corrosion*, 55(11):845–852, 2004.

## Bibliography

- [118] JX Jia, G Song, and A Atrens. Influence of geometry on galvanic corrosion of AZ91D coupled to steel. *Corrosion Science*, 48(8):2133–2153, 2006.
- [119] JX Jia, G Song, and A Atrens. Experimental measurement and computer simulation of galvanic corrosion of magnesium coupled to steel. *Advanced Engineering Materials*, 9(1-2):65–74, 2007.
- [120] Z Shi, JX Jia, and A Atrens. Galvanostatic anodic polarisation curves and galvanic corrosion of high purity Mg in 3.5% NaCl saturated with Mg(OH)<sub>2</sub>. *Corrosion Science*, 60:296–308, 2012.
- [121] KB Deshpande. Validated numerical modelling of galvanic corrosion for couples: Magnesium alloy (AE44)mild steel and AE44aluminium alloy (AA6063) in brine solution. *Corrosion Science*, 52(10):3514–3522, 2010.
- [122] J Xiao and S Chaudhuri. Predictive modeling of localized corrosion: An application to aluminum alloys. *Electrochimica Acta*, 56(16):5630–5641, 2011.
- [123] W Sun, G Liu, L Wang, and T Wu. An arbitrary Lagrangian Eulerian model for studying the influences of corrosion product deposition on bimetallic corrosion. *Journal of Solid State Electrochemistry*, 17(3):829–840, 2012.
- [124] L Kachanov. *Introduction to Continuum Damage Mechanics (Mechanics of Elastic Stability)*. Springer, 1986.
- [125] V Bolotin. Mechanical aspects of corrosion fatigue and stress corrosion cracking. *International Journal of Solids and Structures*, 38(40-41):7297–7318, 2001.
- [126] H Da Costa Mattos, I Bastos, and J Gomes. A simple model for slow strain

## Bibliography

- rate and constant load corrosion tests of austenitic stainless steel in acid aqueous solution containing sodium chloride. *Corrosion Science*, 50(10):2858–2866, 2008.
- [127] M Wenman, K Trethewey, S Jarman, and P Chardtuckey. A finite-element computational model of chloride-induced transgranular stress-corrosion cracking of austenitic stainless steel. *Acta Materialia*, 56(16):4125–4136, 2008.
- [128] D Gastaldi, V Sassi, L Petrini, M Vedani, S Trasatti, and F Migliavacca. Continuum damage model for bioresorbable magnesium alloy devices - application to coronary stents. *Journal of the Mechanical Behavior of Biomedical Materials*, 4(3):352–365, 2011.
- [129] JA Grogan, BJ O’Brien, SB Leen, and PE McHugh. A corrosion model for bioabsorbable metallic stents. *Acta biomaterialia*, 7(9):3523–33, 2011.
- [130] JA Grogan, SB Leen, and PE McHugh. Comparing coronary stent material performance on a common geometric platform through simulated bench-testing. *Journal of the Mechanical Behavior of Biomedical Materials*, 12:129–138, 2012.
- [131] W Wu, L Petrini, D Gastaldi, T Villa, M Vedani, E Lesma, B Previtali, and F Migliavacca. Finite element shape optimization for biodegradable magnesium alloy stents. *Annals of Biomedical Engineering*, 38(9):2829–40, 2010.
- [132] W Wu, D Gastaldi, K Yang, L Tan, L Petrini, and F Migliavacca. Finite element analyses for design evaluation of biodegradable magnesium alloy stents in arterial vessels. *Materials Science and Engineering: B*, 176(20):1733–40, 2011.
- [133] M Iqbal Sabir, EB Liu, Z Li, YF Zheng, and L Li. Magnesium alloy stent expansion behavior simulated by finite element method. *Applied Mechanics and Materials*, 232:697–700, 2012.

## Bibliography

- [134] DR Jones, M Schonlau, and J William. Efficient global optimization of expensive black-box functions. *Journal of Global Optimization*, 13(4):455–492, 1998.
- [135] T Belytschko, WK Liu, and B Moran. *Nonlinear Finite Elements for Continua and Structures*. Wiley, Chichester New York, 2000.
- [136] GA Holzapfel. *Nonlinear Solid Mechanics: A Continuum Approach for Engineering*. Wiley, 2000.
- [137] F Dunne and N Petrinic. *Introduction to Computational Plasticity*. Oxford University Press, USA, 2005.
- [138] L Malvern. *Introduction to the Mechanics of a Continuous Medium*. Prentice-Hall, Englewood Cliffs, N.J, 1969.
- [139] GA Holzapfel, G Sommer, CT Gasser, P Regitnig, and A Gerhard. Determination of layer-specific mechanical properties of human coronary arteries with nonatherosclerotic intimal thickening and related constitutive modeling. *American Journal of Physiology, Heart and Circulatory Physiology*, 289(5):2048–2058, 2005.
- [140] Y Huang. A user-material subroutine incorporating single crystal plasticity in the Abaqus finite element program. Technical report, Division of Applied Sciences, Harvard University, Cambridge, MA, USA, 1991.
- [141] JP McGarry, BP O’Donnell, PE McHugh, and JG McGarry. Analysis of the mechanical performance of a cardiovascular stent design based on micromechanical modelling. *Computational Materials Science*, 31(3-4):421–438, 2004.
- [142] R Hill and JR Rice. Constitutive analysis of elastic-plastic crystals at arbitrary

## Bibliography

- strain. *Journal of the Mechanics and Physics of Solids*, 20(6):401–413, 1972.
- [143] TJR Hughes and J Winget. Finite rotation effects in numerical integration of rate constitutive equations arising in large-deformation analysis. *International Journal for Numerical Methods in Engineering*, 15(12):1862–1867, 1980.
- [144] PD Lax and B Wendroff. Difference schemes for hyperbolic equations with high order of accuracy. *Communications on Pure and Applied Mathematics*, 17(3):381–398, 1964.
- [145] RJ LeVeque. *Finite Volume Methods for Hyperbolic Problems*. Cambridge University Press, Cambridge, 2002.
- [146] J Shi. *Gaussian Process Regression Analysis for Functional Data*. CRC Press, Boca Raton, FL, 2011.
- [147] N Cressie. *Statistics for spatial data*. Wiley, New York, 1993.
- [148] F Etave, G Finet, M Boivin, JC Boyer, G Rioufol, and G Thollet. Mechanical properties of coronary stents determined by using finite element analysis. *Journal of Biomechanics*, 34(8):1065–1075, 2001.
- [149] F Migliavacca, L Petrini, M Colombo, F Auricchio, and R Pietrabissa. Mechanical behavior of coronary stents investigated through the finite element method. *Journal of Biomechanics*, 35(6):803–811, 2002.
- [150] S Prabhu, T Schikorr, T Mahmoud, J Jacobs, A Potgieter, and C Simonton. Engineering assessment of the longitudinal compression behaviour of contemporary coronary stents. *EuroIntervention*, 8(2):275–281, 2011.

## Bibliography

- [151] JM Carson and JM Hawn. Some properties of iron, copper, and selected aluminium alloys including true stress-true strain at reduced temperatures. Technical report, Air Force Materials Laboratory, University of Dayton Research Institute, Dayton, OH, USA, 1968.
- [152] F Gervaso, C Capelli, L Petrini, S Lattanzio, L Di Virgilio, and F Migliavacca. On the effects of different strategies in modelling balloon-expandable stenting by means of finite element method. *Journal of Biomechanics*, 41(6):1206–1212, 2008.
- [153] M De Beule, P Mortier, SG Carlier, B Verheghe, R Van Impe, and P Verdonck. Realistic finite element-based stent design: the impact of balloon folding. *Journal of Biomechanics*, 41(2):383–389, 2008.
- [154] WD Callister and DG Rethwisch. *Fundamentals of Materials Science and Engineering : An Integrated Approach*. John Wiley and Sons, Hoboken, NJ, 2008.
- [155] L Petrini, F Migliavacca, F Auricchio, and G Dubini. Numerical investigation of the intravascular coronary stent flexibility. *Journal of Biomechanics*, 37(4):495–501, 2004.
- [156] W Wu, DZ Yang, M Qi, and WQ Wang. An FEA method to study flexibility of expanded coronary stents. *Journal of Materials Processing Technology*, 184(1-3):447–450, 2007.
- [157] K Mori and T Saito. Effects of stent structure on stent flexibility measurements. *Annals of Biomedical Engineering*, 33(6):733–742, 2005.
- [158] IB Menown, R Noad, EJ Garcia, and I Meredith. The platinum chromium element stent platform: from alloy, to design, to clinical practice. *Advances in Therapy*, 27(3):129–41, 2010.

## Bibliography

- [159] P Lanzer. *Mastering Endovascular Techniques : A Guide To Excellence*. Lippincott Williams and Wilkins, Philadelphia, PA, 2007.
- [160] CM Agrawal, KF Haas, DA Leopold, and HG Clark. Evaluation of poly(L-lactic acid) as a material for intravascular polymeric stents. *Biomaterials*, 13(3):176–182, 1992.
- [161] W Schmidt, P Behrens, and KP Schmitz. Biomechanical aspects of potential stent malapposition at coronary stent implantation. In *World Congress on Medical Physics and Biomedical Engineering, September, Munich, Germany*, pages 136–139. Springer Berlin Heidelberg, 2009.
- [162] S Venkatraman, TL Poh, T Vinalia, KH Mak, and F Boey. Collapse pressures of biodegradable stents. *Biomaterials*, 24(12):2105–2111, 2003.
- [163] R Liao, NE Green, SY Chen, JC Messenger, AR Hansgen, BM Groves, and JD Carroll. Three-dimensional analysis of in vivo coronary stent–coronary artery interactions. *The International Journal of Cardiovascular Imaging*, 20(4):305–313, 2004.
- [164] MF Gross and MH Friedman. Dynamics of coronary artery curvature obtained from biplane cineangiograms. *Journal of Biomechanics*, 31(5):479–484, 1998.
- [165] PK Bowen, J Drelich, and J Goldman. Zinc exhibits ideal physiological corrosion behavior for bioabsorbable stents. *Advanced Materials*, 25(18):2577–82, 2013.
- [166] ASM International. *Atlas of Stress-Strain Curves*. ASM International, OH, USA, 2002.
- [167] JP McGarry, BP ODonnell, PE McHugh, E OCearbhaill, and RM McMeeking.

## Bibliography

- Computational examination of the effect of material inhomogeneity on the necking of stent struts under tensile loading. *Journal of Applied Mechanics*, 74(5):978, 2007.
- [168] FJ Harewood and PE McHugh. Investigation of finite element mesh independence in rate dependent materials. *Computational Materials Science*, 37(4):442–453, 2006.
- [169] B Weiss and A Meissner. Ermüdung und mikrostruktur von koronaren stents. *Materialwissenschaft und Werkstofftechnik*, 37:755–761, 2006.
- [170] SG Chowdhury, S Das, and B Ravikumar. Twinning-induced sluggish evolution of texture during recrystallization in AISI 316L stainless steel after cold rolling. *Metallurgical and Material Transactions*, 37(8):2349–2359, 2005.
- [171] F Fritzen, T Böhlke, and E Schnack. Periodic three-dimensional mesh generation for crystalline aggregates based on Voronoi tessellations. *Computational Mechanics*, 43(5):701–713, 2008.
- [172] CB Barber, DP Dobkin, and H Huhdanpaa. The quickhull algorithm for convex hulls. *ACM Transactions on Mathematical Software*, 22(4):469–483, 1996.
- [173] P Connolly and PE McHugh. Fracture modelling of WC-Co hardmetals using crystal plasticity theory and the Gurson model. *Fatigue and Fracture of Engineering Materials and Structures*, 22(1):77–86, 1999.
- [174] J Teague, E Cerreta, and M Stout. Tensile properties and microstructure of haynes 25 alloy after aging at elevated temperatures for extended times. *Metallurgical and Materials Transactions A*, 35(9):2767–2781, 2004.

## Bibliography

- [175] F Harewood, J Grogan, and P McHugh. A multiscale approach to failure assessment in deployment for cardiovascular stents. *Journal of Multiscale Modelling*, 2(1):1–22, 2010.
- [176] EW Kelley and WF Hosford. Plane-strain compression of magnesium and magnesium alloy crystals. *Transactions of the Metallography Society of AIME*, 242:5, 1968.
- [177] EW Kelley and WF Hosford. The deformation characteristics of textured magnesium. *Transactions of the Metallography Society of AIME*, 242:654, 1968.
- [178] M Vedani, W Ge, Qand Wu, and L Petrini. Texture effects on design of Mg biodegradable stents. *International Journal of Material Forming*, pages 1–8, 2012.
- [179] AK Ghosh. Tensile instability and necking in materials with strain hardening and strain-rate hardening. *Acta Metallurgica*, 25(12):1413–1424, 1977.
- [180] JR Rice and DM Tracey. On the ductile enlargement of voids in triaxial stress fields. *Journal of the Mechanics and Physics of Solids*, 17(3):201–217, 1969.
- [181] J Kadkhodapour, A Butz, S Ziaei-rad, and S Schmauder. A micro mechanical study on failure initiation of dual phase steels under tension using single crystal plasticity model. *International Journal of Plasticity*, 27(7):1103–1125, 2011.
- [182] CA Sweeney, PE Mchugh, JP Mcgarry, and SB Leen. Micromechanical methodology for fatigue in cardiovascular stents. *International Journal of Fatigue*, 2012.
- [183] CA Sweeney, W Vorster, SB Leen, E Sakurada, PE McHugh, and FPE. Dunne. The role of elastic anisotropy, length scale and crystallographic slip in fatigue

## Bibliography

- crack nucleation. *Journal of the Mechanics and Physics of Solids*, 61(5):1224–1240, 2013.
- [184] S Zhang, X Zhang, C Zhao, J Li, Y Song, C Xie, H Tao, Y Zhang, Y He, Y Jiang, and Y Bian. Research on an Mg-Zn alloy as a degradable biomaterial. *Acta Biomaterialia*, 6(2):626–40, 2010.
- [185] L Yang and E Zhang. Biocorrosion behavior of magnesium alloy in different simulated fluids for biomedical application. *Materials Science and Engineering: C*, 29(5):1691–1696, 2009.
- [186] J Lemaitre. *A Course on Damage Mechanics*. Springer, Berlin New York, 1996.
- [187] J Lemaitre and R Desmorat. *Engineering Damage Mechanics Ductile, Creep, Fatigue and Brittle Failures*. Springer, Berlin New York, 2005.
- [188] A Papoulis. *Probability, Random Variables, and Stochastic Processes*. McGraw-Hill, New York, 1991.
- [189] MM Avedesian and H Baker. *Magnesium and Magnesium Alloys*. ASM International, Materials Park, OH, 1999.
- [190] C Di Mario, H Griffiths, O Goktekin, N Peeters, J Verbist, M Bosiers, K Deloose, B Heublein, R Rohde, V Kasese, C Ilsley, and R Erbel. Drug-eluting bioabsorbable magnesium stent. *Journal of Interventional Cardiology*, 17(6):391–5, 2004.
- [191] HM Loree, BJ Tobias, LJ Gibson, RD Kamm, DM Small, and RT Lee. Mechanical properties of model atherosclerotic lesion lipid pools. *Arteriosclerosis, Thrombosis, and Vascular Biology*, 14(2):230–234, 1994.

## Bibliography

- [192] WJ Chung, JW Cho, and T Belytschko. On the dynamic effects of explicit FEM in sheet metal forming analysis. *Engineering Computations*, 15(6):750–776, 1998.
- [193] Y Song, S Zhang, J Li, C Zhao, and X Zhang. Electrodeposition of Ca-P coatings on biodegradable Mg alloy: in vitro biomineralization behavior. *Acta Biomaterialia*, 6(5):1736–42, 2010.
- [194] R Zeng, J Zhang, W Huang, W Dietzel, KU Kainer, C Blawert, and W Ke. Review of studies on corrosion of magnesium alloys. *Transactions of Nonferrous Metals Society of China*, 16(S2):s763–s771, 2006.
- [195] W Wu, DZ Yang, YY Huang, M Qi, and WQ Wang. Topology optimization of a novel stent platform with drug reservoirs. *Medical Engineering and Physics*, 30(9):1177–85, 2008.
- [196] M De Beule, S Van Cauwer, P Mortier, D Van Loo, R Van Impe, P Verdonck, and B Verheghe. Virtual optimization of self-expandable braided wire stents. *Medical Engineering and Physics*, 31(4):448–53, 2009.
- [197] T Santner, BJ Williams, and WI Notz. *The Design and Analysis of Computer Experiments*. Springer, New York, 2003.
- [198] BJ Bichon, MS Eldred, LP Swiler, S Mahedevan, and JM McFarland. Multi-modal reliability assessment for complex engineering applications using efficient global optimization. In *Proceedings of the 48th AIAA/SME/ASCE/AHS/ASC Structures, Structural Dynamics and Materials Conference, Hawaii*. AIAA, 2007.
- [199] D Laroche, S Delorme, T Anderson, and R DiRaddo. Computer prediction of friction in balloon angioplasty and stent implantation. *Biomedical Simulation*, 4072:1–8, 2006.

## Bibliography

- [200] R Hicks and P Henne. Wing design by numerical optimization. *Journal of Aircraft*, 15:407–412, 1978.
- [201] N Li, C Guo, YH Wu, YF Zheng, and LQ Ruan. Comparative study on corrosion behaviour of pure Mg and WE43 alloy in static, stirring and flowing Hank’s solution. *Corrosion Engineering, Science and Technology*, 47(5):6, 2012.
- [202] W Wu, S Chen, D Gastaldi, L Petrini, D Mantovani, K Yang, L Tan, and F Migliavacca. Experimental data confirm numerical modeling of the degradation process of magnesium alloys stents. *Acta Biomaterialia*, In Press, 2012.
- [203] S Scheiner and C Hellmich. Stable pitting corrosion of stainless steel as diffusion-controlled dissolution process with a sharp moving electrode boundary. *Corrosion Science*, 49(2):319–346, 2007.
- [204] J Crank. *Free and Moving Boundary Problems*. Oxford University Press, USA, 1987.
- [205] E Javierre, C Vuik, FJ Vermolen, and S van der Zwaag. A comparison of numerical models for one-dimensional Stefan problems. *Journal of Computational and Applied Mathematics*, 192(2):445–459, 2006.
- [206] G Hill and JS Holman. *Chemistry in Context*. Nelson Thornes, 2000.
- [207] JF Yan, TV Nguyen, RE White, and RB Griffin. Mathematical modeling of the formation of calcareous deposits on cathodically protected steel in seawater. *Journal of the Electrochemical Society*, 140(3), 1993.
- [208] J Chessa, P Smolinski, and T Belytschko. The extended finite element method

## Bibliography

- (XFEM) for solidification problems. *International Journal for Numerical Methods in Engineering*, 53(8):1959–1977, 2002.
- [209] N Zabararas, B Ganapathysubramanian, and L Tan. Modelling dendritic solidification with melt convection using the extended finite element method. *Journal of Computational Physics*, 218(1):200–227, 2006.
- [210] A Burr and JB Cheatham. *Mechanical Analysis and Design*. Prentice Hall, Englewood Cliffs, N.J, 1995.
- [211] P Roberge. *Corrosion Engineering Principles and Practice*. McGraw-Hill, New York, 2008.